Doctoral Dissertation

博士論文

Search for Supersymmetric Partners of the Top Quark with Leptonic Signatures

(レプトニック終状態を用いたトップクォークの
超対称性パートナーの探索)

A Dissertation Submitted for the Degree of
Doctor of Philosophy

April 2020

令和２年４月　博士 (理学) 申請

Department of Physics, Graduate School of Science,
The University of Tokyo

東京大学大学院理学系研究科物理学専攻

Tomohiro Yamazaki

山﨑　友寛

Abstract

Supersymmetry (SUSY) is one of the most elegant theories that can provide solutions to the problems in the Standard Model. Natural SUSY models favor light scalar top quarks (stops) and higgsinos. This dissertation presents two searches for the direct productions of stops using collision data at a center of mass energy of $\sqrt{s} = 13$ TeV collected with the ATLAS detector at the Large Hadron Collider. The first search is performed using data collected in 2015–2016, corresponding to an integrated luminosity of 36 fb^{-1}. The lightest supersymmetric particle (LSP) is assumed to be a higgsino-like particle, and a large mass-splitting between the stop and the LSP is considered. This is the first search where the three decay modes of the stop decaying into the higgsino-like LSP are taken into account. The second search targets a small mass difference between the stop and the LSP, referred to as "compressed signal," using data collected in 2015–2018, corresponding to an integrated luminosity of 139 fb^{-1}. In order to increase the acceptance of the compressed signal, a novel identification technique for low momentum b-hadrons (soft b-tagging) has been developed. The soft b-tagging is an algorithm based on the secondary vertex reconstruction. It shows an improvement by a factor of 10 in the identification efficiency for low momentum b-hadrons compared to the standard b-hadron identification algorithm in ATLAS. In both searches, no significant excess over the Standard Model expectation is observed. Exclusion limits at 95% confidence level are derived for comprehensive decay scenarios. For the large mass-splitting in the higgsino-like LSP scenario, stop masses up to 800 GeV are excluded for the LSP mass of 150 GeV. In the compressed case with the stop four-body decay, the exclusion limit is extended by 240 GeV for the stop mass from the previous results, and stop masses up to 640 GeV for the LSP with a mass of 580 GeV are excluded.

Acknowledgements

First, I would like to express my deepest gratitude to my supervisor, Prof. Junichi Tanaka, for his continuous support, guidance, and encouragement. I would also like to express my appreciation to my former supervisor, Prof. Tatsuo Kawamoto. I appreciate the careful review and discussion during the defense by the reviewers: Prof. Yoshinari Hayato, Prof. Yutaka Ushiroda, Prof. Takeo Moroi, Prof. Wataru Ootani, and Prof. Hidetoshi Yamaguchi. I wish to pay my special regards to Keisuke Yoshihara, who supported me in all topics in this dissertation. Without him, I could not have obtained these results. I was lucky that I was able to start the analysis with SUSY third-generation experts, Takashi Yamanaka and Till Eifert, before starting my Ph.D. course. I learned a lot when I was working on my first stop search with 36 fb^{-1} data, thanks to the powerful analysis organization by Javier Montejo Berlingen and Sophie Pataraia, the excellent analysis framework from Jan Kuechler and Daniela Boerner, and the higgsino team with Christian Herwig and Kouta Onogi. The development of the soft b-tagging was super exciting, though, to be honest, I thought it would not be possible to make such a powerful tool. I wish to thank Hideyuki Oide for the technical support, and the soft b-tag co-developers: Iacopo Vivarelli, Francesca Ungaro, Samuel Jones, Mario Spina, and Peter Mcnamara. I spent a really enjoyable time to work on the full Run 2 analysis with the stop1L team. I thank Michaela Queitsch-Maitland and Frederik Ruehr, Sara Strandberg, Christophe Clement, Paola Arrubarrena Tamae, David Handl, Stefio Yosse Andrean, Prim Pasuwan, Laura Pereira Sanchez, and Julian Wollath for sharing the work and many discussions. We couldn't have done all these works without careful reviews from the SUSY (sub-)conveners: Zach Marshall, Federico Meloni, Rosa Simoniello, and Calum Macdonald. There were many useful discussions in the Tokyo ICEPP group with Yuji Enari, Tatsuya Masubuchi, Ryu Sawada, Yasuyuki Okumura, Koji Terashi, Tomoyuki Saito, and Takuya Nobe. Last but not least, I would like to recognize the invaluable support from my family.

Contents

Preface

This dissertation is based on my work in the ATLAS experiment during my Ph.D. program at The University of Tokyo in 2016-2020. I started physics analysis in 2016 for stop searches focusing on one-lepton final state (a.k.a. stop1L). Since then, I had opportunities to contribute to three publications: the stop1L analysis with data collected in 2015–2016 [1], the development of the soft b-tagging algorithm [2], and stop1L analysis with the full Run 2 data [3]. Here, I briefly describe my contribution to these publications.

Stop search analysis

I joined the stop1L analysis group in 2016. My contributions to the first publication [1] are as follows. I studied a new data-driven background estimation for $t\bar{t}$ with a lepton (electron or muon) and a hadronic tau, by replacing a lepton with a jet in di-leptonic $t\bar{t}$ events in data. I designed new higgsino-like LSP and bino-higgsino mixed signal models with Keisuke Yoshihara (was in UPenn, now in Iowa State) and Christian Herwig (was in UPenn, now in Fermilab), and generated signal MC samples. Targeting the stop-to-higgsino model with a b-quark and a chargino in final states, I designed an analysis by defining a set of regions (signal regions, control regions, and validation regions). I have also contributed to the evaluation of systematic uncertainties and signal acceptance in all regions in this publication. Furthermore, I have contributed to the development of a package called the stop-polarization tool. This is an essential tool to correct for spin polarization of particles emitted from the stop decay and to ensure the line shape of the angular distributions of stop signals.

For the analysis with the full Run 2 dataset [3], I played an essential role as a developer of the analysis software and produced common skimmed datasets for the whole analysis group. I have contributed to the generation of the stop four-body signals. I have designed a signal region (`bffN_softb`) using the soft b-tagging and also studied the background estimation. I implemented the signal regions in a truth-based framework (`SimipleAnalysis`). I performed statistical treatments for the four-body signal regions and implemented a statistical combination of two signal regions. I combined

all two-, three-, and four-body stop decay results and derived an exclusion limit for the paper.

Flavor tagging

I have contributed to the identification of heavy flavor hadrons (flavor tagging). I conducted a study of the b-tagging efficiency for c-jets which are misidentified as b-jets, using $D^{*\pm} \to D^0(\to K^{\mp}\pi^{\pm})\pi^{\pm}$ decays. This method cross-checked the standard c-jet calibration results measured by $t\bar{t}$ with the $W \to cs$ decay. I have been qualified as an ATLAS author with this work.

The development of the soft b-tagging algorithm [2] is a major contribution to the collaboration during my Ph.D. This is the first b-tagging algorithm targeting low momentum b-hadrons. I developed the Track-based Low p_{T} Vertex Tagger (T-LVT) algorithm, including the track selection, vertex fitting, and vertex selection, as well as new variables used in these steps. I evaluated the performance of the algorithm, together with the other soft b-tagging algorithms, which was published as a Conference Note [2]. Finally, I have proposed the calibration strategy of the T-LVT algorithm and performed the calibration, and validated the calibration in the context of the stop searches and applied the soft b-tagging in the analysis.

Detector upgrade

I had been working on the R&D of Micromegas detectors during the master course at The University of Tokyo in 2014-2016 [4]. I performed several irradiation tests for prototype detectors and evaluated the tracking performance at test beams for the New Small Wheel upgrade in ATLAS. I have also contributed to the quality control of the resistive anode foils of the Micromegas detector.

Chapter 1

Introduction

The smallest unit of matter is one of the fundamental questions in science. As of today, it is called an elementary particle, and the best knowledge on the elementary particles is well described by the Standard Model (SM) of particle physics [5–8]. The SM is the most successful achievement of particle physics in the 20th century and explains many experimental results with remarkable precision. The discovery of the Higgs boson in 2012 [9, 10] was a notable achievement in this century, and it was the final piece of the undiscovered SM particles. As the precision of experimental results improved, some observations that cannot be explained by the SM have appeared. For example, the existence of dark matter (DM) is strongly supported by the observation of the universe [11–15], but no SM particle satisfies the properties of DM. The masses of neutrinos should not be zero to explain the neutrino oscillations [16–18], but the masses of neutrinos are exactly zero in the SM due to the lack of right-handed neutrinos. The model itself also contains mysteries of particle physics. There are four forces that interact between particles: the strong, weak, electromagnetic, and gravitational forces. The SM is a framework that summarizes the former three forces but does not contain the gravitational force. There is a huge gap between the energy scale of gravity and the mass of the Higgs boson. It is difficult to explain the unnatural gap in the regime of the SM, and this problem is called the *hierarchy problem*.

The next target of particle physics is to find new physics beyond the SM that solves these problems. An extension of the SM is strongly believed to account for these observations that cannot be explained in the framework of the SM. There are many theories that could explain these mysteries, but none of them is confirmed by an experimental result. A discovery of a non-SM particle could be a smoking gun of a new physics model beyond the SM. *Supersymmetry* (SUSY) [19–25] is one of the leading candidates among theories beyond the SM. SUSY is a symmetry between bosons and fermions and predicts a boson (fermion) partner for each fermion (boson) particle. SUSY was proposed in the 1970s based on the quantum field theory, and it is now a well-established theory in particle physics though no

evidence of SUSY has been found. Despite the lack of experimental evidence, SUSY has been an attractive theory because it provides an elegant solution to the hierarchy problem and DM candidates, and the Grand Unification could be possible if SUSY exists [26–29]. According to the Naturalness [30, 31], the supersymmetric partners of the top quark and Higgs boson, the scalar top quark (stop) and higgsinos, respectively, are considered to be light [32,33]. If the mass of the stop is smaller than around 1 TeV, the Large Hadron Collider (LHC) with the center-of-mass-energy of 13 TeV has the potential to produce enough stop pairs for discovery. Experimental evidence of at least one of these new particles as an excess over the prediction of the SM processes in data would indicate the existence of new physics.

This dissertation presents searches for the stop production at the LHC, mainly focusing on a scenario where the lightest neutral higgsino is the lightest supersymmetric particle (LSP). In this scenario, the stop produced in pp collisions decays into the higgsino-like LSP, which is a stable particle that does not interact with the detector, and SM particles. Two searches are performed to cover the scenario widely. The first search [1] targets a scenario with a large mass difference between the stop and LSP ($\Delta m(\tilde{t}_1, \tilde{\chi}_1^0)$) using data collected in 2015–2016. The higgsino-like LSP scenario is characterized by small mass-splittings (Δm) between three higgsino states. The small Δm emits low-momentum particles, which makes the search difficult. The analysis extends the search sensitivity by exploiting low-momentum leptons. In the context of the stop searches, final states often contain b-hadrons. b-hadrons are identified by the *b-tagging* technique exploiting the long lifetime of b-hadrons. In the compressed stop scenario, where the mass difference between the stop and LSP is small such as 20 GeV, the final states contain low-momentum b-hadrons. Since the standard b-tagging algorithm in ATLAS is sub-optimal for such low-momentum b-hadrons, a new b-tagging algorithm optimized for low-momentum b-hadrons (*soft b-tagging*) [2] has been developed. The second stop search [3] aims for the small $\Delta m(\tilde{t}_1, \tilde{\chi}_1^0)$ signature with the novel soft b-tagging. This analysis is performed with the data collected in 2015–2018, and optimized using a simplified stop signal model [34–36], where a stop decays into the LSP without considering other SUSY particles.

The theoretical framework of the SM and SUSY is reviewed in Chapter 2. The experimental apparatuses, the LHC and ATLAS, are reviewed in Chapter 3. The data and Monte Carlo (MC) simulation used in this dissertation are explained in Chapter 4. The standard reconstruction algorithms used in ATLAS are documented in Chapter 5. The general stop analysis strategy is explained in Chapter 6 before discussing details of the individual analyses. The stop search targeting higgsino-like LSP with large $\Delta m(\tilde{t}_1, \tilde{\chi}_1^0)$ is described in Chapter 7. The details of the soft b-tagging for the small $\Delta m(\tilde{t}_1, \tilde{\chi}_1^0)$ are explained in Chapter 8, which is then applied to the analysis targeting the compressed scenario described

in Chapter 9. The results of the two searches are discussed in Chapter 10. At the end, a conclusion is presented in Chapter 11.

Chapter 2

Theoretical Background

2.1 The Standard Model

The Standard Model (SM) is a quantum field theory that describes behavior of elementary particles. The theory is based on $SU(3)_C \times SU(2)_L \times U(1)_Y$. The Lagrangian of the SM is

$$\begin{aligned}\mathcal{L} = & \overline{\psi}_i \not{\partial} \psi \\ & - g_1 \overline{\psi} \not{B} \psi - \frac{1}{4} B^{\mu\nu} B_{\mu\nu} \\ & - g_2 \overline{\psi} \not{W} \psi - \frac{1}{4} W^{\mu\nu} W_{\mu\nu} \\ & - g_3 \overline{\psi} \not{G} \psi - \frac{1}{4} G^{\mu\nu} G_{\mu\nu} \\ & + \overline{\psi}_i y_{ij} \psi_j \phi + \text{h.c.} \\ & + |D_\mu \phi|^2 - V(\phi), \end{aligned} \tag{2.1}$$

with a fermion field ψ, a Higgs field ϕ, electroweak gauge fields $B^{\mu\nu}$ and $W^{\mu\nu}$, and a gluon field $G^{\mu\nu}$. The first line describes the kinetic term of fermions, and the second, third, and forth lines show interactions between gauge fields and fermions, and interactions of the gauge fields themselves. The fifth and sixth lines are related to the Higgs field with a potential $V(\phi)$. The g_1, g_2, g_3, and y_{ij} are the coupling constants in each interaction. The Lagrangian of the SM is determined from the gauge symmetry, requiring invariant of the Lagrangian under gauge transformations.

The particles in the SM are listed in Tables 2.1–2.2. The last piece of the SM particles, the Higgs boson, was discovered at the LHC in 2012 [9, 10].

2.1.1 Problems of the Standard Model

Nature has two typical energy scales, the electroweak scale at the order of 10^2 GeV and the Planck scale at the order of 10^{19} GeV. The light masses of the gauge bosons and quarks

Table 2.1: List of the SM fermions. All listed particles have a spin of 1/2. The masses are measured values taken from reference [37].

quarks	electric charge	mass	leptons	electric charge	mass
u	$+2/3$	2.2 MeV	e	-1	511 keV
d	$-1/3$	4.7 MeV	ν_e	0	< 225 eV
c	$+2/3$	1.3 GeV	μ	-1	106 MeV
s	$-1/3$	93 MeV	ν_μ	0	0.19 MeV
t	$+2/3$	173 GeV	τ	-1	1.78 GeV
b	$-1/3$	4.2 GeV	ν_τ	0	< 18.2 MeV

Table 2.2: List of the SM bosons. The masses are measured values taken from reference [37].

particles	electric charge	spin	mass
g	0	1	0
γ	0	1	0
$W^\pm$	± 1	1	80.4 GeV
Z	0	1	91.2 GeV
H	0	0	125.1 GeV

are explained by the local gauge symmetry and chiral symmetry in the SM. However, there is no symmetry in the SM that keeps the Higgs mass at the electroweak scale. The huge gap between the Higgs mass and the Planck scale is considered unnatural, which is known as the hierarchy problem. The correction to the Higgs mass contains a loop effect shown in Figure 2.1 left. This loop correction, which induces a quadratic divergence of the Higgs mass contains a term

$$\Delta m_h^2 = \text{const.} \times g^2 \Lambda^2, \tag{2.2}$$

where g is a coupling strength between the Higgs boson and a fermion, and Λ is a cutoff parameter which corresponds to an energy scale from which new physics at the high energy scale needs to be considered.

The strong, weak, and electromagnetic forces could unify to one force at the grand unification scale of 10^{16} GeV. The gap between the EW scale of 10^2 GeV and the grand unification scale introduces a problem because of the quadratic divergent correction. When Λ in equation (2.2) is at the grand unification scale, the correction is an order of 10^{32} GeV^2, while the square of the bare Higgs mass is an order of 10^4 GeV^2. The mass of the Higgs boson is given by the correction, which is 28 orders of magnitude larger than the tree-level

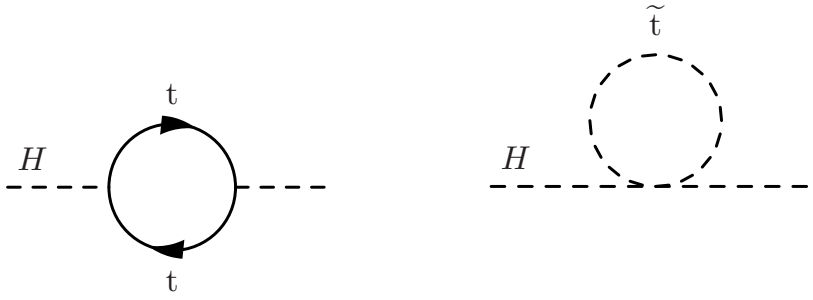

Figure 2.1: Loop corrections to the Higgs mass. The left diagram is the fermion loop that induces the quadratic divergence of the Higgs mass. The right diagram is a bosonic counterpart of the fermion loop, which has an opposite sign of the fermion term, resulting in the cancellation of the divergence.

term. A huge fine-tuning is needed to achieve this correction, and it is not *natural*. The fine-tuning problem is caused by the fermion loop in the Higgs mass. In order to avoid the problem, one possible solution is to cancel the fermion loop by introducing a boson loop with the same coupling and an opposite sign to the fermion loop, as shown in Figure 2.1 right.

Cosmological observations have revealed that visible material that can be observed by telescopes is not enough to account for the material in the universe, and there is more invisible matter than the known visible material. The invisible matter is called dark matter (DM). Figure 2.2 shows two pieces of evidence of DM. The first evidence of DM is the rotation velocity of the galaxy shown in Figure 2.2 left [38]. The expected rotation velocity from the visible disk around the galaxy has a peak at a certain distance from the center (R), and then decreases as a function of R. However, the rotation velocity observed using the 21 cm line emitted from hydrogen atoms shows the different feature, and that indicates additional invisible material around the galaxy (halo). The density of the invisible halo is consistent with the non-relativistic dark matter models (cold dark matter). The right image in Figure 2.2 shows the observation of a bullet cluster [39], which consists of two colliding clusters of galaxies, by two methods, X-ray and gravitational lensing effect. The distribution of gaseous material observed by detecting X-rays is shown in red, while the gravitational lens observation is sensitive to massive material shown in blue. As can be seen in the image, the two distributions do not agree with each other. This can be explained by the existence of DM. The visible gas interacts with the gas of the other galaxy, so that the distribution of the gas remains around the collision area, while DM mostly passes through due to the

feeble interaction of DM. In the SM, there is no candidate particle that is consistent with these observations.

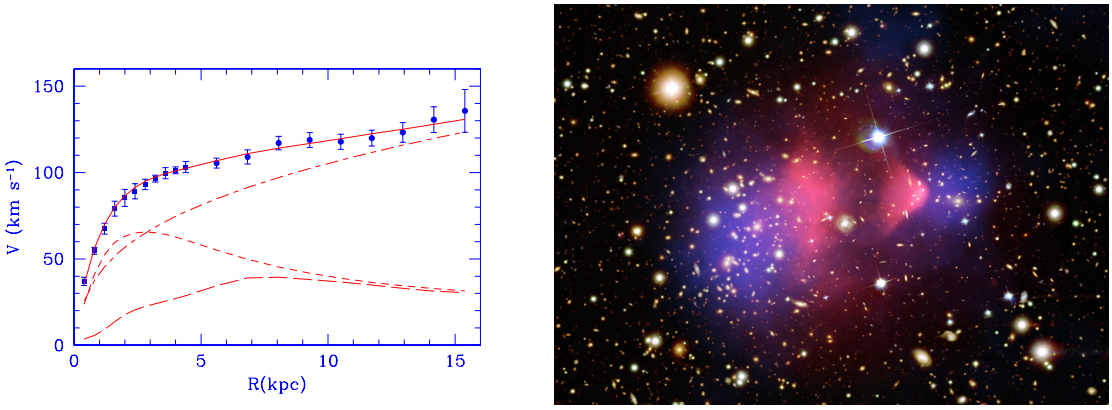

Figure 2.2: Evidences of the DM. (left) The rotation velocity of the galaxy M33 as a function of the distance from the center of the galaxy [38]. The points show the observed M33 rotation curve with the best fit model (solid line). The contribution of the halo (dashed-dotted line), stellar disk (short dashed line) and gas (long dashed line) are shown together. (right) Image of Bullet Cluster 1E0657-558 [39]. Image of the bullet cluster observed by X-ray is shown in red and the cluster observed by gravitational lensing effect is shown in blue.

2.2 Supersymmetry

Supersymmetry is a symmetry between bosons and fermions, which provides boson partners to fermion particles of the SM and vice versa. A supersymmetric operator Q transforms a boson state into a fermion state and vice versa. This can be written as

$$Q\,|\text{Boson}\rangle = |\text{Fermion}\rangle \tag{2.3}$$

$$Q\,|\text{Fermion}\rangle = |\text{Boson}\rangle\,. \tag{2.4}$$

The operator Q satisfies the following anti-commutation and commutation relations,

$$\{Q, Q^\dagger\} = P^\mu \tag{2.5}$$

$$\{Q, Q\} = \{Q^\dagger, Q^\dagger\} = 0 \tag{2.6}$$

$$[P^\mu, Q] = [P^\mu, Q^\dagger] = 0. \tag{2.7}$$

Here P^μ is a generator of spacetime translations, and $Q^\dagger$ is the hermitian conjugate of Q. The third equation (2.7) indicates that Q is exchangeable with $m^2 = P^\mu P_\mu$, resulting in that the operator Q does not change the mass. Hence, fermion and boson partners,

for example, the electron in the SM and its supersymmetric partner, have the same mass. SUSY particles are partners of the SM particles, and the properties of the SUSY particles are described by the same expression as that of the SM except for their spin. In the real world, however, such supersymmetric partners have not been discovered yet; for example, there is no supersymmetric partner of the electron, which is a boson with $m_e = 511$ keV. Supersymmetry should be broken so that fermion and boson partners have different masses to account for the fact. The quantum numbers related to $SU(3) \times SU(2) \times U(1)$ of SUSY particles are identical to ones of the SM particles, and the pair has the same coupling constants.

The electroweak theory combines electromagnetic and weak forces. The grand unification theory (GUT) is a theory that combines the electroweak theory and the theory of the strong force, QCD. These forces have different strengths at the energy scale where the current experiments can reach, but at a much higher energy scale, these interactions could be unified to a single coupling. The three couplings approach together as the energy scale goes higher, which raises hopes for the unification. The precise measurements of the coupling strength at the LEP have unveiled the behavior of the couplings running to the higher scale, as shown in Figure 2.3. Three lines do not cross at a common point, which indicates that the GUT cannot happen in the SM. However, if the SUSY breaking scale is around O(TeV), the three coupling lines share a common point at around 10^{16} GeV. This indicates the possibility of the GUT at that energy scale and above.

2.2.1 MSSM

The Minimal Supersymmetric Standard Model (MSSM) [40, 41] is a minimum supersymmetric extension of the SM. The particles in the MSSM are listed in Table 2.3. Each SM particle has a supersymmetric partner with a spin which is shifted by 1/2 from that of the SM. The Lagrangian of the MSSM can be split into two parts as

$$\mathcal{L}^{\mathrm{MSSM}} = \mathcal{L}^{\mathrm{MSSM}}_{\mathrm{SUSY}} + \mathcal{L}^{\mathrm{MSSM}}_{\mathrm{soft}}, \tag{2.8}$$

where the first part $\mathcal{L}^{\mathrm{MSSM}}_{\mathrm{SUSY}}$ describes the properties of the SUSY particles that are the same as ones of the SM particles. The second part $\mathcal{L}^{\mathrm{MSSM}}_{\mathrm{soft}}$ describes the soft breaking terms of the MSSM, which are essential when discussing the phenomenology of the MSSM particles. The soft breaking Lagrangian can be expanded to

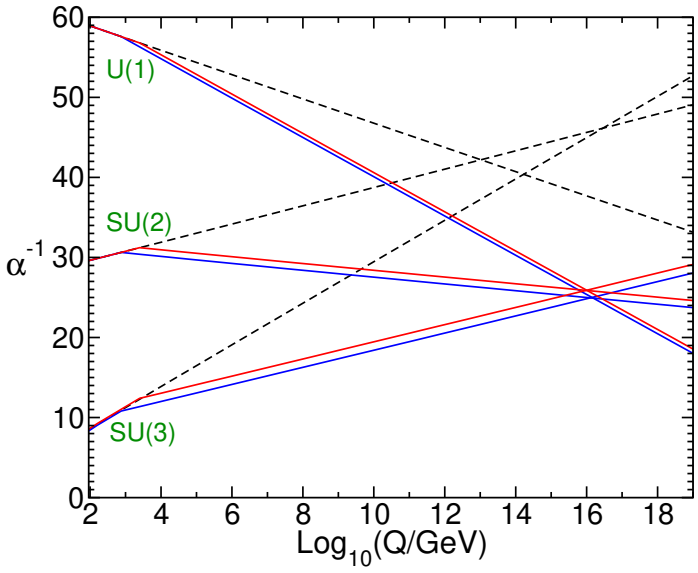

Figure 2.3: Renormalization evolution of the inverse gauge couplings [25]. The renormalization group running is calculated, including up to two-loop effects. The dashed lines show the SM, while the solid lines show the MSSM. The red and blue lines correspond to the threshold of MSSM particle masses at 750 GeV and 2.5 TeV, respectively.

$$
\begin{aligned}
\mathcal{L}_{\rm soft}^{\rm MSSM} = & -\frac{1}{2}\left(M_3\tilde{g}\tilde{g} + M_2\tilde{W}\tilde{W} + M_1\tilde{B}\tilde{B} + \text{c.c.}\right) \\
& - \left(\tilde{\bar{u}}\mathbf{a_u}\tilde{Q}H_u - \tilde{\bar{d}}\mathbf{a_d}\tilde{Q}H_d - \tilde{\bar{e}}\mathbf{a_e}\tilde{L}H_d + \text{c.c.}\right) \\
& - \tilde{Q}^\dagger\mathbf{m_Q^2}\tilde{Q} - \tilde{L}^\dagger\mathbf{m_L^2}\tilde{L} - \tilde{\bar{u}}\mathbf{m_{\bar{u}}^2}\tilde{\bar{u}}^\dagger - \tilde{\bar{d}}\mathbf{m_{\bar{d}}^2}\tilde{\bar{d}}^\dagger - \tilde{\bar{e}}\mathbf{m_{\bar{e}}^2}\tilde{\bar{e}}^\dagger \\
& - m_{H_u}^2 H_u^* H_u - m_{H_d}^2 H_d^* H_d - (bH_uH_d + \text{c.c.}).
\end{aligned} \tag{2.9}
$$

Here $\overline{u}$, $\overline{d}$, and $\overline{e}$ are supermultiplets of right handed fermions, and Q and L are left-handed supermultiplets. A supermultiplet contains a pair of SM and SUSY particles. The symbols for SUSY particles are the same as the ones for the SM particles but a tilde ($\tilde{}$) is added for SUSY particles. The first line represents the gaugino masses. The masses of the gluino, wino, and bino are given by M_3, M_2, and M_1, respectively. The second line shows the trilinear couplings, which describes Yukawa coupling where left-handed and right-handed scalar particles are involved. The third line describes the mass terms of squarks and sleptons, and here $\mathbf{m_Q^2}$, $\mathbf{m_L^2}$, $\mathbf{m_{\bar{u}}^2}$, $\mathbf{m_{\bar{d}}^2}$, and $\mathbf{m_{\bar{e}}^2}$ are complex 3×3 matrices, which correspond to the masses of the particles. The last line corresponds to the Higgs potential in the MSSM.

The name of the supersymmetric particles with a spin 1/2 is given by adding *-ino* to the end of the SM particle's name, and the name of the spin 0 particles is given by adding *scalar* on top of the SM particle's name. The scalar particles are also called by adding *s-*

to the SM particle's name. For example, the supersymmetric partner of the top quark is called *scalar top* (*quark*), or *stop*.

If SUSY exists, at least two Higgs doublets (H_u and H_d) are required while the SM has a Higgs doublet [42]. The ratio between the two vacuum expected values of $v_u = \langle H_u \rangle$ and $v_d = \langle H_d \rangle$,

$$\tan\beta = \frac{v_u}{v_d} \tag{2.10}$$

is an important parameter that governs the phenomenology. The neutral Higgs boson that corresponds to the Higgs boson with $m_H = 125$ GeV is a linear combination of H_u^0 and H_d^0.

Table 2.3: List of supersymmetric partners with the SM particles [25]. For quarks, leptons, squarks, and sleptons, only the first generation is listed.

SM			SUSY		
name	particle	spin	name	particle	spin
quarks	$(u_L,\, d_L)$	1/2	squarks	$(\tilde{u}_L,\tilde{d}_L)$	0
	u_R	1/2		$\tilde{u}_R$	0
	d_R	1/2		$\tilde{d}_R$	0
leptons	$(e_L,\, \nu_L)$	1/2	sleptons	$(\tilde{e}_L,\tilde{\nu}_L)$	0
	e_R	1/2		$\tilde{e}_R$	0
	ν_R	1/2		$\tilde{\nu}_R$	0
Higgs	$(H_u^+,\, H_u^0)$	0	higgsinos	$(\tilde{H}_u^+,\tilde{H}_u^0)$	1/2
	$(H_d^-,\, H_d^0)$	0		$(\tilde{H}_d^-,\tilde{H}_d^0)$	1/2
gluon	g	1	gluino	$\tilde{g}$	1/2
W boson	$W^\pm,\, W^0$	1	wino	$\tilde{W}^\pm,\, \tilde{W}^0$	1/2
B boson	B^0	1	bino	$\tilde{B}^0$	1/2

2.2.2 R-parity

It is possible to add terms that violate either lepton number or baryon number conservation to the potential in the SUSY Lagrangian as can be written as

$$W_{\Delta L=1} = \frac{1}{2}\lambda^{ijk} L_i L_j \overline{e}_k + \lambda'^{ijk} L_i Q_j \overline{d}_k + \mu'^i L_i H_u, \tag{2.11}$$

$$W_{\Delta B=1} = \frac{1}{2}\lambda''^{ijk} \overline{u}_i \overline{d}_j \overline{d}_k. \tag{2.12}$$

In these expressions, λ^{ijk}, λ'^{ijk}, λ''^{ijk}, and μ'^i are coupling constants of each term.

However, in many theories, these terms are considered to be small, mainly due to two reasons. First, there is no experimental observation that supports the violation of these numbers. The fact that the proton decay has not been discovered implies the non-violation of baryon and lepton number conservation since the process of the proton decay changes both

lepton and baryon numbers by a unit of one. The second reason is that introducing these terms is not favored in terms of DM. It becomes difficult to explain a dark matter candidate within the framework of the SUSY including one of these violation terms. To conserve baryon and lepton numbers, a new symmetry called R-parity has been introduced [43] as

$$R = (-1)^{3(B-L)+2s}, \tag{2.13}$$

where B, L, and s are the baryon number, lepton number, and spin of the particle, respectively. All particles in the SM have $R = 1$, while all SUSY particles have $R = -1$. If the R-parity is conserved, SUSY particles must be produced in a pair, and decay into particles in which an odd number of SUSY particles are included. Hence the lightest supersymmetric particle (LSP) must be stable. Due to its stability and weakness of the interaction, the LSP is a leading candidate for DM. From the cosmological constraints, DM cannot have a color or an electric charge; thus, the LSP is considered to be one of the neutral SUSY particles. In many models, the lightest neutralino is the LSP. The neutralino is electrically neutral and does not have colors; hence like neutrinos, the neutralino LSP cannot be detected by the detector in collider experiments.

2.2.3 SUSY Breaking

As mentioned earlier, SUSY must be broken in order to explain the absence of SUSY particles with the same masses as the ones of SM particles. There are some models that describe mechanisms of the SUSY breaking. In these models, the SUSY breaking occurs in a hidden sector, and the effect is propagated to the MSSM sector via a mediator, which depends on the model.

Gravity-mediated supersymmetry breaking (Supergravity, SUGRA)

The supergravity (SUGRA) model [44–46] is the most popular model which describes SUSY breaking with a small number of parameters. The minimal SUGRA model (mSUGRA) is a simplified model that contains five parameters: the scalar mass (m_0) and gaugino mass ($m_{1/2}$) at the GUT scale, $\tan\beta$, trilinear coupling A_0, and the sign of the higgsino mass sign (μ). The masses of the particles at a lower energy scale can be obtained by the renormalization group equations from the masses at the GUT scale, as shown in Figure 2.4.

Gauge-mediated supersymmetry breaking (GMSB)

The gauge-mediated supersymmetry breaking (GMSB) model [47–49] consists of a hidden sector where the SUSY is broken, and a messenger sector with messenger particles, and the MSSM sector. In this scenario, the gauge interactions transfer the

SUSY breaking effects from the messenger sector to the MSSM sector. In this model, the LSP is the supersymmetric partner of the graviton, gravitino, which is considered to be light, such as an order of keV or lower.

Anomaly-mediated supersymmetry breaking (AMSB)

In the anomaly-mediated supersymmetry breaking (AMSB) [50,51] model, the SUSY breaking occurs on a brane, which is separated from the brane where the MSSM lies, and the breaking is mediated via supergravity effects. In this model, a wino-like LSP is favored.

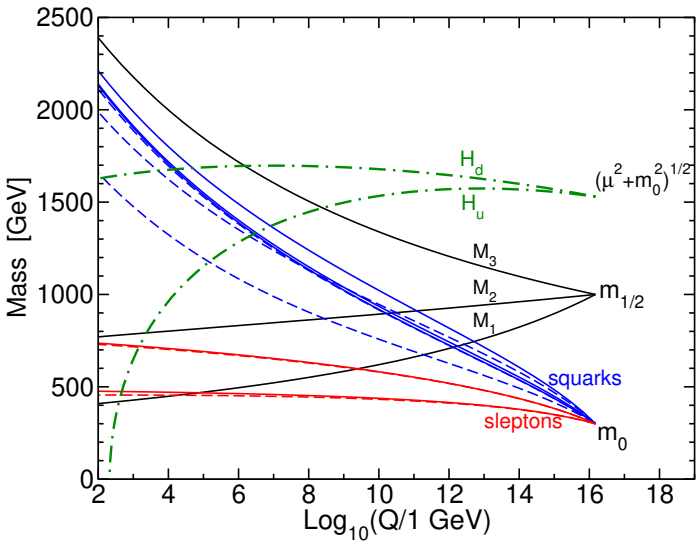

Figure 2.4: Renormalization evolution of the mass parameters in the MSSM with a mSUGRA scenario [25]. The scalar and gaugino masses are given by common masses at the GUT scale, m_0 and $m_{1/2}$ respectively, and the running to lower scale is determined by the renormalization group equations.

2.2.4 Neutralinos and Charginos

The electroweak gauginos and higgsinos mix with each other and form mass eigenstates. The four neutral particles ($\tilde{H}_u^0$, $\tilde{H}_d^0$, $\tilde{B}$, and $\tilde{W}^0$) form *neutralinos* and the charged states ($\tilde{H}_u^+/\tilde{H}_d^-$ and $\tilde{W}^\pm$) form *charginos*. The neutralinos are denoted by $\tilde{\chi}_1^0$, $\tilde{\chi}_2^0$, $\tilde{\chi}_3^0$, and $\tilde{\chi}_4^0$, while the charginos are denoted by $\tilde{\chi}_1^\pm$ and $\tilde{\chi}_2^\pm$. In these expressions, the numbers in the subscript of $\tilde{\chi}$ are assigned in ascending order of their masses. By definition, the LSP is denoted by $\tilde{\chi}_1^0$ when a neutralino is the LSP. The mass matrix of the neutralinos is given as

$$\mathbf{M}_{\tilde{N}} = \begin{pmatrix} M_1 & 0 & -c_\beta s_W m_Z & s_\beta s_W m_Z \\ 0 & M_2 & c_\beta s_W m_Z & -s_\beta s_W m_Z \\ -c_\beta s_W m_Z & c_\beta c_W m_Z & 0 & -\mu \\ s_\beta s_W m_Z & -s_\beta c_W m_Z & -\mu & 0 \end{pmatrix}, \tag{2.14}$$

where $s_\beta = \sin\beta$, $c_\beta = \cos\beta$, $s_W = \sin\theta_W$, and $c_W = \cos\theta_W$ with the electroweak mixing angle θ_W. The masses of the neutralinos are obtained by diagonalizing the mass matrix $\mathbf{M}_{\tilde{N}}$. Similarly, the mass matrix for charginos is given by

$$\mathbf{M}_{\tilde{C}} = \begin{pmatrix} \mathbf{0} & \mathbf{X}^T \\ \mathbf{X} & \mathbf{0} \end{pmatrix}, \tag{2.15}$$

with

$$\mathbf{X} = \begin{pmatrix} M_2 & \sqrt{2} s_\beta m_W \\ \sqrt{2} c_\beta m_W & \mu \end{pmatrix}. \tag{2.16}$$

2.2.5 Scalar Top Quarks

Similar to the mixing in neutralinos and charginos, the right- and left-handed squarks are also mixed. A large mixing could happen for the stop case due to the large Yukawa coupling of the top, while the mixing is negligible for the first and second generation squarks. The Lagrangian of the stop mass term is given as

$$\mathcal{L}_{\text{stop}}^{\text{mass}} = \begin{pmatrix} \tilde{t}_L^* & \tilde{t}_R^* \end{pmatrix} \mathbf{m}_{\tilde{\mathbf{t}}}^{\mathbf{2}} \begin{pmatrix} \tilde{t}_L \\ \tilde{t}_R \end{pmatrix} \tag{2.17}$$

with the stop mass matrix

$$\mathbf{m}_{\tilde{t}}^2 = \begin{pmatrix} m_{Q_3}^2 + m_t^2 + \Delta_{\tilde{u}_L} & v(A_t^* \sin\beta - \mu y_t \cos\beta) \\ v(A_t \sin\beta - \mu^* y_t \cos\beta) & m_{\tilde{u}_3}^2 + m_t^2 + \Delta_{\tilde{u}_R} \end{pmatrix}, \tag{2.18}$$

with $\Delta_{\tilde{u}_L} = \left(\frac{1}{2} - \frac{2}{3}\sin^2\theta_W\right)\cos(2\beta) m_Z^2$ and $\Delta_{\tilde{u}_R} = \left(\frac{2}{3}\sin^2\theta_W\right)\cos(2\beta) m_Z^2$, and A_t is the stop trilinear coupling. The mass eigenstates of the stop are obtained by diagonalizing the mass matrix, as

$$\begin{pmatrix} \tilde{t}_1 \\ \tilde{t}_2 \end{pmatrix} = \begin{pmatrix} c_{\tilde{t}} & -s_{\tilde{t}^*} \\ s_{\tilde{t}} & c_{\tilde{t}^*} \end{pmatrix} \begin{pmatrix} \tilde{t}_L \\ \tilde{t}_R \end{pmatrix}, \tag{2.19}$$

with a condition $|s_{\tilde{t}}|^2 + |c_{\tilde{t}}|^2 = 1$. The off-diagonal terms of the stop mass matrix tend to induce a large mixing. Because of that, the mass of the lighter stop ($\tilde{t}_1$) is typically light, and many models predict that $\tilde{t}_1$ is the lightest squark.

2.2.6 Natural SUSY

In the MSSM, the mass of the Z boson at the tree level with large $\tan\beta$ can be written as

$$-\frac{m_Z^2}{2} = |\mu|^2 + m_{H_u}^2, \tag{2.20}$$

with the higgsino mass parameter μ and the mass of the up-type Higgs boson m_{H_u} [52]. In the natural SUSY scenario, the right terms should not be too large compared to the left side; otherwise, a large cancellation between the two terms on the right side would be needed. That indicates that the higgsino should be light, and the mass is expected to be at the same order as m_Z. There is a contribution from the stop mass to the m_{H_u} at the one-loop level. The m_{H_u} can be split into two parts, the tree level and radiation correction, as $m_{H_u}^2 = m_{H_u}^2|_{\text{tree}} + m_{H_u}^2|_{\text{rad.}}$. The stop mass contributes to the m_{H_u} at the one-loop order. The second term can be written as

$$m_{H_u}^2|_{\text{rad}} = -\frac{3y_t^2}{8\pi^2}\left(m_{Q_3}^2 + m_{U_3}^2 + |A_t|^2\right)\ln\left(\frac{\Lambda}{m_{\tilde{t}}}\right). \tag{2.21}$$

Here m_{Q_3} and m_{U_3} are the masses of the left-handed and right-handed third generation squarks, respectively, and Λ is the scale at which SUSY particles are generated [52]. In order to avoid too large radiative correction, the m_{Q_3} and m_{U_3} should not be too large compared to the Z boson mass scale. Similarly, there is also a gluino mass contribution to the second loop correction to Equation (2.21), which implies that the gluino is not too heavy. The expected masses spectrum from the natural SUSY requirement is summarized in Figure 2.5.

On the other hand, the discovered Higgs boson indicates that too light stop is not favored. The mass of the Higgs boson also provides information for the SUSY particles. The Higgs mass is described as

$$m_h^2 \sim m_Z^2\cos^2 2\beta + \frac{3}{4\pi^2}\frac{m_t^4}{v^2}\left\{\ln\frac{m_{\tilde{t}}^2}{m_t^2} + \frac{X_t^2}{m_{\tilde{t}^2}}\left(1 - \frac{X_t^2}{12m_{\tilde{t}}^2}\right)\right\}, \tag{2.22}$$

where $X_t = A_t - \mu\cot\beta$ is the stop mixing parameter [53]. At the tree level, the observed Higgs boson with a mass of 125 GeV cannot be achieved by the term $m_Z^2\cos^2 2\beta$. Hence, the second term must be large to account for the observed mass. In the case of heavy stops, the first term in the brace contributes to lift up the Higgs mass. The second term becomes maximum when $|X_t| = \sqrt{6}m_{\tilde{t}}$, which is the so-called *maximal mixing* case. Figure 2.6 shows the Higgs mass calculated with Suspect [54] and FeynHiggs [55] packages. The green and purple areas surrounded by the two lines are rough estimates of uncertainty because the two packages have different renormalization prescriptions. If the stop mixing is zero,

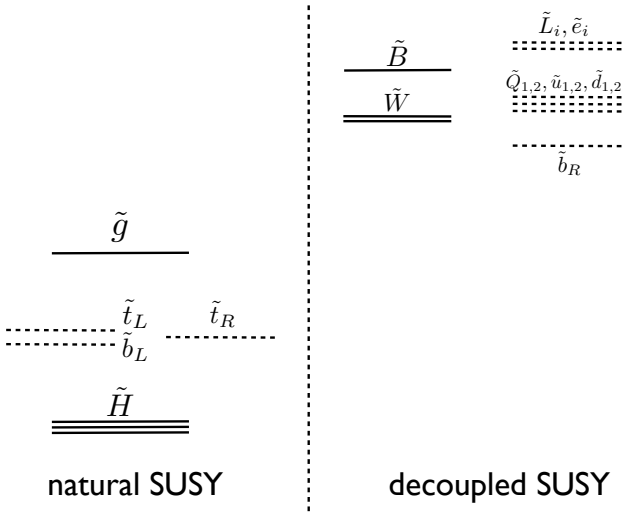

Figure 2.5: Typical mass spectrum with naturalness constrains in the MSSM [52]. The particles on the left side are considered to be light in natural SUSY models, while the other SUSY particle on the right side can be heavy. Light higgsinos, stops, left-handed sbottom, and gluino are expected.

the observed Higgs mass cannot be explained with a light stop below a few TeV, but the maximal mixing scenario gives a solution where a light stop below 1 TeV is possible.

The main target of this dissertation is a natural SUSY scenario where the mass of the lightest stop is below 1 TeV, and the stop decays to the higgsino-like LSP, as shown in Figure 2.5.

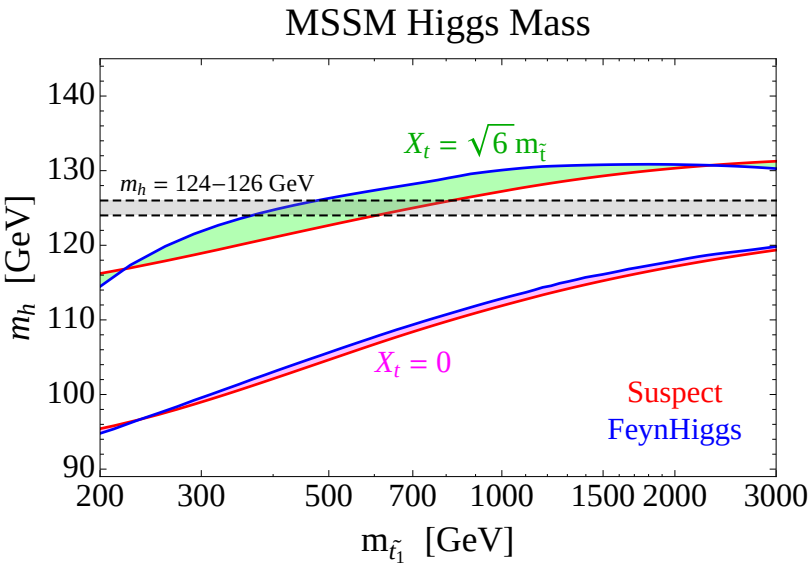

Figure 2.6: The Higgs mass as a function of the lightest stop mass in the MSSM [56] Two calculation packages are used: Suspect in red lines and FeynHiggs in blue. In both colors, the maximal and zero stop mixing parameters are shown. The green (purple) area shows the difference between the Suspect and FeynHiggs calculations at the maximal (zero) stop mixing.

Chapter 3

Experimental apparatus

3.1 Large Hadron Collider

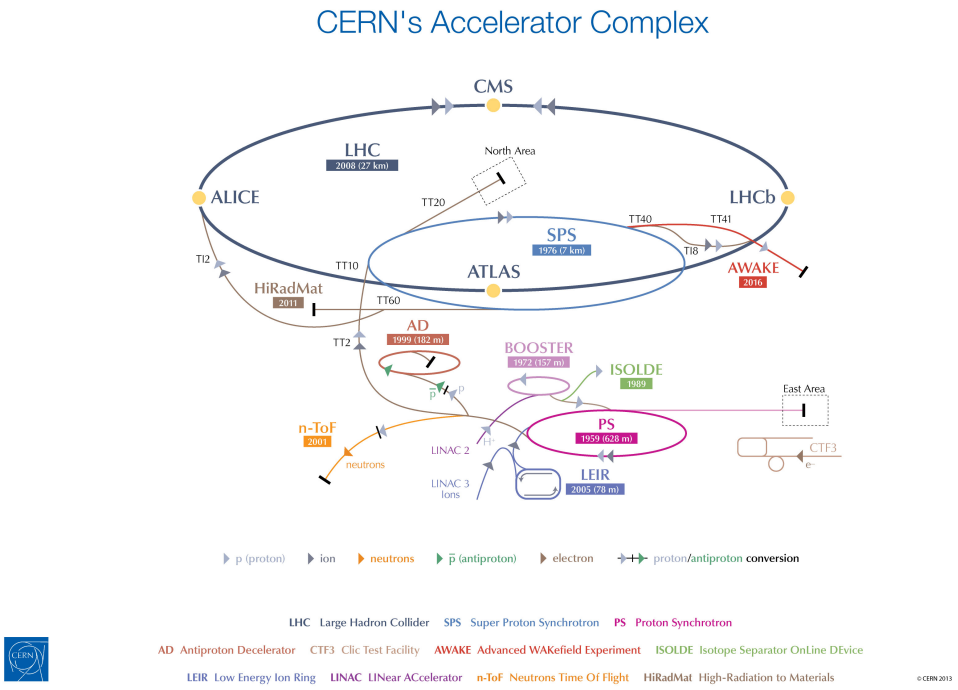

Figure 3.1: The accelerator complex at CERN [57].

The Large Hadron Collider (LHC) is a proton-proton accelerator located in Geneva, Switzerland. It accelerates protons using its 27 km circumference to a 6.5 TeV beam energy. The accelerator complex is shown in Figure 3.1. The LHC is one part of the accelerator complex at CERN. The proton acceleration starts from an injection of hydrogen atoms into Linear accelerator 2 (Linac 2). At the beginning of Linac 2, the hydrogen passes through an electric field to strip off the electrons in the atoms, and only protons are injected into

Linac 2. In Linac 2, pulses of the protons are generated, and the protons are accelerated to the energy of 50 MeV. The accelerated pulse of the protons is extracted from Linac 2 and injected into the Proton Synchrotron Booster (PSB). The protons are accelerated to 1.4 GeV in the Booster for the injection into the Proton Synchrotron (PS). The Booster enhances the number of protons that can be injected into the PS by accelerating protons in advance. The PS takes the protons to the energy of 25 GeV with its 277 electromagnets in a circumference of 628 m. The next step is the Super Proton Synchrotron (SPS). The SPS was originally used as a main ring to collide proton and antiproton beams, and it was the historical place where the W and Z bosons were discovered in 1983. Today, the SPS is used as the last part of the supply chain before the LHC main ring, and accelerates protons to 450 GeV in its nearly 7 km circumference. The LHC is the main ring of the complex and exploits the tunnel that was used for the LEP and LEP2 experiments. Two proton beams with opposite directions are injected from the SPS, and accelerated to the energy of 6.5 TeV. Superconducting magnets are used in the LHC, and the dipole magnets provide an 8 T magnetic field. The LHC has four interaction points, and four major detectors: ATLAS, CMS, ALICE, and LHCb, are installed in these points. The LHC beam has a bunch stricture in which about 10^{11} protons are contained. The interval between bunches is 25 ns at the interaction point except for empty bunches in the chain of bunches.

3.2 The ATLAS Detector

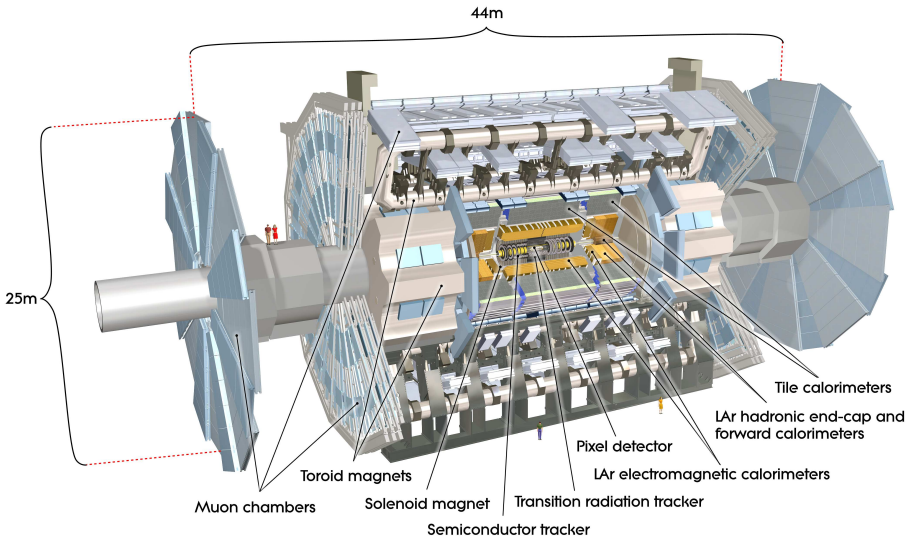

Figure 3.2: ATLAS detector overview [58]

The ATLAS detector is a multi-purpose particle detector designed to cover various

physics programs at the LHC, including the Higgs boson and new physics searches, and precision measurements of the SM. The ATLAS detector is located at Point 1 of the LHC, which is one of the interaction points of the LHC. Figure 3.2 shows the image of the ATLAS detector. It has a cylindrical shape, and the size of the detector is 44 m in height and 25 m in diameter. The side of the cylindrical shape is called the *barrel*, and the cap of the cylinder is called the *endcap* to describe the parts of the detector. The ATLAS detector consists of several subsystems. A tracking system is placed in the most inner part of the ATLAS detector, which consists of the silicon pixel detector, silicon strip tracker (SCT), and Transition Radiation Tracker (TRT) from the inner to outer order. These detectors are used to provide charged particle trajectories, called tracks in the following. The tracking subsystem is surrounded by the solenoid magnet, which provides a magnetic field for the tracking detectors to measure the momenta of tracks using the track curvature. The next outer subsystem is the calorimeter subsystem, which consists of the electromagnetic calorimeter and hadronic calorimeter. The energies of jets, electrons, and photons are measured by the calorimeters. The outermost part of the detector is the muon spectrometer (MS). Together with the muon spectrometer, toroid magnets are installed in both the barrel and endcap regions to provide the magnetic field to measure the momentum of muons. The details of the subsystems are described in the following sections.

3.2.1 Coordinate System

A right-handed coordinate system is used in ATLAS. The center of the coordinate system is defined as the interaction point (IP) at the center of the ATLAS detector, and the x-axis points from the IP to the center of the LHC ring. The y-axis points upwards, and then the z-axis is defined along to the beamline at the IP, pointing to the direction to Geneva International Airport. Polar coordinates are also useful to describe the detector or positions and momentum of particles from the IP. The polar angle ϕ is defined as the angle in the x-y plane (transverse plane) starting from the positive x-axis, and the azimuthal angle θ is defined as the angle from the positive z-axis to the negative z-axis. In the collider experiments, the pseudorapidity η is often used instead of θ as

$$\eta = -\ln\left(\tan\frac{\theta}{2}\right). \tag{3.1}$$

According to this definition, $\theta = 0$, $\pi/2$, and π correspond to $\eta = \infty$, 0, and $-\infty$, respectively. In order to describe the distance of two positions in the $\eta - \phi$ plane,

$$\Delta R = \sqrt{\Delta\eta^2 + \Delta\phi^2} \tag{3.2}$$

is often used, where $\Delta\eta$ and $\Delta\phi$ are the differences between the two positions in the η and ϕ coordinates, respectively.

3.2.2 Inner Detector

The Inner Detector (ID) consists of four trackers: Insertable B-Layer (IBL), Pixel detector, Silicon Strip Tracker (SCT), and Transition Radiation Tracker (TRT). The layout of the ID is shown in Figures 3.3–3.4. In the region of the ID, a 2 T magnetic field is provided by the surrounding solenoid magnet. The magnetic field is parallel to the beam axis, so that charged particles are bent in the transverse plane. In each tracker, different shapes of the layers are used in the barrel and endcap regions to provide tracking information in $|\eta| < 2.5$.

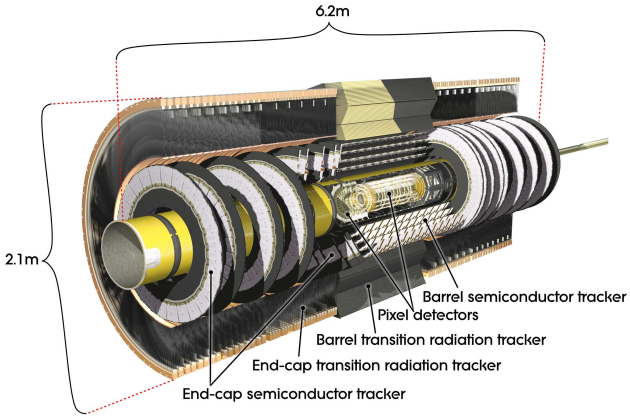

Figure 3.3: An illustration of the Inner Detector [58]. Both barrel and endcap regions are shown.

Insertable B-Layer (IBL)

The IBL is a single pixel layer detector located at 33 mm from the beamline. It was installed during the shutdown of the LHC between Run 1 (2011–2013) and Run 2 (2015–2018) in order to improve the performance of the tracking, especially the resolution of the impact parameter.

Pixel Detector

The pixel detector provides the hit position of tracks of charged particles with high precision. With its pixel structure, the 2D hit position is measured on each layer. It has a higher granularity than the SCT modules to provide precise hit positions, because the hit position measurement on the pixel detector is more important than that on the outer layers in terms of the reconstruction of the primary vertices and b-tagging. Typically three layers of the pixel detector are crossed by each track in both barrel and endcap regions. In total, 80.4 M

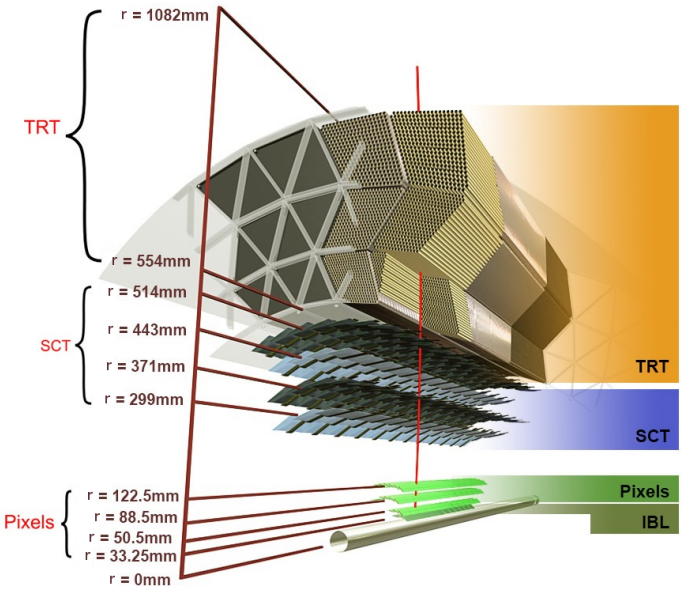

Figure 3.4: The positions of the IBL, Pixel, SCT, and TRT layers in the barrel region [58]. A typical track crosses one IBL, three pixel, and eight SCT layers, and 36 TRT tubes.

readout channels are used in the pixel detector. The nominal size of the pixel is 50×400 μm, and the thickness of the sensors is 250 μm.

Semiconductor Tracker (SCT)

The SCT is a semiconductor detector with a strip structure. One SCT layer provides 1D hit positions. Two layers attached in a module are not placed in parallel with each other, but inclined by 40 mrad. By placing the two layers with the stereo angle, the SCT module can provide 2D hit positions by combining the 1D information from the stereo and nominal SCT layers. Each track typically crosses eight layers. The intrinsic accuracy of hit positions on the SCT modules is 17 μm for $(R-\phi)$ direction in both barrel and endcap, and 580 μm for z (R) direction in the barrel (endcap). Strip structure with a pitch of 80 μm is used to collect signals, and the thickness of the sensors is 285 μm.

Transition Radiation Tracker (TRT)

The TRT [59] is made up of proportional drift tubes (straws) with a diameter of 4 mm. It provides continuous tracking in $|\eta| < 2.0$. The straw tube wall is made of Kapton coated with aluminum and graphite-polyamide. Tungsten wires plated with gold are used as anodes and supported at the ends of the straw tubes. The straws are filled with 70 % Xe, 27% CO_2 and 3% O_2. For modules in which gas leakage is observed, Ar is filled instead of Xe. The TRT has the ability of electron identification by exploiting transition radiation photons

because the intensity of the transition radiation depends on the Lorentz γ factor. Tracks produce typically 36 hits per track, which have an intrinsic accuracy of 130 μm per straw in $R - \phi$.

3.2.3 Calorimeters

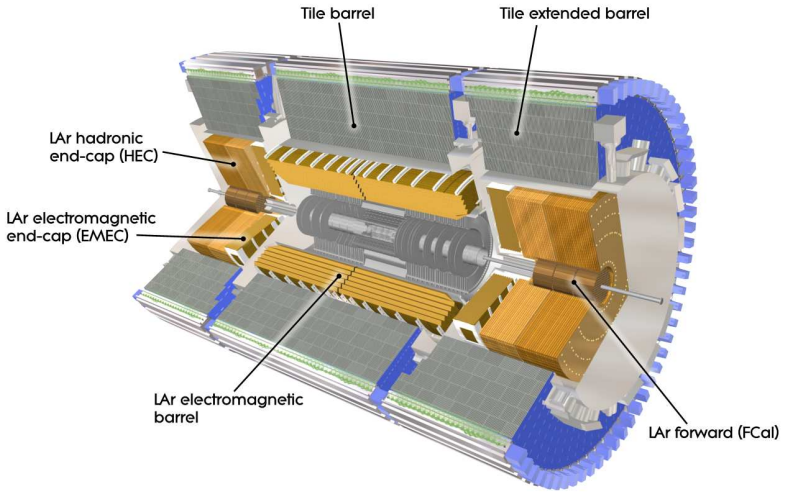

Figure 3.5: An overview of the ATLAS calorimeter system [58]. The calorimeter covers $|\eta| < 4.9$ using different types of modules. The electromagnetic calorimeters are surrounded by the hadronic calorimeters.

The calorimeter was designed to measure the energy and identify particle types for electrons, photons, taus, and jets. It also plays an important role in measuring missing transverse energy. The electromagnetic calorimeter is placed in small radii, surrounded by the hadron calorimeter, as shown in Figure 3.5.

Electromagnetic Calorimeter

The main role of the electromagnetic (EM) calorimeter is precise measurements and particle identification of electrons and photons. It covers the barrel ($|\eta| < 1.475$) and endcap ($1.375 < |\eta| < 3.2$) regions. It is a sampling calorimeter in which liquid Ar (LAr) and lead are used as active material and absorber plates, respectively. The lead absorber has an accordion shape, as shown in Figure 3.6, to cover the full range in ϕ without azimuthal cracks. The thickness of the EM calorimeter corresponds to $\sim$ 22 (24) radiation length in the barrel (endcap) region. The designed energy resolution of the EM calorimeter is $\sigma_E/E = 10\%/\sqrt{E} \oplus 0.7\%$ for the measured energy of E (GeV).

Hadronic Calorimeter

The hadronic calorimeter is divided into three parts: the tile calorimeter in the range of $|\eta| < 1.0$, the LAr hadronic endcap calorimeter (HEC) located behind the endcap EM calorimeter, and the LAr forward calorimeter (FCal) in $3.1 < |\eta| < 4.9$. The tile calorimeter is a sampling calorimeter with scintillating tiles as active material and steel as absorbers, as shown in Figure 3.6 right. The HEC and FCal are sampling calorimeters using liquid argon as active media. As absorbers, copper (copper-tungsten) plates are used in the HEC (FCal). Copper was chosen for the good heat removal and resolution, and tungsten was used in the outer FCal modules to minimize the lateral spread of hadronic showers. The total thickness of the detector is 9.7 (10) interaction length in the barrel (endcaps).

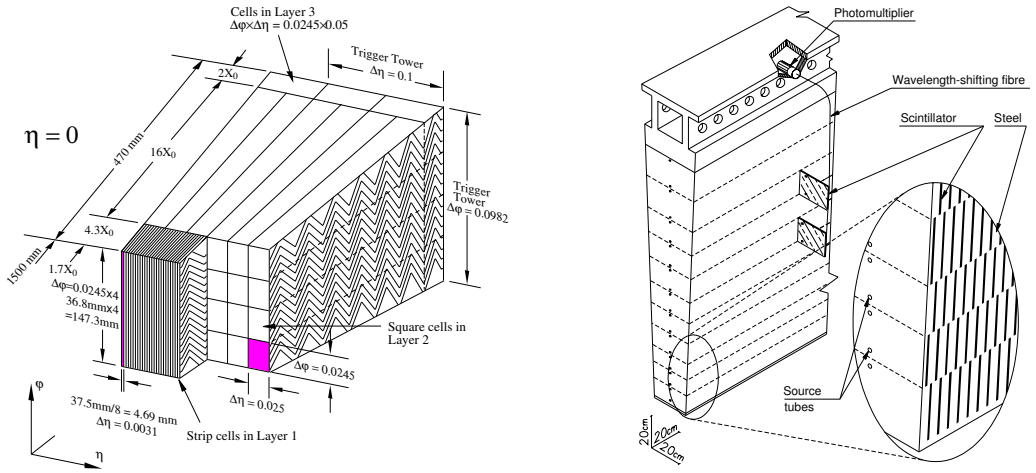

Figure 3.6: Illustrations of the LAr calorimeter (left) and tile calorimeter (right) in the barrel region [58]. The LAr EM calorimeter has three layers with different sizes of segments in $\Delta\eta \times \Delta\phi$. In the Tile hadron calorimeter, signals in the scintillators are read by photomultipliers installed at the edge of the detector.

3.2.4 Muon Spectrometer

The muon spectrometer (MS) [58, 60] is the outermost part of the ATLAS detector and identifies muons and measures their momenta in $|\eta| < 2.7$. Figure 3.7 shows the muon spectrometers together with the toroid magnets, which provide a magnetic field for the muon momentum measurements. The four muon chambers are divided into two types by their purposes. The Monitored Drift Tubes (MDT) and Cathode Strip Chambers (CSC) are detectors used for precise measurements of the muon momentum. The Resistive Plate Chambers (RPC) and Thin Gap Chambers (TGC) are mainly used online for the trigger decision. The trigger chambers also contribute to the determination of the second coordinates in the offline muon reconstruction to complement the MDT's 1D measurements in

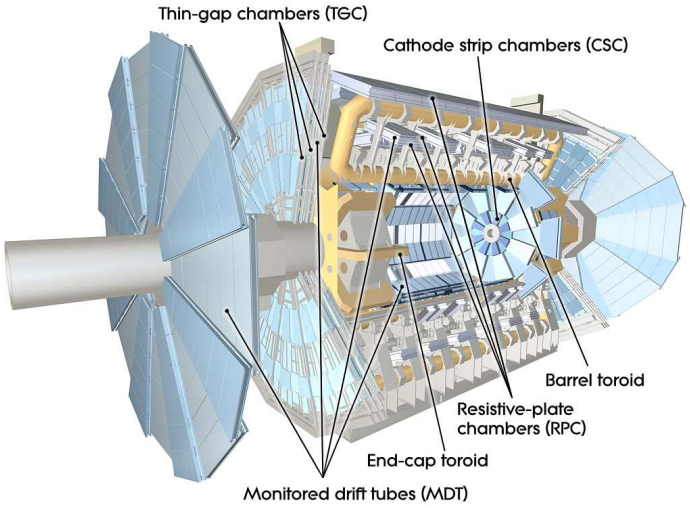

Figure 3.7: ATLAS muon spectrometers: MDT, CSC, RPC, and TGC [58]. The toroid magnets are shown in yellow.

the bending direction. The MS is designed to provide a transverse momentum with a resolution of 10% for 1 TeV muon tracks. The muon chambers in the barrel are placed in three concentric cylindrical shells around the beam axis at $R = 5$, 7.5, and 10 m. The chambers in the endcaps that form big wheels are placed at $|z| = 7.4$, 10.8, 14, and 21.5 m.

Monitored Drift Tube (MDT)

The MDT is used in both barrel and endcap regions to provide high precision tracking for muons. The spatial resolution of the track position in the z direction is 35 μm. The MDT consists of three to eight layers of drift tubes with a diameter of 3 cm filled with Ar (93%) and CO_2 (7%) at 3 bar. At the center of the tubes, a tungsten-rhenium wire is used as an anode of the drift chamber.

Cathode Strip Chamber (CSC)

The CSC is used as a precision muon tracker in the innermost forward region ($2 < |\eta| < 2.7$) instead of the MDT because the CSC provides better tracking performance than the MDT in the high-hit-rate environment. The CSC consists of a set of multi-wire proportional chambers. The cathode plane is divided into strips in the orthogonal direction to the wires to provide 2D hit positions. The resolution of the CSC is 40 μm in the bending plane and 5 mm in the transverse plane.

Resistive Plate Chamber (RPC)

The RPC works as a trigger chamber in the barrel ($|\eta| < 1.05$) region. The RPC is a gaseous parallel electrode-plate detector with a 2 mm distance between the two electrodes. The pick-up strips are connected to the electrodes capacitively. The signal is read out through readout strips via capacitive coupling, and electrodes are separated by PET foils. The readout strips in both sides are placed in the orthogonal direction so that 2D information of the hit position is available. A mixture of $C_2H_2F_4$/Iso-C_4H_4/SF_6 is filled in the chambers.

Thin Gap Chamber (TGC)

In the endcap region ($1.05 < |\eta| < 2.4$), the TGC provides muon track information for the online trigger decision. The TGC is made up of multi-wire proportional chambers with a 2.8 mm gap between graphite coated FR4 plates, as the name suggests. Copper strips on the other side of the plate provide azimuthal position measurements. In the middle of the gap, anode wires are arranged with a wire-to-wire distance of 1.8 mm. A highly quenching gas mixture of CO_2/n-pentane is used to prevent continuous current.

3.2.5 Magnet System

As mentioned with the ID and muon spectrometer, the ATLAS detector has solenoid and toroid magnets. The former provides the 2 T magnetic field for the ID, while the latter provides approximately 0.5 T and 1 T for the muon detectors in the barrel and endcap regions, respectively. The solenoid magnet is installed between the ID and EM calorimeter in the barrel, and the inner and outer radii are 2.46 m and 2.56 m, respectively. The nominal operating current is 7.7 kA, which corresponds to the stored energy of 40 MJ. The solenoid is designed to keep as thin as possible to reduce material in front of the calorimeters. An Al-stabilized NbTi conductor is surrounded by a single-layer coil. The barrel toroid consists of eight coils installed between muon detectors. The conductor of the barrel and endcap toroid magnets is made up of Al-stabilized Nb/Ti/Cu. The endcap toroid is placed between the inner and middle layers of the endcap muon wheels.

3.2.6 Luminosity Detector

LUCID-2

The luminosity recorded in ATLAS is monitored by the luminosity detectors during all data-taking periods. The LUCID-2 detector [61] consists of several sets of Cherenkov detectors installed at the forward region of the ATLAS detector. The LUCID-2 detector measures the relative luminosity, which is used to extrapolate from the absolute luminosity measurements

to the luminosity of the data for physics analyses. In each side of the ATLAS detector, 16 photomultiplier tubes (PMT) are installed surrounding the beam pipe at approximately $z = \pm 17$ m and detect Cherenkov light produced in the quartz window of the PMTs. Four additional PMTs are installed on the muon shielding to detect Cherenkov light from quartz fibers situated around the beam pipe as Cherenkov medium.

3.2.7 Trigger and Data Acquisition System

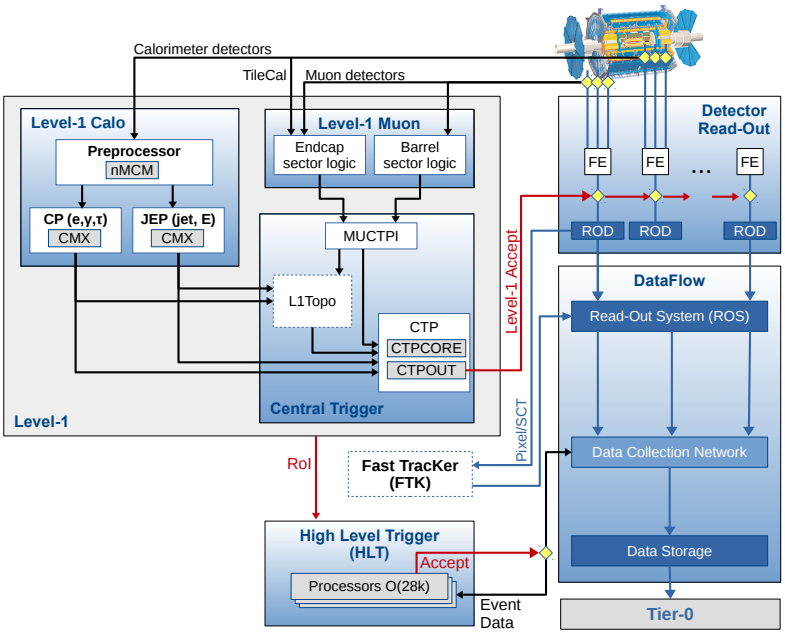

Figure 3.8: The ATLAS trigger and data acquisition system [62]. The trigger system consists of two stages: Level-1 and HLT. The hardware-based Level-1 trigger uses information from the calorimeter and muon detectors, and issues Level-1 Accept and provides region of interest (ROI) information to the HLT. The software-based HLT issues final accept signals to record events using offline-like reconstruction algorithms.

At the interaction point, proton bunches collide in every 25 ns, which corresponds to 40 MHz bunch crossings. Since it is not possible to record all collision data due to the huge collision rate, the ATLAS trigger system performs an online selection of the collision data in two steps: the Level 1 (L1) and High Level Trigger (HLT). An overview of the trigger and data acquisition system is shown in Figure 3.8. The L1 trigger is a hardware-based

trigger, which reduces the trigger rate from 40 MHz to about 100 kHz. The information from the calorimeters and muon trigger detectors (RPC and TGC) is used for the trigger decision. If an event satisfies a certain trigger requirement, an L1 Accept signal is issued by the Central Trigger Processor (CTP), and the data is transferred to the downstream. The HLT is a software-based trigger system, which reduces the trigger rate from 100 kHz to about 1 kHz. The selected events by the HLT trigger processor are then recorded in the storage.

Chapter 4

Data and simulation

4.1 Data Acquisition in LHC Run 2

This dissertation uses pp collisions at a center-of-mass energy of $\sqrt{s} = 13$ TeV recorded with the ATLAS detector during LHC Run 2 in 2015–2018. A subset of the data recorded in 2015–2016 is used in the search discussed in Chapter 7, while the full Run 2 data is used in Chapters 8–9.

From 2015 to 2016, the total integrated luminosity delivered by LHC is 42.7 fb^{-1}, and 39.5 fb^{-1} pp collision data was recorded by ATLAS. During the full Run 2 period, 156 fb^{-1} data was delivered, and 147 fb^{-1} data was recorded by ATLAS. Figure 4.1 shows the history of the integrated luminosity in Run 2. The total good quality data in 2015–2016 (2015–2018) corresponds to 36.1 (139.0) fb^{-1}. Figure 4.2 shows the mean number of interactions per event ($\langle\mu\rangle$). LHC Run 2 started with a low instantaneous luminosity in 2015, and the luminosity was increased as the LHC and ATLAS became in stable condition.

Luminosity measurement

The LUCID 2 detector measures a visible interaction rate per bunch crossing μ_{vis} [63]. The per-bunch instantaneous luminosity is

$$\mathcal{L}_b = \frac{\mu_{\text{vis}} f_r}{\sigma_{\text{vis}}}, \tag{4.1}$$

where f_r is the LHC revolution frequency, which is defined as the ratio of the speed of light to the circumferences of the LHC (11246 Hz). The visible cross section σ_{vis} is a calibration constant, which is specific to the luminosity calibration algorithm. Here $\mathcal{L}_b \sigma_{\text{vis}} = \mu_{\text{vis}} f_r$ corresponds to the number of visible pp collisions by a given bunch crossing pair. With LHC beam parameters, a per-bunch instantaneous luminosity is given by

$$\mathcal{L}_b = \frac{f_r n_1 n_2}{2\pi \Sigma_x \Sigma_y}, \tag{4.2}$$

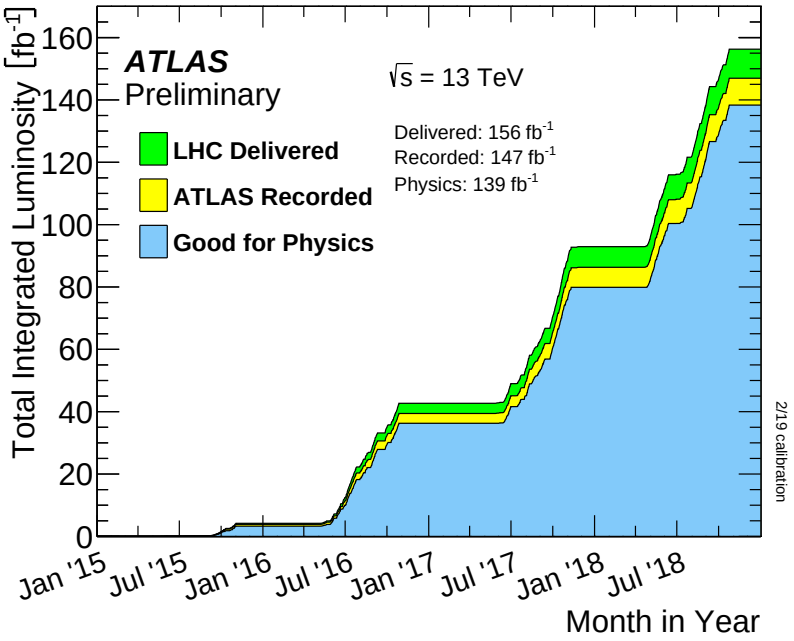

Figure 4.1: Integrated luminosity recorded with ATLAS in LHC Run 2 [57]

where n_1 and n_2 are the numbers of protons in the beam-1 and beam-2 colliding bunches, and Σ_x (Σ_y) is the horizontal (vertical) convoluted beam width. The width Σ_x and Σ_y are measured by the van de Meer (vdM) method [64, 65], in which the beam position in the transverse plane is scanned in a special vdM run once per year. The $n_1 n_2$ is determined based on the measurement of beam-gas event rates by the LHCb experiment [66].

Triggers

In SUSY searches in Chapters 7 and 9, data recorded by the missing transverse momentum ($E_{\mathrm{T}}^{\mathrm{miss}}$) trigger are used. The soft b-tagging study in Chapter 8 uses data recorded by the single muon or single electron trigger. The threshold of the triggers are summarized in Table 4.1. The trigger thresholds were raised as the instantaneous luminosity increased. The same trigger conditions are implemented in the simulation. In the offline selection, a higher $E_{\mathrm{T}}^{\mathrm{miss}}$ or lepton transverse momentum (p_{T}) cut is required to avoid the uncertainty associated with the resolution of the lepton p_{T} or $E_{\mathrm{T}}^{\mathrm{miss}}$. In SUSY searches, $E_{\mathrm{T}}^{\mathrm{miss}} > 230$ GeV is required and in soft b-tagging study leptons with $p_{\mathrm{T}} > 27$ GeV are used.

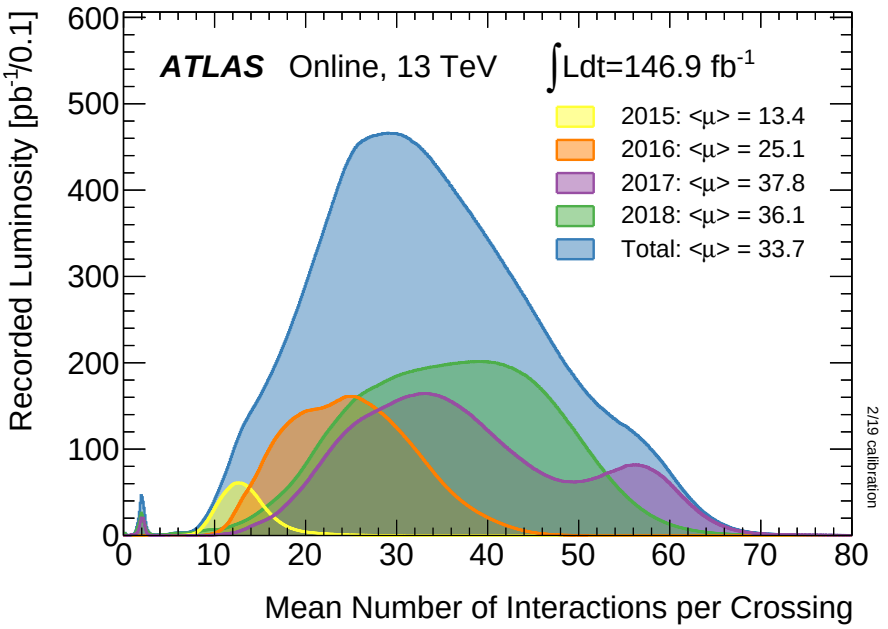

Figure 4.2: Mean number of interactions per crossing ($\langle\mu\rangle$) distribution [57].

Table 4.1: Overview of online trigger thresholds in each year. The $E_{\mathrm{T}}^{\mathrm{miss}}$ trigger is used in stop searches, and the single electron or single muon trigger is used in the soft b-tagging study.

	$E_{\mathrm{T}}^{\mathrm{miss}}$ (GeV)	electron p_{T} (GeV)	muon p_{T} (GeV)
2015	70	20	24
2016	$90-110$	$24-26$	$24-26$
2017	$90-110$	26	26
2018	110	26	26

4.2 Monte Carlo Simulation

The Monte Carlo (MC) simulation is of great importance in collider experiments in almost all aspects, such as designing experiments and detectors, developing algorithms, and estimating signal and background processes in analyses. In this section, MC simulation for SM background processes, as well as SUSY signal processes used in the following chapters, are explained [67].

4.2.1 Description of pp Collisions

The simulation of pp collisions is split into two parts in terms of the energy scale of the process. Processes at high energy scale are calculated using perturbation theory at a fixed order of α_S. Processes at low energy scale are described by models parameterized by experimental results, because it is difficult to calculate low energy QCD processes due to non-perturbative effects with large α_S. A cross section of a process with a final state n is described as

$$\sigma = \sum_{a,b} \int dx_a dx_b \int f_a^{p_1}(x_a, \mu_F) f_b^{p_2}(x_b, \mu_F) d\hat{\sigma}_{ab\to n}(\mu_F, \mu_R), \tag{4.3}$$

with

$$d\hat{\sigma}_{ab\to n}(\mu_F, \mu_R) = d\Phi_n \frac{1}{2\hat{s}} |\mathcal{M}_{ab\to n}|^2(\Phi_n; \mu_F, \mu_R). \tag{4.4}$$

The $f_a^{p_i}(x_a, \mu_F)$ is a parton distribution function (PDF), which describes distributions of quarks and gluons in an incoming proton p_i, $(i = 1, 2)$ as shown in Figure 4.3. It is a function of the momentum fraction x_a, which is a fraction of the momentum of the parton a, with respect to the momentum of the proton. The PDF also depends on a factorization scale μ_F, which is an energy scale splitting the low- and high-energy for the PDF and perturbative calculation. The parton-level cross section is described as $\hat{\sigma}_{ab\to n}(\mu_F, \mu_R)$, which is a cross section of initial partons a and b to a final state n. The factor $1/2\hat{s} = 1/(2x_a x_b s)$ is the parton flux, where s is the parton level center of energy squared, and Φ_n is the phase space of the final state n. $\mathcal{M}_{ab\to n}$ represents the *matrix element* (ME) of $ab \to n$ process, which corresponds to a sum over Feynman diagrams. It depends on μ_F and the renormalization scale μ_R. The total cross section σ is obtained by summing up all initial partons in proton p_1 and p_2, and integrating over the phase space of the final state n as well as the momentum fraction of the partons a and b.

Figure 4.4 shows a schematic view of a pp collision. The ME calculation does not take into account low energy scales to avoid divergence in soft and collinear limits. *Parton showers* (PS) perform an evolution from the energy scale of initial and final state partons

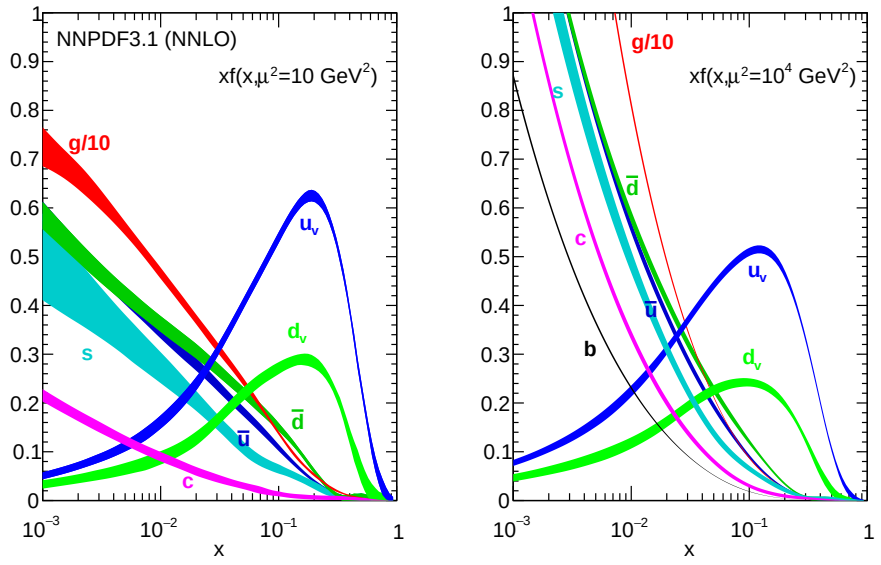

Figure 4.3: Parton distribution functions from NNPDF3.1 at $Q^2 = 10$ GeV^2 (left) and $Q^2 = 10^4$ GeV^2 [68].

towards a hadron confinement scale at an order of 1 GeV, taking into account all effects of higher orders. Below that scale reached after the evolution by the PS, the perturbation theory does not work. The low energy non-perturbation treatment is performed by the *hadronization*, which describes the confinement of QCD to generate colorless hadrons from colored partons.

4.2.2 Simulation Samples

Two sets of MC samples are used in this dissertation. The first set `sampleA` summarized in Table 4.2 is used in the analysis for large $\Delta m(\tilde{t}_1, \tilde{\chi}_1^0)$ in Chapter 7. The second set `sampleB` in Table 4.3 is used in the soft b-tagging study in Chapter 8 and analysis targeting small $\Delta m(\tilde{t}_1, \tilde{\chi}_1^0)$ in Chapter 9. The $t\bar{t}$ and single top samples were generated with POWHEG-BOX (at next leading order (NLO) accuracy) interfaced to PYTHIA 6 [70] and PYTHIA 8 [71] for PS in `sampleA` and `sampleB`, respectively. The cross sections of $t\bar{t}$ and single top were calculated at next-to-next-to-leading order (NNLO) with the resummation of soft gluon emission at next-to-next leading-logarithm (NNLL) accuracy. The W+jets and Z+jets samples were generated with SHERPA 2.2.0 [69] for `sampleA` and SHERPA 2.2.1 for `sampleB` at NLO, and the cross sections were calculated up to NNLO [72]. The multiboson samples were generated with SHERPA 2.2.1–2.2.2, and merged with SHERPA PS [73]. The cross sections of the multiboson processes were calculated at NLO. The SHERPA sam-

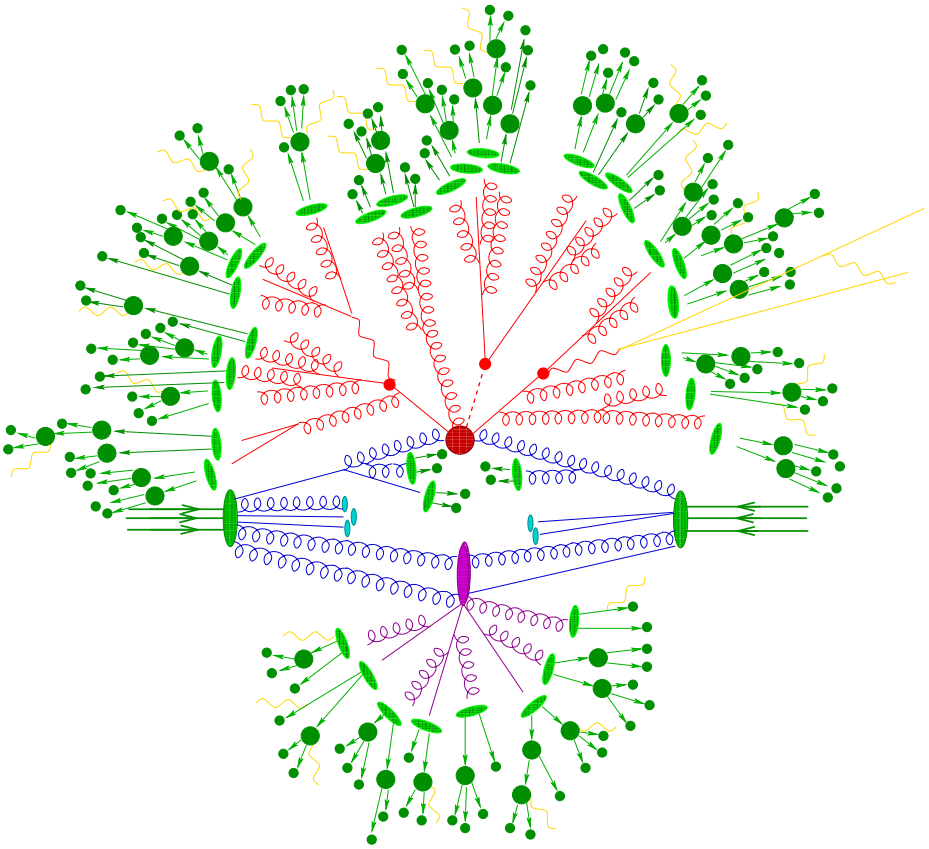

Figure 4.4: A schematic view of a *pp* collision [69]. From protons coming from left and right sides, gluons and quarks in blue are produced according to the PDF. The big red blob represents the hard scatter interaction, which emits outgoing particles of the hard process. ISR (FSR) radiation shown in blue (red) is produced below (above) the hard process blob. Hard QCD radiations are also shown in red, and hadronization occurs in the light green blobs. The dark green blobs are hadrons produced in the hadronization step, and photon radiation in yellow occurs at any step. The purple blob shows a secondary interaction (underlying event) generated by the same proton.

ples used Comix [74] and OpenLoops [75], and were merged with Sherpa PS using the ME+PS@NLO prescription [76]. The SUSY signals in `sampleA` were generated at leading order with MG5_aMC@NLO2.3.3 [69] interfaced to Pythia 8 PS, and the cross section is calculated up to NLO and NLL for soft gluon emission. The signals in `sampleB` were generated with MadGraph2.6.2 [69], and Pythia 8 PS was used. The stop four-body samples were decayed with MadSpin [77], and the cross sections were calculated at NNLO+NNLL accuracy. The P2012 [78] and A14 [79] tuning for the underlying events (UE), which are secondary scattering interactions from beam remnants, are used with Pythia 6 and Pythia 8 PS, respectively.

The Geant 4 [80] simulation framework is used to describe interactions of particles and

the ATLAS detector [81]. In the signal samples, the fast simulation [81] is used for the shower evolution in the calorimeters.

Table 4.2: Overview of the MC samples (`sampleA`) used in the analysis for large $\Delta m(\tilde{t}_1, \tilde{\chi}_1^0)$ (Chapter 7).

Process	ME event generator	PDF	PS and harmonization	UE tune	Cross-section calculation
$t\bar{t}$	Powheg-Box v2 [82]	CT10 [83]	Pythia 6 [70]	P2012 [78]	NNLO+NNLL [84–89]
Single-top					
t-channel	Powheg-Box v1	CT104f [83]	Pythia 6	P2012	NNLO+NNLL [90]
s- and Wt-channel	Powheg-Box v2	CT10	Pythia 6	P2012	NNLO+NNLL [91, 92]
V+jets ($V = W/Z$)	Sherpa 2.2.0 [69]	NNPDF3.0 [93]	Sherpa	Sherpa default	NNLO [72]
Multiboson	Sherpa 2.1.1 – 2.2.1	CT10/NNPDF3.0	Sherpa	Sherpa default	NLO
SUSY signal	MG5_aMC@NLO 2.2 – 2.4	NNPDF2.3 [94]	Pythia 8 [71]	A14 [79]	NLO+NLL [95]

Table 4.3: Overview of the MC samples (`sampleB`) used in the soft b-tagging study (Chapter 8) and analysis for small $\Delta m(\tilde{t}_1, \tilde{\chi}_1^0)$ (Chapter 9).

Process	ME event generator	PDF	PS and harmonization	UE tune	Cross-section calculation
$t\bar{t}$	Powheg-Box v2	NNPDF3.0	Pythia 8	A14	NNLO+NNLL [84–89]
Single-top					
t-channel	Powheg-Box v1	NNPDF3.0	Pythia 8	A14	NNLO+NNLL [90]
s- and Wt-channel	Powheg-Box v2	NNPDF3.0	Pythia 8	A14	NNLO+NNLL [91, 92]
V+jets ($V = W/Z$)	Sherpa 2.2.1	NNPDF3.0	Sherpa	Sherpa default	NNLO [72]
Multiboson	Sherpa 2.2.1 – 2.2.2	NNPDF3.0	Sherpa	Sherpa default	NLO
SUSY signal	MadGraph 2.3.3	NNPDF2.3	Pythia 8	A14	NNLO+NNLL [96, 97]

Chapter 5

Event Reconstruction

5.1 Tracks and Primary Vertex

Trajectories of charged particles, *tracks*, are reconstructed from hit information in the ID [98]. Tracks themselves are not directly used in many physics analyses, but they are basic objects as a seed of higher-level reconstruction such as the b-tagging, τ identification, muons, and electrons. It is also used to measure low p_{T} activities such as the soft term of the missing transverse momentum ($E_{\mathrm{T}}^{\mathrm{miss}}$) and the isolation of leptons. Tracks are reconstructed and track parameters: the p_{T}, η, ϕ, d_0, z_0, and charge of tracks, are measured using the magnetic field provided by the solenoid magnet. The d_0 and z_0 are transverse and longitudinal impact parameters, respectively. They are defined as the distances from the beam spot to the perigee of the track in the transverse plane and z direction.

The first step of the tracking algorithm starts with the clustering of Pixel and SCT hits to define three-dimensional coordinates (*space points*) on each layer of the tracker. On the layers of the Pixel detector, adjacent hits are assembled, and a space point is obtained. On the SCT layer, two sensor layers on both sides of the SCT module are used to estimate a 3D position. From three space points created in the clustering, track seeds are formed. In order to limit the number of track seeds and increase purity, a set of criteria is applied. The track seeds are extended by incorporating additional space points on the IBL, the Pixel, and the SCT using Kalman filter [99, 100], and track candidates are reconstructed. At this stage, the collection of the track candidates still contains overlaps of track candidates that are incorrectly assigned. This ambiguity is solved by the track selection using the scoring of tracks in a reward/penalty schema, considering the properties of the track candidates such as shared hits and holes of the ID sensors. In the ambiguity solver, the track candidates are required to satisfy the basic quality criteria, such as $p_{\mathrm{T}} > 500$ MeV, $|\eta| > 2.5$, and requirements on the transverse and longitudinal impact parameters, and the numbers of pixel and SCT holes and shared clusters. For the track candidates that pass the ambiguity

solving process, a high-resolution fit is performed to measure the track parameters precisely. The high-resolution fit utilizes all available information, such as the position and uncertainty of clusters of hits determined by the artificial neural network (NN). The NN is also consulted to identify the merged clusters that are formed by multiple particles. Finally, the track candidates found in the silicon detectors are extended into the TRT, which are then used in the high-level reconstruction algorithms, as explained in the following.

The interaction points of the *pp* collisions are reconstructed from the reconstructed tracks [101, 102]. The vertex is reconstructed by the adaptive vertex fitter [103], using the beam spot as a seed position in the transverse plane. The resolution of the vertex position is about 30 μm in the longitudinal direction and of the order of 10 μm in the transverse plane. The vertex with the highest sum of squared p_{T} of the tracks is selected as the hard scattered vertex, which is considered as a production position of the physics process of interest. In the following, the hard scatter vertex is referred to as the primary vertex (PV), and the other vertices of *pp* collisions are referred to as pile-up vertices.

5.2 Topological Clusters

Energy deposits in the calorimeters are clustered, collecting the measured energies in neighboring cells, and *topological clusters*, or *topo-clusters* are formed [104, 105]. The reconstruction of topo-clusters uses the three-dimensional distribution of energy deposits in the calorimeter cells. The energy of an input particle is calculated by summing all the energies in these cells, and the direction of the input particle is also calculated. Topo-clusters are formed based on the cell signal significance $\varsigma_{\mathrm{cell}}^{\mathrm{EM}}$, which is defined as the measured energy in the cell divided by the average level of the noise in the cell,

$$\varsigma_{\mathrm{cell}}^{\mathrm{EM}} = \frac{E_{\mathrm{cell}}^{\mathrm{EM}}}{\sigma_{\mathrm{noise,cell}}^{\mathrm{EM}}}. \tag{5.1}$$

Here $E_{\mathrm{cell}}^{\mathrm{EM}}$ is the energy measured in the calorimeter cell and $\sigma_{\mathrm{noise,cell}}^{\mathrm{EM}}$ is the noise of the cell. Both of them are measured by the EM energy scale. The measured calorimeter signal is converted to the energy for electrons and photons (EM scale) by recovering the energy loss of these particles due to the detector response. The energy of hadrons is different from the EM energy scale due to the different responses between the EM showers and hadron showers. The reconstruction of topo-clusters starts with the reconstruction of *proto-cluster*s as follows.

1. The proto-cluster reconstruction starts from a seed cell with $\varsigma_{\mathrm{cell}}^{\mathrm{EM}} > 4$.
2. If the neighboring cells of the cell have significant energy with $\varsigma_{\mathrm{cell}}^{\mathrm{EM}} > 0$, the cells are added to the proto-cluster.

3. If a cell contained in the proto-cluster has $\varsigma_{\text{cell}}^{\text{EM}} > 2$, step 2 is done for the cell, and step 3 is repeated.

The proto-clusters reconstructed by the procedure above can be too large compared to the shower structure to measure the energy and direction of incoming particles. To provide fine structures of showers, a proto-cluster is split if it has two or more local maxima in terms of the cell energy. The split cluster is then used as a topo-cluster. The direction of a topo-cluster is calculated from the weighted average of positions of cells in η and ϕ.

5.3 Jets

Quarks and gluons produced at the interaction point are not observed as themselves. In the hadronization process, quarks and gluons form hadrons. Hadrons interact with the detector material, which spread in the transverse plane of the travel direction, resulting in shower-shaped structures, called *jets*. In order to obtain the four-momentum of the original quark or gluon, the anti-k_t algorithm [106] is used, and the jet energy is scaled to recover the energy loss due to the detector response or invisible particles. The jet reconstruction is performed within the FastJet software package [107].

In the anti-k_t algorithm, jets are formed from topo-clusters using the distance between two topo-clusters defined as

$$d_{ij} = \min\left(\frac{1}{p_{\text{T},i}^2}, \frac{1}{p_{\text{T},j}^2}\right)\frac{\Delta R_{ij}^2}{R^2}, \tag{5.2}$$

where $p_{\text{T},i}$ and $p_{\text{T},j}$ are the p_{T} of the i-th and j-th topo-clusters and ΔR_{ij} is the angular distance between the two topo-clusters. The parameter R controls the cone size of the jets, and in the following analyses, $R = 0.4$ is used. The algorithm proceeds by merging two topo-clusters, which have the smallest d_{ij}, and the merged object is then treated as another cluster and this step is repeated. When the minimum d_{ij} becomes equal to $1/p_{\text{T},i}^2$, the iteration stops, and the i-th object is called as a jet, and the clusters used are removed from the topo-cluster collection. As the negative power of the p_{T} is used in the distance definition, the algorithm prioritizes the highest p_{T} object and the soft objects around the highest p_{T} object are merged into the hard cluster. Therefore, the shape and p_{T} of the jets are not sensitive to soft radiation.

The energy of jets needs to be calibrated from the EM-scale, which is measured for the topo-cluster, to the particle-level energy. The sequence of the calibration steps below corrects the jet energy and angles using the MC and data [108].

Origin correction

The four momentum of each jet is recalculated so that it points to the hard-scatter vertex rather than the center of the detector to improve the resolution of the jet angles.

Pile-up correction

The effect of the pile-up is corrected [109] as

$$p_{\mathrm{T}}^{\mathrm{corr}} = p_{\mathrm{T}}^{\mathrm{reco}} - \rho \times A - \alpha \times (N_{\mathrm{vtx}} - 1) - \beta \times \mu, \tag{5.3}$$

where $p_{\mathrm{T}}^{\mathrm{reco}}$ is the reconstructed jet p_{T} at the EM scale. The second term corresponds to the area-based pile-up subtraction. ρ is the p_{T} density, which is the pile-up contribution to the jet p_{T} per unit area, and A is the area of the jet. The third and fourth terms refer to the residual correction based on the number of reconstructed vertices (N_{vtx}), and the mean number of additional pp collisions per bunch crossing (μ), and α and β are coefficients used in the correction.

Absolute MC-based calibration

The jet energy is scaled to the particle-level energy by applying the average energy response, which is defined as the mean of the Gaussian fit to the $E^{\mathrm{reco}}/E^{\mathrm{truth}}$ distributions binned in E^{truth} and η. E^{reco} is the EM-scale energy calculated from the topo-clusters, and E^{truth} is the energy of the truth jet that matched to the reco jet. Truth jets are reconstructed using final-state particles from MC generators as input.

Global sequential calibration

The calorimeter response is sensitive to the fluctuation of the particles in jets. Due to the different numbers of color charges for quarks and gluons, a jet originating from a quark tends to have hadrons with higher p_{T} and fewer soft particles than a gluon-initiated jet. In order to correct the dependence on the fraction of constituents, the energy response is corrected using the fractions of the jet energy measured in the last layer of the EM calorimeter and the first layer of the hadron calorimeter, the number of tracks associated with the jet, the average transverse distance of these tracks with respect to the jet axis, and the number of the muon track segments.

***In situ* calibration**

As the last step, the difference between data and MC is corrected in the *in situ* calibration. In the *in situ* calibration, the data and MC differences are quantified by the p_{T} ratio of a jet to other well-measured reference objects. The response $R_{in\ situ}$ is defined as the average ratio of jet p_{T} to the p_{T} of the reference object binned in the

reference p_{T}. The ratio of the $R_{in\ situ}$ between data and MC is used to correct the p_{T} of jets as a function of jet p_{T} and η. In order to utilize good reference objects balancing to the jet that is being calibrated, Z boson, photon, and multijet events are used. The uncertainties in the *in situ* calibration are mainly arising from the mismodeling of physics effects and the p_{T} balance, and measurement of the kinematics of the reference objects.

The calibration steps above correct the mean of the response of the calorimeter, but it is also needed to calibrate the width of the response, the jet energy resolution (JER) [110]. The JER is parameterized as

$$\frac{\sigma_{p_{\mathrm{T}}}}{p_{\mathrm{T}}} = \frac{N}{p_{\mathrm{T}}} \oplus \frac{S}{\sqrt{p_{\mathrm{T}}}} \oplus C, \tag{5.4}$$

where N refers to the pile-up and electronic noise, S is the statistical Poisson fluctuations in the sampling nature of the calorimeters, and C is the constant term. The calibration of JER is to measure these parameters and it is performed with Z+jets, γ+jets, and dijet events.

Jet Vertex Tagger (JVT) [109], which is a likelihood discriminating algorithm that rejects jets originating from pile-up vertices using tracks and the PV, is used for 20 GeV $< p_{\mathrm{T}} <$ 120 GeV. Jets that are likely produced by non-collision backgrounds such as the beam remnant or detector noise are removed by the jet cleaning [111] using the signal pulse shape in the LAr calorimeters, energy ratios in the calorimeter cells, and track-based variables.

5.4 b-tagging

Jets originating from b-quarks, b-jets, are identified by the b-tagging algorithm [112, 113], which is one of the most powerful tools in physics analyses in ATLAS. The signature of b-hadrons in the detector is characterized by the long flight distance compared to the other quarks or the gluon, due to their long lifetimes of about 1.5 ps, which correspond to $c\tau =$ 450 μm. The flight distance l is larger than $c\tau$ due to the boost factor ($\beta\gamma$) of the particle, resulting in $l = \beta\gamma c\tau$ of a few mm. In this section, the standard b-tagging algorithm, which is based on the reconstructed jets, is described. The low-p_{T} b-tagging, which is a key of this dissertation, is written in Chapter 8.

The b-tagging algorithm is applied to jets, utilizing tracks ghost-associated [114][1] with the jet, and returns a score for each jet, which describes how likely the jet is a b-jet. The b-tagging score is evaluated by a high-level tagger based on Boosted Decision Tree (BDT),

[1] Tracks are associated to a jet as ghost particles with negligible momentum by the jet reconstruction algorithm.

which is one of the multi-variate analysis tools. The input variables of the high-level tagger are provided by low-level algorithms. There are three low-level algorithms, which make use of the properties of long-lived particles. The characteristics of long-lived b-hadrons are the presence of a displaced vertex with a few mm distance from the PV, large impact parameters of tracks originating from the displaced vertices, and multiple displaced vertices produced in the cascade decay of b-hadrons.

The presence of a secondary vertex (SV) displaced from the PV can be clear evidence of a long-lived particle. The SV1 [115] algorithm reconstructs one secondary vertex in a jet. All possible pairs of tracks are used to fit two-track vertices, and tracks that are not associated with a good two-track vertex are rejected. Two-track vertices that are consistent with an SV of K_s, Λ, photon conversion, or hadronic interaction with the detector material are removed by exploiting the invariant mass of the two tracks or the detector layout. The final good-quality vertices are reconstructed using the set of tracks associated with the two-track vertices.

Two impact parameter-based algorithms, IP2D and IP3D [116], are used as another low-level tagger. The former algorithm uses the signed transverse impact parameter significance d_0/σ_{d_0}, while the latter utilizes signed transverse and longitudinal impact parameter significance (d_0/σ_{d_0} and $z_0 \sin\theta/\sigma_{z_0 \sin\theta}$) accounting for their 2D correlation. A positive sign of the impact parameter d_0 is assigned if the perigee of the track is in front of the PV with respect to the jet direction. Probability density functions (pdf) of the track impact parameters on a per-track basis are constructed from simulated b-, c-, and light-flavor jets separately. For each flavor of jets, a log-likelihood ratio is calculated e.g., $\sum_{\text{track}} \log(p_b/p_u)$, where p_b and p_u are the per-track pdfs under the b- and light-flavor hypothesizes, respectively.

In most cases, a b-hadron decays into a c-hadron, and the c-hadron decays into s-hadron via the weak interaction. Since these downstream particles also have long lifetimes, though they are shorter than that of b-hadrons, a b-hadron and its cascade decay can produce multiple displaced vertices. In order to find a common line on which the primary, secondary, and tertiary vertices lie, the JetFitter algorithm [117] is used. It is a modified Kalman filter, which provides eight discriminant variables related to vertices and the tracks associated with the vertices to the high-level tagger.

A BDT-based high level tagger, called MV2c10 [116], is used to classify jets as a signal (b-jet) or background (light-flavor jet, or c-jet). The BDT is trained with simulated $t\bar{t}$ events for jets with $p_{\text{T}} < 250$ GeV, while Z' events are used for the jet p_{T} above 250 GeV. In the training sample, the fraction of the c-jets (light-flavor jet) is set to 7% (93%). The kinematic variables, p_{T} and η, are included in the input variables for the BDT to account for their correlation with the discriminant variables. From the output of SV1, eight discriminant

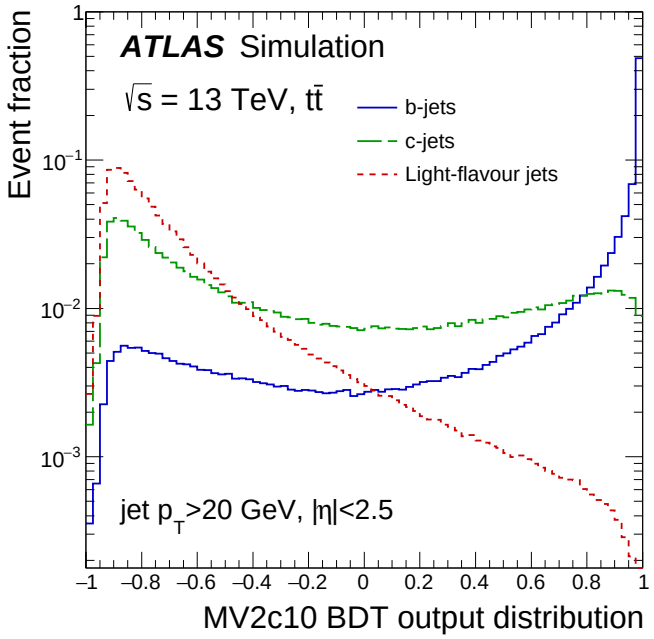

Figure 5.1: MV2c10 distribution of b-jets, c-jets, and light-flavor jets [118]. The histograms are normalized to unity. Scores close to one are given to b-jet-like jets, while jets with low scores are less likely b-jets.

variables related to the SV, such as the vertex mass[2], the number of associated tracks, the distance between the primary and secondary vertex and its significance, are included in the input of MV2c10. Three variables from IP2D and IP3D, the per-jet likelihood ratios between b-, c-, and light-flavor jets, $\log(P_b/P_{\text{light}})$, $\log(P_b/P_c)$, and $\log(P_c/P_{\text{light}})$, are added. From JetFitter, variables that describe properties of the cascade decay, such as the number of vertices, the total number of tracks, and the vertex mass, are used. The MV2c10 distributions of b-jet, c-jets, and light-flavor jets are shown in Figure 5.1. The performance of the MV2c10 classifier evaluated with MC simulation is shown in Figure 5.2. Along the line showing the MV2c10 performance, working points (WPs) are defined by selecting a certain threshold of the MV2c10 score above which the b-jet candidates are taken. The WP with 77% b-tagging efficiency is used in this dissertation. In the 77% WP, the rejection factors[3] for the light-flavor and c-jets are 110 and 4.9, respectively.

The b-tagging efficiency in data is measured for b-, c-, and light-flavor jets, in terms of the generator-level flavor composition. The b-jet tagging efficiency (ϵ_b) is measured using di-leptonic $t\bar{t}$ events selecting an electron and a muon with opposite charges and exactly

[2]The vertex mass is defined as the invariant mass calculated from the attached tracks using the charged pion mass for each track.

[3]a rejection factor of 100 means that 1% of jets are misidentified as b-tagged.

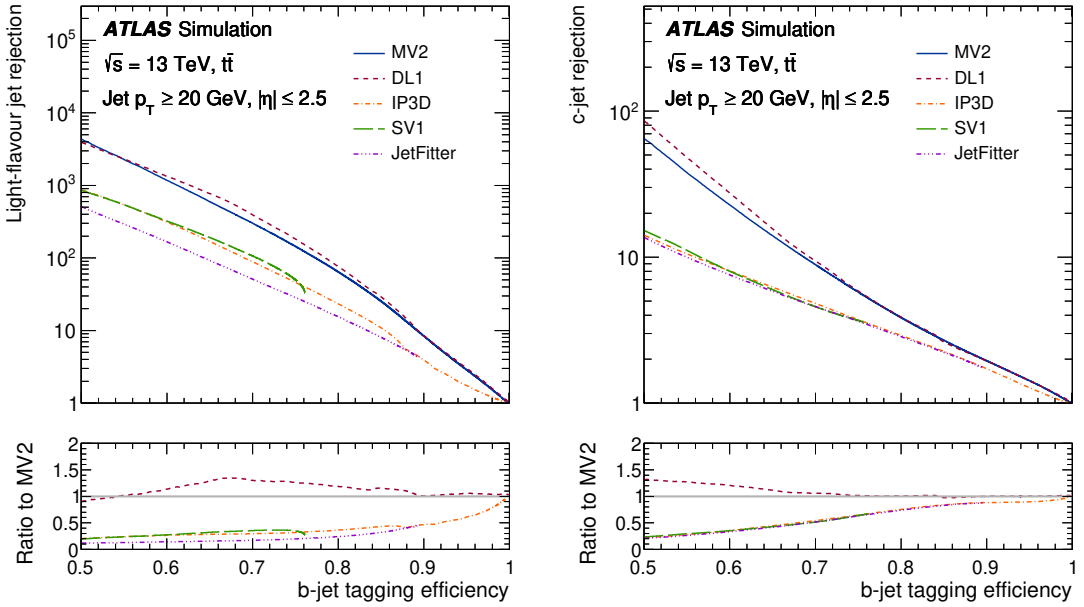

Figure 5.2: The performance of the low- and high-level taggers [112]. The light fake rejection factor (left) and charm rejection factor (right) as a function of the efficiency are shown. The DL1 algorithm is not used in this dissertation.

two jets, which are candidates of b-tagged jets [112]. The b-tagging efficiency is extracted using a likelihood fit. The scale factor (SF) is defined as the ratio of the ϵ_b in data to the ϵ_b in MC. The SF for the 77% efficiency WP is shown in Figure 5.3. The uncertainties in the measurement is dominated by the systematic uncertainties in the modeling of the $t\bar{t}$ and single top, as well as the statistics of data. The c-jet mistag efficiency (ϵ_c) is measured using $t\bar{t}$ events with a W boson decaying into charm and strange quarks [119]. Charm jets are extracted by KLFitter [120], which assigns reconstructed jets to quarks of the $t\bar{t}$ process, exploiting the decay topology of $t\bar{t}$ events. In order to measure the light-flavor mistagging efficiency, a high-purity light-flavor sample is needed. A light flavor jet could be mistagged when the jet contains tracks with large impact parameter significance d_0/σ_{d_0} with the positive sign due to the finite resolution of the impact parameters. In order to evaluate the mistag rate, the sign of the track impact parameter is flipped, and the flipped version of the tracks is used as the input of the b-tagging algorithm [121]. For ϵ_c and ϵ_{light}, events that contain charm or light-flavor jets are fitted with the efficiency as a parameter of interest.

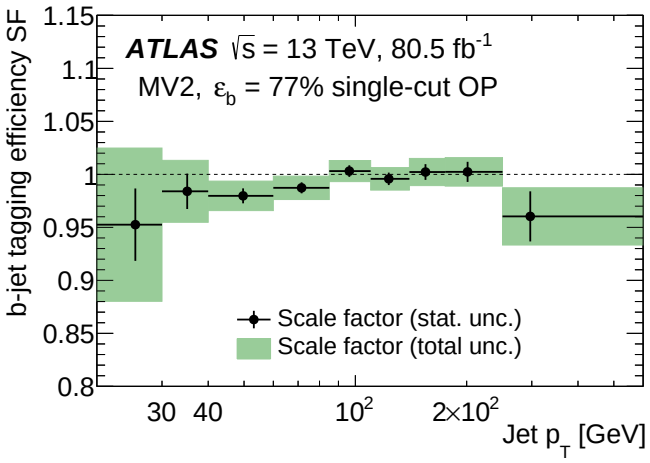

Figure 5.3: b-tagging scale factor as a function of jet p_{T} for b-jets [112].

5.5 Muons

The signature of muons is characterized by the long trajectory penetrating the detector due to the small energy deposit dE/dx. Depending on the use of the ID, MS, and calorimeter components, muons are classified as follows [122].

Combined (CB) muon

Muon candidate tracks are reconstructed in the ID and MS separately, and then the candidate tracks from each detector are combined as a single muon (combined muon) by a global refit using the hits from the ID and MS together.

Segment-tagged (ST) muon

Segment-tagged muons are used when the muon track is not fully reconstructed in the MS due to its low p_{T} or inefficiency of the MS. An ID track is labeled as an ST muon if the extrapolated track from the ID is associated with at least one track segment in the MDT or CSC.

Calorimeter-tagged (CT) muon

In order to recover the muon reconstruction inefficiency at $|\eta| < 0.1$, which is not fully covered by the muon detectors due to the detector support structure, CT muons are reconstructed from ID tracks and energy deposits in the calorimeters. If the ID track matches energy deposit in the calorimeter which is compatible with the minimum ionizing energy loss of a particle, the ID track is identified as a CT muon.

Extrapolated (ME) muon

ME muons are reconstructed using only MS tracks. The muon track parameters are

estimated, taking into account the energy loss in the calorimeters. ME muons are mainly used in the forward region where ID tracks cannot be reconstructed due to the acceptance of the ID.

Muons mainly required in physics analyses are *prompt* muons produced directly from decays of W/Z bosons or BSM particles. The background muons mainly from pion or kaon decays are suppressed at the muon identification step. Since background muons are produced from in-flight decays of long-lived particles, the difference between the track parameters measured in the ID and MS are used to suppress background muons. The quality of the combined track fit based on χ^2 is also used to suppress background tracks with inconsistent ID and MS measurements. Depending on the tightness of the muon identification, several working points (e.g., *Loose*, *Medium*, *Tight*) are provided, and an appropriate working point is selected in each analysis. The muon efficiency with the Medium identification WP is shown in Figure 5.4.

Muons originating from heavy particles such as W/Z bosons or BSM are isolated, while muons from semi-leptonic decays of the heavy hadrons (b- or c-hadrons) often have other particles around the muon track. To reduce these background muons from hadron decays, the following isolation variables are used.

- $p_{\mathrm{T}}^{\mathrm{varcone30}}$ is the scalar sum of the p_{T} of the tracks with $p_{\mathrm{T}} > 1$ GeV in a cone of size $\Delta R = \min(10\ \mathrm{GeV}/p_{\mathrm{T}}\ (\mathrm{GeV}), 0.3)$ around the muon track.
- $E_{\mathrm{T}}^{\mathrm{topocone20}}$ is the scalar sum of the transverse energy of topological clusters measured in the calorimeters in a cone of size $\Delta R = 0.2$ around the muon. The contribution of the muon itself is subtracted.

The isolation working points used in this dissertation are shown in Table 5.1. The analysis with 2015–2016 data in Chapter 7 uses WP1, while the analysis with 2015–2018 data in Chapter 9 uses WP2.

Table 5.1: The definitions of muon isolation working points

Working Point	Calorimeter-based isolation	Track-based isolation
WP1	$E_{\mathrm{T}}^{\mathrm{topocone20}}/p_{\mathrm{T}} < 0.15$	$p_{\mathrm{T}}^{\mathrm{varcone30}}/p_{\mathrm{T}} < 0.04$
WP2	–	$p_{\mathrm{T}}^{\mathrm{varcone30}}/p_{\mathrm{T}} < 0.06$

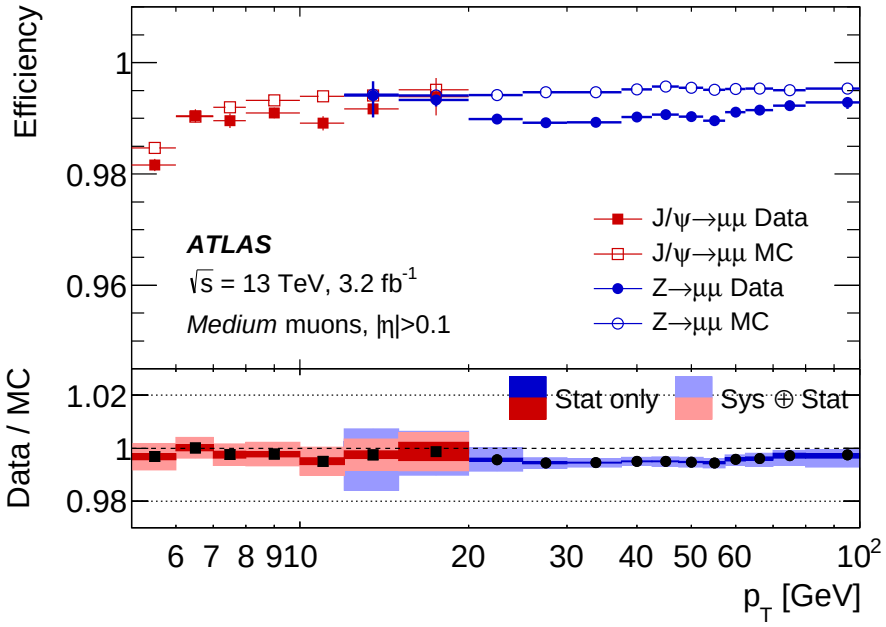

Figure 5.4: Muon efficiency for the Medium muon ID WP as a function of muon p_{T} [122]. The efficiency of high p_{T} muon is measured with $Z \to \mu\mu$ while $J/\psi \to \mu\mu$ is used for low p_{T}. The efficiencies measured with data and MC agree within 0.5%.

5.6 Electrons

An electron produced at the IP passes through the ID creating hits and forms a shower in the EM calorimeter. Figure 5.6 shows an illustration of an electron trajectory passing through the detectors. The electron reconstruction [124] is based on three components: the track reconstruction, cluster reconstruction, and track-cluster matching. On top of the track fit presented in Section 5.1, an additional fit is tried if the first fit fails. Due to the pion hypothesis used in the primary fit, the energy loss of the electron tracks in the inner detectors is not considered in the first fit. In the second fit attempt, the bremsstrahlung losses from electrons are considered by an additional degree of freedom using a Gaussian-sum filter (GSF) [125] to recover the inefficiency for the electrons. Clusters of the calorimeter cells are reconstructed using the topo-cluster algorithm. In the electron reconstruction, the energy from cells in the EM calorimeter is used except for the transition region of $1.37 < |\eta| < 1.63$. Figure 5.6 shows the electron reconstruction efficiency. Electrons with $p_{\mathrm{T}} > 4.5$ GeV are used in physics analyses, and the low p_{T} electron reconstruction is limited by the cluster finding and cluster-track matching efficiency.

The reconstructed electron candidates need to satisfy the identification criteria to enhance the purity of the prompt electrons. Likelihood-based criteria are applied with dis-

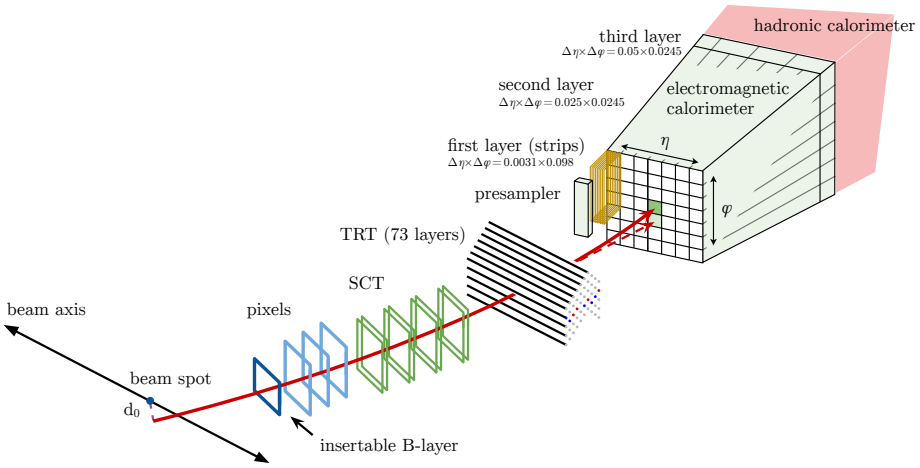

Figure 5.5: An illustration of the electron trajectory [123]

criminating variables such as the fraction of the energy in each layer of the calorimeter, the lateral spread of the calorimeter shower, and the intensity of the transition radiation in the TRT.

The isolation requirements are also applied to the electrons. The isolation variables for electrons are similar to the ones for muons. For electrons, $p_{\mathrm{T}}^{\mathrm{varcone20}}/p_{\mathrm{T}} < 0.06$ and $E_{\mathrm{T}}^{\mathrm{topocone20}}/p_{\mathrm{T}} < 0.06$ are required, where these variables are calculated around the electron track in the same way as for muons, but the maximum cone size for the track-based isolation ($p_{\mathrm{T}}^{\mathrm{varcone20}}$) is set to 0.2 for the electron isolation.

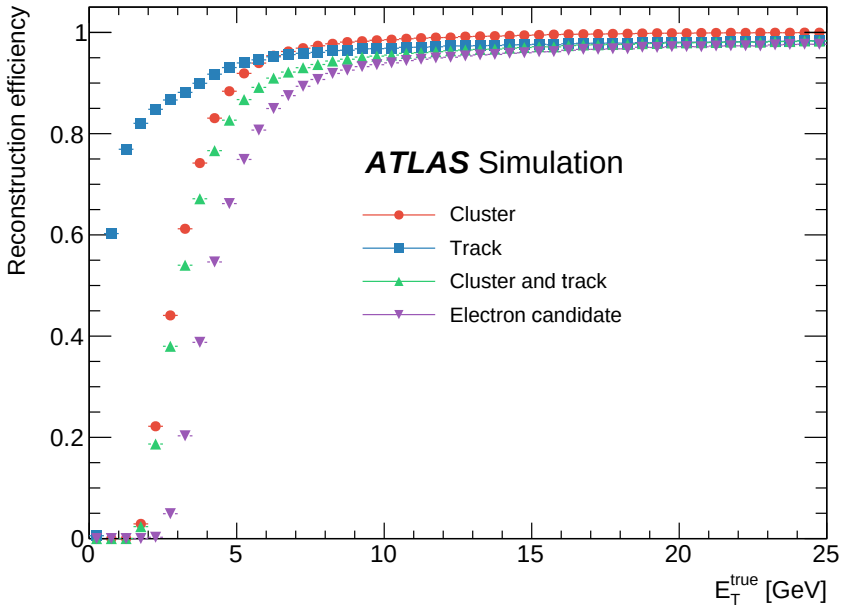

Figure 5.6: Electron reconstruction efficiency as a function of the electron truth energy [124]. Electron identification or isolation is not applied. The total efficiency shown in purple is mainly limited by the cluster efficiency in red and also cluster-track matching.

5.7 Missing E_{T}

Particles that do not interact with detector materials are observed as *missing energy* [126] in the ATLAS detector. Due to the momentum conservation before and after the collision, the sum of the transverse momenta of the particles must be zero. Only the transverse momentum is considered in the hadron detector because the initial momenta of the partons are unknown. The momentum of the invisible particles, like neutrinos or neutralinos, is measured as the missing transverse momentum ($\vec{E}_{\mathrm{T}}^{\mathrm{miss}}$). The magnitude of the $\vec{E}_{\mathrm{T}}^{\mathrm{miss}}$ is referred to as missing transverse energy $E_{\mathrm{T}}^{\mathrm{miss}}$. The $\vec{E}_{\mathrm{T}}^{\mathrm{miss}}$ is reconstructed as the negative sum of the reconstructed objects as

$$\vec{E}_{\mathrm{T}}^{\mathrm{miss}} = \vec{E}_{\mathrm{T}}^{\mathrm{miss,hard}} + \vec{E}_{\mathrm{T}}^{\mathrm{miss,soft}}, \tag{5.5}$$

with

$$\vec{E}_{\mathrm{T}}^{\mathrm{miss,hard}} = -\sum_{\text{electrons}} \vec{p_{\mathrm{T}}}^{e} - \sum_{\text{muons}} \vec{p_{\mathrm{T}}}^{\mu} - \sum_{\text{jets}} \vec{p_{\mathrm{T}}}^{\mathrm{jet}}, \tag{5.6}$$

$$\vec{E}_{\mathrm{T}}^{\mathrm{miss,soft}} = -\sum_{\text{unused tracks}} \vec{p_{\mathrm{T}}}^{\mathrm{track}}. \tag{5.7}$$

The hard objects have their lower p_{T} threshold so low p_{T} activities are not considered in the $E_{\mathrm{T}}^{\mathrm{miss}}$ hard term. The soft activity from the hard-scatter vertex is therefore included in the $E_{\mathrm{T}}^{\mathrm{miss}}$ soft term. The soft term is calculated using the vectorial sum of the tracks that are not associated with any hard objects. Tracks emerging from the hard-scatter vertex is used in the soft term, but tracks associated with the hard objects are removed. The particles added to the $E_{\mathrm{T}}^{\mathrm{miss}}$ calculation are calibrated in the dedicated calibrations for each object. Hence, the systematic uncertainties related to the hard objects are not directly shown as $E_{\mathrm{T}}^{\mathrm{miss}}$ uncertainties, but they are included in the uncertainties in each hard object.

5.8 Overlap Removal

The reconstructed objects described above can be overlapped. To avoid double-counting the same detector signal as more than one objects, the overlap needs to be removed. In the overlap removal procedure, a shared track, ghost matching [114], or distance between the two objects based on ΔR_y are used as matching criteria. In the overlap removal procedure, the angular distance between the two objects ΔR_y is calculated with rapidity $y = \frac{1}{2} \ln \frac{E+p_z}{E-p_Z}$ instead of pseudorapidity η. If an electron and jet are separated by $\Delta R < 0.2$, then the jet is discarded, and the electron is retained. If a muon is ghost-associated with a jet and the jet is muon-like ($n_{\mathrm{track}} < 3$ or $p_{\mathrm{T}}^{\mu}/p_{\mathrm{T}}^{j} > 0.7$), then the jet is discarded and the muon is kept[4]. If a jet and a lepton are overlapped within $\Delta R < \min(0.4, 0.04 + \frac{10}{p_{\mathrm{T}}^{\ell}/\mathrm{GeV}})$, then the lepton is removed and the jet is retained.

[4] In the analysis in Chapter 7, this is not applied if the jet is b-tagged.

Chapter 6

Stop Search Strategies

In the following chapters, the searches for the stop direct production in pp collisions are presented. The searches are performed by looking for excesses over the SM prediction in the collected data. In order to predict the SM events, we rely on the MC simulation by making use of the established knowledge of the SM. The observed data is compared to the SM background prediction estimated from the MC with scale factors, which correct the imperfect modeling of the MC simulation. The analyses are performed as follows.

- Signal models are constructed for the considered scenario. Signal and background MC events are generated.
- Good discriminating variables for extracting the signal events from overwhelming background events are selected.
- Signal regions (SRs) are defined to maximize the sensitivity for a benchmark signal. The signal region is determined based on the MC simulation, and the data in the signal regions are blinded to avoid human biases in the selection.
- Control regions (CRs), in which MC yields are scaled to data yields, are defined to estimate background events in the SRs. In validation regions (VRs), the background estimation strategy is validated.
- Experimental and theoretical systematic uncertainties are evaluated.
- Signal regions are unblinded. Hypothesis tests are performed to discover or exclude the signals.

Given that our analysis strategy is common in the stop searches described in Chapters 7–9, the common details are written in this section before individual analyses are presented.

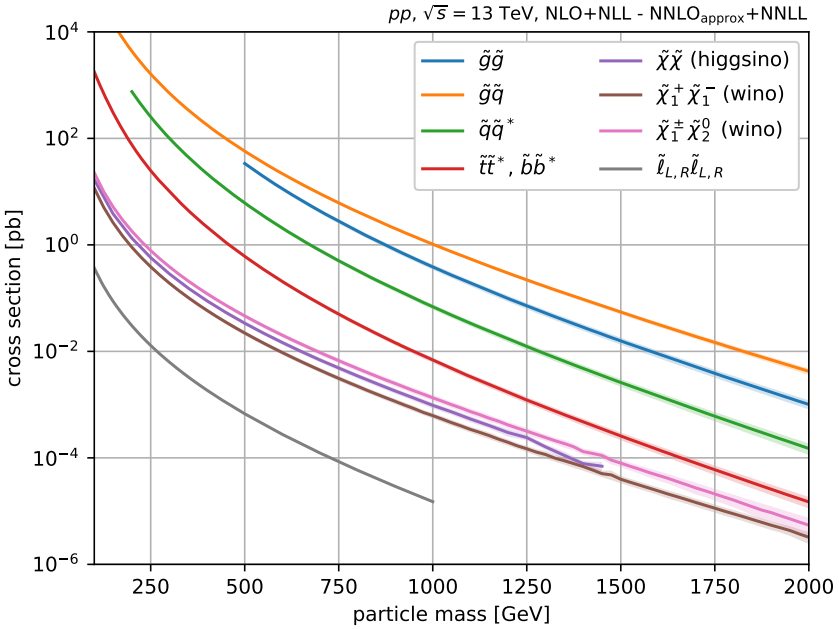

Figure 6.1: Cross sections of SUSY signals as a function of the mass of the particle [97, 127–130]. The cross sections are calculated at the NNLO + NNLL precision for the squarks and gluino productions, and the NLO+NLL precision for the electroweak productions. For a pair of different types of particles, the two particles are assumed to have the same mass. The colored bands show the uncertainties on the cross sections estimated from the variation of renormalization and factorization scales and the PDF.

6.1 Signal Models

The target signal of this dissertation is the direct production of a $\tilde{t}_1$ pair in the R-parity conserved scenario with neutralino LSPs. Figure 6.1 shows the production cross sections of SUSY particles in pp collisions at $\sqrt{s} = 13$ TeV. The cross sections depend on the masses of the SUSY particles. Decay branching ratios (BRs) and types of particles in the final state depend on the masses of the $\tilde{t}_1$ and $\tilde{\chi}_1^0$, as well as the presence of other SUSY particles into which the $\tilde{t}_1$ can decay. Figure 6.2 shows the mass spectra of SUSY particles in two models considered in this dissertation.

Simplified model

When there is only one SUSY particle involved in the $\tilde{t}_1$ decay, the particle must be the LSP and the decay modes can be simplified as shown in Figure 6.3. In the simplified model [34–36], the possible decay modes of $\tilde{t}_1$ are $\tilde{t}_1 \to t\tilde{\chi}_1^0$, $\tilde{t}_1 \to bW\tilde{\chi}_1^0$, and $\tilde{t}_1 \to bff'\tilde{\chi}_1^0$, where f

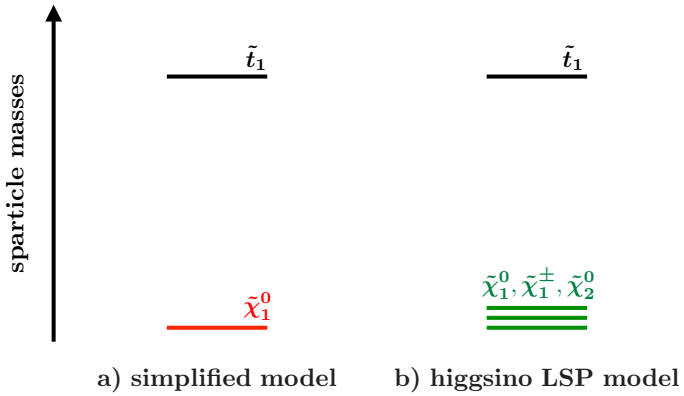

Figure 6.2: Mass spectra of considered scenarios. In the simplified model (left), $\tilde{t}_1$ always decays into $\tilde{\chi}_1^0$ and SM particles. The higgsino-like LSP scenario (right) has three higgsino states shown in green, and the branching ratio of the $\tilde{t}_1$ decay depends on the MSSM parameters. The higgsino-like LSP is characterized by the small splittings among the higgsino states.

and f' denote fermions[1]. The diagrams of these decay models are shown in Figure 6.4. The region where $m_{\tilde{t}_1} < m_{\tilde{\chi}_1^0}$ is not considered, as the lightest neutralino is assumed as the LSP (through this dissertation). The decay modes depend on the mass difference between $\tilde{t}_1$ and $\tilde{\chi}_1^0$ ($\Delta m(\tilde{t}_1, \tilde{\chi}_1^0)$). When $\Delta m(\tilde{t}_1, \tilde{\chi}_1^0) > m_t$, $\tilde{t}_1$ directly decays into the same flavor SM particle, top quark, with the LSP ($\tilde{t}_1 \to t\tilde{\chi}_1^0$). If $\Delta m(\tilde{t}_1, \tilde{\chi}_1^0)$ is smaller than m_t, then the $\tilde{t}_1$ decay becomes the three-body decay, via an off-shell top quark. For the most compressed case where $\Delta m(\tilde{t}_1, \tilde{\chi}_1^0) < m_W + m_b$, the four-body decay is observed via an off-shell W boson. For each decay modes, 100% branching ratios are considered.

Higgsino LSP

The higgsino-like LSP scenarios is favored by the naturalness as discussed in Section 2.2.6. There are three higgsino states: two neutralinos ($\tilde{\chi}_2^0$ and $\tilde{\chi}_1^0$) and a chargino ($\tilde{\chi}_1^\pm$). The signature is characterized by small mass-splittings among the higgsino states, which are typically below 5 GeV. This dissertation targets two scenarios: $\Delta m(\tilde{t}_1, \tilde{\chi}_1^0) > m_t$ and $\Delta m(\tilde{t}_1, \tilde{\chi}_1^0) < m_t$.

$\Delta m(\tilde{t}_1, \tilde{\chi}_1^0) > m_t$

In this case, three $\tilde{t}_1$ decay modes are considered: $\tilde{t}_1 \to t\tilde{\chi}_1^0$, $\tilde{t}_1 \to t\tilde{\chi}_2^0$, $\tilde{t}_1 \to b\tilde{\chi}_1^\pm$. The diagram of $\tilde{t}_1 \to b\tilde{\chi}_1^\pm$ decay is shown in Figure 6.5. The diagram of $\tilde{t}_1 \to t\tilde{\chi}_2^0$ is similar

[1] A flavor changing decay $\tilde{t}_1 \to c\tilde{\chi}_1^0$ is not considered in this dissertation.

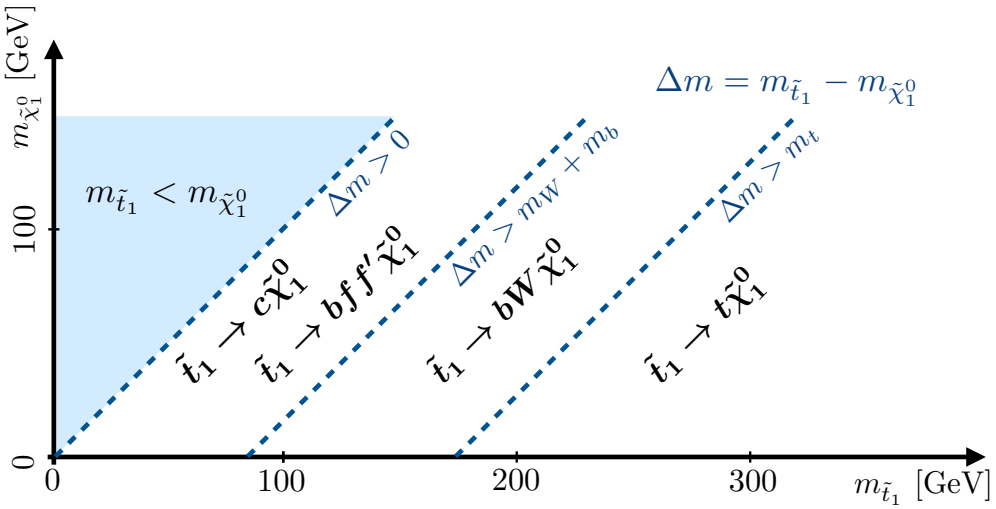

Figure 6.3: Possible decay modes in the simplified model. The decay modes depends on $\Delta m(\tilde{t}_1, \tilde{\chi}_1^0)$, and in each phase space, 100% branching ratio is assumed.

to that of the $t\tilde{\chi}_1^0$ decay, except for an additional decay of $\tilde{\chi}_2^0$. If $\tilde{t}_1$ decays into $\tilde{\chi}_2^0$ or $\tilde{\chi}_1^\pm$, these intermediate SUSY particles further decay into the LSP and SM particles. Due to the small mass-splitting, the SM particles from the $\tilde{\chi}_1^\pm$ or $\tilde{\chi}_2^0$ decay tend to have low momenta. The branching ratio of these decays depend on MSSM parameters. In order to cover a wide range of possible scenarios, three models summarized in Table 6.1 with different branching ratios are considered. To build the three models, $M_3 = 2.2$ TeV, $M_S = \sqrt{\tilde{t}_1\tilde{t}_2} = 1.2$ TeV, and $M_1 = M_2 \sim 1.5$ TeV are assumed. The $\tilde{t}_1$ branching ratios depends on the $\tilde{t}_R$ and $\tilde{t}_L$ composition of the $\tilde{t}_1$. When $\tilde{t}_1$ is composed of mainly $\tilde{t}_L$, $t\tilde{\chi}_1^0$ and $t\tilde{\chi}_2^0$ decays are favored, while $b\tilde{\chi}_1^\pm$ is favored when $\tilde{t}_1$ is mainly composed of $\tilde{t}_R$ in the small $\tan\beta$ case. When $\tan\beta$ is large and $\tilde{t}_1 \sim \tilde{t}_L$, the three decay modes have similar branching ratios, which is considered in the third scenario.

Table 6.1: Higgsino LSP scenarios. The branching ratios are fixed in all signal points for each scenario.

Scenario	Left/Right	$\tan\beta$	BR ($t\tilde{\chi}_1^0$, $t\tilde{\chi}_2^0$, $b\tilde{\chi}_1^\pm$)
mostly left	$\tilde{t}_1 \sim \tilde{t}_L$	20	45 : 45 : 10
mostly right	$\tilde{t}_1 \sim \tilde{t}_R$	20	25 : 25 : 50
large $\tan\beta$	$\tilde{t}_1 \sim \tilde{t}_L$	60	33 : 33 : 33

For each scenario, two 2D plane signal grids are generated as follows:

- $m_{\tilde{\chi}_1^\pm}$–$m_{\tilde{\chi}_1^0}$ plane with a fixed $\Delta m(\tilde{t}_1, \tilde{\chi}_1^0)$ of 5 GeV.

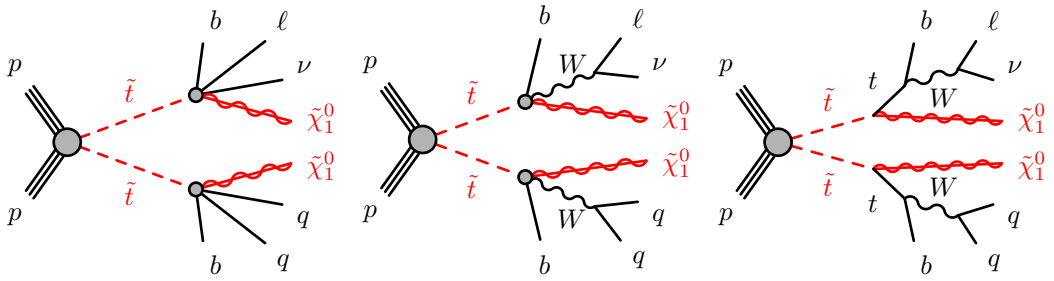

Figure 6.4: Diagrams of $\tilde{t}_1$ decaying into $\tilde{\chi}_1^0$. The four-body decay (left) is the most compressed case where the $\Delta m(\tilde{t}_1, \tilde{\chi}_1^0)$ is too small to decay via an on-shell W boson. In the three-body decay (middle), $\tilde{t}_1$ decays into a b-quark, an on-shell W boson and a $\tilde{\chi}_1^0$. If $\Delta m(\tilde{t}_1, \tilde{\chi}_1^0)$ is large enough to decay to an on-shell top quark, the two-body decay (right) is considered.

- $m_{\tilde{t}_1}$–$\Delta m(\tilde{\chi}_1^\pm, \tilde{\chi}_1^0)$ plane with a fixed $\tilde{\chi}_1^\pm$ mass of 150 GeV.

In both planes, $\Delta m(\tilde{\chi}_2^0, \tilde{\chi}_1^0) = 2 \times \Delta m(\tilde{\chi}_1^\pm, \tilde{\chi}_1^0)$ is assumed. The branching ratios and the mass relations are fixed over the signal grids. A stop and higgsino search based on this model is performed in the analysis in Chapter 7.

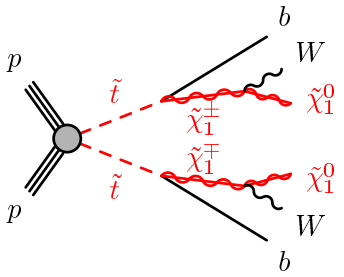

Figure 6.5: A diagram of $\tilde{t}_1$ decaying into a b-quark and a $\tilde{\chi}_1^\pm$. The $\tilde{\chi}_1^\pm$ decays into the LSP ($\tilde{\chi}_1^0$). The momentum of the W boson and its decay products depends on the mass-splitting between $\tilde{\chi}_1^\pm$ and $\tilde{\chi}_1^0$.

$\Delta m(\tilde{t}_1, \tilde{\chi}_1^0) < m_t$

If the decay of $\tilde{t}_1$ into $t\tilde{\chi}_1^0$ or $t\tilde{\chi}_2^0$ is kinematically forbidden due to a small mass-splitting between $\tilde{t}_1$ and $\tilde{\chi}_1^0$ ($\Delta m(\tilde{t}_1, \tilde{\chi}_1^0) < m_t$), the decay of $\tilde{t}_1$ becomes simple. Only possible decay of $\tilde{t}_1$ is $\tilde{t}_1 \to b\tilde{\chi}_1^\pm$ with $\tilde{\chi}_1^\pm$ decaying into $W^{(*)}\tilde{\chi}_1^0$. In this case, the final state is similar to that in the simplified model. The compressed scenario search is presented in Chapter 9, using the simplified model. In particular, the most compressed region where $\tilde{t}_1$ decays into four-body ($\tilde{t}_1 \to bff'\tilde{\chi}_1^0$) is considered.

6.2 Background Events

In this dissertation, the stop searches are performed by requiring exactly one lepton and $E_{\mathrm{T}}^{\mathrm{miss}}$ in final states. The presence of b-hadrons in the final states is also one of the distinctive features of the stop signals. Background processes in the stop searches with one lepton final states are explained below and Feynman diagrams of main processes are shown in Figure 6.6. The cross sections of the SM background processes are summarized in Figure 6.7. Compared to the cross section of the targeting $\tilde{t}_1$ production, which is an order of pb or lower, the SM background processes have significantly higher cross sections. To reduce these overwhelming backgrounds, a variety of discriminating variables are introduced in the following chapters.

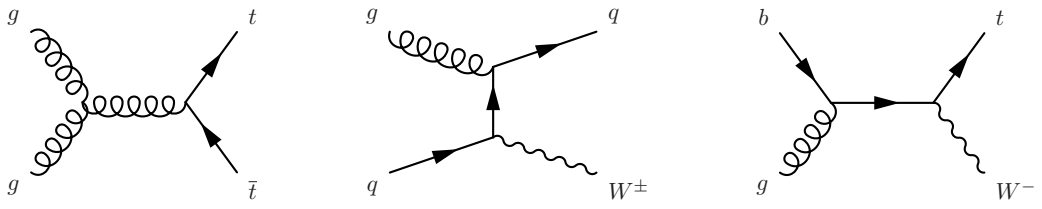

Figure 6.6: Feynman diagrams of the main background processes: $t\bar{t}$ (left), W+jets (middle), and single top (right).

$t\bar{t}$

In many signal regions, the top pair production ($t\bar{t}$) is the dominant background process because a typical stop signal topology is $t\bar{t} + E_{\mathrm{T}}^{\mathrm{miss}}$, including off-shell top cases. The cross section of the $t\bar{t}$ process at $\sqrt{s} = 13$ TeV is 818 pb [132]. The $t\bar{t}$ background is classified into three categories in terms of the decay modes of the top quarks. When both top quarks decay hadronically ($t \to bW(\to qq)$), it is called *full-hadronic* $t\bar{t}$, and $t\bar{t}$ with two leptonically decaying tops ($t \to bW(\to \ell\nu)$) is referred to as *di-leptonic* $t\bar{t}$. When one top decays hadronically and another top decays leptonically, the event is categorized in the *semi-leptonic* $t\bar{t}$. Both semi-leptonic and di-leptonic $t\bar{t}$ enter in the signal regions because of $E_{\mathrm{T}}^{\mathrm{miss}}$ originating from neutrinos. Despite the exactly one lepton requirement, the di-leptonic $t\bar{t}$ is a dominant background in some cases when one of the leptons is lost due to the inefficiency of the lepton ID or the lepton is out of acceptance.

W+jets

The W boson production associated with jets has a large cross section at $\sqrt{s} = 13$ TeV,

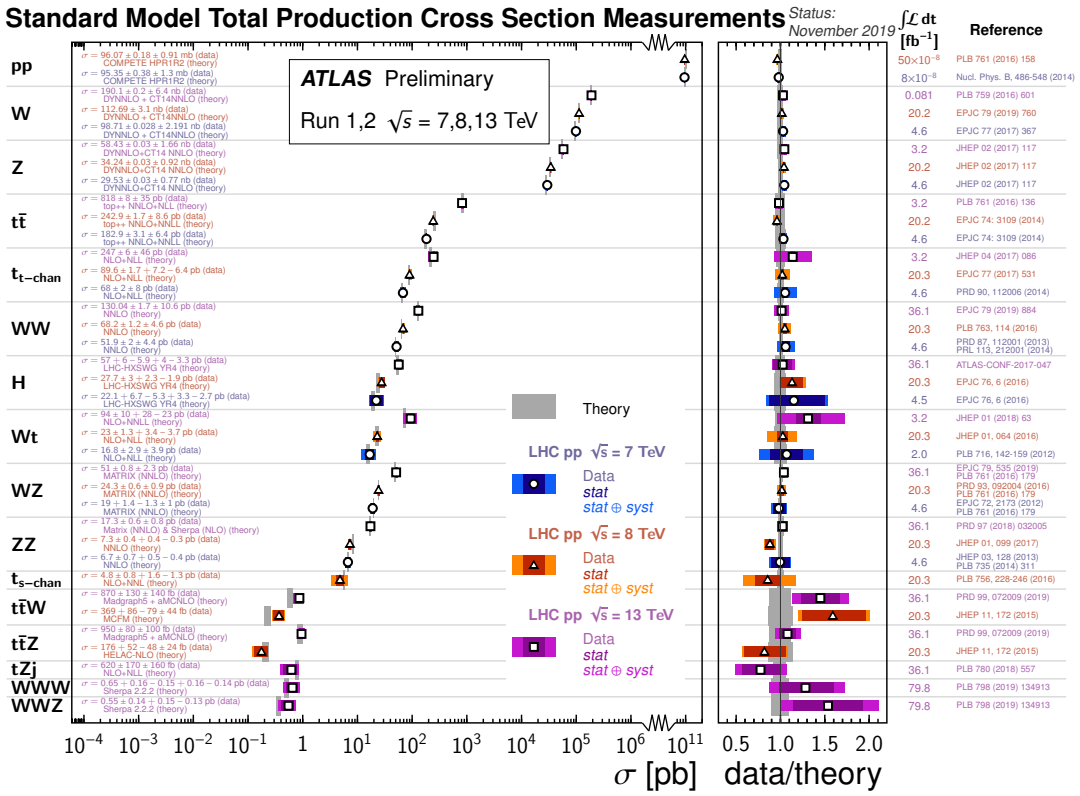

Figure 6.7: The production cross sections of the SM processes at the LHC [131]. The measurements at ATLAS are compared to the theoretical prediction.

190 nb [133]. Events with a leptonically decaying W boson pass the one lepton and high $E_{\mathrm{T}}^{\mathrm{miss}}$ selection. The W+jets events are strongly suppressed by requirements of b-tagging, but the events with a gluon splitting to $b\bar{b}$ pair ($g \to b\bar{b}$) from initial or final state radiation enter the signal regions.

Single top

A process with a single top quark is also a non-negligible background in some signal regions. In the following searches, the single top production in association with a W boson (Wt) gives a large contribution. The cross section of the Wt process is 94 pb [134].

$t\bar{t}+V$

In spite of a small cross section, $t\bar{t}+V$ (V is Z or $W^{\pm}$) is a tough background process. In particular, $t\bar{t}+Z$ with $Z \to \nu\nu$ is an irreducible background in some signal regions. Due to the small cross section, the process has not been precisely studied yet in SM measurements, which makes the background estimation of this process difficult.

Multiboson

Events with more than one electroweak bosons ($W^{\pm}$ and Z) are not main background processes, but still these events account for some fraction of the background in the signal regions. Large $E_{\mathrm{T}}^{\mathrm{miss}}$ is created by neutrinos from $Z \to \nu\nu$ or leptonically decaying W bosons. Contributions are mainly from the diboson process, which has exactly two electroweak bosons.

Z+jets

The Z boson production is a minor background process in signal regions with one lepton and $E_{\mathrm{T}}^{\mathrm{miss}}$ selections. The $Z \to \ell\ell$ process is suppressed by the one lepton and b-tagging requirements.

Multijet

Most pp collisions do not contain leptons produced via electroweak interactions, but they create quarks and gluons via QCD interactions, resulting in multijet signatures. The multijet processes do not contain isolated leptons, but some of the tracks or clusters can be misidentified as leptons. When the jet energy is mismeasured, the transverse energy does not conserve, and non-zero $E_{\mathrm{T}}^{\mathrm{miss}}$ is obtained. The probability of having a jet mimicking a lepton and creating large $E_{\mathrm{T}}^{\mathrm{miss}}$ is very small. However, events with a fake lepton are observed mainly in low $E_{\mathrm{T}}^{\mathrm{miss}}$ regions due to the significantly large cross section of the QCD processes compared to the EW processes. The contribution of the multijet to the following analyses are found to be negligible since large $E_{\mathrm{T}}^{\mathrm{miss}}$ is required in the analyses.

6.3 Discriminating Variables

The transverse mass m_{T} is defined as

$$m_{\mathrm{T}} = \sqrt{2p_{\mathrm{T}}^{\ell} E_{\mathrm{T}}^{\mathrm{miss}} (1 - \cos\Delta\phi(\vec{\ell}, \vec{E}_{\mathrm{T}}^{\mathrm{miss}}))}, \tag{6.1}$$

where $\Delta\phi(\vec{\ell}, \vec{E}_{\mathrm{T}}^{\mathrm{miss}})$ is the angle between the lepton (ℓ) and $E_{\mathrm{T}}^{\mathrm{miss}}$ directions in the transverse plane. This quantity corresponds to the transverse component of the invariant mass of the W boson, and is used to discriminate $t\bar{t}$ and W+jets events exploiting the mass of the leptonically decaying W boson. If an event has a lepton and $E_{\mathrm{T}}^{\mathrm{miss}}$ originating from a W boson decay and there are no additional contributions to the $E_{\mathrm{T}}^{\mathrm{miss}}$ from other particles or the pile-up, the m_{T} of the event has an end point at the mass of the W boson (80.4 GeV). By requiring the high m_{T}, W+jets and $t\bar{t}$ backgrounds with a leptonic W boson are reduced significantly.

The stransverse mass m_{T2} [135] is used for decay topology with two branches (a and b in the following); one branch is fully reconstructed while the other is not fully reconstructed due to an invisible particle. The measured four-momentum is referred to as $\vec{p} = (E_i, \vec{p}_{\mathrm{T},i}, p_{z,i})$, while the unmeasured momentum is referred to as $\vec{q} = (F_i, \vec{q}_{\mathrm{T},i}, q_{z,i})$. For each branch $i \in (a, b)$,

$$m_{\mathrm{T}i}^2 = \left(\sqrt{p_{\mathrm{T}i}^2 + m_{p_i}^2} + \sqrt{q_{\mathrm{T}i}^2 + m_{q_i}^2}\right)^2 - (\vec{p}_{\mathrm{T}i} + \vec{q}_{\mathrm{T}i})^2 \tag{6.2}$$

with $m_{p_i}^2 = E_i^2 - \vec{p}_i{}^2$ and $m_{q_i}^2 = F_i^2 - \vec{q}_i{}^2$. If the invisible momentum and the masses of the particles are correctly assigned, the $m_{\mathrm{T}i}$ must be smaller than the mass of the pair-produced parent. The observed missing momentum $\vec{E}_{\mathrm{T}}^{\mathrm{miss}}$ is split into $\vec{q}_{\mathrm{T}a}$ and $\vec{q}_{\mathrm{T}b}$, and then the stransverse mass is defined as

$$m_{\mathrm{T2}} = \min_{\vec{q}_{\mathrm{T}a} + \vec{q}_{\mathrm{T}b} = \vec{E}_{\mathrm{T}}^{\mathrm{miss}}} \{\max(m_{\mathrm{T}a}, m_{\mathrm{T}b})\}\,. \tag{6.3}$$

The asymmetric transverse mass (am_{T2}) [136–138] is a variation of this variable targeting the di-leptonic $t\bar{t}$ with a missing lepton, as shown in Figure 6.8. For branch a, the measured particle is the b-jet from the top quark decay, and the unmeasured particle is the W boson with a missing lepton. For branch b, the measured particles are the b-jet and charged lepton, while the neutrino is the unmeasured particle. For the masses of the particles needed for the calculation above, $m_{q_a} = m_W = 80.4$ GeV and $m_{q_b} = m_\nu = 0$ GeV are used. According to the discussion above, the distribution of the am_{T2} in the di-leptonic $t\bar{t}$ events has a boundary at the mass of the top quark.

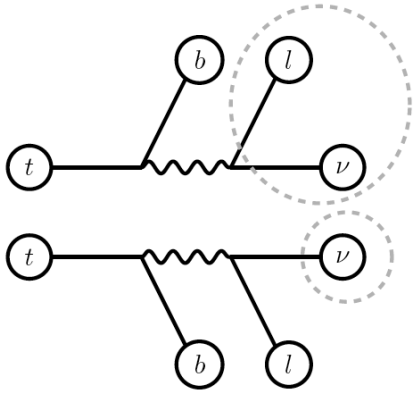

Figure 6.8: An illustration of a di-leptonic $t\bar{t}$ event for the am_{T2} calculation. The unmeasured particles on the top branch (branch a) form a W boson, i.e., a missing lepton and a neutrino, while the one in the bottom branch (branch b) is a neutrino. The assignment of the measured b-jets to either branch a or b is unknown, so both assumptions are tested.

6.4 Background Estimation

The background events in SRs are estimated mainly based on the MC simulation. In order to reduce the uncertainties in the modeling of the MC simulation, the normalization of the MC events is scaled with normalization factors (NF), which are measured ratios of data to MC in CRs. Each SR has a CR for each dominant background process which contributes to the SR yields at roughly above 20%. Once a SR selection is defined with a maximum significance of the signal events as a figure of merit, corresponding CRs are defined with similar selections to the one for the SR. VRs are defined to check if the normalization factors give a proper data/MC normalization in a region which is closer to the SR than the CR. The SR, CR, and VR are statistically independent with each other. Figure 6.9 shows how to define these regions. The CRs should have enough statistics of data to minimize the statistical fluctuation of the normalization factor. The CR selection needs to be as close as possible to the SR selection so that the normalization factor is obtained in similar phase space. If the CR and SR have different MC modeling, the normalization factor obtained in the CR would overestimate or underestimate the background yields in the SR. It is important to design the CR where the contribution of signal events to the total CR yields is negligible; otherwise the normalization factor would become large due to the signal contamination if there are signal events. The CRs for all dominant backgrounds are then fitted simultaneously to obtain the normalization factor for each background process. The normalization factors are applied to each background in the SRs, CRs, and VRs. The CR and VR for each process need to have a good purity of the background process that is being

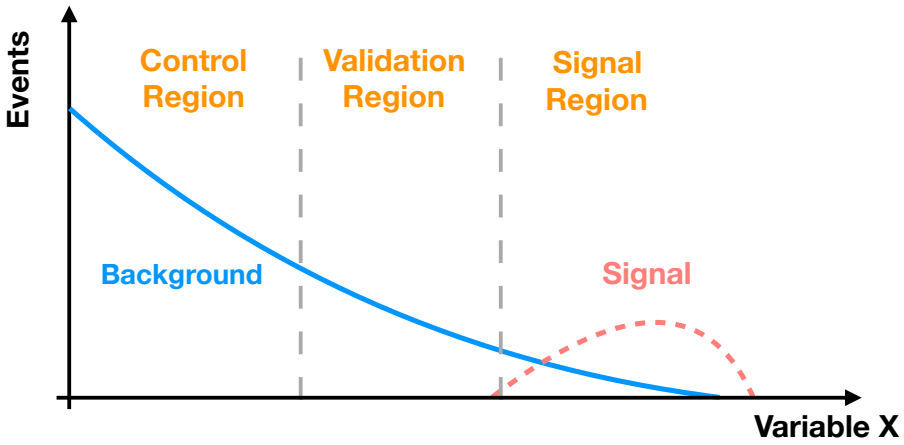

Figure 6.9: An illustration of the background estimation strategy. The SR is defined to maximize the sensitivity to discover the signal. The CR is defined in the region where enough background events are available and the signal contamination is negligible. Between the SR and CR, the VR is defined to validate the extrapolation from the CR to the SR.

normalized. To increase the purity of the process, additional requirements that can enhance the process or suppress the other are used.

6.5 Systematic Uncertainties

Systematic uncertainties are classified into two types: the experimental and theoretical uncertainties. The former is generally associated with the calibration of the physics objects, and the latter is caused by the imperfect modeling of the MC simulation. The impact of uncertainties on each analysis are described in the following chapters, but details of the uncertainties are explained here. The systematic uncertainties are incorporated in profile likelihood fits as nuisance parameters.

6.5.1 Experimental Uncertainty

The experimental uncertainties associated with each object come from the uncertainties in the calibration of each object. The variations of the number of events in the SR, CR, and VR from each source of uncertainty are included in the fit as nuisance parameters, as described in Section 6.6.

Jets

The jet energy scale (JES) and jet energy resolution (JER) are the main components of the uncertainty in the momentum of jets. As already discussed in Section 5.3, these uncertainties are associated with the calibration of them. The uncertainties affect the event yields directly from the jet p_{T} cuts or via indirect effects on the magnitude and direction of the $E_{\mathrm{T}}^{\mathrm{miss}}$. The uncertainty in the JVT explained in Section 5.3 is also considered.

Leptons

The uncertainties in the electron and muon calibrations: the scale and resolution of the lepton momentum and the isolation efficiency measurements are considered. The size of the lepton uncertainties is typically small compared to that for the jet measurements.

Flavor tagging

For the standard b-tagging, the uncertainties in the calibration of the efficiencies for b-, c-, and light-flavor jets in Section 5.4 are treated separately. These uncertainties affect SR event yields if CR selections have different b-tagging requirements or flavor composition of a b-tagged jets. The uncertainties in the soft b-tagging are discussed in Section 8.4.

Luminosity

For the minor backgrounds that do not have a dedicated CR and the signal, the uncertainty in the luminosity measurement is considered. The uncertainties are mainly coming from the vdM scan and calibration transfer from the scan to the data for physics analyses. The uncertainty for the 2015–2016 data is 2.1%, and for the full Run 2 data is 1.7%.

Pile-up reweighting

The distribution of the number of pp interactions per event in the MC simulation is reweighted to match the distribution of data. The uncertainty in the reweighting is included to account for the residual imperfect pile-up modeling in the MC simulation.

$E_{\mathrm{T}}^{\mathrm{miss}}$ soft term

The uncertainty in the $E_{\mathrm{T}}^{\mathrm{miss}}$ originating from hard objects such as jets or leptons are considered in the uncertainties of each hard objects. In addition to them, the data and MC difference of the $E_{\mathrm{T}}^{\mathrm{miss}}$ soft term is evaluated in the $E_{\mathrm{T}}^{\mathrm{miss}}$ calibration with $Z \to \mu\mu$ events [126]. The uncertainties in the scale and resolution of the soft term from the calibration are included.

Normalization

The uncertainties in the NFs of the dominant background processes are originating from limited statistics of the data in the CRs.

MC statistics

Due to the tight selections for the SRs, the background and signal MC events are limited in some cases, which could be one of the main uncertainties.

6.5.2 Theoretical Uncertainty

The main uncertainty in the MC simulation is caused by the limited accuracy of the QCD perturbation calculation. The missing higher orders cause the uncertainties in the MC simulation. The treatment of the evaluation depends on the generators used for the process. The methods used for the evaluation are given below. The uncertainties in the choice of proton PDFs are evaluated by using different sets of PDF and are found to be negligible.

For the main background processes which have a dedicated CR, the impacts on the extrapolation of the NFs from the CR to the other regions are evaluated. The transfer factor (TF) is defined as the ratio between the event yields in the CR and the other region for each main background process. For example, the $t\bar{t}$ TF which controls the number of $t\bar{t}$ events in the SR is

$$TF^{t\bar{t}}_{\mathrm{SR}} = \frac{N^{t\bar{t}}_{\mathrm{SR}}}{N^{t\bar{t}}_{\mathrm{TCR}}}, \tag{6.4}$$

where $N^{t\bar{t}}_{\mathrm{SR}}$ and $N^{t\bar{t}}_{\mathrm{TCR}}$ are the number of $t\bar{t}$ events in the SR and $t\bar{t}$ CR, respectively. The uncertainties are also evaluated for the transfer factors corresponding to the extrapolation from the $t\bar{t}$ CR to the other CRs (e.g., W+jets CR) and VRs. The uncertainties that affect the overall normalization of the background process are canceled because these effects are common in all regions. For the systematic uncertainties which have $\pm 1\sigma$ variations, the difference between them is taken as the uncertainty. For the systematic uncertainties which have only one variation, such as the generator comparison, the difference between the alternative and default settings are taken. For the minor background processes without a dedicated CR, the direct impact on the event yield in each region is evaluated.

$t\bar{t}$ modeling

The uncertainty in the hard scatter process is evaluated by comparing generators with different matrix element (ME) calculations. The nominal $t\bar{t}$ sample with Powheg (ME) and Pythia (PS) is compared with an alternative $t\bar{t}$ sample generated with MG5_aMC@NLO(ME)

and Pythia (PS), and the difference is taken as the uncertainty in the hard scatter. The uncertainty in the PS is evaluated with an alternative sample with Powheg (ME) and Herwig (PS). Alternative samples with the same generator but with different ISR radiation hardness are used to evaluate the uncertainty in the ISR jet.

W+jets modeling

The uncertainties in the renormalization and factorization scales are evaluated by varying these scales from 1/2 to 2 with respect to the nominal scales in the nominal Sherpa sample. The parameters used for the resummation of the soft gluon emission and the matching between ME and PS are varied to evaluate the uncertainties in them. In addition to that, the nominal Sherpa sample is compared with MadGraph (ME) + Pythia (PS) sample to evaluate the uncertainty in the Sherpa PS.

Single top modeling

The uncertainty in the single top process is dominated by the interference between the $t\bar{t}$ and single top Wt processes. The uncertainty is evaluated by comparing the diagram removal (DR) scheme and diagram subtraction (DS) scheme [139], and the difference is taken as the uncertainty. The uncertainties in the hard scatter, PS, and ISR radiation are taken into account in the same way as for the $t\bar{t}$ modeling. This treatment is included in the analysis targeting the higgsino-like LSP scenario, where the contribution of the single top is visible. Given the small single top contribution to the signal region and control regions in the analyses with soft b-tagging, a flat 30% uncertainty is added.

Modeling of minor backgrounds

The uncertainties in the production cross sections are taken into account in the minor background processes that do not have a dedicated control region, and the signal processes. Given the small impact of the uncertainties from the minor backgrounds on the total yields, flat uncertainties in the event yields in each region is added as an inclusive modeling uncertainty.

6.6 Statistical Treatments

Fitting is performed based on a likelihood function:

$$L(\boldsymbol{\mu}, \boldsymbol{\theta}; \boldsymbol{n}) = \prod_r \frac{1}{n_r!} \left(\sum_i \mu^i y_r^i \right)^{n_r} \exp\left(- \sum_i \mu^i y_r^i \right) \prod_j C(\theta_j). \tag{6.5}$$

The first part is a product of the probabilities to observe n_r events in a region r, where $\mu^i y_r^i$ events are predicted for the i-th process in a set of background or signal processes. The μ^i is a NF applied to the events predicted by MC (y_r^i). The μ^i is fixed to unity for minor backgrounds that do not have a dedicated CR. Systematic uncertainties are incorporated into the likelihood as nuisance parameters (NPs). The NPs vary the predicted signal and background events. The yields are parameterized with the NPs as

$$y_r^i = y_r^{i0} + \sum_{\theta_j \in \boldsymbol{\theta}} \theta_j \Delta y_r^{ij}, \tag{6.6}$$

where y_r^{i0} is the pre-fit yield without systematics, and Δy_r^{ij} is a size of the variation of the yield y_r^i from the effect of the nuisance parameter θ_j. The Δy_r^{ij} corresponds to the 1σ variation of the uncertainty, which is calculated before fitting. If $\theta_j = 0$, the event yields are not changed by the j-th NP in all regions. The nuisance parameters are constrained by the second part of the likelihood. For each nuisance parameter θ_j, the $C(\theta_j)$ is a term that constrains the nuisance parameter typically using a Gaussian form.

In order to discover or exclude certain models like an SM-only prediction or existence of a new physics beyond the SM, hypothesis tests are performed [140]. In the following, μ refers to the μ^{signal}, the signal strength compared to the theoretically predicted signal yield. The test statistic for hypothesis tests is defined with as a ratio of the likelihoods

$$\lambda(\mu) = \frac{L(\mu, \hat{\hat{\boldsymbol{\theta}}})}{L(\hat{\mu}, \hat{\boldsymbol{\theta}})} \quad (0 \leq \hat{\mu} < \mu), \tag{6.7}$$

where a set of $\hat{\mu}$ and $\hat{\boldsymbol{\theta}}$ maximizes L, and $\hat{\hat{\boldsymbol{\theta}}}$ is the value that maximizes L for a given μ. The ratio $\lambda(\mu)$ varies between 0 and 1, and a larger value of λ means that the value gives better description of the observed data. The likelihood ratio is converted to

$$q_\mu = -2 \ln \lambda(\mu), \tag{6.8}$$

as a test statistic for hypothesis tests.

To quantify the incompatibility of observed data with a hypothesis with a signal strength μ, a p-value is defined as

$$p_\mu = \int_{q_{\mu,\text{obs}}}^{\infty} f(q'_\mu|\mu) dq'_\mu, \tag{6.9}$$

where $q_{\mu,\text{obs}}$ is an observed value of q_μ, and $f(q_\mu|\mu)$ is a probability density function of the q_μ for a given μ. By definition, a smaller p-value means that the hypothesis with the μ is more incompatible with the observed data.

Background only fit

The background only fit is performed without signal samples to estimate background contribution in SRs and VRs. Only CRs are used in the background only fit, and the obtained μ values (NPs) for the background processes are applied to the SR and VR yields to estimate the background yields in these regions.

Model-dependent signal fit (Exclusion fit)

The model-dependent signal fit is a fit to exclude a signal model. The SRs and CRs are used in the fit, considering a signal contribution in these regions. In the following chapters, signal regions for the exclusion fit are defined as multi-bin signal regions. The exclusion fit over the multi-bin SR (shape-fit) exploits the shapes of the signal and background distributions so that the sensitivity to exclude the model is improved by considering the correlation among the multiple bins. When a signal model contributes to more than one SRs, it is beneficial to combine these SRs. In that case, a simultaneous fit is performed using these SRs as if these SRs were a single multi-bin SR so that more powerful exclusion sensitivity is achieved than the individual SRs.

Using the background only hypothesis and signal and background hypothesis, corresponding to p_0 and p_1, respectively, the CLs [141] is defined as

$$\mathrm{CLs} = \frac{p_1}{p_0}. \tag{6.10}$$

The p-value for the signal plus background hypothesis (p_1) itself is not used, but a penalty $1/p_0$ is applied in order to avoid rejecting a signal model when observed data is less likely to the background only prediction either. A model is considered as excluded at 95% confidence level (CL) when the CLs is lower than 0.05, which corresponds to the modified probability of having a signal model to be below 5%.

6.7 Previous Results

6.7.1 Higgsino-like LSP Model

A similar scenario to the higgsino LSP model with large $\Delta m(\tilde{t}_1, \tilde{\chi}_1^0)$ was searched in the previous analysis at ATLAS with Run 1 data corresponding to an integrated luminosity of 20 fb^{-1} of pp collisions at $\sqrt{s} = 8$ TeV [142]. A model where $\tilde{t}_1$ decays to $t\tilde{\chi}_1^0$ or $b\tilde{\chi}_1^\pm$, with $\tilde{\chi}_1^\pm$ decaying into $W^*\tilde{\chi}_1^0$ was considered. In this analysis, $t\tilde{\chi}_2^0$ decay was not considered. For the mass-splitting between $\tilde{\chi}_1^\pm$ and $\tilde{\chi}_1^0$, both 5 GeV and 20 GeV mass-splittings were considered. The branching ratios of the $\tilde{t}_1$ decay were scanned as the Br($t\tilde{\chi}_1^0$:$b\tilde{\chi}_1^\pm$) of 75:25, 50:50, and 25:75. Figure 6.10 shows the exclusion limit at 95% CL for each assumption. The

analysis was performed using two b-jets, a lepton, and $E_{\mathrm{T}}^{\mathrm{miss}}$ in the final states. The right-handed $\tilde{t}_1$ scenario in Run 2 analysis is similar to the assumption with $\Delta m(\tilde{\chi}_1^{\pm}, \tilde{\chi}_1^0) = 5$ GeV and $\mathrm{Br}(t\tilde{\chi}_1^0{:}b\tilde{\chi}_1^{\pm}) = (50{:}50)$ %, ignoring the difference between $t\tilde{\chi}_1^0$ and $t\tilde{\chi}_2^0$ decays. In that scenario, masses of $\tilde{t}_1$ up to 515 GeV with $\tilde{\chi}_1^0 = 100$ GeV were excluded and the limit reached to 160 GeV for the mass of $\tilde{\chi}_1^0$. Because of a small excess observed in the Run 1 search, the observed limits were weaker than the expected ones.

6.7.2 Simplified Model

The simplified model has been a benchmark scenario in the stop searches at ATLAS and CMS since the beginning of the experiments [1, 142–163]. Figure 6.11 shows the summary of ATLAS results as of 2018, including the results in Run 1 and Run 2 in 2015–2016. In general, the searches have been carried out using the full-hadronic (0L), semi-leptonic (1L) and di-leptonic (2L) analyses. For the $\tilde{t}_1 \to t\tilde{\chi}_1^0$ (2-body) decay region, the 0L and 1L analyses have strong sensitivities, while in the compressed region with $\tilde{t}_1 \to bW\tilde{\chi}_1^0/bff'\tilde{\chi}_1^0$ (3-body / 4-body) decays, 1L, and 2L analyses have compatible sensitivities. At the very compressed region of the 4-body decay, the mono-jet analysis which utilizes high $E_{\mathrm{T}}^{\mathrm{miss}}$ and a high p_{T} ISR signature has high sensitivity while the 1L and 2L analyses lose sensitivity due to the inefficiency of the lepton reconstruction. The bottom right corner of the exclusion region with large $\Delta m(\tilde{t}_1, \tilde{\chi}_1^0)$ has been extended up to around 1 TeV stop mass, while in the compressed region the search sensitivities were lower due to the difficulties of the reconstruction of low p_{T} particles. In the large $\Delta m(\tilde{t}_1, \tilde{\chi}_1^0)$ region, the $\tilde{t}_1$ decay depend on the assumption of the LSP, and the simplified model does not have sufficient power to cover the higgsino like LSP. In addition, the excluded region in the small $\Delta m(\tilde{t}_1, \tilde{\chi}_1^0)$ was smaller compared to the large $\Delta m(\tilde{t}_1, \tilde{\chi}_1^0)$. Therefore, the search in Chapter 9 is performed targeting the stop in the 4-body region with a new soft b-tagging technique.

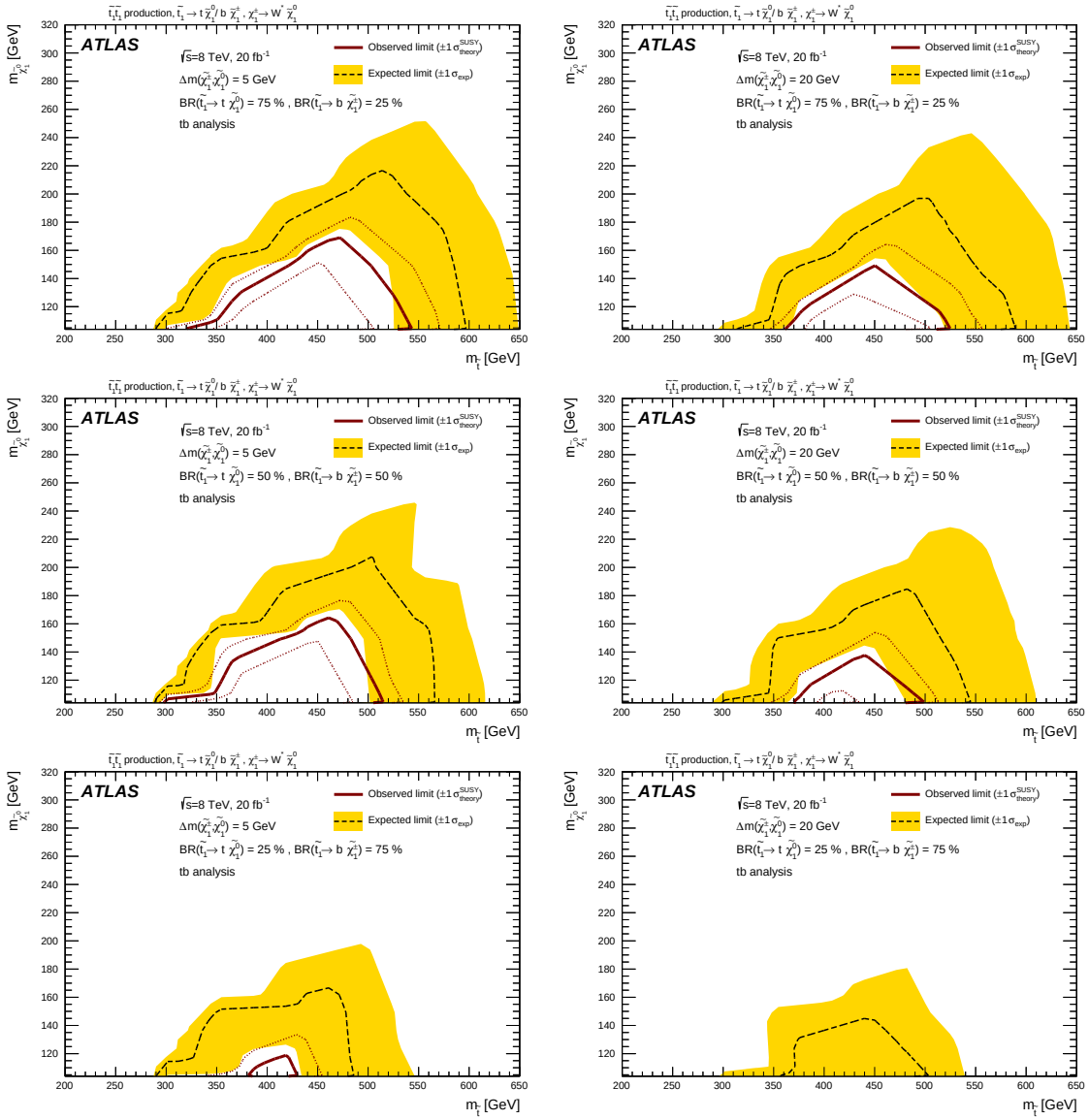

Figure 6.10: Exclusion limits for the $t\tilde{\chi}_1^0 \to t\tilde{\chi}_1^0/b\tilde{\chi}_1^\pm$ decays with $\mathrm{BR}(b\tilde{\chi}_1^\pm) = 25$, 50, and 75% (in descending rows) and $\Delta m(\tilde{\chi}_1^\pm, \tilde{\chi}_1^0) = 5$ (left) and 20 (right) GeV from the Run 1 analysis [142]. Following the $\tilde{t}_1 \to b\tilde{\chi}_1^\pm$ decay, $\tilde{\chi}_1^\pm$ decays into $W^*\tilde{\chi}_1^0$. The analysis was performed with one lepton final states requiring two b-jets and high $E_{\mathrm{T}}^{\mathrm{miss}}$.

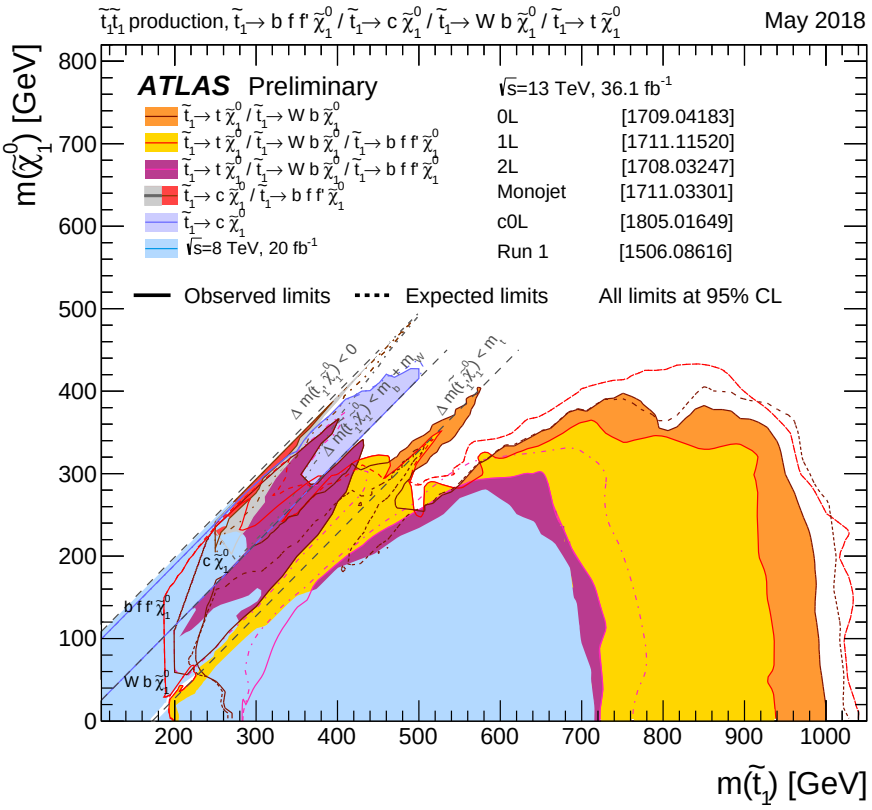

Figure 6.11: Exclusion contours from previous searches at ATLAS [164]. The results of Run 1 analyses [142] and Run 2 analyses [1,143–145] with the data collected in 2015-2016 are displayed. Another scenario in which $\tilde{t}_1$ decays into a charm quark and the LSP [165] is overlaid, but it assumes a different model with a flavor-changing neutral-current decay. The dashed lines show the expected exclusion limits while the solid lines show the observed exclusion limits. The gray dashes lines separate the $\tilde{t}_1$ decay modes depending on the mass difference between $\tilde{t}_1$ and $\tilde{\chi}_1^0$. If the on-shell top decay is kinematically allowed ($\Delta m(\tilde{t}_1, \tilde{\chi}_1^0) > m_t$), $\tilde{t}_1 \to t\tilde{\chi}_1^0$ is considered. In the diagonal region where $m_b + m_W < \Delta m(\tilde{t}_1, \tilde{\chi}_1^0) < m_t$ and $\Delta m(\tilde{t}_1, \tilde{\chi}_1^0) < m_b + m_W$, the 3-body decay ($\tilde{t}_1 \to bW\tilde{\chi}_1^0$) and 4-body decay ($\tilde{t}_1 \to bff'\tilde{\chi}_1^0$) are considered, respectively. For each decay mode, 100% branching ratio is considered.

Chapter 7

Search for Stop with Large $\Delta m(\tilde{t}_1, \tilde{\chi}_1^0)$ Scenarios

In this chapter, a stop search with the data recorded in 2015–2016 is presented. The integrated luminosity of the data that satisfies good quality criteria is 36.1 fb^{-1}. The main target of the search is the stop pair production under the higgsino-like LSP scenario. As discussed in Section 6.1, the higgsino-like LSP scenario is a complicated model where many decay modes of $\tilde{t}_1$ are possible, and the branching ratio depends on the MSSM parameters. The difficulties of the higgsino-like LSP scenario lies in the compressed mass spectra of the higgsino states, which generate low p_{T} objects in the final states. Given the small mass-splitting between $\tilde{\chi}_2^0$ and $\tilde{\chi}_1^0$, $\tilde{t}_1 \to t\tilde{\chi}_1^0$ and $\tilde{t}_1 \to t\tilde{\chi}_2^0$ have similar signatures except for the soft activity emitted from the decay of $\tilde{\chi}_2^0$. Both decay modes contain high p_{T} top quarks when $\tilde{t}_1$ is sufficiently heavier than $\tilde{\chi}_1^0/\tilde{\chi}_2^0$. Hence the signal regions designed for the $\tilde{t}_1 \to t\tilde{\chi}_1^0$ decay[1] can be exploited for $\tilde{t}_1 \to t\tilde{\chi}_2^0$ as well. In this chapter, $\tilde{t}_1 \to b\tilde{\chi}_1^\pm$ decay[2] is targeted so that the whole decay modes of the higgsino signals are covered.

7.1 Event Selection

A benchmark signal, which is used in the optimization of the signal region, is the higgsino simplified model with masses of $m(\tilde{t}_1, \tilde{\chi}_2^0, \tilde{\chi}_1^\pm, \tilde{\chi}_1^0) = (600, 210, 205, 200)$ GeV. The mostly right-handed $\tilde{t}_1$ assumption in which the branching fractions of $t\tilde{\chi}_1^0$, $t\tilde{\chi}_2^0$, and $b\tilde{\chi}_1^\pm$ are 25%, 25%, and 50%, respectively, are considered, since the signature is not well covered by the $t\tilde{\chi}_1^0$ decay searches [1, 142, 146].

As seen in the diagram in Figure 6.5, the final state contains b-jets, LSPs, and soft decay products from the $\tilde{\chi}_1^\pm$ decay via a virtual W boson. A simple selection with only high p_{T} objects, like a b-jets and $E_{\mathrm{T}}^{\mathrm{miss}}$ selection, cannot be good for that signal due to overwhelming

[1] The diagram of the $\tilde{t}_1 \to t\tilde{\chi}_1^0$ decay is the right diagram in Figure 6.4.
[2] The diagram of the $\tilde{t}_1 \to b\tilde{\chi}_1^\pm$ decay is shown in Figure 6.5.

backgrounds such as Z+jets with a b-quark pair from a gluon. Adding an object on top of the b-quark and $E_{\mathrm{T}}^{\mathrm{miss}}$ selection can suppress the background significantly. In this case, the additional object is a low p_{T} lepton from the $\tilde{\chi}_1^{\pm}$ decay. The presence of a low p_{T} lepton can be distinctive for such compressed signatures.

The preselection, which is a set of loose cuts on variables before designing dedicated signal selections, for this search is summarized in Table 7.1. The events are collected by the $E_{\mathrm{T}}^{\mathrm{miss}}$ trigger. Events that satisfy offline $E_{\mathrm{T}}^{\mathrm{miss}} > 230$ GeV are selected. Figures 7.1–7.2 show comparisons between the data and MC after the preselection.

Table 7.1: Preselection criteria used for the stop search with 2015–2016 data. The lepton refers to an electron or a muon, including a lepton from a leptonic decay of τ.

	Preselection
Trigger	$E_{\mathrm{T}}^{\mathrm{miss}}$ triggers only
Data quality	jet cleaning, primary vertex
Number of leptons	$= 1$ lepton
Lepton p_{T} [GeV]	> 4 for μ
	> 5 for e
Number of jets	≥ 2 ($p_{\mathrm{T}} > 25$ GeV)
Number of b-tags	> 0
$E_{\mathrm{T}}^{\mathrm{miss}}$ [GeV]	> 230
$\lvert\Delta\phi(j_{1,2}, \vec{E}_{\mathrm{T}}^{\mathrm{miss}})\rvert$	> 0.4

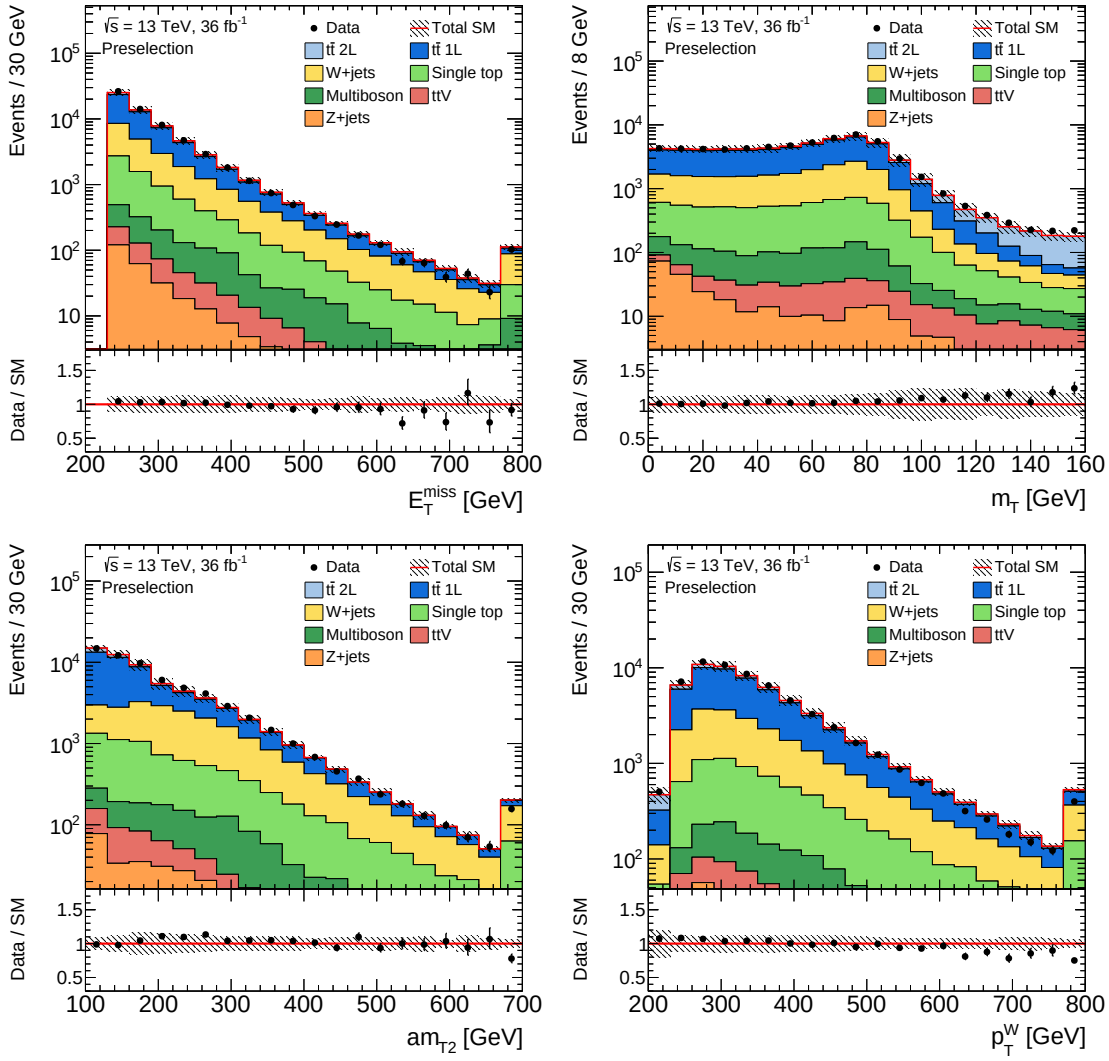

Figure 7.1: Comparison of data and simulation distributions with the preselection: $E_{\mathrm{T}}^{\mathrm{miss}}$ (top left), m_{T} (top right), am_{T2} (bottom left), and p_{T}^{W} (bottom right). The statistical and experimental uncertainties are displayed. The overflow is included in the last bin.

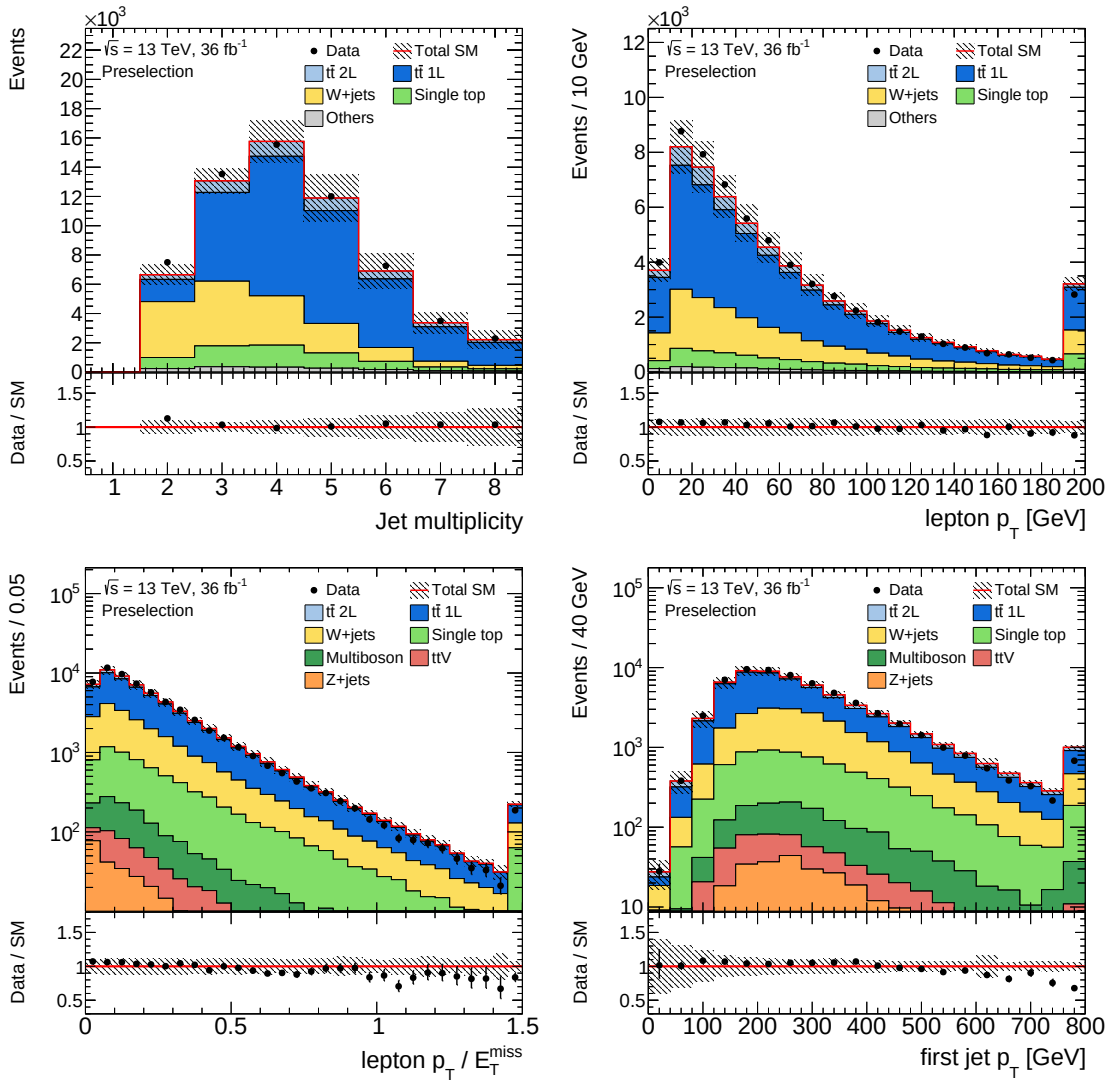

Figure 7.2: Comparison of data and simulation distributions with the preselection: the jet multiplicity (top left), lepton p_{T} (top right), $p_{\mathrm{T}}^{\ell}/E_{\mathrm{T}}^{\mathrm{miss}}$ (bottom left), and leading jet p_{T} (bottom right). The statistical and experimental uncertainties are displayed. The overflow is included in the last bin.

On top of the preselection, a series of cuts are required to define a SR. The selection is optimized by trying several variables and changing cut values to search for the best set of selections that maximizes the significance of the benchmark signal yields over the background prediction. The selection is summarized in Table 7.2, and the SR is named `bCsoft_med`. The p_{T}^{W} is the magnitude of the vectorial sum of the lepton and $E_{\mathrm{T}}^{\mathrm{miss}}$. Since the signal tends to have very low p_{T} leptons, the SR is defined in small m_{T}. Figure 7.3 shows distributions used to define the SR. All selections of the SR definition but the selections of the variables that are shown are applied in these plots. Since the signature of the signal is characterized by a low p_{T} lepton and large $E_{\mathrm{T}}^{\mathrm{miss}}$ created by the LSP, the ratio between the lepton p_{T} and $E_{\mathrm{T}}^{\mathrm{miss}}$ tends to be small for the signal, while the lepton p_{T} and $E_{\mathrm{T}}^{\mathrm{miss}}$ tend to balance in the background processes. The shape of the $p_{\mathrm{T}}^{\ell}/E_{\mathrm{T}}^{\mathrm{miss}}$ variable is exploited to maximize the experimental sensitivity. In the shape fit for the exclusion, the $p_{\mathrm{T}}^{\ell}/E_{\mathrm{T}}^{\mathrm{miss}}$ is binned into three bins. The small $\Delta m(\tilde{t}_1, \tilde{\chi}_1^0)$ signal tends to appear in the small bins, while the high $\Delta m(\tilde{t}_1, \tilde{\chi}_1^0)$ signal would be seen in the high $p_{\mathrm{T}}^{\mathrm{lepton}}/E_{\mathrm{T}}^{\mathrm{miss}}$ bins. Table 7.3 shows the event yields after applying the SR selection, and the fraction of the background components is summarized in Figure 7.4. The background events are dominated by the W+jets and semi-leptonic $t\bar{t}$, followed by the single top.

Table 7.2: The event selection for the signal region. The preselection is applied before the selection shown here. For the p_{T} of jets and b-jets, requirements on the top four (two) highest p_{T} jets (b-jets) are described. For the exclusion, a shape-fit on $p_{\mathrm{T}}^{\ell}/E_{\mathrm{T}}^{\mathrm{miss}}$ is performed with a boundary shown in the bottom row.

	`bCsoft_med`
Preselection	Table 7.1
Number of jets	≥ 3
Number of b-jets	≥ 2
Jet p_{T}	$> (120, 60, 40, 25)$ GeV
b-jet p_{T}	$> (120, 60)$ GeV
$E_{\mathrm{T}}^{\mathrm{miss}}$	> 230 GeV
m_{T}	< 160 GeV
am_{T2}	> 200 GeV
$\min(\Delta\phi(\vec{p}_{\mathrm{T}}^{\mathrm{miss}}, b\text{-jet}))$	> 0.8
p_{T}^{W}	> 400 GeV
$p_{\mathrm{T}}^{\ell}/E_{\mathrm{T}}^{\mathrm{miss}}$ (single-bin SR)	< 0.03
$p_{\mathrm{T}}^{\ell}/E_{\mathrm{T}}^{\mathrm{miss}}$ (multi-bin SR)	[0, 0.015, 0.03, 0.1]

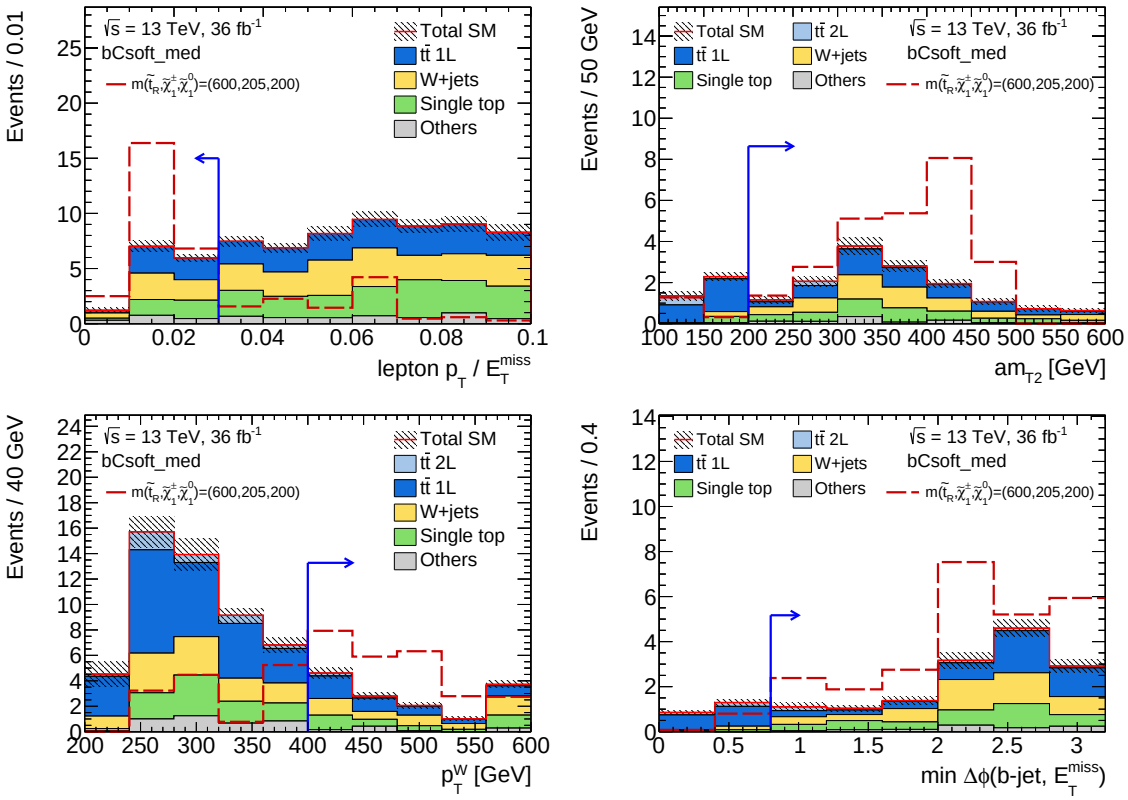

Figure 7.3: Distribution of the variables used to define the `bCsoft_med` discovery SR: $p_{\mathrm{T}}^{\ell}/E_{\mathrm{T}}^{\mathrm{miss}}$ (top left), am_{T2} (top right), p_{T}^{W} (bottom left), and $\min(\Delta\phi(\vec{p}_{\mathrm{T}}^{\,\mathrm{miss}}, b\text{-jet}))$ (bottom right). All `bCsoft_med` cuts except the one on the displayed distribution are applied. Only statistical uncertainty is included. The overflow is added in the last bin.

Table 7.3: Expected number of events in `bCsoft_med` SR with 36.1 fb^{-1} before applying the NFs. Only the statistical uncertainty of the MC samples is given. The background yields are compared with that of the benchmark signal with $m(\tilde{t}_1, \tilde{\chi}_1^{\pm}, \tilde{\chi}_1^0) = (600, 205, 200)$ GeV in the higgsino-like LSP model with the mostly right-handed stop assumption.

Process		Events
Background	$t\bar{t}$ 1L	4.68 ± 0.28
	$t\bar{t}$ 2L	0.59 ± 0.08
	W+jets	4.72 ± 0.41
	Single top	3.29 ± 0.32
	Multiboson	0.31 ± 0.24
	Z+jets	0.17 ± 0.05
	$t\bar{t} + V$	0.44 ± 0.10
	Total	14.21 ± 0.65
Benchmark signal		25.69 ± 3.98

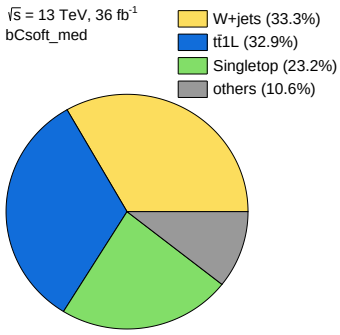

Figure 7.4: Breakdown of the individual SM contributions to the signal region. The prefit background yields are used. The minor backgrounds are merged into "Others."

7.2 Background Estimation

The background estimation follows the strategy discussed in Section 6.4. The number of background events estimated from the MC simulation is normalized to the data. The prediction from the MC simulation is scaled by a parameter μ for each main background process. To extract the NFs μ for the $t\bar{t}$, W+jets, and single top, CRs are defined for each process with accompanied VRs, as summarized in Table 7.4. For the other minor background processes, the estimation relies on the MC prediction with the theoretical cross sections, i.e., $\mu = 1$. The $t\bar{t}$ CR (TCR) and VR (TVR) are defined by inverting the am_{T2} cut for the SR selection to enhance the $t\bar{t}$ events. The $p_{\mathrm{T}}^{\ell}/E_{\mathrm{T}}^{\mathrm{miss}}$ condition is inverted for TCR, while the same value as for the SR is used for the TVR. The W+jets and single top CRs (WCR and STCR) are defined as $p_{\mathrm{T}}^{\ell}/E_{\mathrm{T}}^{\mathrm{miss}} > 0.2$ to minimize the signal contamination and increase the statistics in the CRs, while VRs (WVR and STVR) are defined as $0.1 < p_{\mathrm{T}}^{\ell}/E_{\mathrm{T}}^{\mathrm{miss}} < 0.2$. Other cut values are also modified from the SR selection in order to enhance the background process or increase the statistics in the regions, as shown in Table 7.4. The event yields in these CRs are shown in Table 7.5. In the table, the yield of the benchmark signal is also shown, and the signal contamination in the CR is found to be negligible. As shown in Figure 7.5, each CR has a high purity ($>\sim 50\%$) of the corresponding background process. The yields in the VRs are also shown in Table 7.6. The selections for the VRs are close to the ones for the SRs, but the signal contamination in the VRs is suppressed to a negligible level. The composition of the background processes in each VR is shown in Figure 7.6.

Table 7.4: Selections for the control and validation regions. The SR definition is also shown for comparison. The preselection is summarized in Table 7.1. The "–" indicates that there is no requirement.

	SR	TCR/VR	WCR/VR	STCR/VR
Preselection	preselection in Table 7.1			
Number of (jets, b-tags)	$(\geq 3, \geq 2)$	$(\geq 3, \geq 2)$	$(\geq 3, = 1)$	$(\geq 3, \geq 2)$
b-tagged jet p_{T} [GeV]	$> (120,\ 60)$	$> (120,\ 60)$	> 120	$> (120,\ 60)$
Jet p_{T} [GeV]	$> (120,\ 60,\ 40,\ 25)$			
$E_{\mathrm{T}}^{\mathrm{miss}}$ [GeV]	> 230			
m_{T} [GeV]	< 160			
p_{T}^{W} [GeV]	> 400			
$p_{\mathrm{T}}^{\ell}/E_{\mathrm{T}}^{\mathrm{miss}}$	< 0.03	> 0.03 / < 0.03	> 0.2 / $[0.1, 0.2]$	> 0.2 / $[0.1, 0.2]$
am_{T2} [GeV]	> 200	< 200	> 200	> 200
$\min(\Delta\phi(\vec{p}_{\mathrm{T}}^{\mathrm{miss}}, b\text{-jet}))$	> 0.8	–	$[0.8, 2.5]$	> 0.8
$\Delta R(b_1, b_2)$	–	–	–	> 1.2

Table 7.5: Pre-fit expected events in `bCsoft_med` CRs for 36.1 fb^{-1}. Only the statistical uncertainties of the MC samples are given. The benchmark signal is the higgsino simplified model with the masses of $m(\tilde{t}_1, \tilde{\chi}_1^{\pm}, \tilde{\chi}_1^0) = (600, 205, 200)$ GeV, and the mostly right-handed scenario is considered.

	TCR	WCR	STCR
$t\bar{t}$ 1L	1086.66 ± 8.36	72.73 ± 1.99	35.79 ± 1.88
$t\bar{t}$ 2L	99.01 ± 3.31	9.19 ± 0.67	4.18 ± 0.43
W+jets	10.26 ± 0.71	156.72 ± 3.38	37.71 ± 1.23
Single top	73.80 ± 4.03	70.59 ± 1.95	164.75 ± 2.74
Multiboson	2.34 ± 0.63	12.93 ± 1.84	7.08 ± 3.25
Z+jets	0.39 ± 0.07	1.91 ± 0.24	0.50 ± 0.14
$t\bar{t} + V$	11.94 ± 0.55	1.53 ± 0.18	3.02 ± 0.21
Total Background	1284.40 ± 9.91	325.60 ± 4.81	253.04 ± 4.84
Benchmark signal	6.56 ± 2.10	1.24 ± 0.74	0.67 ± 0.50

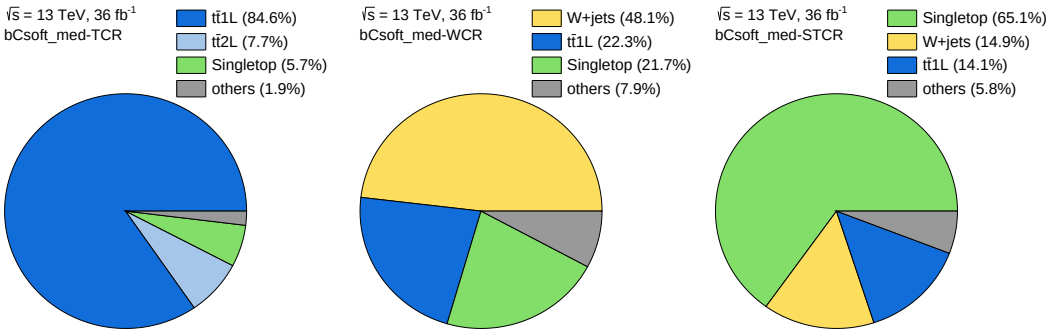

Figure 7.5: Breakdown of the individual SM contributions to the $t\bar{t}$ (left), W+jets (middle), and single top (right) control regions. The pre-fit yields are displayed. The minor backgrounds are merged into the "Others" category.

The distributions of some key variables in TCR, WCR, and STCR are shown in Figures 7.7, 7.8, and 7.9, respectively. The NFs obtained by the background only fit in the three CRs are shown in Table 7.7. The NFs are close to unity for $t\bar{t}$ and W+jets, while the NF for the single top is small. In the nominal single top Wt process, the DR scheme [139] is used, but the interference term of the $WWbb$ final states between the single top and $t\bar{t}$ is poorly modeled in this phase space [166]. The distributions in VRs after applying the NF are shown in Figures 7.10–7.12. In all validation regions, reasonable agreement between the data and MC within the uncertainties is observed. The post-fit yields in the CRs and VRs are summarized in Table 7.8.

Table 7.6: Pre-fit expected events in `bCsoft_med` VRs for 36.1 fb^{-1}. Only the statistical uncertainty of the MC samples is given. The benchmark signal is the higgsino simplified model with the masses of $m(\tilde{t}_1, \tilde{\chi}_1^{\pm}, \tilde{\chi}_1^0) = (600, 205, 200)$ GeV, and the mostly right-handed scenario is considered.

	TVR	WVR	STVR
$t\bar{t}$ 1L	35.82 ± 0.68	14.48 ± 0.51	8.01 ± 0.37
$t\bar{t}$ 2L	5.79 ± 0.30	2.29 ± 0.17	1.24 ± 0.19
W+jets	0.99 ± 0.20	46.24 ± 2.02	11.02 ± 0.62
Single top	3.72 ± 0.64	10.01 ± 0.63	22.41 ± 0.89
Multiboson	0.02 ± 0.01	2.87 ± 0.57	0.24 ± 0.11
Z+jets	0.05 ± 0.04	0.39 ± 0.10	0.16 ± 0.05
$t\bar{t} + V$	0.47 ± 0.12	0.65 ± 0.10	0.77 ± 0.13
Total Background	46.86 ± 1.01	76.93 ± 2.26	43.86 ± 1.18
Benchmark Signal	2.04 ± 0.83	1.43 ± 0.98	0.64 ± 0.47

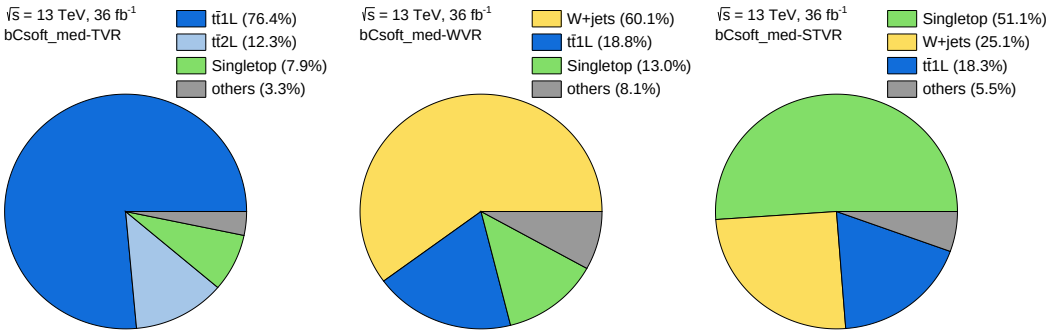

Figure 7.6: Breakdown of the individual SM contributions to the $t\bar{t}$ (left), W+jets (middle), and single top (right) validation regions. The pre-fit yields are displayed. The minor backgrounds are merged into the "others" category.

Table 7.7: Normalization factors for the main background processes obtained by the background only fit in the three control regions. The errors of the NFs include statistical, experimental, and theoretical uncertainties.

Background process	NF
$t\bar{t}$	0.92 ± 0.07
W+jets	1.35 ± 0.24
single top	0.47 ± 0.14

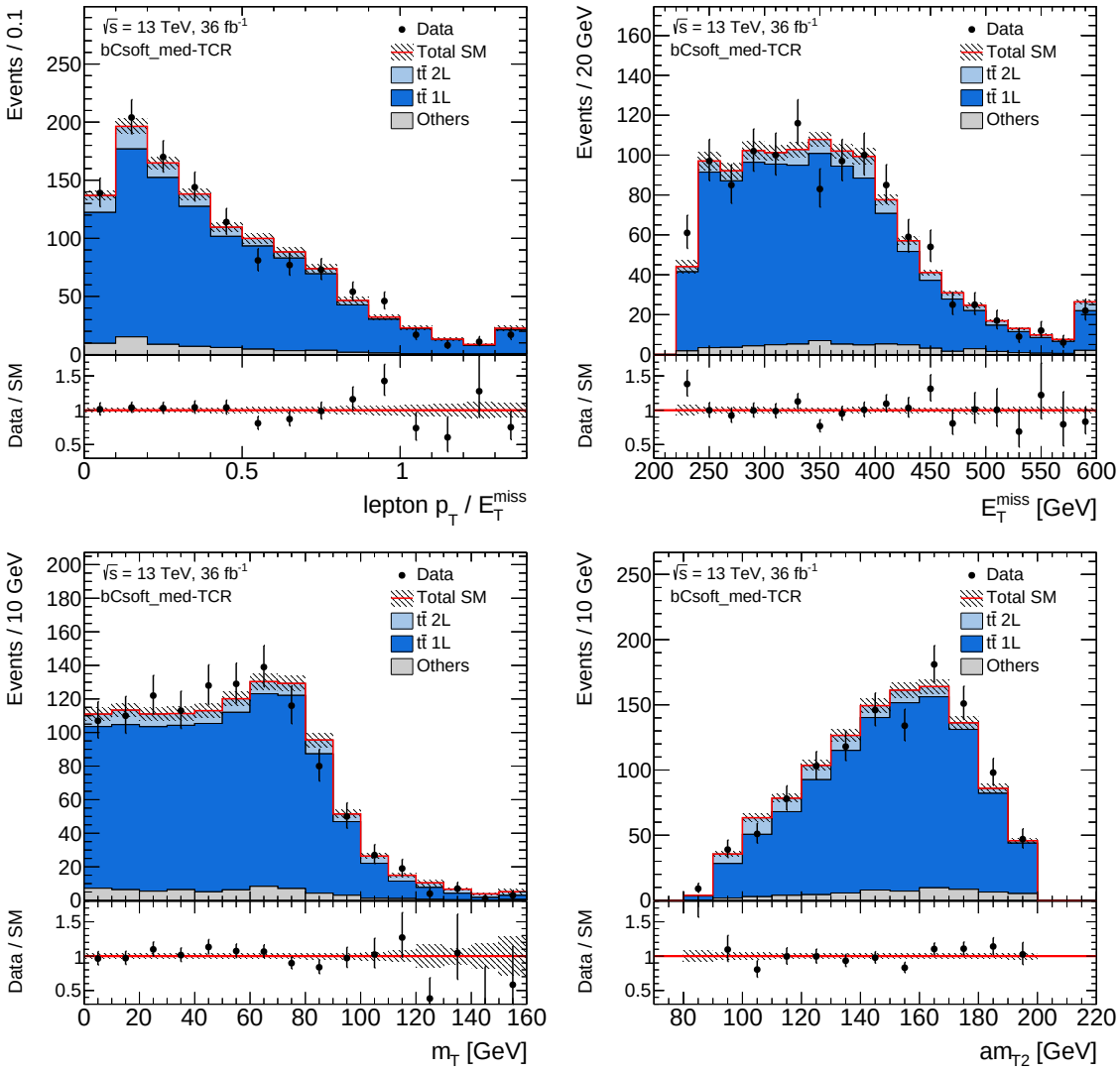

Figure 7.7: Comparison of data and simulation distributions for the $t\bar{t}$ CR after applying the normalization factors: the $p_{\mathrm{T}}^{\ell}/E_{\mathrm{T}}^{\mathrm{miss}}$ (top left), $E_{\mathrm{T}}^{\mathrm{miss}}$ (top right), m_{T} (bottom left), and am_{T2} (bottom right). The statistical and experimental uncertainties are displayed. The last bin includes the overflow.

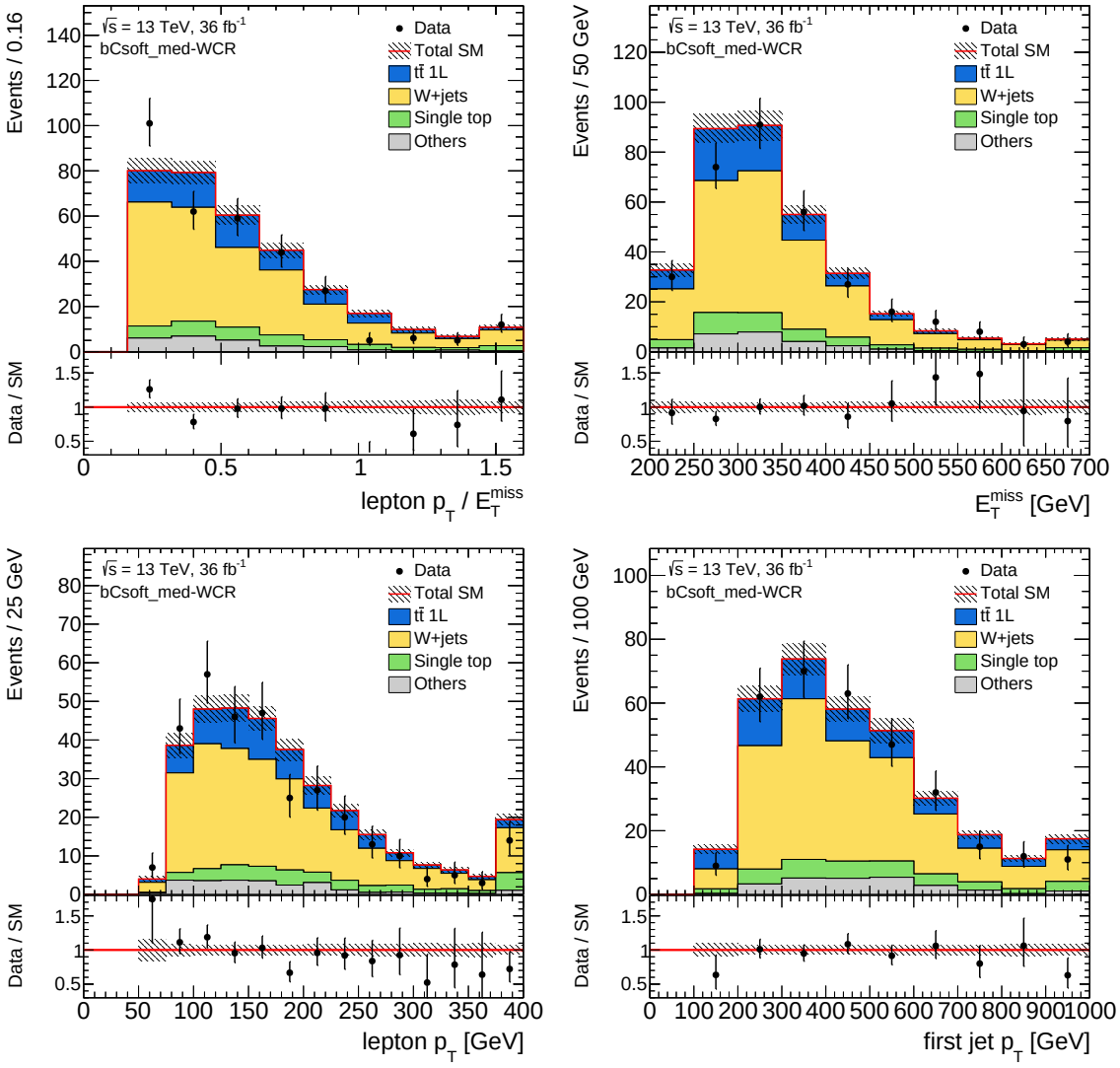

Figure 7.8: Comparison of data and simulation distributions for the W+jets CR after applying the normalization factors: the $p_{\mathrm{T}}^{\ell}/E_{\mathrm{T}}^{\mathrm{miss}}$ (top left), $E_{\mathrm{T}}^{\mathrm{miss}}$ (top right), lepton p_{T} (bottom left), and leading jet p_{T} (bottom right). The statistical and experimental uncertainties are displayed. The last bin includes the overflow.

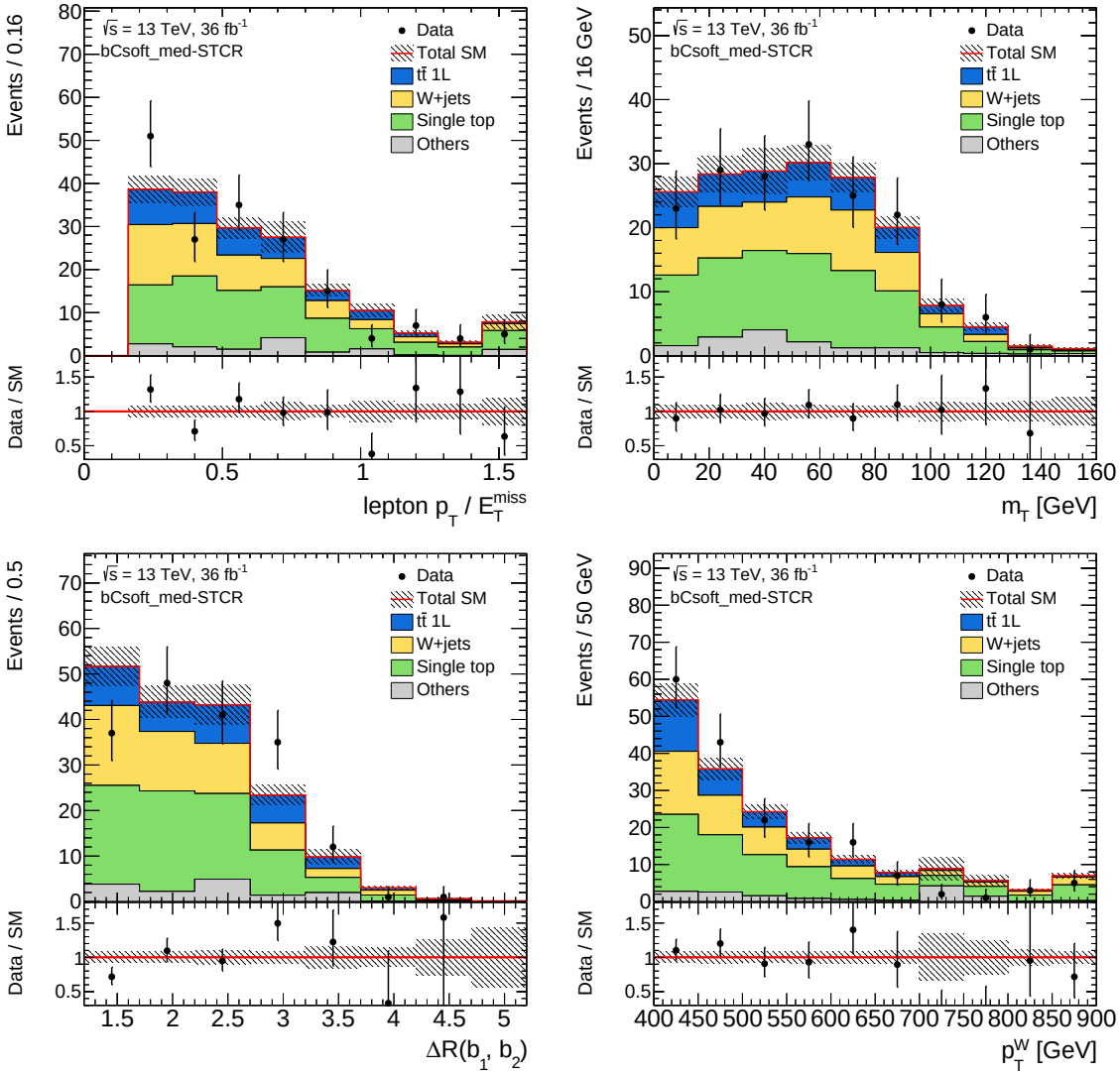

Figure 7.9: Comparison of data and simulation distributions for the single top CR after applying the normalization factors: the $p_{\mathrm{T}}^{\ell}/E_{\mathrm{T}}^{\mathrm{miss}}$ (top left), m_{T} (top right), $\Delta R(b_1, b_2)$ (bottom left), and p_{T}^{W} (bottom right). The statistical and experimental uncertainties are displayed. The last bin includes the overflow.

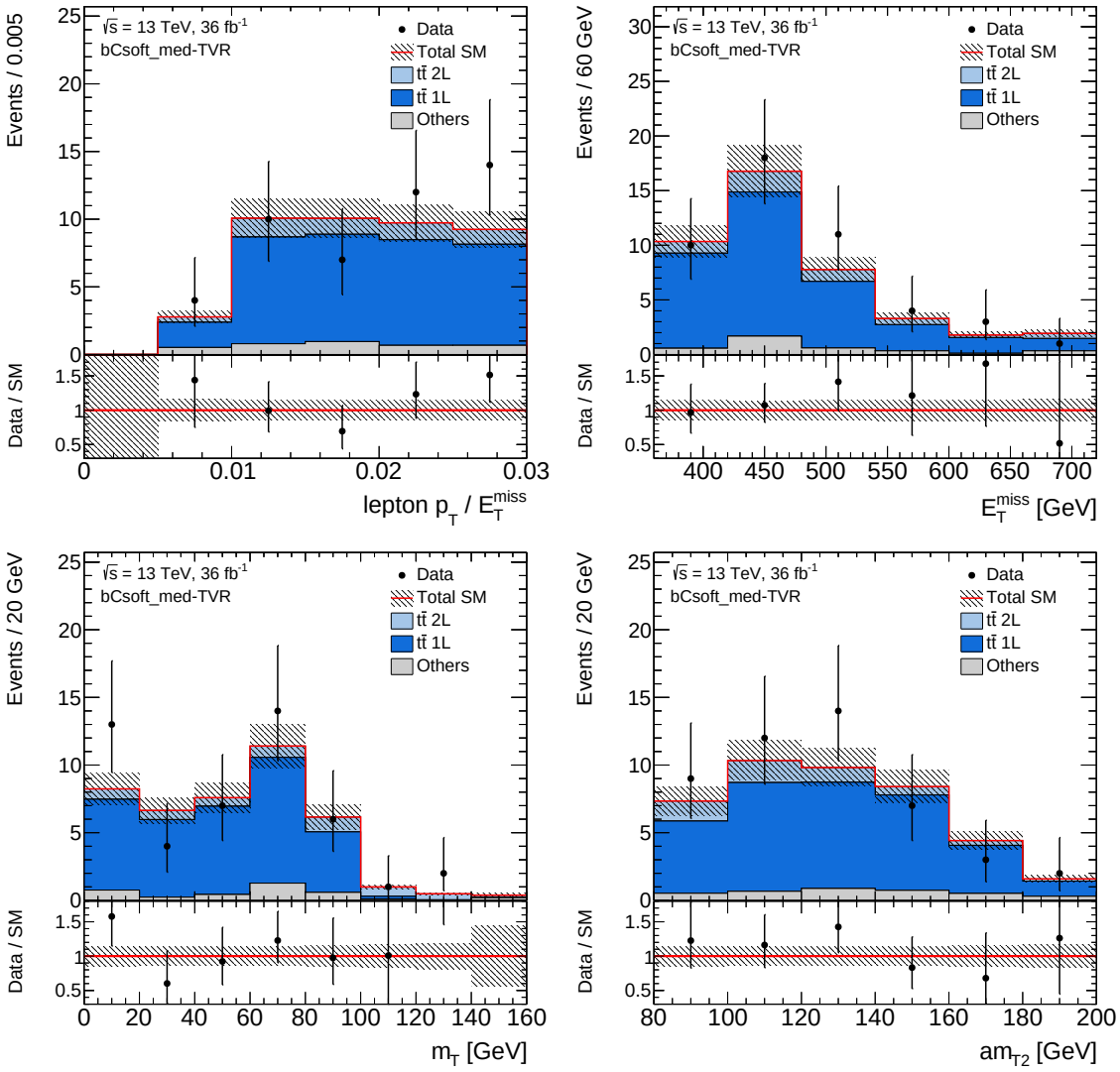

Figure 7.10: Comparison of data and simulation distributions for the $t\bar{t}$ VR after applying the normalization factors: the $p_{\mathrm{T}}^{\ell}/E_{\mathrm{T}}^{\mathrm{miss}}$ (top left), $E_{\mathrm{T}}^{\mathrm{miss}}$ (top right), m_{T} (bottom left), and am_{T2} (bottom right). The statistical and experimental uncertainties are displayed. The last bin includes the overflow.

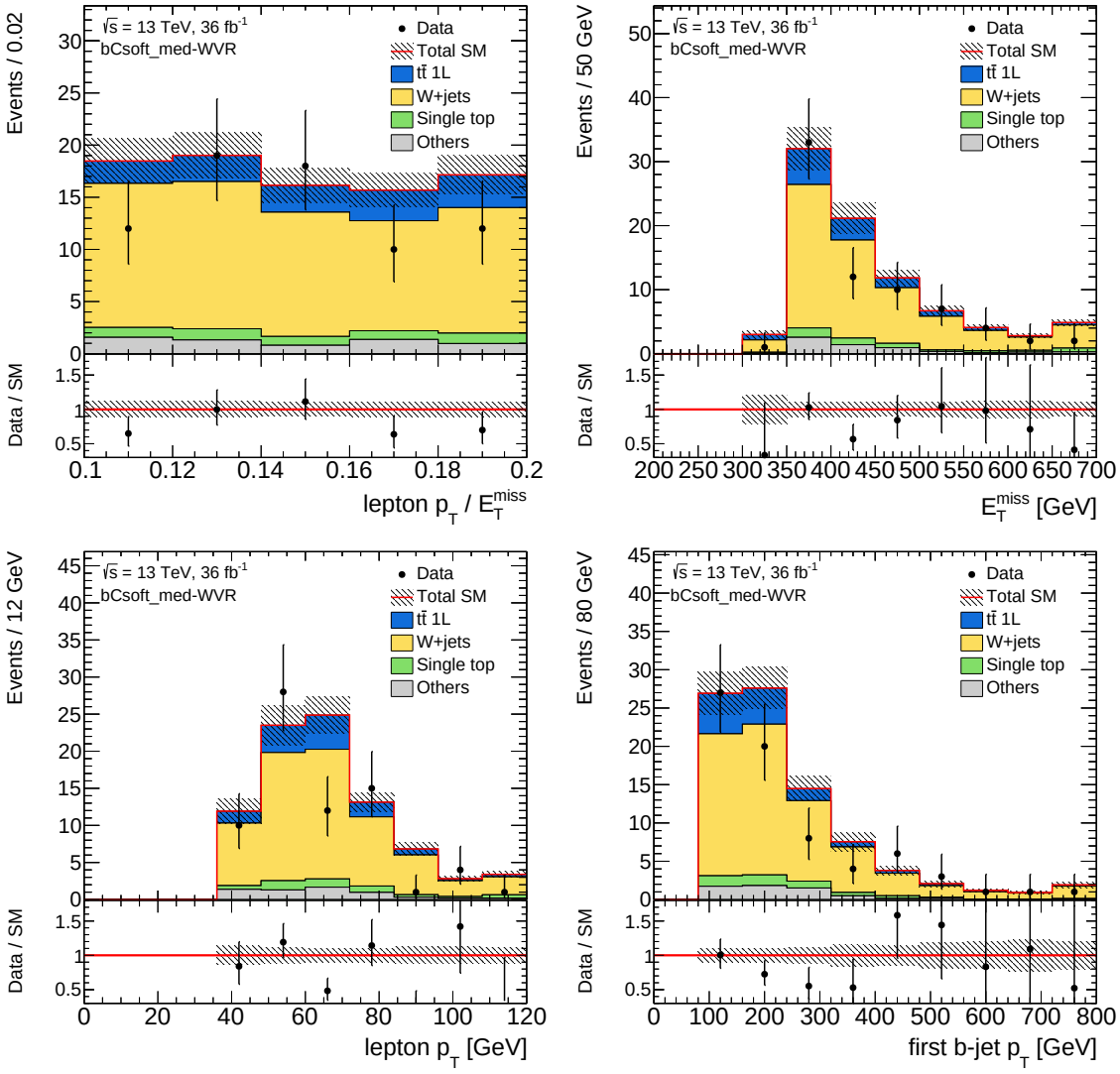

Figure 7.11: Comparison of data and simulation distributions for the W+jets VR after applying the normalization factors: the $p_{\mathrm{T}}^{\ell}/E_{\mathrm{T}}^{\mathrm{miss}}$ (top left), $E_{\mathrm{T}}^{\mathrm{miss}}$ (top right), lepton p_{T} (bottom left), and leading b-jet p_{T} (bottom right). The statistical and experimental uncertainties are displayed. The last bin includes the overflow.

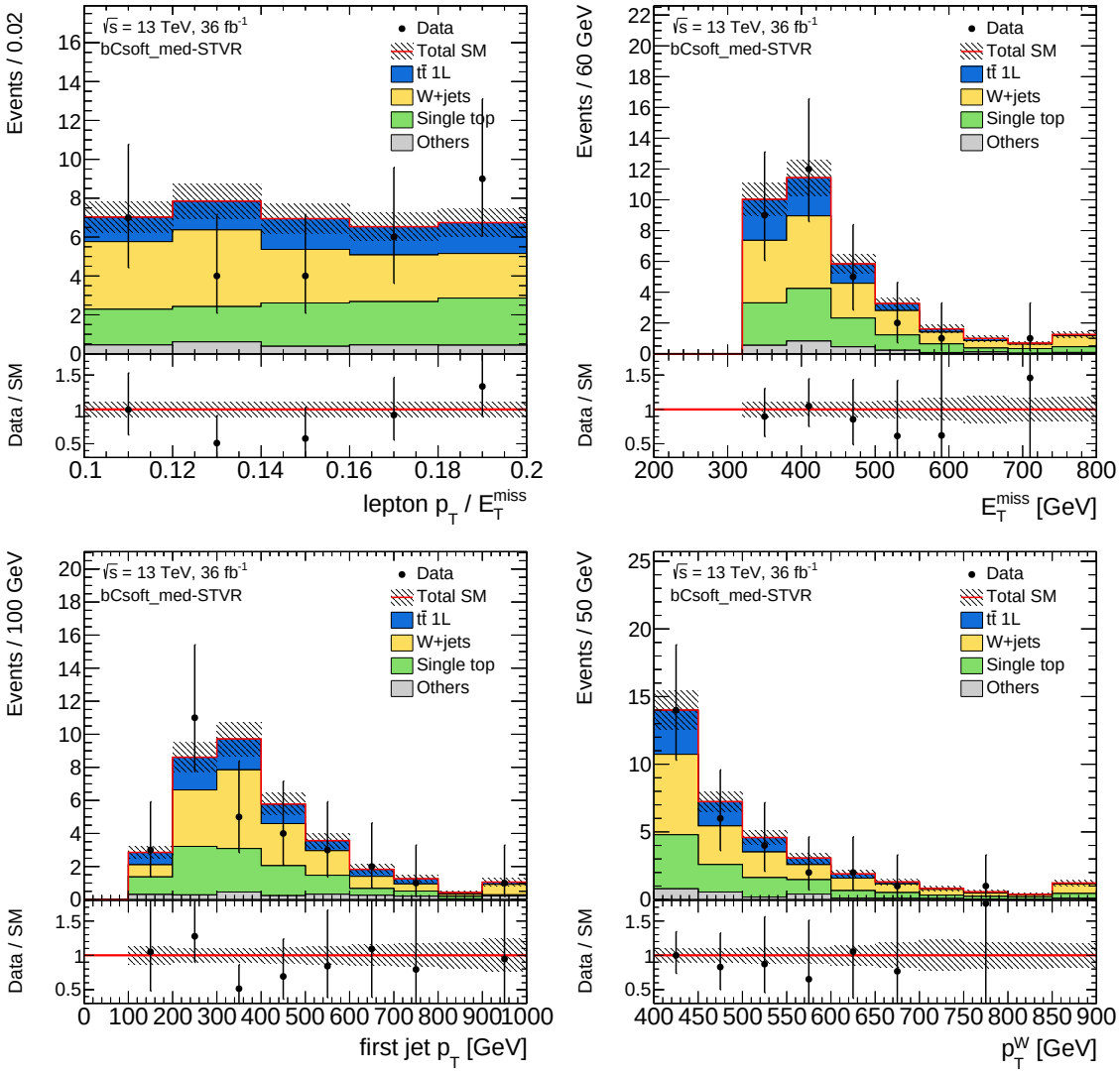

Figure 7.12: Comparison of data and simulation distributions for the single top VR after applying the normalization factors: the $p_{\mathrm{T}}^{\ell}/E_{\mathrm{T}}^{\mathrm{miss}}$ (top left), $E_{\mathrm{T}}^{\mathrm{miss}}$ (top right), leading jet p_{T} (bottom left), and p_{T}^{W} (bottom right). The statistical and experimental uncertainties are displayed. The last bin includes the overflow.

Table 7.8: Number of observed events and post-fit event yields in the CRs and VRs obtained by the background only fit in the CRs. The statistical, experimental, and theoretical uncertainties are included. The minor background processes are merged into the "Others" category.

	TCR	WCR	STCR	TVR	WVR	STVR
Observed events	1155	321	175	47	71	30
Fitted background	1155.0 ± 34.0	321.0 ± 17.9	175.0 ± 13.2	42.0 ± 5.8	82.7 ± 7.2	34.6 ± 3.2
$t\bar{t}$	1092.7 ± 39.6	75.5 ± 13.2	36.8 ± 8.0	38.3 ± 5.9	15.5 ± 2.8	8.5 ± 1.9
W+jets	12.8 ± 4.0	195.6 ± 26.4	49.9 ± 12.5	1.3 ± 0.5	58.6 ± 8.6	14.3 ± 4.0
Single top	34.8 ± 19.8	33.3 ± 11.0	77.7 ± 21.2	1.8 ± 1.0	4.7 ± 1.7	10.6 ± 3.2
Multiboson	2.3 ± 0.8	12.9 ± 4.2	7.1 ± 2.4	0.0 ± 0.0	2.9 ± 0.9	0.2 ± 0.2
Others	12.3 ± 2.0	3.4 ± 1.7	3.5 ± 0.7	0.5 ± 0.1	1.0 ± 0.4	0.9 ± 0.2

7.3 Systematic Uncertainties

The experimental systematic uncertainties associated with each object are estimated in the calibration of each object, as explained in Section 6.5, and the $\pm 1\sigma$ variations are included in the fit. The theoretical uncertainties for each background process, which affect the event yields in each region are summarized in Table 7.9. The details on these uncertainties are described in Section 6.5.

Table 7.9: Theoretical uncertainties (%) in the $t\bar{t}$, W+jets, single top, and multiboson processes. The relative uncertainties with respect to the number of events for the background process in each region are shown. For $t\bar{t}$, W+jets, and single top, the uncertainties in the transfer factors from the control region of the background process to the other regions are calculated. Due to the lack of the multiboson CR, the uncertainties in the multiboson yields contain the uncertainty related to the normalization.

	$t\bar{t}$	W+jets	single top	multiboson
SR	14.3	7.3	9.9	32.0
SR1	18.5	6.8	12.0	22.9
SR2	13.5	7.1	11.5	64.1
SR3	13.4	4.1	14.1	11.6
TCR	–	11.0	48.9	18.2
WCR	14.1	–	5.2	15.2
STCR	17.2	2.3	–	14.7
TVR	6.5	12.4	49.4	21.8
WVR	14.6	1.2	10.6	11.1
STVR	17.6	2.5	9.3	20.8

The systematic uncertainties in the background prediction in the SR are summarized in Table 7.10. The statistical uncertainty which corresponds to the expected number of background events is 28%, and the systematic uncertainty in the background prediction is 15%. The largest systematic uncertainty comes from the flavor tagging uncertainty, which is caused by the b-tagging efficiency measurements. It contains the uncertainties in the b-jet tagging efficiency, the c-jet and light-jet mistag efficiencies, and the extrapolation of the efficiency to high-p_{T} jets. The main flavor-tagging uncertainty in this analysis is from the charm mistag calibration. If a c-jet in a $t\bar{t}$ event is b-tagged, the final state particles are wrongly assigned in the am_{T2} calculation. In that case, the event tends to have a large am_{T2} value and enter the SR. The second largest uncertainty in the `bCsoft_med` SR is the uncertainty in the W+jets normalization, which is mainly from the limited statistics in the W+jets CR.

Table 7.10: Summary of the dominant systematic uncertainties (%) in the background prediction in the `bCsoft_med` SR. The statistical uncertainty is calculated from the expected number of events in the SR.

SR Uncertainty (%)	`bCsoft_med`
Statistical uncertainty ($\sqrt{N_{\text{exp}}}$)	28
Total systematic uncertainty	15
Flavor tagging	13.9
W+jets normalization	8.1
$E_{\text{T}}^{\text{miss}}$ soft term	7.8
$t\bar{t}$ modeling	7.0
MC statistics	4.6
Single top normalization	3.4
W+jets modeling	3.2
$t\bar{t}$ normalization	2.6
JES	2.6
JER	2.1

7.4 Results

Table 7.11 shows the observed events in the SRs. The background events in the SR are normalized by the NFs obtained by the background only fit. No significant excess over the expected background yields is observed. The observed p-value for the background-only hypothesis is $p_0 = 0.12$, which corresponds to 1.17σ. The distributions of key variables after the single-bin SR selection are shown in Figure 7.13. The $p_{\text{T}}^{\ell}/E_{\text{T}}^{\text{miss}}$ distribution with the shape-fit binning is shown in Figure 7.14.

Table 7.11: Post fit yields in the SRs. The "SR" is the single bin SR, and "SR1-3" are the multi-bin SRs for the exclusion.

	SR	SR1	SR2	SR3
Observed events	19	4	15	57
Fitted Background	13.7 ± 2.1	4.9 ± 0.9	8.9 ± 1.3	52.9 ± 6.2
$t\bar{t}$	4.9 ± 1.5	1.4 ± 0.4	3.5 ± 1.0	16.3 ± 4.0
W+jets	6.4 ± 2.0	2.5 ± 0.8	3.9 ± 1.2	24.5 ± 6.5
Single top	1.6 ± 0.5	0.5 ± 0.2	1.1 ± 0.4	8.6 ± 2.6
Multiboson	0.3 ± 0.2	0.4 ± 0.1	0.0 ± 0.0	1.8 ± 0.7
Others	0.6 ± 0.2	0.2 ± 0.1	0.4 ± 0.1	1.7 ± 0.3

Figure 7.15 shows the expected and observed limits from `bCsoft_med` SR as well as the expected limits from other SRs in reference [1]. Figures 7.16–7.17 show the combined

exclusion contours at 95% CL for the higgsino-like LSP scenario. For the exclusion contours, other SRs described in reference [1] are also used to cover the whole phase space and branching ratios[3].

The `bCsoft_med` SR contributes mainly to the mostly-right-handed-stop scenario due to the large branching ratio of $b\tilde{\chi}_1^{\pm}$ decay as designed. To cover all decay modes: $t\tilde{\chi}_1^0$, $t\tilde{\chi}_2^0$, and $b\tilde{\chi}_1^{\pm}$, a hard-lepton SR and a soft-lepton SR are combined so that the $t\tilde{\chi}_1^0$ or $t\tilde{\chi}_2^0$ branch can be caught by the hard-lepton SR while the $b\tilde{\chi}_1^{\pm}$ branch is covered by the soft lepton SRs. The soft-lepton and hard-lepton SRs are then fitted simultaneously. The `bCsoft_med` SR contributes significantly to the $\tilde{t}_1 \sim \tilde{t}_R$ scenario in which the $b\tilde{\chi}_1^{\pm}$ decay is favored. All three BR assumptions are well covered, and stop masses are excluded up to 800 GeV for the LSP mass of 150 GeV. With an assumption of $m_{\tilde{\chi}_1^{\pm}} = 150$ GeV, the limits reach $\Delta m(\tilde{\chi}_1^{\pm}, \tilde{\chi}_1^0) \sim 2$ GeV in all three scenarios.

[3]In reference [1], hard lepton SRs (`tN_med`, `tN_high`, `bC2x_diag`, `bC2x_med`) and soft lepton SRs (`bCsoft_med`, `bCsoft_diag`, and `bCsoft_high`) and other SRs that are not used for the result in this dissertation are described. The contributions of these SRs to the exclusion limits are shown in Appendix A.

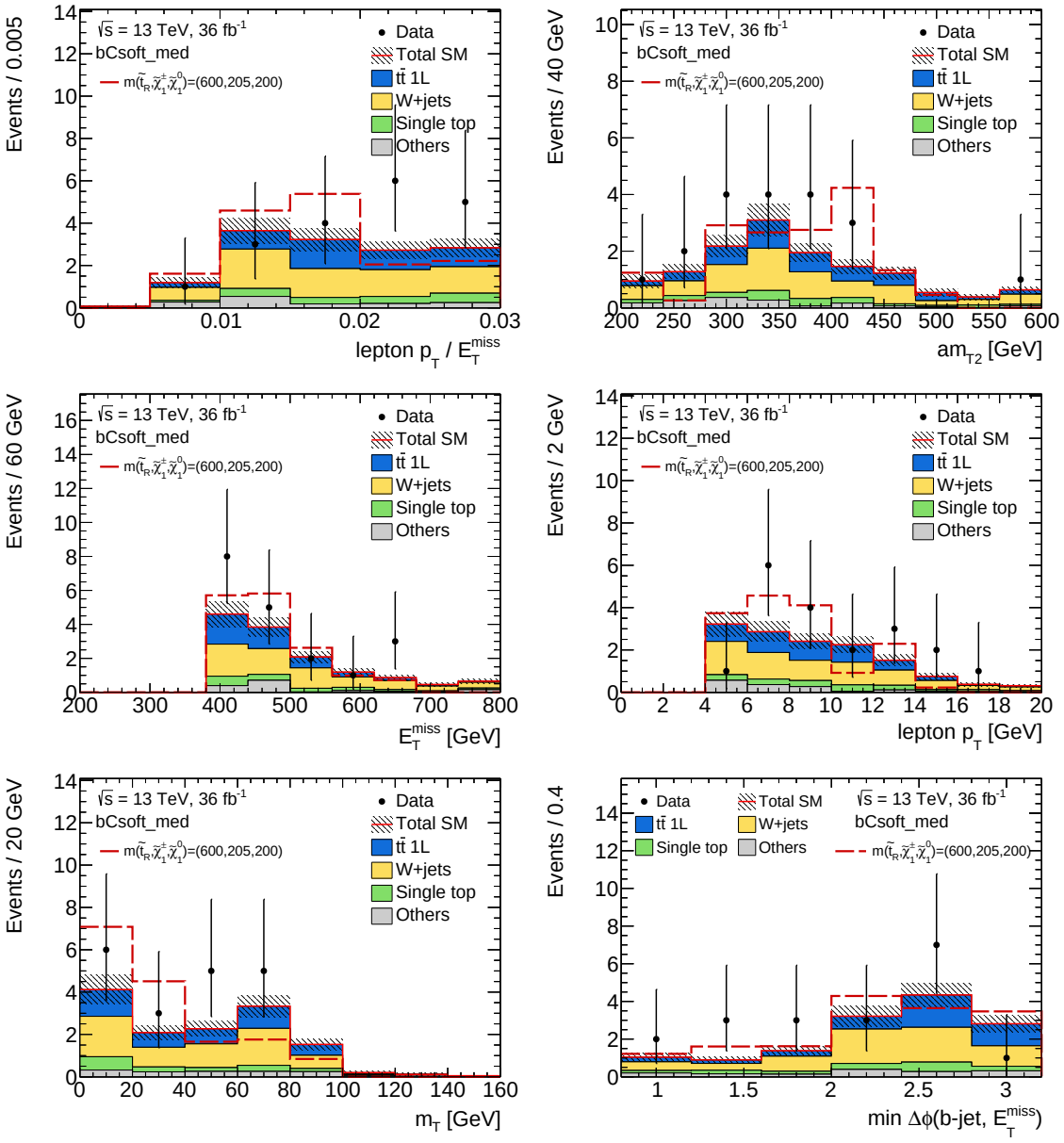

Figure 7.13: Distribution of the variables used to define the `bCsoft_med` discovery SR: (left column) $p_{\mathrm{T}}^{\ell}/E_{\mathrm{T}}^{\mathrm{miss}}$, $E_{\mathrm{T}}^{\mathrm{miss}}$, m_{T}, (right column) am_{T2}, lepton p_{T}, and $\min(\Delta\phi(\vec{p}_{\mathrm{T}}^{\mathrm{miss}}, b\text{-jet}))$, in descending rows. The benchmark signal is overlaid.

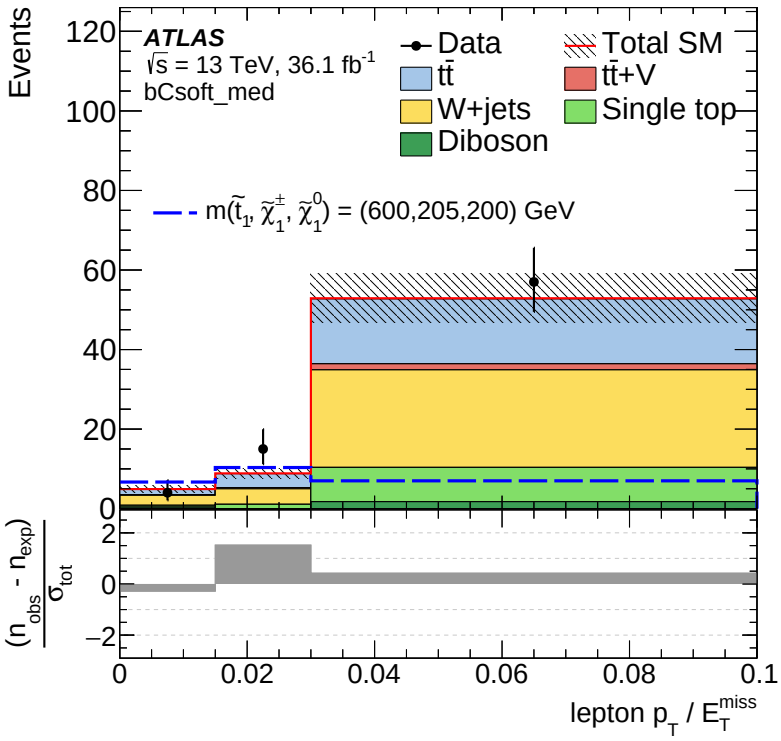

Figure 7.14: The observed data and post-fit background prediction in the shape-fit SRs. The binning of the plot is the same as the shape-fit binning. On the bottom panel, the difference between the observed data and predicted yield divided by the total uncertainty is shown.

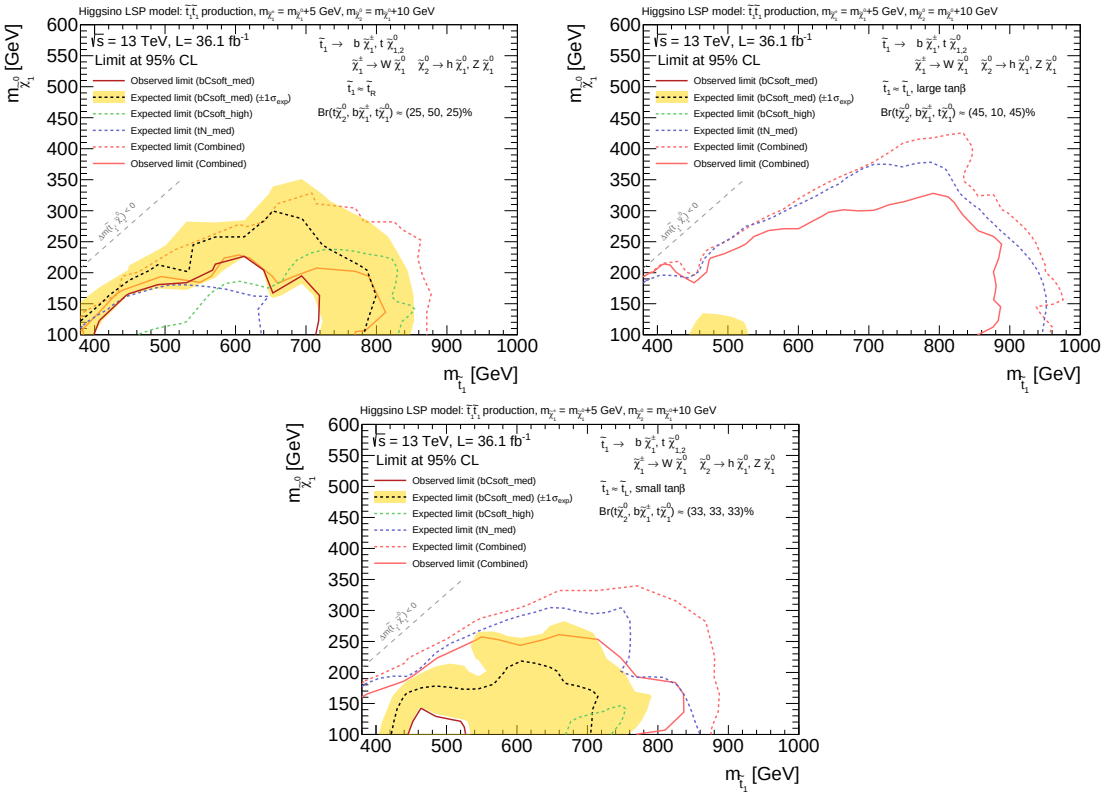

Figure 7.15: Expected and observed limits obtained from the `bCsoft_med` SR and expected limits from other SRs in reference [1] (`tN_med` and `bCsoft_high`), for (top left) $\tilde{t}_1 \sim \tilde{t}_R$, (top right) $\tilde{t}_1 \sim \tilde{t}_L$, and (bottom) large tan β scenarios. The combined limits are obtained from the simultaneous fits using a soft-lepton SR (one of `bCsoft_med`, `bCsoft_high`, and `bCsoft_diag`) and the `tN_med` SR. Limits from `bCsoft_diag` SR are not shown because it does not have sensitivity in the off-diagonal region ($\Delta m(\tilde{t}_1, \tilde{\chi}_1^0) > m_t$). The choice of the SRs at each mass point is summarized in Appendix A.

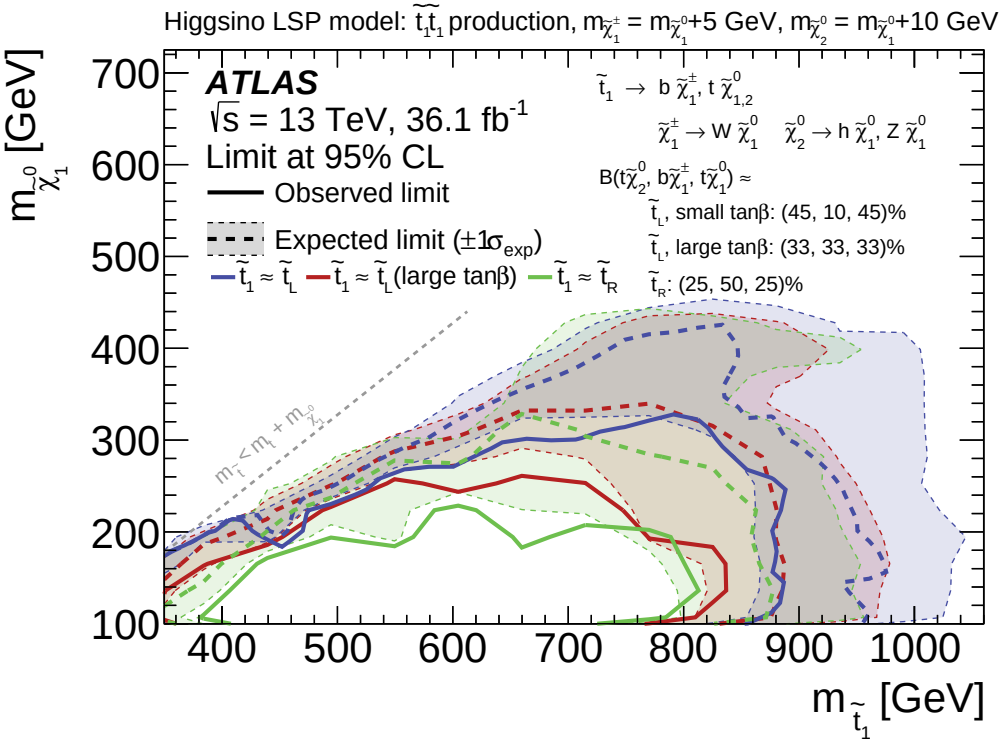

Figure 7.16: Observed (solid lines) and expected (dashed lines) exclusion limit at 95% CL in the plane of $m_{\tilde{t}_1}$ versus the mass of the neutralino LSP ($m_{\tilde{\chi}_1^0}$). The higgsino-like LSP model with $m_{\tilde{\chi}_1^\pm} = m_{\tilde{\chi}_1^0} + 5$ GeV and $m_{\tilde{\chi}_2^0} = m_{\tilde{\chi}_1^0} + 10$ GeV is considered. The three scenarios: $\tilde{t}_1 \sim \tilde{t}_R$ (green), $\tilde{t}_1 \sim \tilde{t}_L$ (blue), and large $\tan\beta$ (red) are shown. In the region below the gray dashed line, the $\tilde{t}_1$ is kinematically allowed to decay into an on-shell top quark and the LSP.

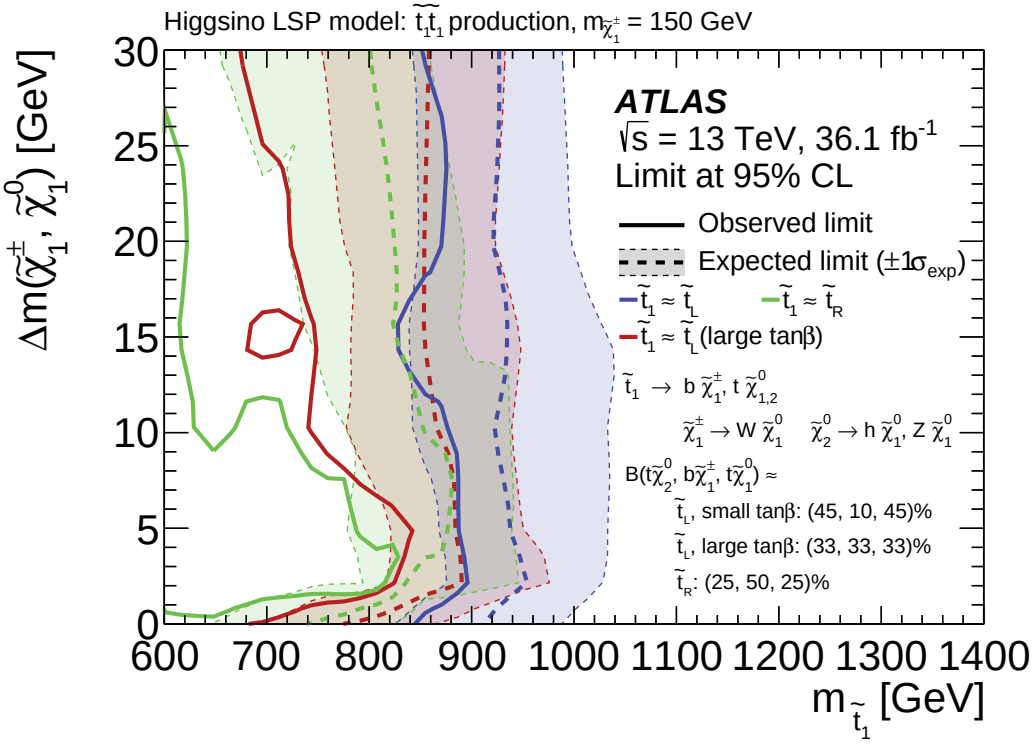

Figure 7.17: Observed (solid lines) and expected (dashed lines) exclusion limit at 95% CL in the plane of $m_{\tilde{t}_1}$ versus $\Delta m(\tilde{\chi}_1^\pm, \tilde{\chi}_1^0)$. The mass of $\tilde{\chi}_1^\pm$ is fixed to 150 GeV. The higgsino-like LSP model with $m_{\tilde{\chi}_1^\pm} = m_{\tilde{\chi}_1^0} + 5$ GeV and $m_{\tilde{\chi}_2^0} = m_{\tilde{\chi}_1^0} + 10$ GeV is considered. The three scenarios: $\tilde{t}_1 \sim \tilde{t}_R$ (green), $\tilde{t}_1 \sim \tilde{t}_L$ (blue), and large $\tan\beta$ (red) are shown. In the region below the gray dashed line, the $\tilde{t}_1$ is kinematically allowed to decay into an on-shell top quark and the LSP.

Chapter 8

Soft b-tagging for Compressed Signatures

8.1 Targets of Soft b-tagging

When the mass-splitting between $\tilde{t}_1$ and $\tilde{\chi}_1^0$ is small, the final state contains low p_{T} b-hadrons. The p_{T} of the b-hadrons is typically below 20 GeV. In the standard b-jet tagging algorithm optimized for higher p_{T} b-hadrons, the reconstruction efficiency for these low-p_{T} b-hadrons is too low to be useful because the b-tagging algorithm relies on jets reconstructed from EM topo clusters (EM topo jets). Due to the difficulties in the reconstruction and calibration of low p_{T} jets, the EM topo jets are only used in $p_{\mathrm{T}} > 20$ GeV. Furthermore, the MV2c10 algorithm is not optimized for such low p_{T} b-hadrons. In order to expand the ability to tag b-hadrons in such a low p_{T} regime, a new algorithm without relying on the presence of reconstructed jets has been developed. The new algorithm targeting low p_{T} b-hadrons referred to as *soft b-tagging* in the following, reconstructs secondary vertices of b-hadrons using tracks outside reconstructed jets. Figure 8.1 shows the p_{T} and the transverse distance between the PV and SV (L_{xy}) of b-hadrons in the stop signal with $\Delta m(\tilde{t}_1, \tilde{\chi}_1^0) = 20$ GeV. Most of the SVs from the signal are populated in the vicinity of the PV, and the goal of the algorithm is to reconstruct secondary vertices whose distances from the PV are smaller than 2 mm. Figure 8.2 is an event display of a typical simulated stop signal. In order to reconstruct a SV, at least two charged particles need to be generated at the SV position. However, about half of the b-hadrons do not satisfy that condition, as can be seen in this event, which is one of the main limitations of the soft b-tagging efficiency. The soft b-tag algorithm is named Track-based Low p_{T} Vertex Tagger (T-LVT) [2], and it is implemented in the `athena` software framework [167] for the event reconstruction in ATLAS. In the next section, the algorithm of T-LVT is presented. After that, the performance of the algorithm and an ad-hoc calibration method are introduced.

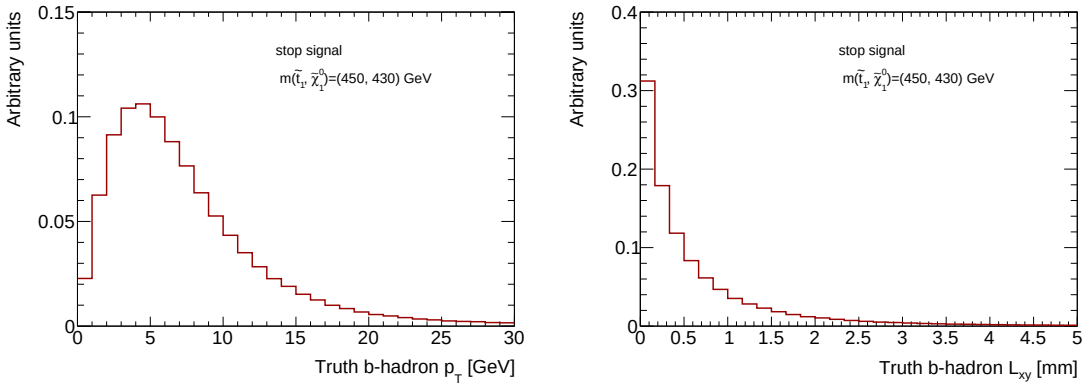

Figure 8.1: p_{T} (left) and L_{xy} (right) of the stop four-body signal with $m(\tilde{t}_1, \tilde{\chi}_1^0) = (450, 430)$ GeV.

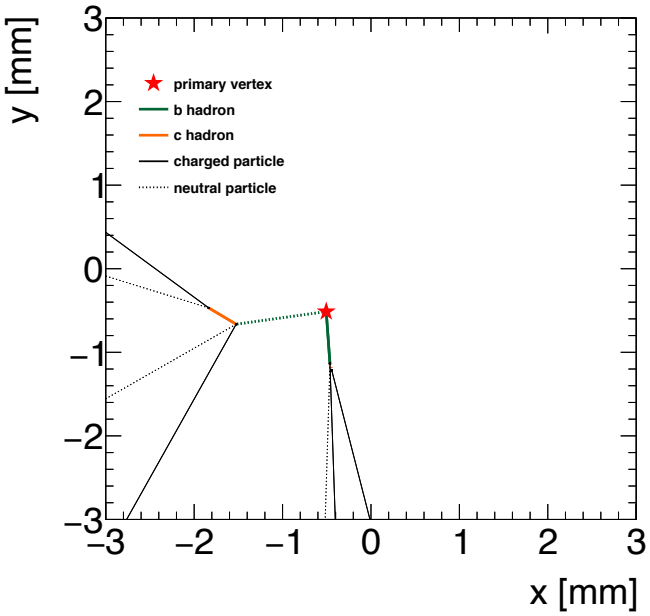

Figure 8.2: A display of a simulated stop signal event with $m(\tilde{t}_1, \tilde{\chi}_1^0) = (450, 430)$ GeV in the transverse plane. The position of the PV is shown as the red star. The b-hadrons from the stop decay and the decay products of the b-hadrons are shown, while the other particles from the PV or pile-up vertices are not displayed. The green (orange) lines show $b(c)$-hadrons, and the solid (dashed) lines represent charged (neutral) particles with $p_{\mathrm{T}} > 0.5$ GeV.

8.2 Algorithm

The soft b-tagging algorithm consists of three steps: the track selection, the vertex fitting, and the vertex selection. The algorithm starts from the selection of reconstructed tracks. As mentioned in Section 5.1, tracks of charged particles are reconstructed from hits in the ID, and the track parameters (q/p_{T}, η, ϕ, d_0, z_0) are calculated using Kalman Filter. Tracks with $p_{\mathrm{T}} > 500$ MeV are used as the input of the soft b-tagging. It is not feasible to use all available tracks to find the secondary vertices because the processing time and the number of fake vertices from random crossings increase explosively as the number of combinations of track pairs increases. A dedicated track selection is performed before finding secondary vertices in order to reduce the number of tracks that are used in the vertex fitting. The algorithm is developed using the stop four-body signal with $m(\tilde{t}_1, \tilde{\chi}_1^0) = (450, 430)$ GeV as a benchmark signal, and W+jets without b- or c-hadrons as background.

8.2.1 Track Selection

There are many tracks reconstructed by the tracking algorithm. Some of them are coming from SVs, but many of them are not. There are three types of tracks that are considered as background in this selection: tracks from the PV, tracks from pile-up vertices, and tracks reconstructed with a bad quality fit. The track selection is summarized in Table 8.1. Figure 8.3 illustrates the key components of the track selection: the selection of large d_0 tracks, the overlap removal with jets, and the pile-up track suppression. There is no p_{T} requirement in addition to $p_{\mathrm{T}} > 500$ MeV imposed in the track reconstruction. Since particles from the decay of the stop signal tend to be localized at the central part, i.e., the small η region, compared to the background tracks, $|\eta| < 2$ is required. The tracks from a decay of a long-lived b-hadron tend to have large transverse impact parameter (d_0) and longitudinal impact parameter (z_0). The impact parameters of the tracks from the PV are zero if the resolution of the parameter is ignored, but in reality they are non zero due to the finite resolutions of the parameters. For the longitudinal direction, the z_0^{PV}, which is the track z_0 with respect to the z coordinate of the PV, is used. The requirement on d_0 and z_0 are thus intended to remove tracks from the PV. Tracks with small errors of the parameters are selected to reduce PV tracks with large impact parameters due to the poor accuracy of the parameters. The significance of the impact parameter is defined as the impact parameter divided by the error of that. The large impact parameter significance is required to account for the parameter itself as well as the error of that. For the pile-up suppression, upper limits are set for the $|z_0^{\mathrm{PV}}|$ and $|z_0^{\mathrm{PV}} \sin\theta|$. The loose upper limits on $|d_0|$ and $|z_0|$ are set to remove tracks produced in the detector materials. To suppress fake tracks that are reconstructed

from wrong combination of hits, the track quality criteria based on the χ^2 of the track fit and the number of hits on the Pixel, SCT, and IBL detectors are applied. Since the target of the soft b-tagging is b-hadrons that are not reconstructed as a jet, tracks overlapping with a jet are removed. Tracks within $\Delta R < 0.4$ with respect to any EM topo jets with $p_{\mathrm{T}} > 30$ GeV are removed. The threshold of the jet p_{T} is optimized to maximize the signal efficiency while keeping strong background rejection. Figures 8.4–8.5 show the distributions of these variables. The tracks from b-hadrons in the benchmark signal and background tracks in the W+jets without heavy flavor hadrons are compared. All cuts used in the track selection are applied except for the cut on the displayed variable.

Table 8.1: Track selection used in the T-LVT algorithm

Variable	Cut
p_{T} (MeV)	> 500
$\lvert\eta\rvert$	< 2
$\lvert d_0\rvert$ (mm)	$\in (0.05, 10.0)$
d_0 significance	> 1.7
d_0 error (mm)	< 0.13
$\lvert z_0^{\mathrm{PV}}\rvert$ (mm)	< 2
z_0 error (mm)	< 0.3
z_0^{PV} significance	> 0.5
$\lvert z_0\rvert$ (mm)	< 100.0
$\lvert z_0^{\mathrm{PV}} \sin\theta\rvert$ (mm)	< 1.2
track χ^2	< 4.0
Pixel hits	≥ 3
SCT hits	≥ 1
B-Layer hits	≥ 1
min $\Delta R(\mathrm{track}, \mathrm{jet}^{30\ \mathrm{GeV}})$	> 0.4

8.2.2 Vertex Fitting

The two-track vertex reconstruction is performed for all possible pairs of tracks selected in the previous section. Using a pair of tracks, an approximate vertex position is estimated by a Kalman Filter based fitting algorithm, *VKalVrt* [168]. First, track parameters measured at the perigee with respect to the beam spot are used. If a vertex has a small transverse radius and small impact parameters of the tracks with respect to the fitted vertex, the vertex is refitted by a precision fitting using an accurate track extrapolation. Only vertices which satisfy the fitting quality requirement are used in the following steps. In order to reduce the tracks originating from the PV, the two-track vertex is discarded if the distance between

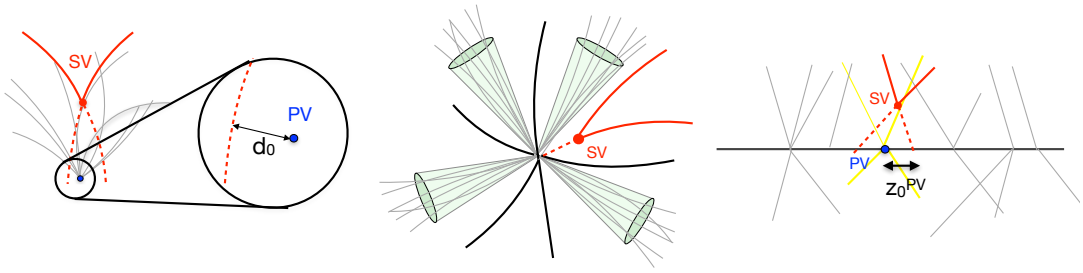

Figure 8.3: Illustrations of the key components in the track selection. (left) The tracks with a large transverse impact parameter (d_0) are selected. (middle) The tracks within the high p_{T} jets are removed ($\Delta R < 0.4$). (right) The tracks with a large longitudinal impact parameter are removed to discard tracks from the pile-up vertices.

the PV and a two-track vertex is smaller than 0.2 mm. The momentum of the vertex is defined as the vectorial sum of the momenta of the associated tracks, and the direction of the vertex is defined as the direction from the PV to the two-track vertex. The momentum of the two-track vertex is required to be consistent with the flight direction of the vertex. If the cosine of the angle between the two-track vertex momentum and the flight direction is smaller than 0.7, the two-track vertex is removed. A track can be used in different two-track vertices, and a single b-hadron can be reconstructed as multiple two-track vertices. In order to solve the ambiguity, a set of tracks is created by selecting tracks that share the same two-track vertex using incompatibility graph technique [169]. A multi-track vertex is fitted using the set of tracks used in the two-track vertices. A single track is not allowed to be used in more than one SV. If a track is shared by multiple multi-track vertices, the track is assigned to the vertex with the best fitting quality, and it is removed from the other vertices. Finally, vertices are fitted again, and the position and the associated tracks are stored.

8.2.3 Vertex Selection

The reconstructed vertices still contain backgrounds: fake vertices reconstructed from randomly crossing tracks originating from the PV and the secondary vertices of long-lived light flavor particles. The vertex selection is defined to reduce such background vertices. The selection is summarized in Table 8.2. The long-lived SM background is mainly from K_s meson decaying into a pair of charged pions. This background can be efficiently suppressed by requiring the mass of the reconstructed vertex above 600 MeV, because the mass of K_s is 498 MeV [37]. The mass of the vertex is calculated from the associated tracks, assuming all the tracks associated with the vertex are charged pions. The L_{xy} and the three dimen-

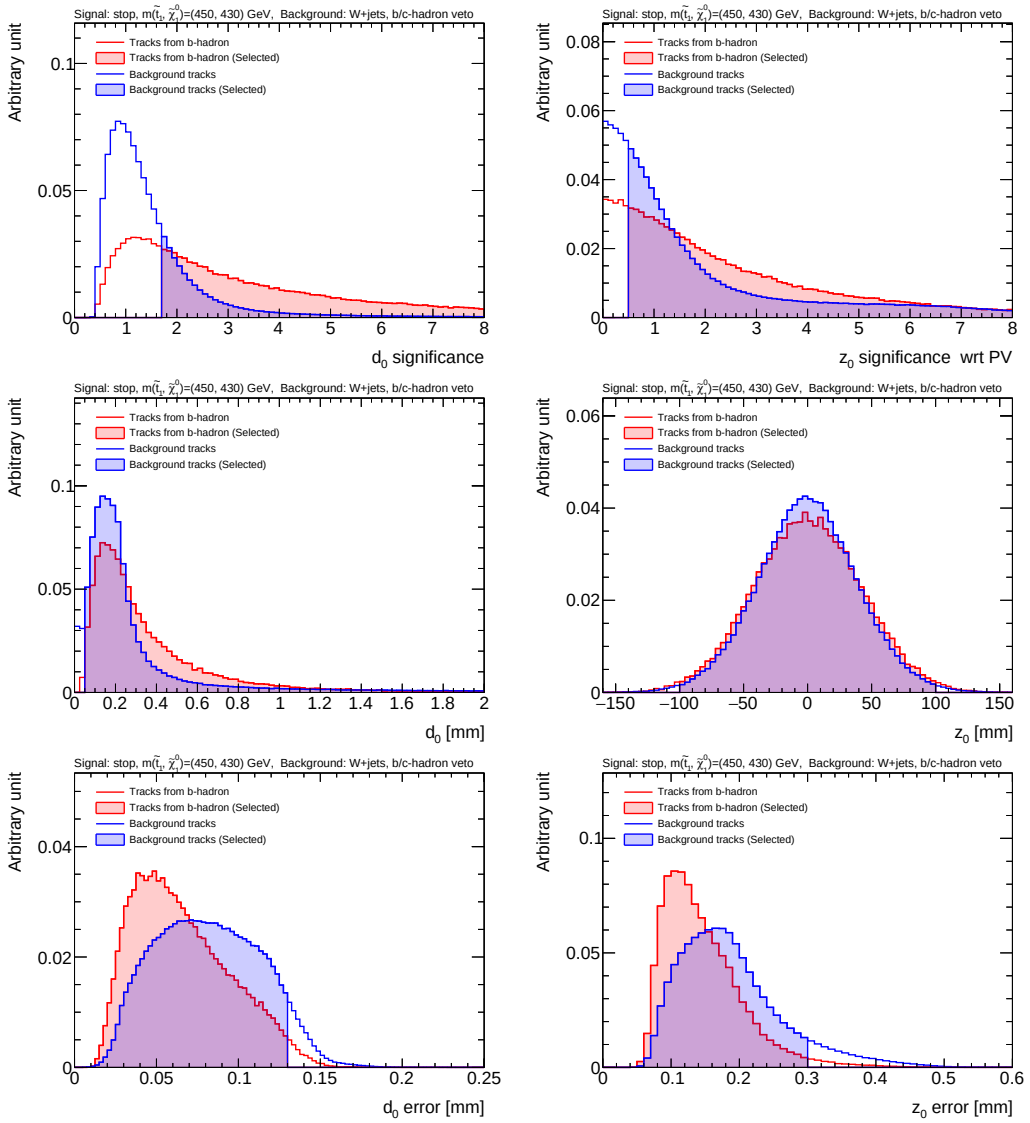

Figure 8.4: Track variables used to define the track selection: (top left) the d_0 significance, (top right) z_0^{PV} significance, (middle left) d_0, (middle right) z_0, (bottom left) d_0 error, and (bottom right) z_0 error. The red histograms show the tracks from b-hadrons in the stop signal events, and the blue histograms show the tracks in the W+jets. W+jets events that have b- or c-hadrons are not used. All cuts described in Table 8.1 are applied, except for the cut on the variable that is shown in each plot. The shaded part of the histograms shows the distribution adding the cut on the displayed variable.

sional distance divided by its uncertainty ($L_{3\mathrm{D}}$ significance) are variables which describe the displacement of the SV, and the p_{T} of SV is used to suppress the random combination backgrounds. A cut on the η of the SV can improve the background rejection. Variables related to the angle of the SV are used. The cut on the $\cos\theta$ used in the two-track vertex selection is tightened in the final vertex selection. The spread of the tracks with respect to

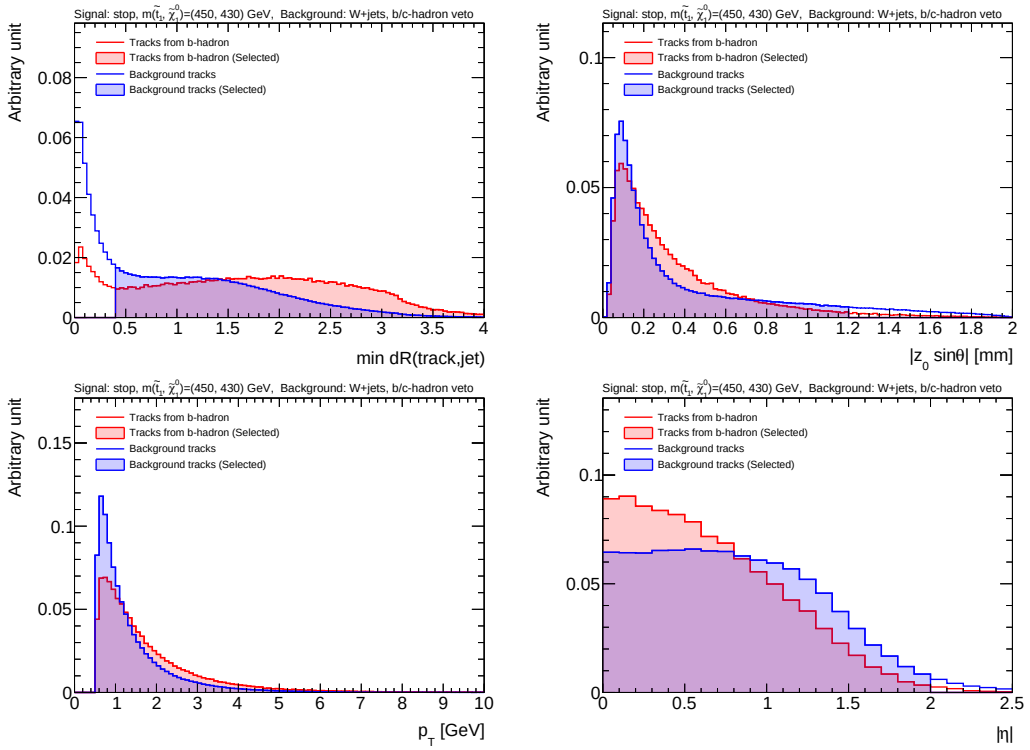

Figure 8.5: Track variables used to define the track selection: (top left) the minimum ΔR between the track and EM topo jets with $p_{\mathrm{T}} > 30$ GeV, (top right) $|z_0^{\mathrm{PV}} \sin\theta|$, (bottom left) p_{T}, and (bottom right) $|\eta|$. The red histograms show the tracks from b-hadrons in the stop signal events, and the blue histograms show the tracks in the W+jets. W+jets events that have b- or c-hadrons are not used. All cuts described in Table 8.1 are applied, except for the cut on the variable that is shown in each plot. The shaded part of the histograms shows the distribution adding the cut on the displayed variable.

the vertex direction is measured by

$$\Delta R_{\mathrm{mean}} = \frac{\sum_{\mathrm{track}} \Delta R\left(\mathbf{p}_{\mathrm{track}}, \mathbf{p}_{\mathrm{vtx}}\right)}{N_{\mathrm{track}}}, \tag{8.1}$$

where $\mathbf{p}_{\mathrm{track}}$, $\mathbf{p}_{\mathrm{vtx}}$, and N_{track} are the momentum of the track, momentum of the vertex, and the number of tracks attached to the secondary vertex. The vertex selection criteria are optimized to maximize the sensitivity of the stop signal with $\Delta m(\tilde{t}_1, \tilde{\chi}_1^0) = 20$ GeV in the analysis described in Chapter 9. Figures 8.6–8.7 show the distributions of the variables used in the vertex selection. The reconstructed SVs matched to the truth SV in the stop benchmark signal and fake SVs in the background events are compared.

Table 8.2: Vertex selection used in the T-LVT algorithm

Variable	Cut
SV mass (GeV)	> 0.6
SV L_{xy} (mm)	$\in (0.5, 5.0)$
SV L_{3D} significance	> 7.0
SV p_{T} (GeV)	> 3
SV $\lvert\eta\rvert$	< 1.5
SV $\cos\theta$	> 0.95
ΔR_{mean}	< 1.0

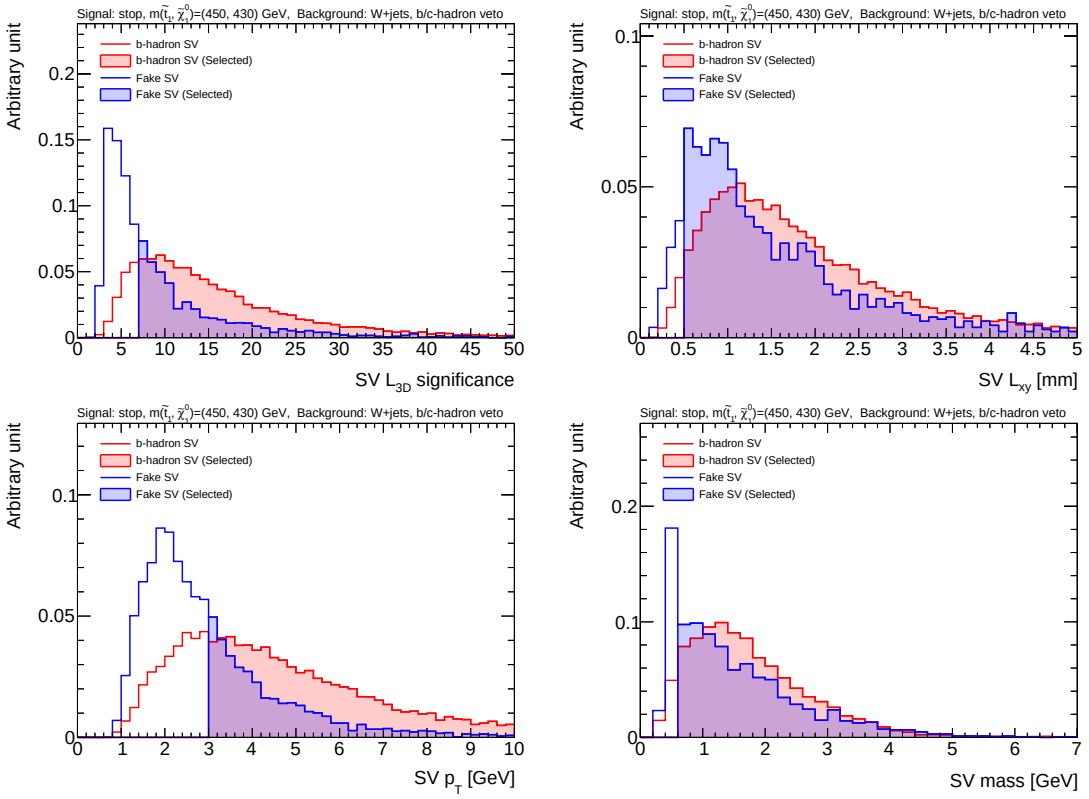

Figure 8.6: Distributions of the SV variables used in the vertex selection: (top left) the L_{3D} significance, (top right) SV L_{xy}, (bottom left) SV p_{T}, and (bottom right) SV mass. All cuts in Table 8.2 are applied except for the cut on the displayed variable. The red histograms are reconstructed SV that matched to a truth SV in the stop four-body signal with $m(\tilde{t}_1, \tilde{\chi}_1^0) = (450, 430)$ GeV. The blue histograms are reconstructed SV in the W+jets with no b- or c-hadrons. The shaded part shows the SV accepted by the algorithm.

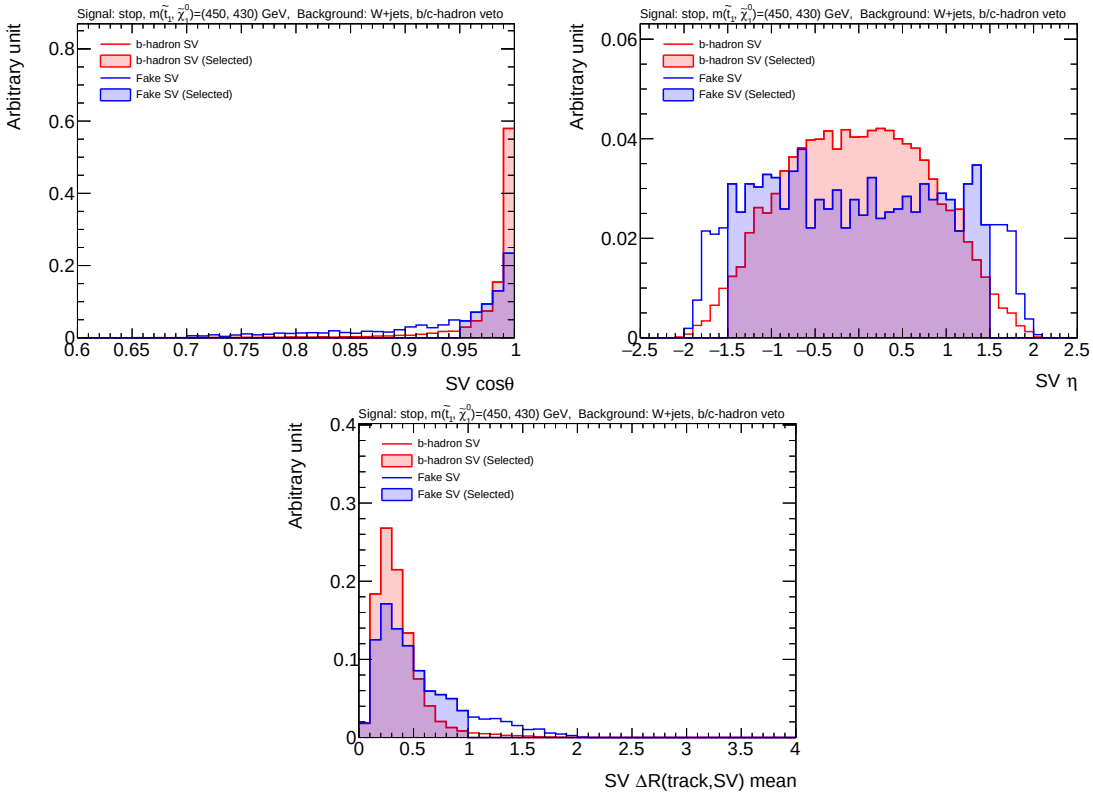

Figure 8.7: Distributions of the SV variables used in the vertex selection: (top left) the $\cos\theta$, (top right) SV $|\eta|$, and (bottom) ΔR_{mean}. All cuts in Table 8.2 are applied except for the cut on the displayed variable. The red histograms are reconstructed SV that matched to a truth SV in the stop four-body signal with $m(\tilde{t}_1, \tilde{\chi}_1^0) = (450, 430)$ GeV. The blue histograms are reconstructed SV in the W+jets with no b- or c-hadrons. The shaded part shows the SV accepted by the algorithm.

8.3 Performance

The performance of the soft b-tagging is evaluated using the MC simulation. The efficiency of the tagger is defined as the fraction of the tagged b-hadrons using generator level b-hadrons (truth b-hadrons). For truth b-hadrons, all the simulated b-hadrons are used, and no p_{T} cut is applied. Only b-hadrons that decay into another flavor are considered to avoid double counting of b-hadrons with the same origin. The truth matching is based on the angle ΔR between the truth b-hadron and the reconstructed object (the SV for T-LVT and the b-tagged jet for the standard b-tagging). In the calculation of ΔR, the direction of the T-LVT SV is defined as the pointing vector from the PV to the SV. For the jet-based b-tagging, the jet axis is used as the direction. If a reconstructed object is found around the truth b-hadron within $\Delta R < 0.3$, the b-hadron is labeled as tagged. The reconstructed object cannot be shared by more than one b-hadrons. If multiple truth b-hadrons have the same reconstructed objects within $\Delta R < 0.3$, the b-hadron with the smallest ΔR is kept as tagged, and the other b-hadrons are not considered as tagged by that object. Figure 8.8 shows the efficiency of the T-LVT tagger together with that of the standard b-tagging on the EM topo jets.

Each reconstructed object is also labeled as b-matched, charm-fake, or fake as follows:

- If a weakly decaying b-hadrons is found within $\Delta R < 0.3$, the object is labeled as matched to a b-hadron.
- If the object is not matched as b-hadron, but a weakly decaying c-hadron is found with the same criteria, then the object is labeled as a charm fake.
- If the object is not matched to b- or c- hadron, then the object is labeled as a fake.

With this label, the fake rate (charm fake rate) is defined as the average number of fake (charm) objects per event. Figure 8.9 shows the efficiency as a function of the fake or charm rate in two p_{T} ranges of b-hadrons. For the comparison of the T-LVT and the standard b-tagging, the fake and charm rate are evaluated with the signal events. In both $p_{\mathrm{T}} \in (5, 15)$ GeV and $p_{\mathrm{T}} \in (15, 20)$ GeV, the T-LVT algorithm shows better performance than the standard b-tagging. It is notable that in the low p_{T} range, the T-LVT efficiency is about 10 times better than that of the standard b-tagging at the same fake rate.

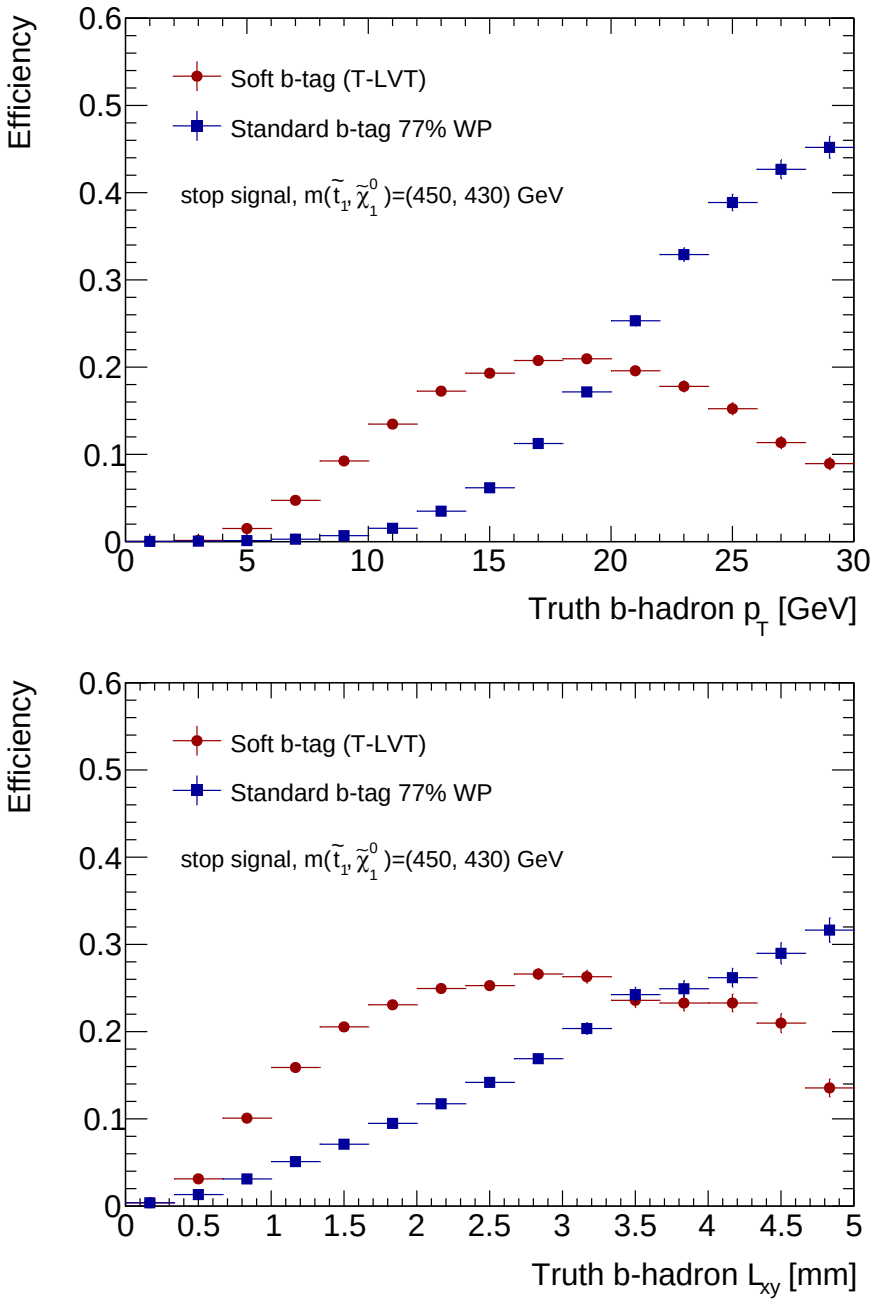

Figure 8.8: Efficiencies of the soft b-tagging algorithm and the standard b-tagging as a function of truth b-hadron p_{T} (top) and L_{xy} (bottom). Weakly decaying b-hadrons in the stop signal are considered. The efficiency is a fraction of b-hadrons which are tagged by the b-tagger based on the truth matching described in the text.

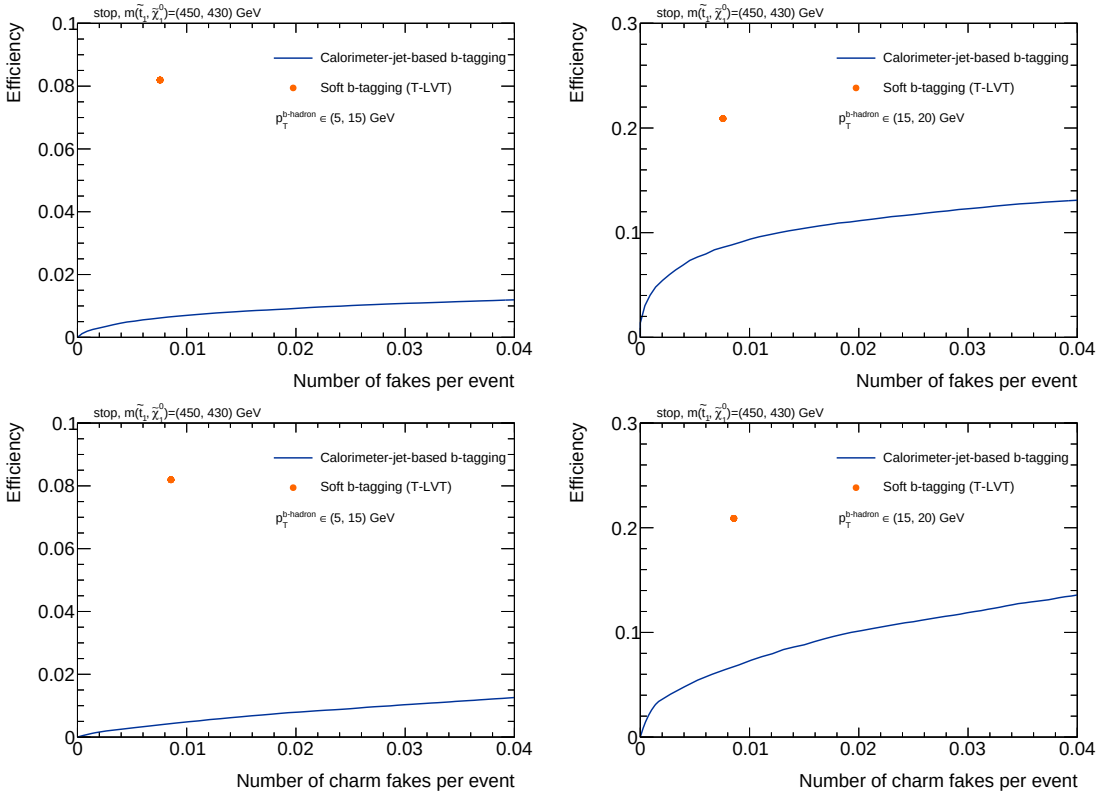

Figure 8.9: Efficiencies as a function of the average number of fake objects per event (top row) and average number of charm objects per event (bottom row). The plot in the left column show the lower-p_{T} region $p_{\mathrm{T}}^{b-\mathrm{hadron}} \in (5, 10)$ and the right plots are for higher-p_{T} region $p_{\mathrm{T}}^{b-\mathrm{hadron}} \in (15, 20)$. The orange point is the T-LVT working point, and the blue curve shows the standard b-tagging performance by changing the cut value on the MV2c10 score.

8.4 Calibration

In order to evaluate the data and MC agreement in the soft b-tagging variables, two calibration regions are defined, as shown in Table 8.3. One is a $t\bar{t}$ region dominated by di-leptonic $t\bar{t}$ events, and the other is a W+jets region. For both regions, events are collected with the single lepton trigger. For the $t\bar{t}$ region, a pair of leptons with opposite sign of their charges and opposite flavor (e and μ) (OSOF) and exactly one b-jet are required. The W+jets region is defined with exactly one lepton and no b-jets, and requirements on the $E_{\mathrm{T}}^{\mathrm{miss}}$ and m_{T} are imposed to remove the contribution from multijet events. After the selection, the simulated $t\bar{t}$ and W+jets events are normalized to data. Figure 8.10 shows distributions of the soft b-tagging variables. In both regions, the SV yields are underestimated in the MC simulation.

Table 8.3: Event selection to define calibration regions

Selection	$t\bar{t}$ selection	W+jets selection
Trigger	single lepton trigger	
Number of jets	≥ 2 (20 GeV)	
Number of leptons ($p_{\mathrm{T}} > 27$ GeV)	$= 2$ (OSOF)	$= 1$
b-jets (MV2c10)	$= 1$	$= 0$
$E_{\mathrm{T}}^{\mathrm{miss}}$	–	> 80 GeV
m_{T}	–	> 30 GeV

It is not feasible to use the SV without any correction in physics analysis due to the poor modelings, and a calibration is needed to correct the MC before application. For the standard b-tagging algorithm, the efficiencies of the taggers are measured in both data and MC, and the scale factor (SF), which is the ratio of the efficiency in data to that in MC, is measured. The efficiency is defined as the number of jets tagged by the algorithm over the number of jets, for a given set of jets that contain a truth b-hadron. In the physics analyses, the b-tagging efficiency in MC is corrected by applying the scale factor. However, it is difficult to use the same method to calibrate the T-LVT algorithm because the denominator of the efficiency can not be defined. The efficiency of the standard b-tagging is the probability to be labeled as b for a given jet, while the T-LVT is not an algorithm that labels something as b-tagged, but it creates a new object.

In order to reduce the discrepancy between data and MC, the source of the mismodeling is corrected, instead of directly measuring the efficiency of the T-LVT. The main source of the discrepancy comes from the mismodeling of tracks in the MC simulation. Figure 8.11 shows the number of selected tracks at the track selection step discussed in the previous

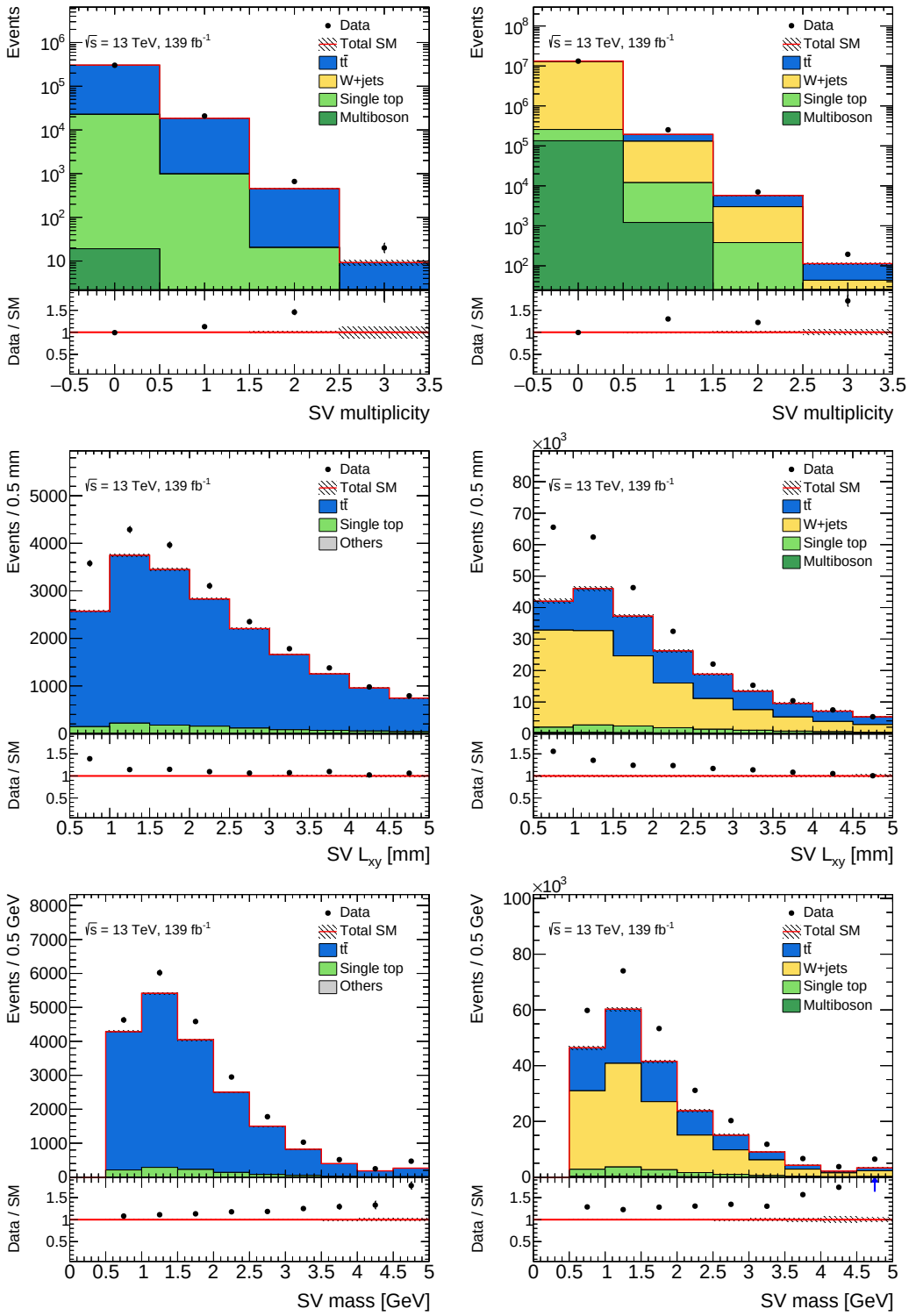

Figure 8.10: Distribution of the T-LVT variables: (top) the SV multiplicity, (middle) SV L_{xy}, and (bottom) SV mass in (left column) the $t\bar{t}$ and (right column) W+jets selections. Only statistical uncertainty is added.

section. The track multiplicity is underestimated in MC, and the discrepancy is more visible in the W+jets region. Since the T-LVT algorithm relies heavily on the reconstructed tracks, this mismodeling directly affects the SV yields. To correct the mismodeling observed in simulation, the distribution of the number of selected tracks (N_{trk}) is reweighted. The MC events are scaled to match the data in each bin of the N_{trk} distribution in both $t\bar{t}$ and W+jets regions separately. Figure 8.12 shows the T-LVT variables after the reweighting. Compared to the same variables before the reweighting in Figure 8.10, the agreements become much better after the reweighting.

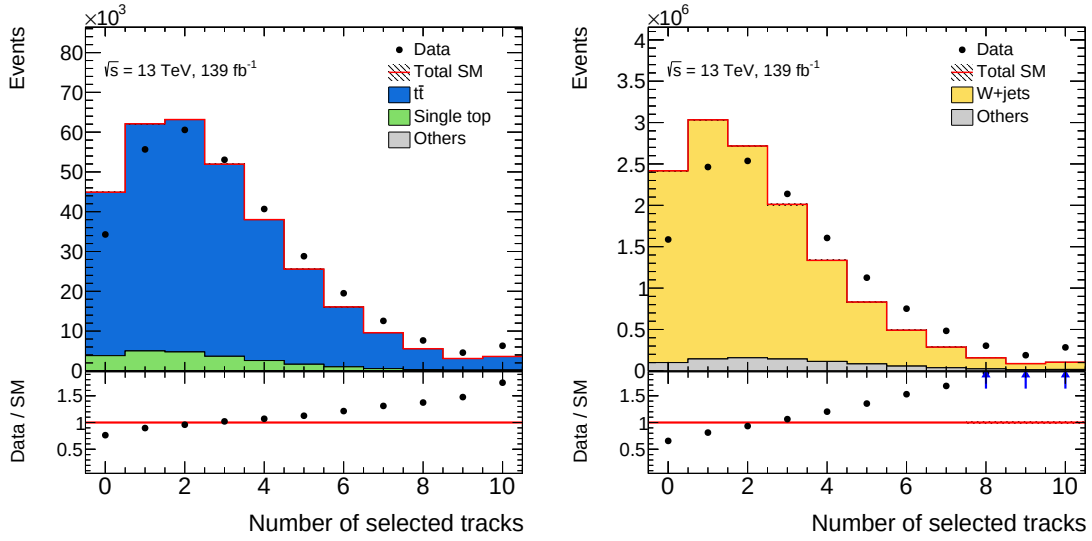

Figure 8.11: Number of selected tracks in T-LVT algorithm before the vertex fitting step in (left) $t\bar{t}$ and (right) W+jets regions. Only statistical uncertainty is included. The last bin includes overflow.

Figure 8.13 shows how much the SV yields are scaled by the reweighting for each SV truth label in $t\bar{t}$ and W+jets MC samples. The ratio of the post-reweighting number of events to that before reweighting is taken as the scale factor of the T-LVT algorithm. The scale factors are derived for the $t\bar{t}$ and W+jets separately, as summarized in Table 8.4. To account for the residual discrepancy between data and MC after the reweighting, flat 20% uncertainty is added on the SF for each flavor and each sample. The size of the uncertainty is determined to cover the data and MC disagreement in Figure 8.12.

Figure 8.14 shows comparisons of different generators in $t\bar{t}$ events. These plots indicate that the modeling of the N_{trk} distribution is different between the Sherpa sample and other samples. In the analysis described in Chapter 9, the $t\bar{t}$ and single top, and signal samples are generated with Powheg-Box +Pythia 8 and MadGraph+Pythia 8, respectively, while the W+jets, Z+jets, and multiboson are generated with Sherpa. The scale factors from the $t\bar{t}$ sample are applied to the former samples, and the ones from the W+jets are

Table 8.4: Soft b-tagging scale factors derived by the N_{trk} reweighting in $t\bar{t}$ and W+jets samples. The scale factors are measured for each truth flavor label of the SV.

Selection	$t\bar{t}$	W+jets
SF (truth b-hadron)	1.23	1.56
SF (truth c-hadron)	1.21	1.36
SF (Fake)	1.27	1.56

applied to the latter. For further cross-checks, Figure 8.15 shows the distribution of the SV variables in the $t\bar{t}$ selection, in which the MG5_aMC@NLO+Pythia 8 $t\bar{t}$ is used instead of the nominal $t\bar{t}$. In these plots, the N_{trk} reweight factor obtained from the nominal $t\bar{t}$ is used. The MC and data agree well within the 20% systematic uncertainty.

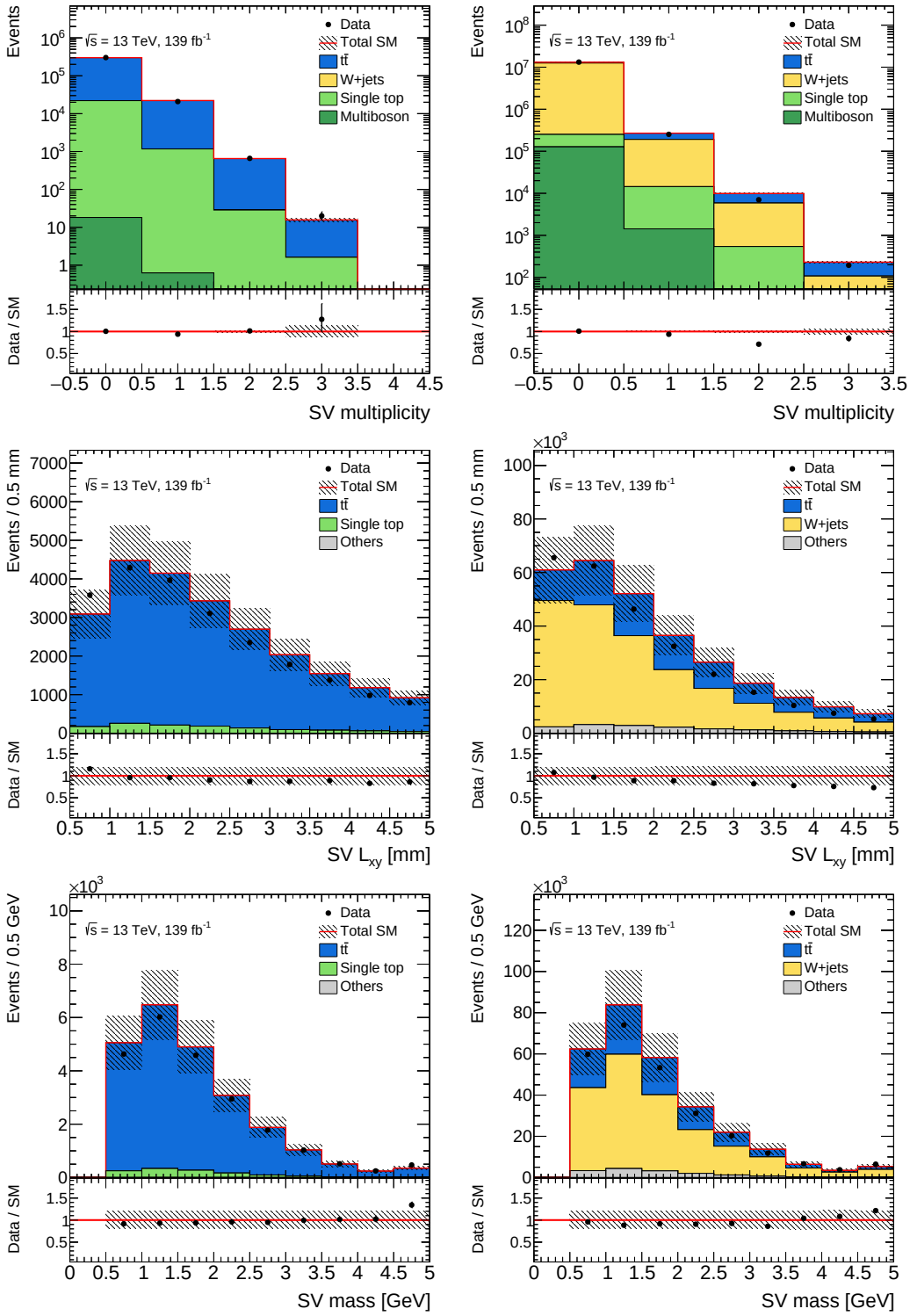

Figure 8.12: Distribution of the T-LVT variables after the N_{trk} reweighting: (top) the SV multiplicity, (middle) SV L_{xy}, and (bottom) SV mass in (left column) the $t\bar{t}$ and (right column) W+jets selections. Only statistical uncertainty is added in the top plots. For SV L_{xy} and mass distributions, the uncertainty includes 20% systematic uncertainty as well as statistical uncertainty.

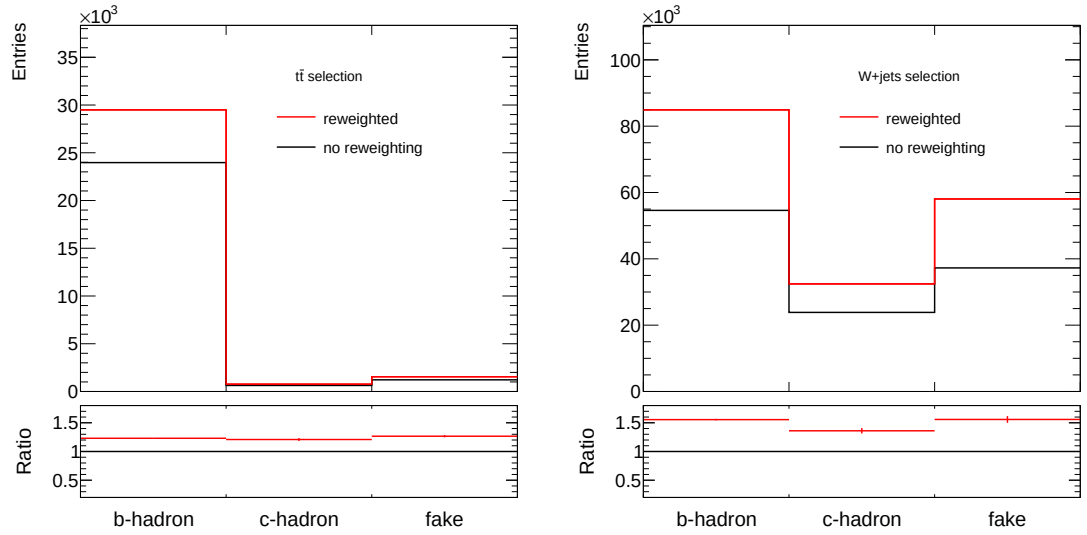

Figure 8.13: SV truth label before and after applying the N_{trk} reweighting for the $t\bar{t}$ selection (left) and the W+jets selection (right). The ratio on the bottom panel corresponds to the soft b-tag SF.

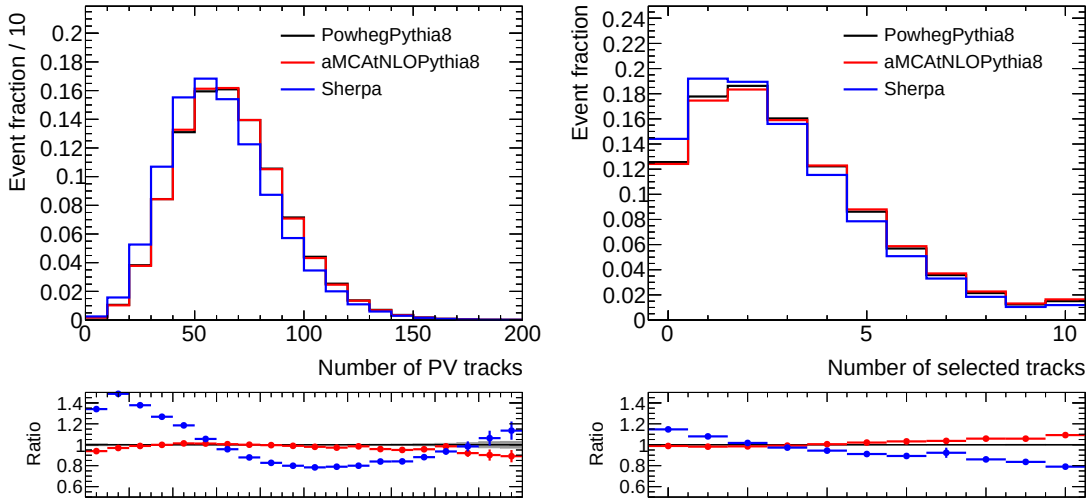

Figure 8.14: $t\bar{t}$ Generator comparison for the track multiplicity: (left) the number of tracks associated with the PV, and (right) the number of tracks selected in T-LVT algorithm. The black nominal POWHEG-BOX +PYTHIA 8 $t\bar{t}$ is compared with the MG5_aMC@NLO+PYTHIA 8 in red and the SHERPA in blue. The distributions are normalized to unity. The bottom panels show the ratio to the nominal sample.

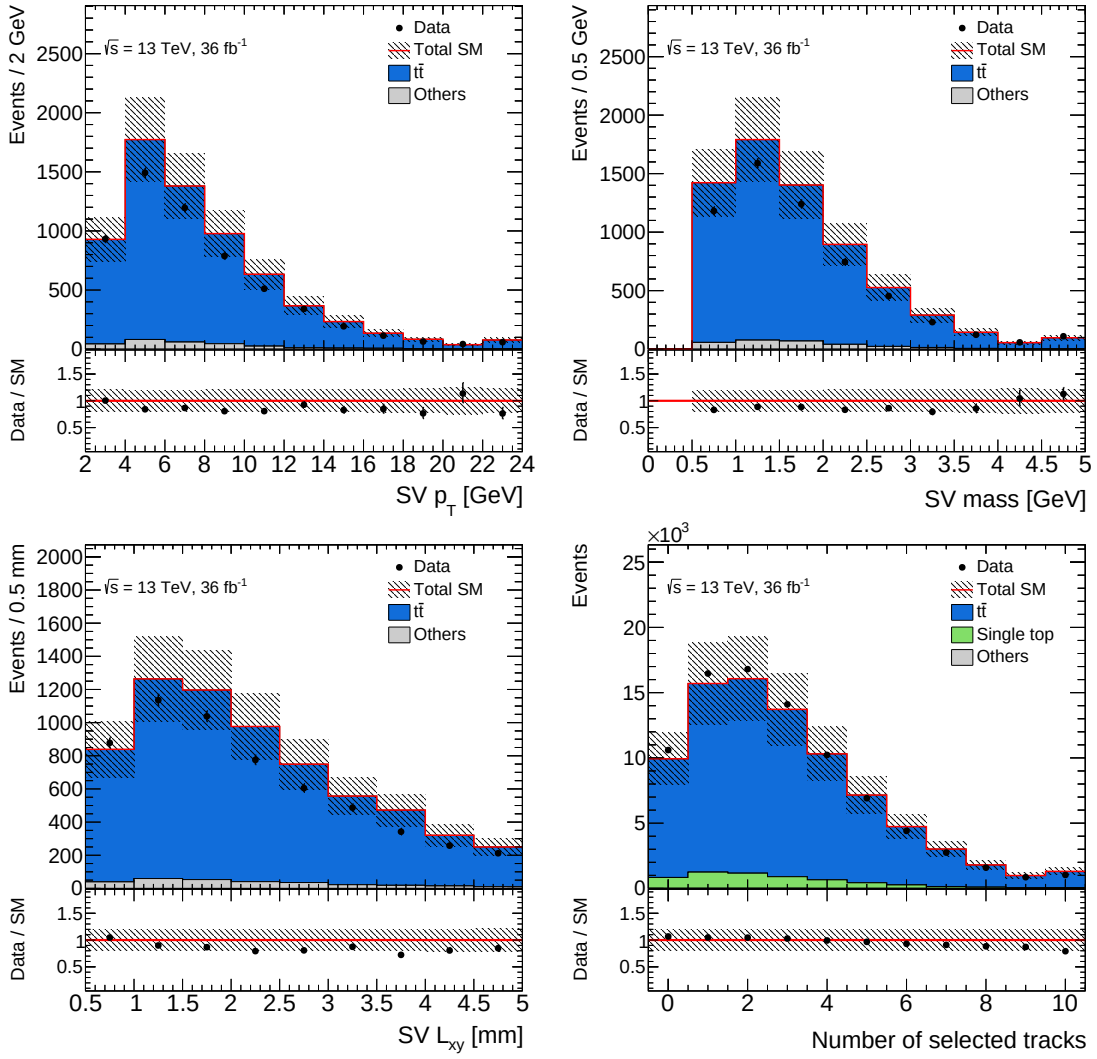

Figure 8.15: Comparison of distributions between data and simulation with the $t\bar{t}$ selection: (top left) the SV p_{T}, (top right) SV mass, (bottom left) SV L_{xy}, and (bottom right) the number of selected tracks in T-LVT. The MG5_aMC@NLOwith Pythia8 $t\bar{t}$ is used instead of the nominal $t\bar{t}$ (Powheg-Box +Pythia 8). The N_{trk} reweighting factor calculated with the nominal $t\bar{t}$ is applied. The 20% systematic uncertainty is added.

Chapter 9

Search for Stop with Small $\Delta m(\tilde{t}_1, \tilde{\chi}_1^0)$ Scenarios

In this chapter, a stop search with the data recorded in 2015–2018 is presented. The integrated luminosity of the data which satisfies good quality criteria is 139.0 fb^{-1}. The search targets the most compressed signature, the $\tilde{t}_1 \to bff'\tilde{\chi}_1^0$ decay. Under the higgsino-like LSP assumption, the $\tilde{t}_1$ decays to $t\tilde{\chi}_1^0$ or $t\tilde{\chi}_2^0$ are forbidden kinematically if the $\Delta m(\tilde{t}_1, \tilde{\chi}_1^0)$ is smaller than m_t. The other decay, $b\tilde{\chi}_1^\pm$ becomes $bW^*\tilde{\chi}_1^0 \to bff'\tilde{\chi}_1^0$ eventually. In the following, this search is presented using the simplified model, which is explained in Section 6.1.

9.1 Event Selection

In this analysis, the stop four-body decay ($\tilde{t}_1 \to bff'\tilde{\chi}_1^0$) with $m(\tilde{t}_1, \tilde{\chi}_1^0) = (450, 430)$ GeV signal is used as a benchmark signal to define a SR. We use the events with exactly one lepton with high $E_{\mathrm{T}}^{\mathrm{miss}}$. The first set of the event selection criteria (preselection) is summarized in Table 9.1. The distributions of key variables: the $E_{\mathrm{T}}^{\mathrm{miss}}$, m_{T}, $\Delta\phi(\vec{E}_{\mathrm{T}}^{\mathrm{miss}}, \ell)$, lepton charge, number of b-tagged jets, lepton p_{T}, $p_{\mathrm{T}}^{\ell}/E_{\mathrm{T}}^{\mathrm{miss}}$, and SV, after the preselection are shown in Figures 9.1 and 9.2. The events are collected with the $E_{\mathrm{T}}^{\mathrm{miss}}$ trigger along with the requirement of the offline $E_{\mathrm{T}}^{\mathrm{miss}} > 230$ GeV. The hardest vertex is selected as the PV as explained in Section 5.1. The tight jet-cleaning criteria are applied for the leading jet in order to avoid having events that mimic an ISR + high $E_{\mathrm{T}}^{\mathrm{miss}}$ topology due to a fake high-p_{T} jet. The preselection for this search uses muons with $p_{\mathrm{T}} > 4$ GeV and electrons with $p_{\mathrm{T}} > 4.5$ GeV. Due to the small mass-splitting between $\tilde{t}_1$ and $\tilde{\chi}_1^0$ in the benchmark four-body signal, many events do not have large $E_{\mathrm{T}}^{\mathrm{miss}}$ which satisfies the $E_{\mathrm{T}}^{\mathrm{miss}}$ trigger and the $E_{\mathrm{T}}^{\mathrm{miss}}$ requirement in this search. To improve the signal-to-background ratio, the leading jet p_{T} is required to be larger than 200 GeV to select boosted topology with a high-p_{T} ISR, in which the $\tilde{t}_1$ pair is recoiled into the opposite hemisphere to the ISR jet. This results in the large $E_{\mathrm{T}}^{\mathrm{miss}}$ from the two LSPs. In order to reduce $t\bar{t}$ and W+jets events which

have a leptonically decaying W boson, $m_{\mathrm{T}} > 90$ GeV is required in the selection. Finally, the $|\Delta\phi|$ between the $E_{\mathrm{T}}^{\mathrm{miss}}$ and leading jet is required to be larger than 0.4 in order to reduce multijet events produced by QCD processes with a jet that is misreconstructed as a lepton and large $E_{\mathrm{T}}^{\mathrm{miss}}$ created by misaligned jets. If there are more than one jets, the same requirement is also applied to the second leading jet.

Table 9.1: Preselection criteria.

	Preselection
Trigger	$E_{\mathrm{T}}^{\mathrm{miss}}$ triggers only
Data quality	jet cleaning, primary vertex
Number of leptons	$= 1$ lepton
Lepton p_{T} [GeV]	> 4 for μ
	> 4.5 for e
Number of jets	≥ 1 ($p_{\mathrm{T}} > 200$ GeV)
$E_{\mathrm{T}}^{\mathrm{miss}}$ [GeV]	> 230
m_{T} [GeV]	> 90
$\lvert\Delta\phi(j_{1,(2)}, \vec{E}_{\mathrm{T}}^{\mathrm{miss}})\rvert$	> 0.4

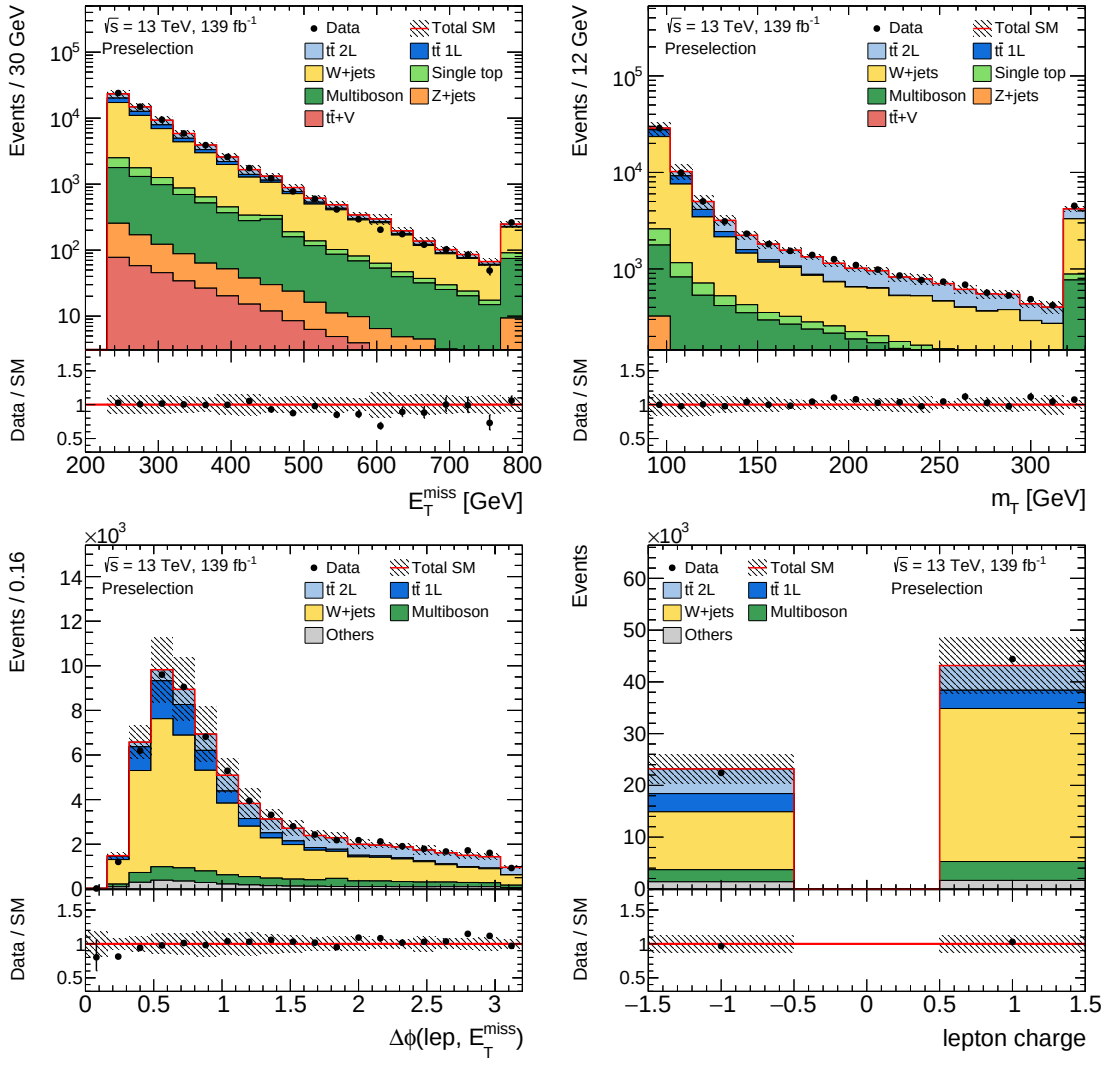

Figure 9.1: Comparison of data and simulation for the main discriminating variables before fitting MC to data at the preselection level: (top left) $E_{\mathrm{T}}^{\mathrm{miss}}$, (top right) m_{T}, (bottom left) $\Delta\phi(\vec{E}_{\mathrm{T}}^{\mathrm{miss}}, \ell)$, and (bottom right) lepton charge. Statistical and experimental uncertainties are displayed. The overflow is included in the last bin.

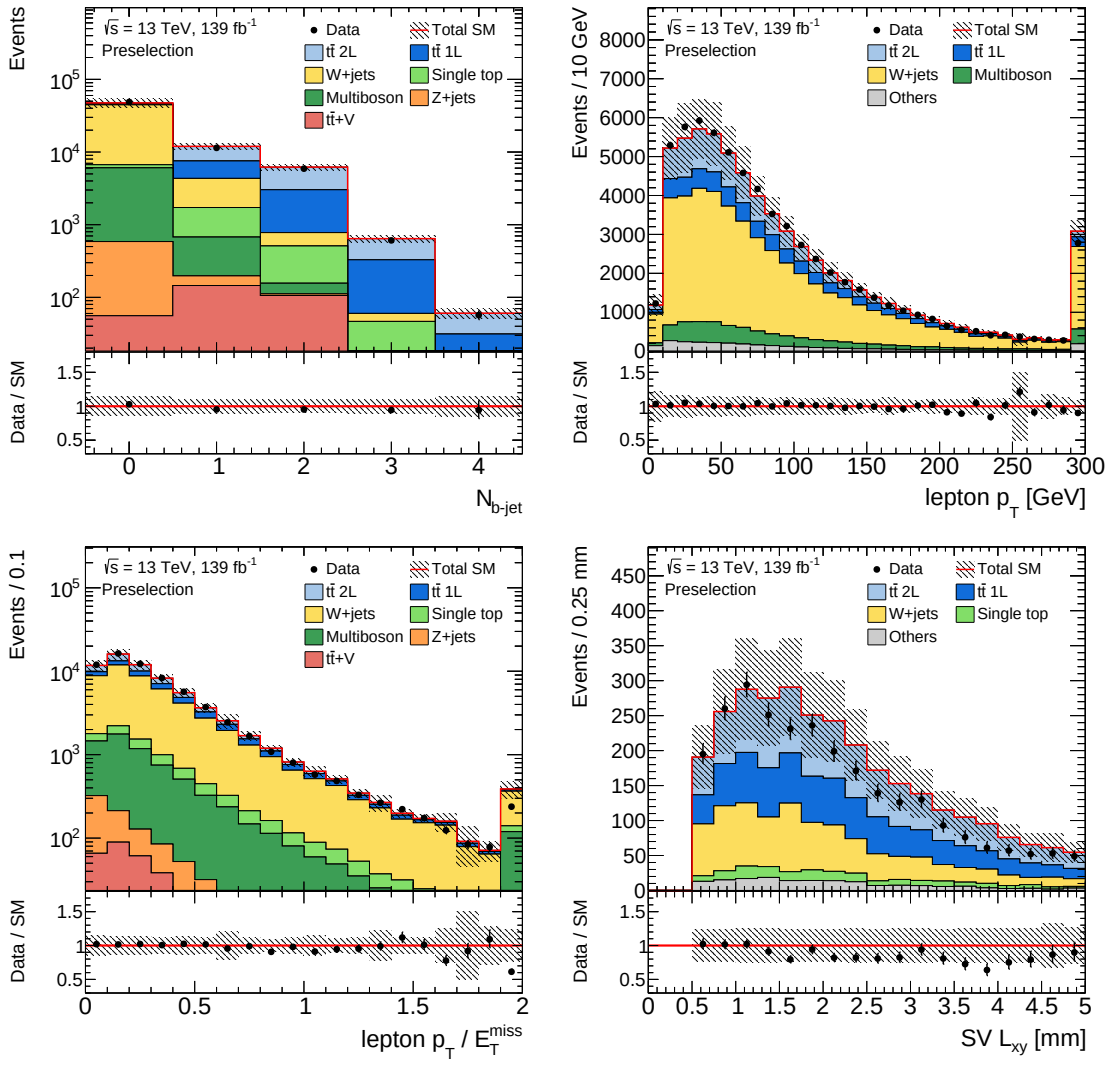

Figure 9.2: Comparison of data and simulation for the main discriminating variables before fitting MC to data at the preselection level: (top left) b-jet multiplicity, (top right) lepton p_{T}, (bottom left) $p_{\mathrm{T}}^{\ell}/E_{\mathrm{T}}^{\mathrm{miss}}$, and (bottom right) SV L_{xy}. Statistical and experimental uncertainties are displayed. The overflow is included in the last bin.

On top of the preselection, tighter selection criteria are applied to define the SR. The SR targeting the four-body decay using the soft b-tagging technique is named `bffN_softb`. The event selection for the `bffN_softb` SR is summarized in Table 9.2. The distributions of the variables used to define the SR are shown in Figure 9.3. A tighter $E_{\mathrm{T}}^{\mathrm{miss}}$ requirement than the preselection is added to enhance the signal-to-background ratio. Since signal events have low-p_{T} b-hadrons while the $t\bar{t}$ background has b-hadrons with higher p_{T}, events that have any b-jets tagged by the standard b-tagging algorithm are rejected. After removing events with high-p_{T} b-jets, the background processes are dominated by the W+jets process. In order to select events with low p_{T} b-hadrons, it is required to have at least one secondary vertex reconstructed by the soft b-tagging algorithm. Since there is no b-hadron in typical W+jets events, the soft b-tagging requirement significantly reduces the W+jets background. The remaining background is dominated by W+jets events with low p_{T} b-hadrons produced from a gluon ($g \to b\bar{b}$). In general, the p_{T} of the lepton and the magnitude of $E_{\mathrm{T}}^{\mathrm{miss}}$ are balanced in $t\bar{t}$ and W+jets events because a lepton and a neutrino, which makes $E_{\mathrm{T}}^{\mathrm{miss}}$, tend to be emitted from the same W boson. The signal events have a low-p_{T} lepton and large $E_{\mathrm{T}}^{\mathrm{miss}}$. Therefore, $p_{\mathrm{T}}^{\ell}/E_{\mathrm{T}}^{\mathrm{miss}}$ is a good estimator to separate the signal from the background. Two types of SRs are defined: a single-bin SR targeting for a discovery and a shape-fit SR for excluding signals when there is no discovery. The single-bin SR is defined with $p_{\mathrm{T}}^{\ell}/E_{\mathrm{T}}^{\mathrm{miss}} < 0.04$, while the shape-fit SR has five bins using the $p_{\mathrm{T}}^{\ell}/E_{\mathrm{T}}^{\mathrm{miss}}$ distribution. The event yields after applying the single-bin SR selection are shown in Table 9.3 for background and the benchmark signal. The fractions of the background processes before applying the NFs are displayed in Figure 9.4.

Table 9.2: Overview of the event selection defining the `bffN_softb` SR.

	`bffN_softb`
Preselection	Preselection in Table 9.1
$E_{\mathrm{T}}^{\mathrm{miss}}$	$> 250\,\mathrm{GeV}$
Number of secondary vertices (N_{SV})	≥ 1
Number of b-jets ($p_{\mathrm{T}} > 20$ GeV)	$= 0$
$\Delta\phi(\vec{E}_{\mathrm{T}}^{\mathrm{miss}}, \ell)$	< 2
$p_{\mathrm{T}}^{\ell}/E_{\mathrm{T}}^{\mathrm{miss}}$	< 0.04 (discovery)
$p_{\mathrm{T}}^{\ell}/E_{\mathrm{T}}^{\mathrm{miss}}$	$[0, 0.015, 0.025, 0.04, 0.06, 0.08]$ (exclusion)

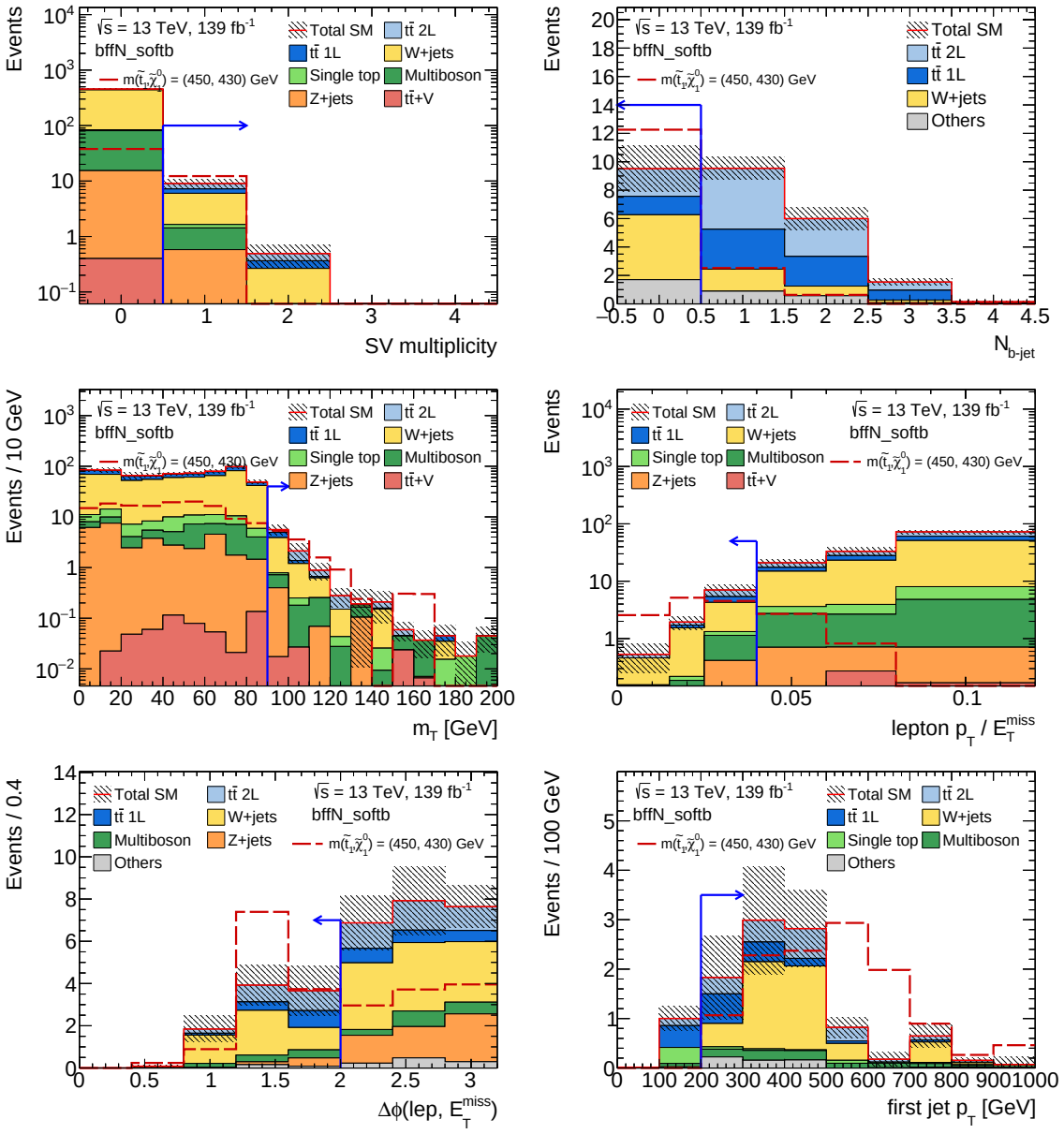

Figure 9.3: Distributions of the variables used to define the `bffN_softb` single-bin SR after applying all `bffN_softb` cuts, except the one on the displayed distribution: (top left) the soft b-tag SV multiplicity, (top right) number of b-jets tagged by the standard b-tagging algorithm, (middle left) m_{T}, (middle right) $p_{\mathrm{T}}^{\ell}/E_{\mathrm{T}}^{\mathrm{miss}}$, (bottom left) $\Delta\phi(\vec{E}_{\mathrm{T}}^{\mathrm{miss}}, \ell)$, and (bottom right) leading jet p_{T}. The events are not scaled by the normalization factors, and only statistical uncertainty is displayed. The last bin includes the overflow.

Table 9.3: Expected number of events in `bffN_softb` for 139 fb^{-1} before applying the NFs. Only the statistical uncertainty of the MC samples is given.

Process		Events
Background	$t\bar{t}$ 1L	1.3 ± 0.2
	$t\bar{t}$ 2L	1.9 ± 0.4
	W+jets	4.6 ± 1.6
	Single top	0.2 ± 0.1
	Multiboson	0.9 ± 0.1
	Z+jets	0.5 ± 0.2
	$t\bar{t} + V$	0.1 ± 0.1
	Total	9.5 ± 1.6
Benchmark signal		12.3 ± 1.9

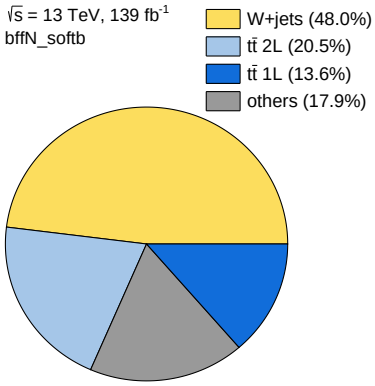

Figure 9.4: Breakdown of the individual SM contributions to the signal region. The pre-fit yields are shown. The minor background processes are merged into "Others."

9.2 Background Estimation

The dominant backgrounds entering the signal region are W+jets and $t\bar{t}$ processes. The single top process is a minor background in this analysis because no am_{T2} cut is used. Dedicated CRs and VRs are defined for W+jets, and $t\bar{t}$. The other minor background processes are normalized by their theoretical cross sections. Table 9.4 summarizes the event selections for the CRs and VRs for W+jets and $t\bar{t}$, comparing with the SR selection. The CRs are defined with high $p_{\text{T}}^{\ell}/E_{\text{T}}^{\text{miss}}$ compared to the SR requirement to increase the background events and minimize the signal contamination. The intermediate $p_{\text{T}}^{\ell}/E_{\text{T}}^{\text{miss}}$ is used for the VR. The same soft b-tag requirement ($N_{\text{SV}} > 0$) is used in all regions to cancel the soft b-tagging uncertainty for the main background processes. To increase the purity of the background process in each CR and VR, additional requirements on the number of

the standard b-tag and lepton charge are added. At least one b-jet is required in the $t\bar{t}$ CR and VR, which enhances $t\bar{t}$ events effectively by requiring two b-hadrons by both b-tagging algorithms. A positive charged lepton is required in W+jets CR and VR, and the opposite requirement is added in $t\bar{t}$ regions to enhance the purity of the backgrounds. There are more positive charged leptons in the W+jets selection than negative ones because of the different cross sections between $ug \to W^+d$ and $dg \to W^-u$ due to the proton property. The event yields in the $t\bar{t}$ and W+jets CRs are shown in Table 9.5, and breakdown of the background processes are shown in Figure 9.5. Table 9.6 shows the $t\bar{t}$ and W+jets VR yields, and the breakdown is shown in Figure 9.6. In all CRs and VRs, the signal contamination is found to be negligible.

Table 9.4: Overview of the event selections defining `bffN_softb` and the associated control and validation regions.

	SR	TCR/TVR	WCR/WVR
Preselection		Preselection in Table 9.1	
$E_{\mathrm{T}}^{\mathrm{miss}}$		$> 250\,\mathrm{GeV}$	
N_{SV}		≥ 1	
$\Delta\phi(\vec{E}_{\mathrm{T}}^{\mathrm{miss}}, \ell)$		< 2	
Number of b-jets	$= 0$	≥ 1	$= 0$
Lepton charge	–	< 0	> 0
$p_{\mathrm{T}}^{\ell}/E_{\mathrm{T}}^{\mathrm{miss}}$	< 0.04	$\in (0.12, 0.25)/\in (0.08, 0.12)$	$\in (0.16, 0.32)/\in (0.08, 0.16)$

Table 9.5: Pre-fit expected events in `bffN_softb` TCR and WCR for 139 fb^{-1}. Only the statistical uncertainty of the MC samples is given. The benchmark signal is the stop four-body decay signal with the masses of $m(\tilde{t}_1, \tilde{\chi}_1^0) = (450, 430)$ GeV.

	TCR	WCR
$t\bar{t}$ 1L	57.5 ± 2.0	22.0 ± 1.2
$t\bar{t}$ 2L	74.6 ± 1.7	19.7 ± 0.9
W+jets	10.7 ± 1.9	72.7 ± 5.6
Single top	5.9 ± 0.8	6.1 ± 1.1
Multiboson	2.0 ± 0.3	9.3 ± 1.8
Z+jets	0.2 ± 0.1	0.9 ± 0.2
$t\bar{t} + V$	2.0 ± 0.3	0.9 ± 0.1
Total	152.8 ± 3.4	131.5 ± 6.2
Benchmark signal	< 0.1	< 0.1

Comparisons of the distributions of key variables are shown in Figures 9.7–9.8 for $t\bar{t}$ and W+jets CRs, respectively. The data and MC distributions of variables in $t\bar{t}$ and W+jets VRs are shown in Figures 9.9–9.10. The $t\bar{t}$ and W+jets NFs obtained by the simultaneous

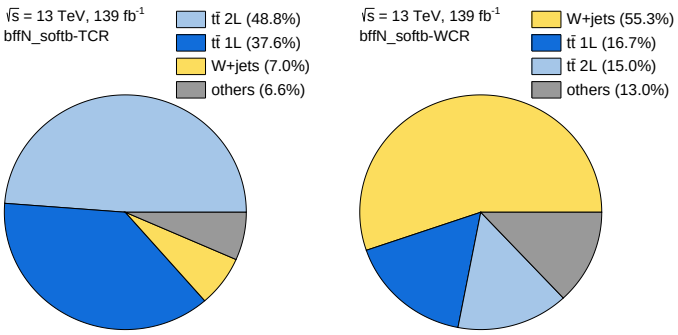

Figure 9.5: Breakdown of the individual SM contributions to the TCR (left) and WCR (right). The pre-fit yields are shown. The minor background processes are merged into "Others."

Table 9.6: Pre-fit expected events in `bffN_softb` TVR and WVR for 139 fb^{-1}. Only the statistical uncertainty of the MC samples is given. The benchmark signal is the stop four-body decay signal with the masses of $m(\tilde{t}_1, \tilde{\chi}_1^0) = (450, 430)$ GeV.

	TVR	WVR
$t\bar{t}$ 1L	15.7 ± 1.1	10.7 ± 0.9
$t\bar{t}$ 2L	25.8 ± 0.8	12.2 ± 0.7
W+jets	5.0 ± 1.3	59.4 ± 6.2
Single top	2.3 ± 0.5	4.4 ± 0.9
Multiboson	0.6 ± 0.1	4.5 ± 0.9
Z+jets	0.1 ± 0.1	0.6 ± 0.2
$t\bar{t} + V$	0.9 ± 0.2	0.2 ± 0.1
Total	50.5 ± 2.0	91.9 ± 6.5
Benchmark signal	< 0.1	< 0.1

fit in both CRs are summarized in Table 9.7, which are applied in the VRs and SR. Table 9.8 is the summary of the post-fit yields in all CRs and VRs.

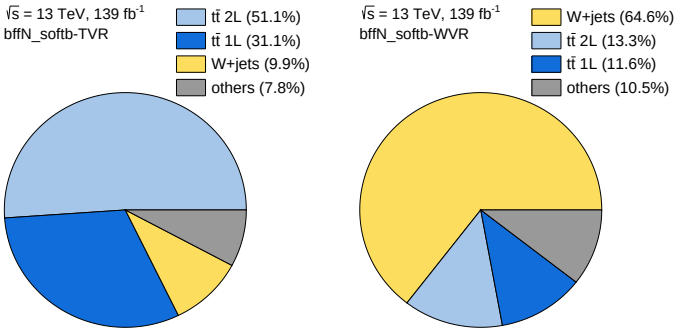

Figure 9.6: Breakdown of the individual SM contributions to the TVR (left) and WVR (right). The pre-fit yields are shown. The minor background processes are merged into "Others."

Table 9.7: Normalization factors obtained by the background only fit in $t\bar{t}$ and W+jets CRs.

Background process	NF
$t\bar{t}$	0.68 ± 0.10
W+jets	$1.04 \pm ^{+0.22}_{-0.20}$

Table 9.8: Post-fit yields in the CRs and VRs.

	TCR	WCR	TVR	WVR
Observed events	111	121	38	77
Fitted background	111.1 ± 10.6	121.0 ± 11.1	37.5 ± 4.1	87.2 ± 14.7
$t\bar{t}$	89.9 ± 12.2	28.4 ± 6.0	28.3 ± 4.6	15.6 ± 4.0
W+jets	11.1 ± 3.9	75.5 ± 13.5	5.2 ± 2.1	62.0 ± 15.3
Single top	5.9 ± 2.3	6.1 ± 2.2	2.3 ± 0.9	4.4 ± 1.8
Multiboson	2.0 ± 0.6	9.3 ± 2.9	0.6 ± 0.2	4.5 ± 1.4
Others	2.2 ± 1.2	1.7 ± 0.6	1.0 ± 0.5	0.8 ± 0.2

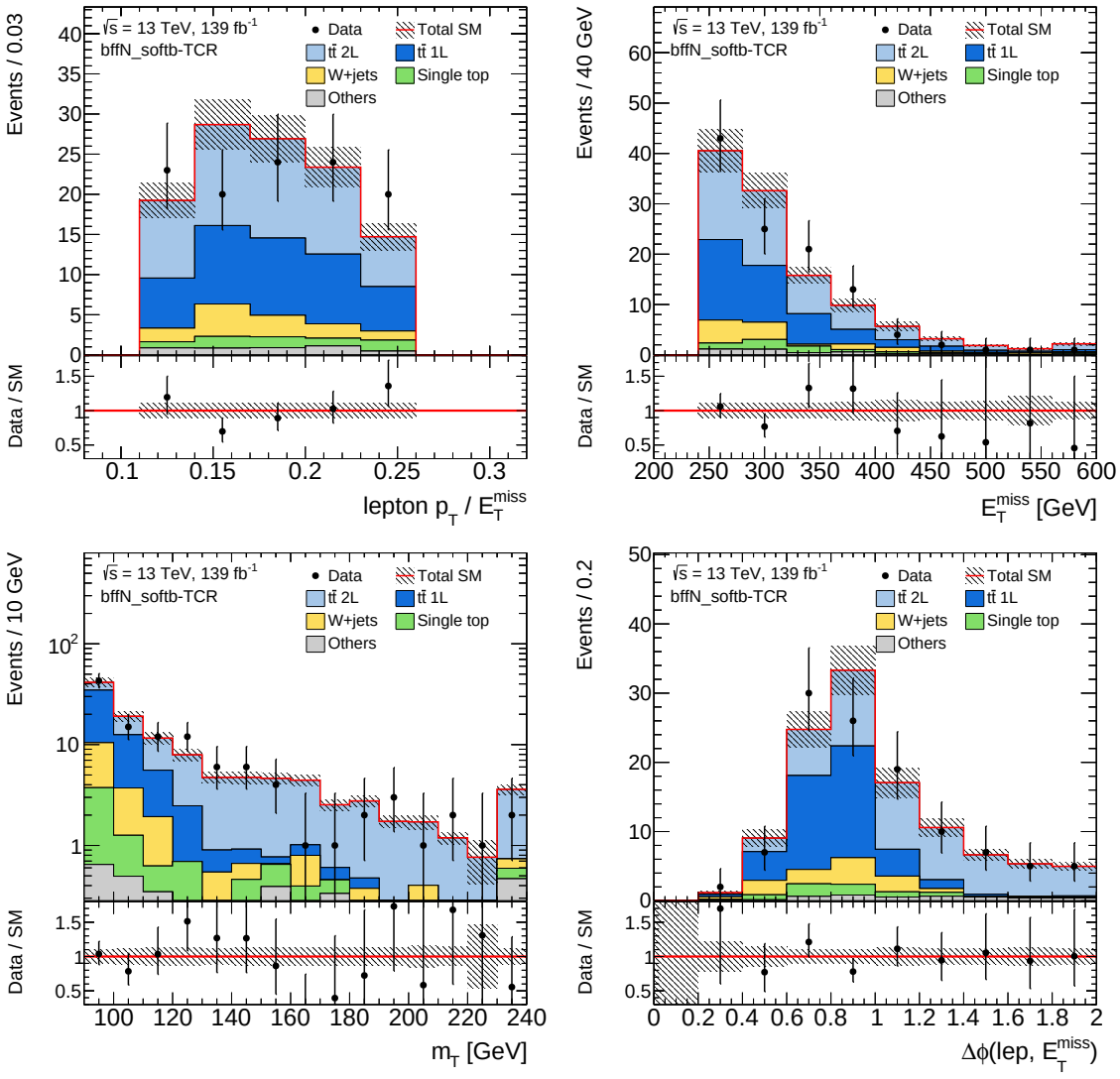

Figure 9.7: Comparison of data and simulation for the $t\bar{t}$ CR after applying the normalization factors: (top left) the $p_{\mathrm{T}}^{\ell}/E_{\mathrm{T}}^{\mathrm{miss}}$, (top right) $E_{\mathrm{T}}^{\mathrm{miss}}$, (bottom left) m_{T}, and (bottom right) $\Delta\phi(\vec{E}_{\mathrm{T}}^{\mathrm{miss}}, \ell)$. Statistical and experimental uncertainties are displayed. The last bin includes the overflow.

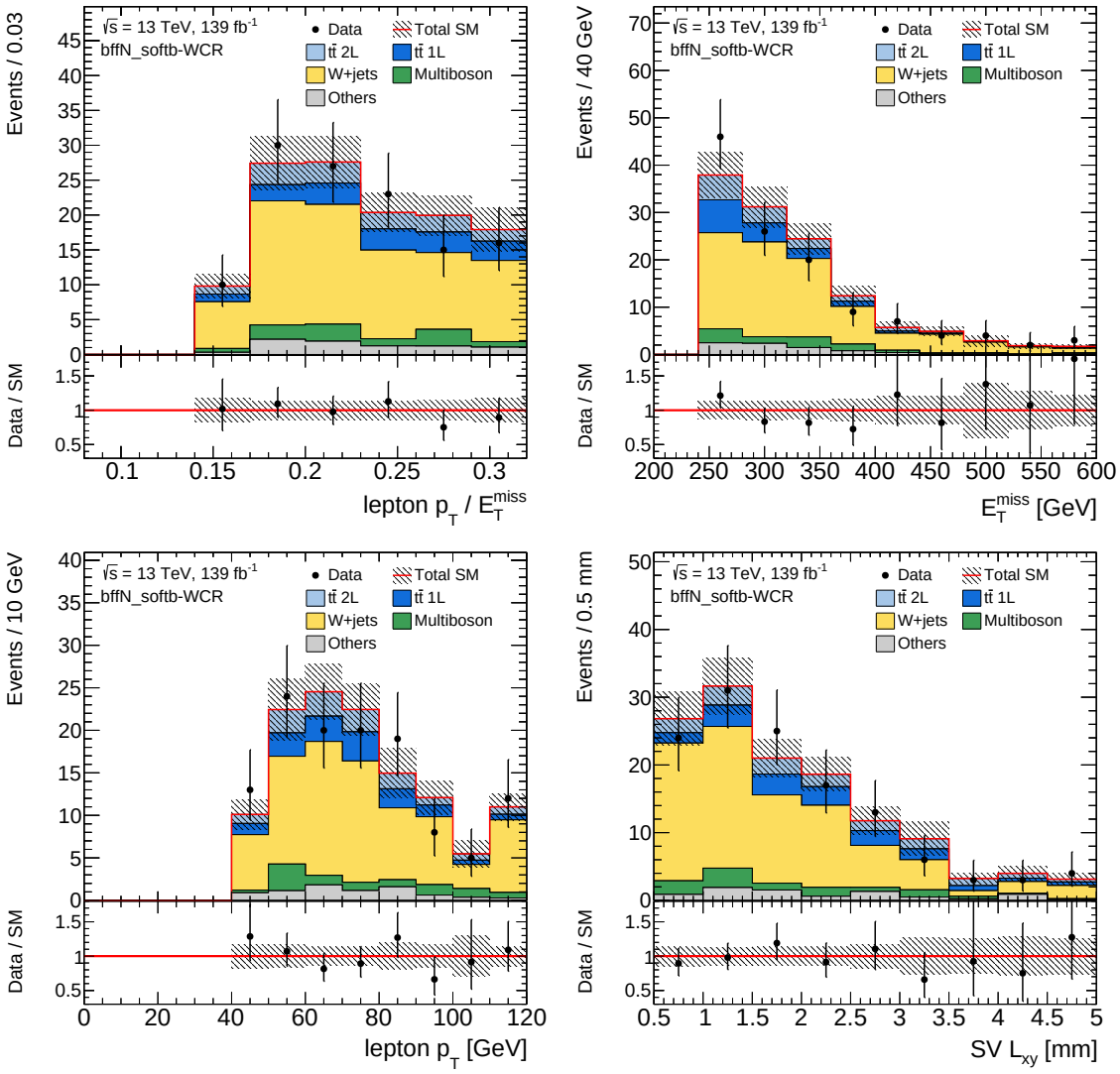

Figure 9.8: Comparison of data and simulation for the W+jets CR after applying the normalization factors: (top left) the $p_{\mathrm{T}}^{\ell}/E_{\mathrm{T}}^{\mathrm{miss}}$, (top right) $E_{\mathrm{T}}^{\mathrm{miss}}$, (bottom left) lepton p_{T}, and (bottom right) soft b-tag SV L_{xy}. Statistical and experimental uncertainties are displayed. The last bin includes the overflow.

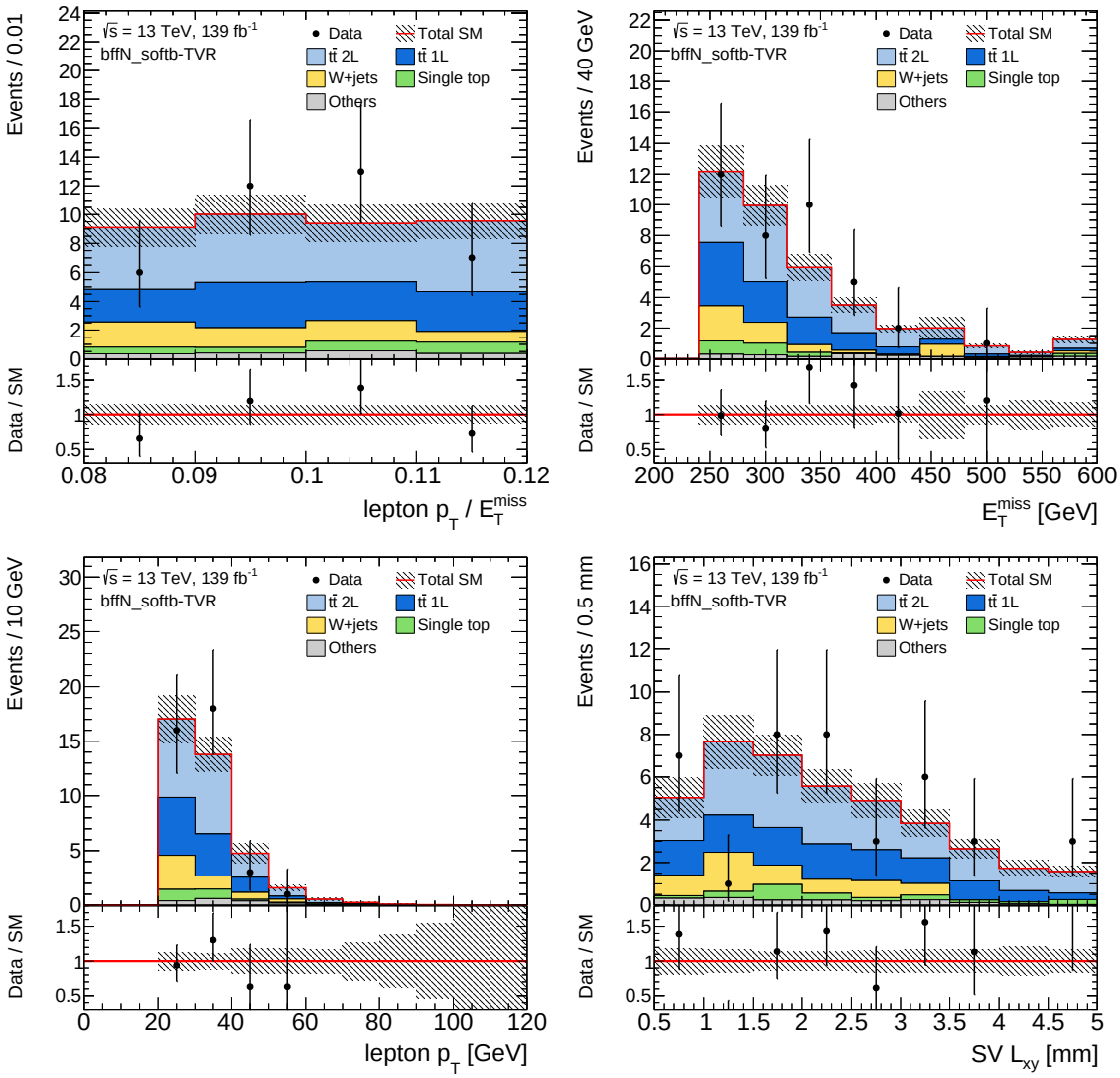

Figure 9.9: Comparison of data and simulation for the $t\bar{t}$ VR after applying the normalization factors: (top left) the $p_{\mathrm{T}}^{\ell}/E_{\mathrm{T}}^{\mathrm{miss}}$, (top right) $E_{\mathrm{T}}^{\mathrm{miss}}$, (bottom left) lepton p_{T}, and (bottom right) soft b-tag SV L_{xy}. Statistical and experimental uncertainties are displayed. The last bin includes the overflow.

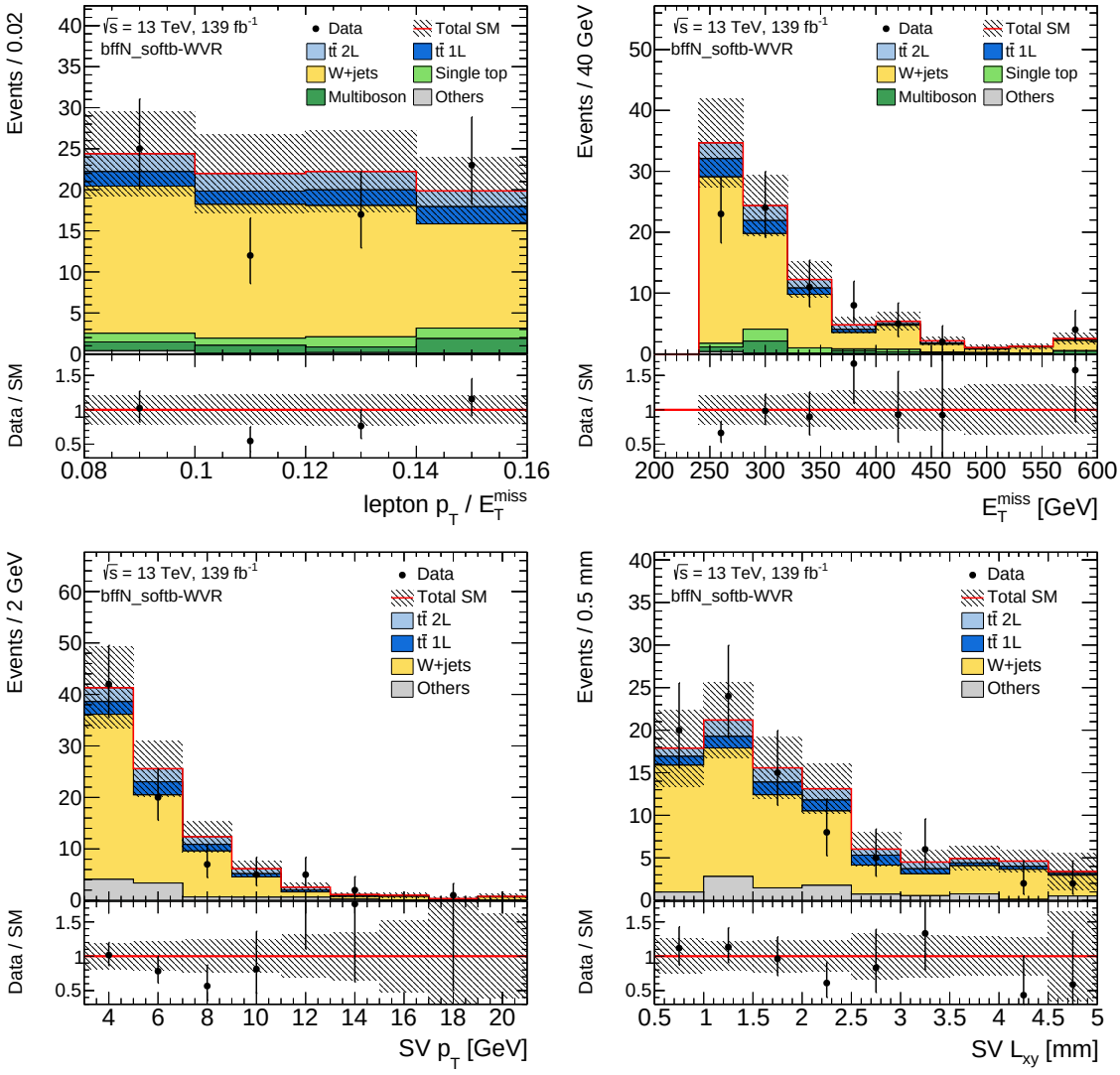

Figure 9.10: Comparison of data and simulation for the W+jets VR after applying the normalization factors: (top left) the $p_{\mathrm{T}}^{\ell}/E_{\mathrm{T}}^{\mathrm{miss}}$, (top right) $E_{\mathrm{T}}^{\mathrm{miss}}$, (bottom left) p_{T} of the soft b-tag SV, and (bottom right) soft b-tag SV L_{xy}. Statistical and experimental uncertainties are displayed. The last bin includes the overflow.

9.3 Systematic Uncertainties

Details of the systematic uncertainty were already discussed in Section 6.5. The theoretical uncertainties in each region are summarized in Table 9.9. The uncertainties in the transfer factors from the TCR or WCR to the other regions are estimated by the same method as for the analysis described in Chapter 7. Due to the small contributions from the other minor background processes, a flat 30% uncertainty is included for the minor background processes which do not have a dedicated CR. For the $t\bar{t}$ background process, the main contributions come from the uncertainties in the parton shower and hard scatter. For the W+jets background, the main contribution comes from the generator comparison with the alternative MadGraph +Pythia 8 sample.

Table 9.9: Theoretical uncertainties (%) in the $t\bar{t}$ and W+jets processes. The relative uncertainties with respect to the number of events for the background process in each region are shown. The uncertainties in the transfer factors from the control region of the background process to the other regions are calculated.

	$t\bar{t}$	W+jets
SR	12.8	17.7
SR1	32.4	23.2
SR2	11.1	28.2
SR3	14.4	16.1
SR4	9.0	4.9
TCR	–	8.3
WCR	9.9	–
TVR	1.9	11.8
WVR	11.8	1.8

The uncertainties in the background prediction in the SR are summarized in Table 9.10. The total statistical uncertainty is 34% for the expected SM events, and the systematic uncertainty is 27%. The sources of these uncertainties are explained in Section 6.5. The dominant systematic uncertainty comes from the MC statistical uncertainty for the W+jets sample due to the tight SR selection. The number of events in the SR is also affected by the uncertainties originating from the jet calibration (JES and JER). The W+jets normalization uncertainty is caused by the limited statistics in the WCR, and the W+jets modeling uncertainty is the theoretical uncertainty as discussed above.

Table 9.10: Summary of the dominant systematic uncertainties in the background prediction in the `bffN_softb` SR.

SR Uncertainty (%)	`bffN_softb`
Statistical uncertainty ($\sqrt{N_{\text{exp}}}$)	34
Total systematic	27
MC statistics	17.2
JES	11.7
W+jets normalization	11.1
W+jets modeling	9.7
JER	7.6
Lepton	4.9
Other modeling	3.7
$t\bar{t}$ normalization	3.7
$E_{\text{T}}^{\text{miss}}$ soft term	3.4
$t\bar{t}$ modeling	3.3

9.4 Results

The observed data in the SR is summarized in Table 9.11, together with the predicted background events. No significant excess is found in the SR. The observed p-value for the background-only hypothesis is $p_0 = 0.37$, which corresponds to 0.34σ. The distributions of the key variables with the SR selection is shown in Figure 9.11. Since no deviation from the SM prediction is found, exclusion limits are derived from the shape-fit SR. For the exclusion, the SR with soft b-tagging (`bffN_softb`) and another SR with the standard b-tagging [3] are simultaneously fitted. The `bffN_softb` is sensitive to the low $\Delta m(\tilde{t}_1, \tilde{\chi}_1^0)$ region, while the SR with the standard b-tagging has better sensitivity for $\Delta m(\tilde{t}_1, \tilde{\chi}_1^0) > 40$ GeV. Figure 9.12 shows the gain of soft b-tagging comparing the expected exclusion limits with the standard b-tagging only and the combination of the two b-taggers. For the $\Delta m(\tilde{t}_1, \tilde{\chi}_1^0) = 20$ GeV, the expected limit is improved from 460 GeV to 600 GeV for the $m_{\tilde{t}_1}$ by introducing the soft b-tagging.

In exclusion limits, other signal regions in reference [3] are also used for the 2-body and 3-body regions. Figure 9.13 shows the observed and expected exclusion limits at 95% CL in the $m_{\tilde{t}_1}$ versus $m_{\tilde{\chi}_1^0}$ plane, and Figure 9.14 shows the same limits with $\Delta m(\tilde{t}_1, \tilde{\chi}_1^0)$ on the vertical axis. In the four-body decay region ($\Delta m(\tilde{t}_1, \tilde{\chi}_1^0) < m_b + m_W$), the limit reaches 640 GeV in the stop mass, and the limit is lowered to $\Delta m(\tilde{t}_1, \tilde{\chi}_1^0) = 20$ GeV owing to the novel soft b-tagging technique.

Table 9.11: Post fit yields in the `bffN_softb` SRs. The "SR" is the single bin SR, while "SR1-5" are the multi-bin SRs for the exclusion.

	SR	SR1	SR2	SR3	SR4	SR5
Observed events	10	0	2	8	19	25
Fitted background events	8.7 ± 2.3	0.4 ± 0.3	1.8 ± 0.7	7.0 ± 1.7	19.4 ± 3.0	25.6 ± 3.4
$t\bar{t}$	2.2 ± 0.6	0.0 ± 0.0	0.3 ± 0.1	2.0 ± 0.5	4.1 ± 1.1	6.8 ± 1.7
W+jets	4.8 ± 2.1	0.2 ± 0.2	1.3 ± 0.7	3.6 ± 1.6	11.7 ± 2.6	14.9 ± 3.3
Multiboson	0.9 ± 0.3	0.03 ± 0.02	0.15 ± 0.06	0.8 ± 0.3	2.0 ± 0.7	1.9 ± 0.6
Others	0.80 ± 0.21	0.10 ± 0.08	0.07 ± 0.04	0.62 ± 0.15	1.01 ± 0.54	2.02 ± 1.06

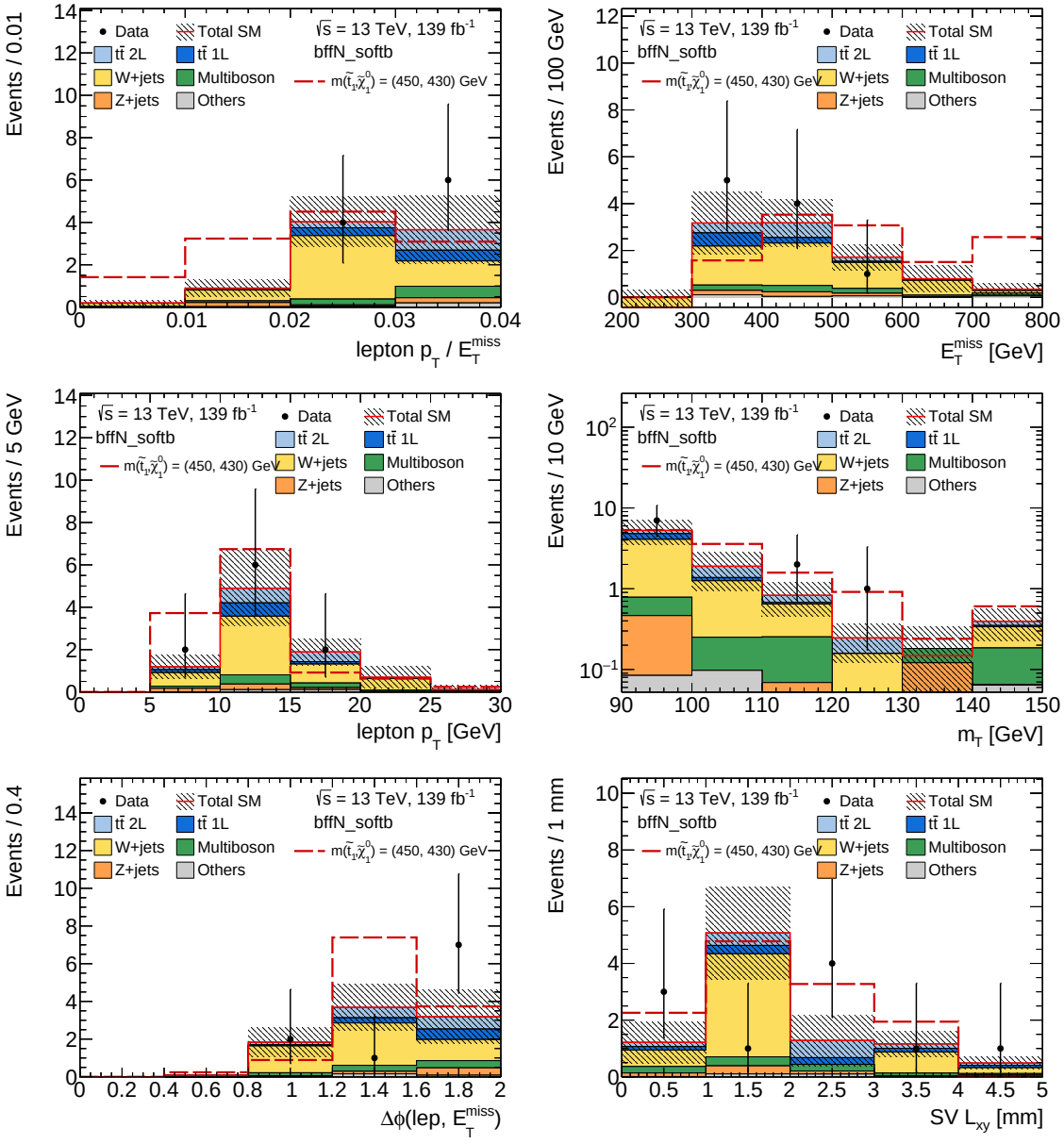

Figure 9.11: Distribution of the variables used to define the `bffN_softb` discovery SR with the SR selection: (top left) the $p_{\mathrm{T}}^{\ell}/E_{\mathrm{T}}^{\mathrm{miss}}$, (top right) $E_{\mathrm{T}}^{\mathrm{miss}}$, (middle left) lepton p_{T}, (middle right) m_{T}, (bottom left) $\Delta\phi(\vec{E}_{\mathrm{T}}^{\mathrm{miss}}, \ell)$, and (bottom right) soft b-tag SV L_{xy}. The NFs are applied to the $t\bar{t}$ and W+jets backgrounds. Statistical, theoretical, and experimental uncertainties are included. The last bin includes the overflow.

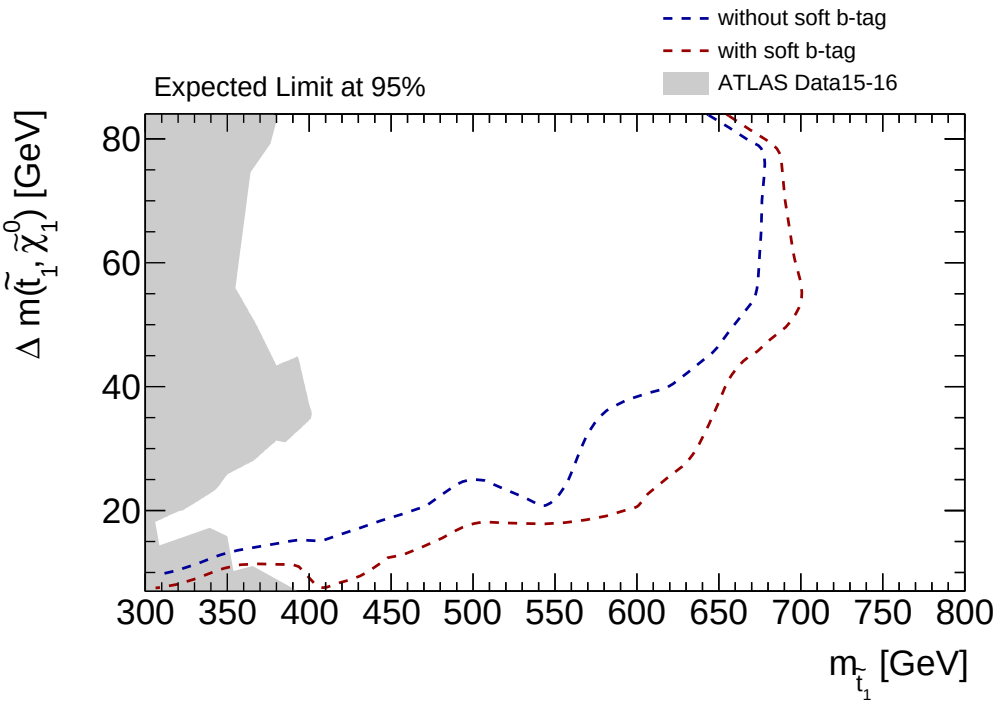

Figure 9.12: Expected exclusion limits at 95% CL in the plane of $m_{\tilde{t}_1}$ versus $\Delta m(\tilde{t}_1, \tilde{\chi}_1^0)$. The blue line shows the limit obtained from the signal region with the standard b-tagging. The red line shows the limit from the simultaneous exclusion fit using both soft b-tagging and standard b-tagging SRs. The gray region shows the previous ATLAS results with data collected in 2015–2016, which corresponds to 36 fb^{-1} [1, 143–145].

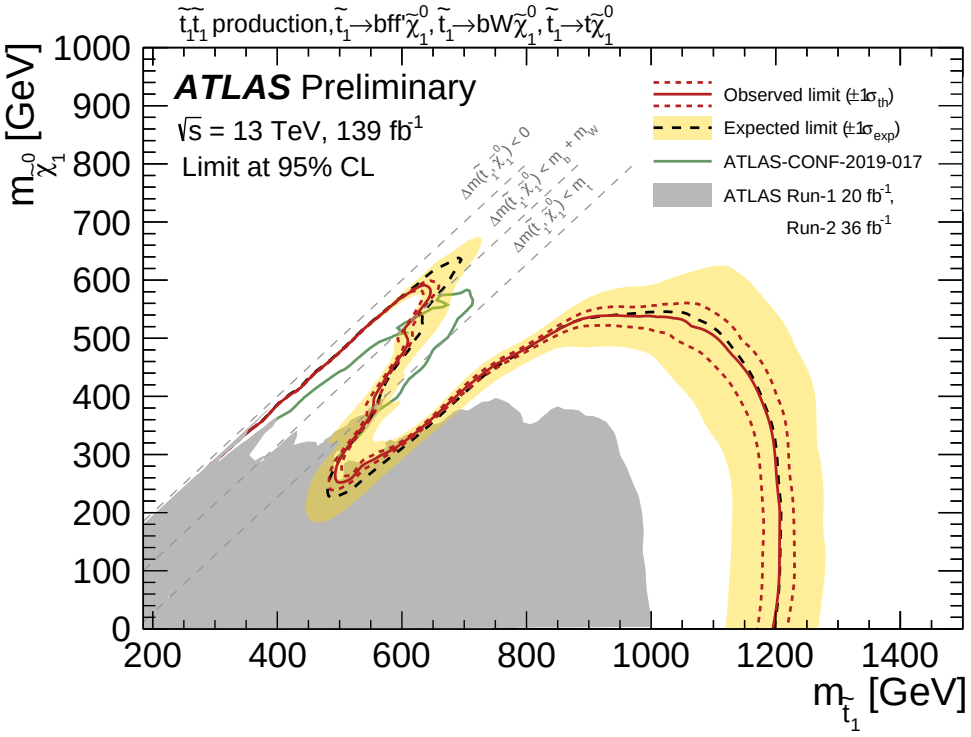

Figure 9.13: Expected (black dashed) and observed (red solid) limits at 95% CL in the plane of $m_{\tilde{t}_1}$ versus $m_{\tilde{\chi}_1^0}$. The yellow band displays the ± 1 σ variation of the expected limit, and the red dotted lines along the observed line show the uncertainty in the stop cross section. The gray dashed lines separate the $\tilde{t}_1$ decay modes: $t\tilde{\chi}_1^0$ (2-body), $bW\tilde{\chi}_1^0$ (3-body), and $bff'\tilde{\chi}_1^0$ (4-body). The gray region shows the previously excluded area from the ATLAS Run 1 and Run 2 with data15–data16 results [1,142–145]. The green line is the result from a dedicated 3-body analysis [170] with one lepton final states using 139 fb^{-1} data.

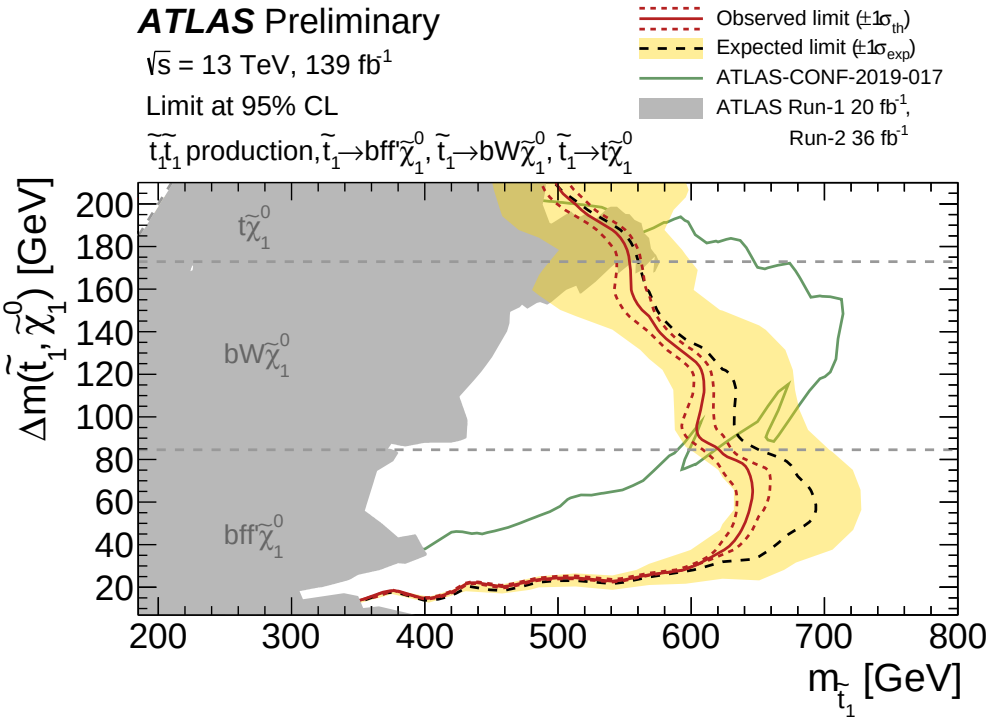

Figure 9.14: Expected (black dashed) and observed (red solid) limits at 95% CL in the plane of $m_{\tilde{t}_1}$ versus $\Delta m(\tilde{t}_1, \tilde{\chi}_1^0)$. The yellow band displays the ± 1 σ variation of the expected limit, and the red dotted lines along the observed line show the uncertainty in the stop cross section. The gray dashed lines separate the $\tilde{t}_1$ decay modes: $t\tilde{\chi}_1^0$ (2-body), $bW\tilde{\chi}_1^0$ (3-body), and $bff'\tilde{\chi}_1^0$ (4-body). The gray region shows the previously excluded area from the ATLAS Run 1 and Run 2 with data15–data16 results [1,142–145]. The green line is the result from a dedicated 3-body analysis [170] with one lepton final states using 139 fb^{-1} data.

Chapter 10

Discussion

10.1 Bino-Higgsino Mixed LSP Scenario

In Chapter 7 and Chapter 9, the results of the stop searches for large $\Delta m(\tilde{t}_1, \tilde{\chi}_1^0)$ and small $\Delta m(\tilde{t}_1, \tilde{\chi}_1^0)$ are presented, respectively. A dedicated higgsino-like LSP model was designed in the former search, while the simplified model is used for the latter. In the compressed region where only $\tilde{t}_1 \to b\tilde{\chi}_1^\pm$ decay is kinematically allowed, the final state particles are always $bff'\tilde{\chi}_1^0$, which do not depend on the components of the neutralino LSP. Hence, from the two searches, the higgsino-like LSP scenario has been excluded in a wide range of $\Delta m(\tilde{t}_1, \tilde{\chi}_1^0)$, considering all possible decay modes with various branching ratios.

The observed relic density of the DM indicates the cross section of the DM annihilation process. A large annihilation cross section results in small relic density of DM, and vice versa. From cosmological observations, the relic density[1] of the DM is estimated to be $\Omega h^2 \sim 0.1$ [171]. Figure 10.1 shows the LSP mass and the DM relic density of the possible SUSY models after the LHC Run 1 results [172]. In order to achieve $\Omega h^2 \sim 0.1$, scenarios of light higgsino LSP or wino LSP below 1 TeV are not possible for most cases. On the other hand, the pure bino LSP cannot be a good solution due to the small cross section of the bino-bino annihilation. However, the DM relic density of $\Omega h^2 \sim 0.1$ could be realized if the LSP is a mixed state of bino-higgsino or bino-wino. This is the so-called well-tempered neutralino scenario [173].

The result in Chapter 7 is interpreted into the bino-higgsino mixed LSP scenario. Here, we can use the results presented in Chapter 7 to set constraints to the bino-higgsino mixed LSP scenario. Signal grids are generated with a requirement of $0.10 < \Omega h^2 < 0.12$. The scanned parameters are M_1 and the third generation squark mass, with the fixed parameters of $M_2 = 2.0$ TeV and $M_3 = 1.8$ TeV. A parameter with a large $\tilde{t}_R - \tilde{t}_L$ mixing is chosen in the range of $700-1300$ GeV in order to be consistent with the mass of the Higgs boson. Since

[1] The relic density is expressed with the density parameter (Ω) and Hubble constant (h).

$\tilde{t}_L$ and $\tilde{b}_L$ have similar masses because they consists of a doublet of the third generation squarks, the sbottom direct production is also considered when $\tilde{t}_1 \sim \tilde{t}_L$. In this model, $\tilde{t}_1$ can decay into $t\tilde{\chi}_1^0$, $t\tilde{\chi}_2^0$, $t\tilde{\chi}_3^0$, and $b\tilde{\chi}_1^\pm$, and $\tilde{b}_1$ can decay into $b\tilde{\chi}_1^0$, $b\tilde{\chi}_2^0$, $b\tilde{\chi}_3^0$, and $t\tilde{\chi}_1^\pm$. The other SRs in reference [1] are also used to set the limits. Figure 10.2 shows the exclusion limits at 95% CL for the bino-higgsino well-tempered LSP scenario[2].

The observed exclusion contour is weaker than the expected one because of the small excess of the data in `bCsoft_med` SR, as shown in Table 7.11. In the right-handed stop scenario, no observed exclusion contour is obtained due to the small excess.

The exclusion limits shown in the higgsino-like LSP and simplified model in Figures 7.16 and 9.13 may give an impression that the stop is strongly excluded for $m_{\tilde{t}_1} < 800$ GeV. However, such conclusions strongly depend on models. As shown in Figure 10.2, a light stop or natural SUSY scenarios are still alive when the mass spectrum is more complicated. The searches for such complicated scenarios like the well-tempered neutralino are important and will be performed in future analyses of the data from the LHC.

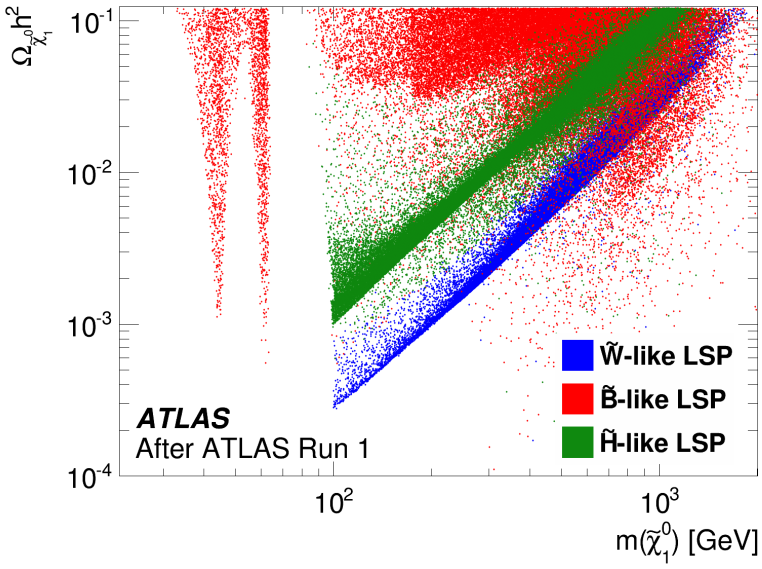

Figure 10.1: The DM relic density and LSP mass of possible models after the ATLAS Run1 results [172]. Wino-like, bino-like, and higgsino-like LSPs are plotted separately. The two triangle areas in $m_{\tilde{\chi}_1^0} < 100$ GeV correspond to the annihilation of the DM via s-channel of Z boson and the Higgs boson.

[2]The SR in this dissertation mainly contributes to $m_{\tilde{t}_1} < 700$ GeV in the right-handed stop scenario as shown in Appendix A.

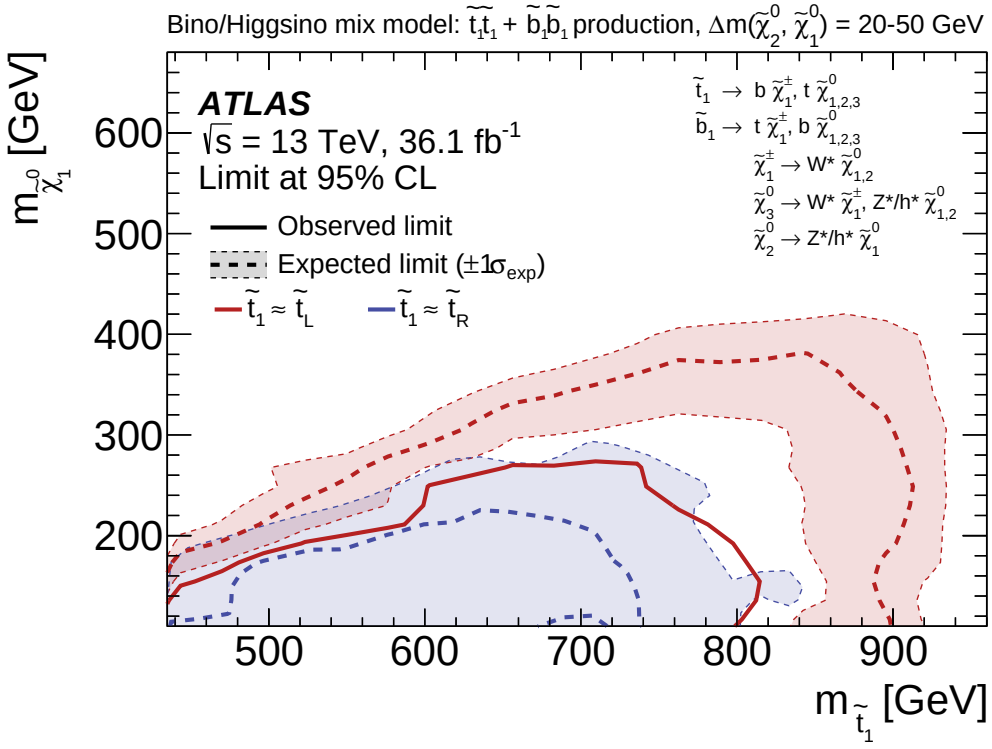

Figure 10.2: Observed (solid) and expected (dashed) exclusion limits at 95% CL for the bino-higgsino mixed model in the plane of $m_{\tilde{t}_1}$ versus $m_{\tilde{\chi}_1^0}$. Mostly right-handed $\tilde{t}_1$ (blue) and left-handed $\tilde{t}_1$ (red) are considered. The parameters, such as the masses and branching ratios, are determined by choosing the DM relic density that is consistent with the observed value. Decay modes and branching ratios of $\tilde{t}_1$ decays ($t\tilde{\chi}_1^0$, $t\tilde{\chi}_2^0$, $t\tilde{\chi}_3^0$, and $b\tilde{\chi}_1^{\pm}$) are determined at each signal point in the plane. The masses of $\tilde{\chi}_2^0$, $\tilde{\chi}_3^0$, $\tilde{\chi}_1^{\pm}$ depend on the signal point. In the left-handed $\tilde{t}_1$ scenario, the $\tilde{b}_1$ pair production is also included with possible $\tilde{b}_1$ decay modes of $b\tilde{\chi}_1^0$, $b\tilde{\chi}_2^0$, $b\tilde{\chi}_3^0$, and $t\tilde{\chi}_1^{\pm}$.

10.2 Comparison of Results with CMS Results

The analysis presented in Chapter 7 is the first stop search with the higgsino-like LSP where the three decay modes are considered. The simplified model used in the analysis for the small $\Delta m(\tilde{t}_1, \tilde{\chi}_1^0)$ presented in Chapter 9 is also used in the CMS stop searches. The latest results of searches for the stop four-body signature from CMS is based on the partial Run-2 data collected in 2015–2016, which corresponds to an integrated luminosity of 35.9 fb^{-1}. Figure 10.3 shows the expected and observed exclusion limits at 95% confidence level from the CMS analyses [156]. The results obtained from the one-lepton analysis with the multivariate analysis technique shown in light green excluded the stop masses up to 560 GeV. The best exclusion limit from the CMS is obtained from the combination of the all-hadronic and one-lepton analyses as shown in dark green, and stop masses up to 600 GeV

are excluded. Comparing the limit with the one presented in Chapter 9, it is concluded that the stringent limit is derived by the analysis in this dissertation.

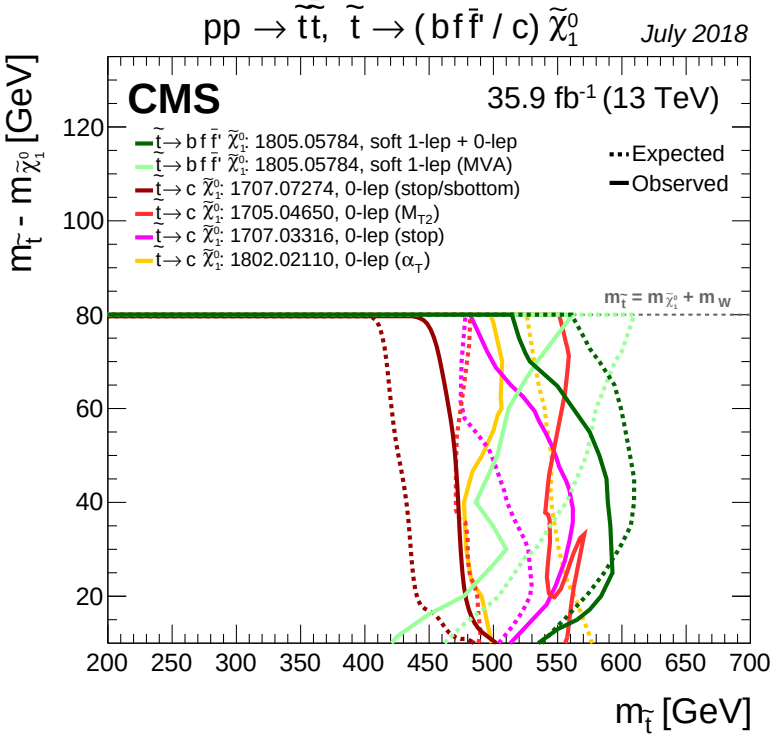

Figure 10.3: The latest observed and expected exclusion limits for the simplified model with the stop four-body decay from the CMS collaboration [174]. The results for the four-body signature are shown in dark green and light green [156]. The light green lines show the exclusion limits obtained from the search using one charged lepton. The dark green lines are the combined results obtained from the all-hadronic and one-lepton modes. The other lines show the $\tilde{t}_1 \to c\tilde{\chi}_1^0$ decay, which is not considered in this dissertation.

10.3 Fine-tuning

As discussed in Chapter 2, the Natural SUSY is the outcome of small fine-tuning. The degree of fine-tuning [56] is quantified as the maximum logarithmic derivative of the Higgs boson mass (m_h) with respect to the fundamental parameters p_i,

$$\Delta_{m_h} = \max_i \left| \frac{\partial \ln m_h^2}{\partial \ln p_i} \right|. \tag{10.1}$$

As the parameter p_i, the fundamental parameters at the messenger scale: μ, b, $m_{Q_3}^2$, m_{u3}^2, A_t, $m_{H_u}^2$, and $m_{H_d}^2$ are taken into account. The fine-tuning measure Δ_{m_h} represents how stable the Higgs boson mass is against the variation of these fundamental parameters. Figure 10.4

shows the fine-tuning Δ_{m_h} as a function of the stop mass and stop mixing parameter. In order to achieve the observed Higgs boson mass, the maximal mixing ($|X_t| \sim \sqrt{6} m_{\tilde{t}}$) gives the minimal fine-tuning.

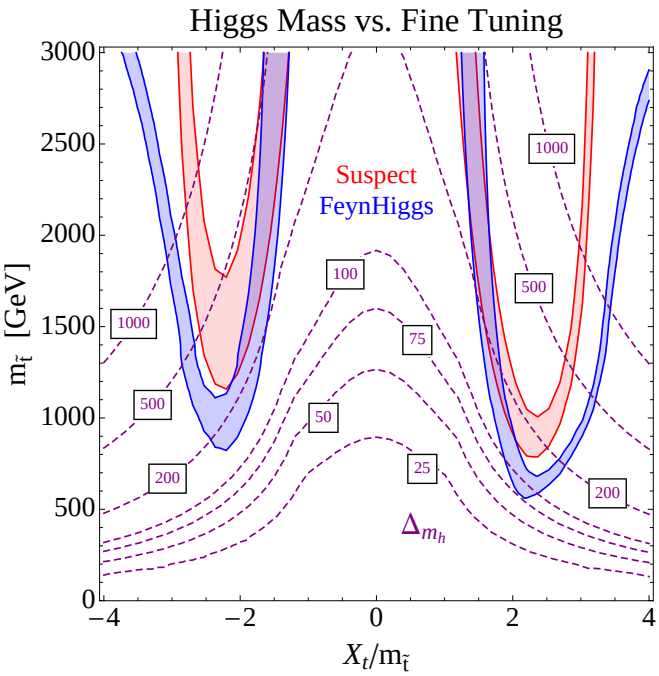

Figure 10.4: Contours of fine-tuning Δ_{m_h} with the stop mass $m_{\tilde{t}}$ and the stop mixing parameter X_t [56]. The dashed purple lines show the contours of fine-tuning. The red and blue bands correspond to the observed Higgs boson mass in the range of 124–126 GeV calculated with Suspect and FeynHiggs, respectively.

In this dissertation, the stop masses up to 800 (640) GeV are excluded for the large (small) $\Delta m(\tilde{t}_1, \tilde{\chi}_1^0)$ scenario. Assuming the maximal mixing with $X_t/m_{\tilde{t}} = \sqrt{6} \sim 2.45$, the stop exclusion limits correspond to the exclusion of $\Delta_{m_h} < 200$ (100) for the small (large) $\Delta m(\tilde{t}_1, \tilde{\chi}_1^0)$ scenario.

10.4 Comparison with Searches for the Direct Higgsino Production

This dissertation considers the light stop and light higgsinos, which are favored by the Natural SUSY. The search for the large $\Delta m(\tilde{t}_1, \tilde{\chi}_1^0)$ in Chapter 7 excluded the LSP masses up to 200 GeV, and the search for the small $\Delta m(\tilde{t}_1, \tilde{\chi}_1^0)$ in Chapter 9 excluded the LSP masses up to 580 GeV. Those searches for the stop decaying into the higgsino-like LSP set the limits for higher higgsino masses compared with the searches for the direct production

of higgsinos. Figure 10.5 shows the summary of the higgsino direct production searches. The mass splitting $\Delta m(\tilde{\chi}_1^{\pm}, \tilde{\chi}_1^0)$ higher than 1 GeV is covered by the search which exploits two soft leptons from the $\tilde{\chi}_2^0 \to \ell\ell\tilde{\chi}_1^0$ decay [175] (2L analysis), while the very small mass splitting $\Delta m(\tilde{t}_1, \tilde{\chi}_1^0) < 0.3$ GeV is searched by the disappearing track analysis [176]. The 2L analysis excluded the higgsinos up to 150 GeV, and the disappearing track analysis also excluded the higgsinos up to 150 GeV for the pure higgsino model. Comparing the direct production limits and the LSP mass limits obtained in this dissertation, the stop search results set limits for higher higgsino masses by exploiting the large cross sections of stop direct production and the distinctive signatures of the stop decays.

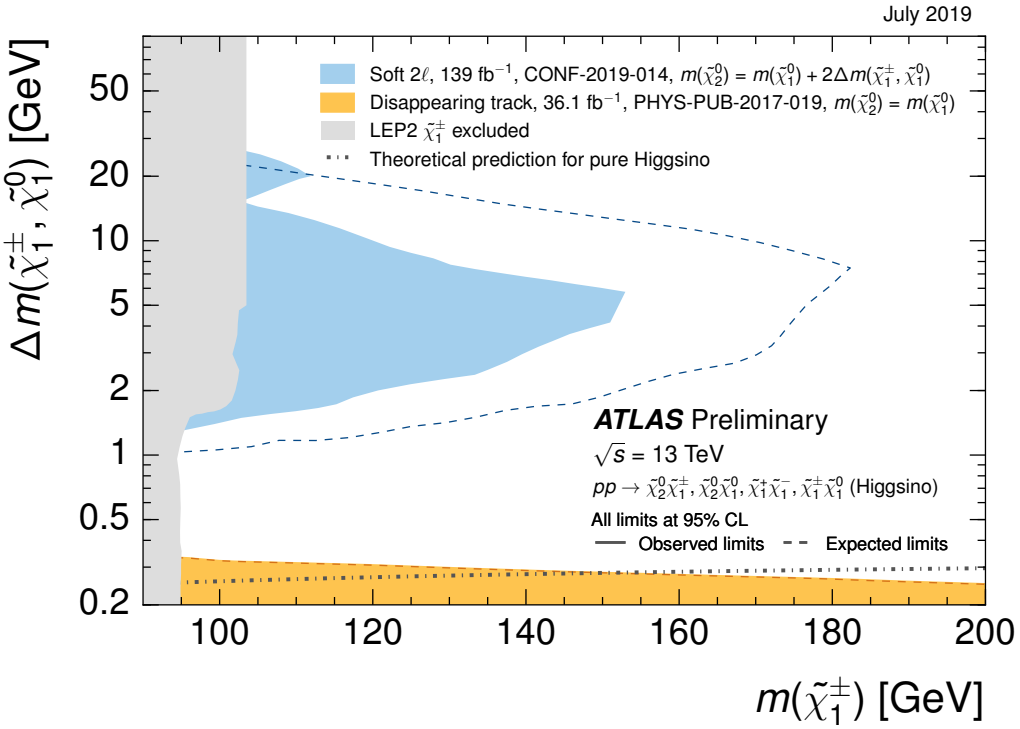

Figure 10.5: The excluded region obtained by the searches for the direct higgsino production [164]. The gray regions shows the exclusion of light charginos by LEP2 [177]. The search with two soft leptons [175] excluded the blue area and the disappearing track search [176] excluded the orange area below $\Delta m(\tilde{\chi}_1^{\pm}, \tilde{\chi}_1^0) < 0.3$ GeV.

The mass-splitting below 1 GeV but above the disappearing track coverage has not been covered by searches at the LHC. The 2L search loses the sensitivity due to the inefficiency of the very low-p_{T} lepton reconstruction. The disappearing track search loses the sensitivity due to the short flight length of the charginos. This uncovered region is expected to be searched in the future with new ideas such as a search with soft displaced tracks [178].

Chapter 11

Conclusion

This dissertation presents the searches for the stop direct production using the data collected with the ATLAS detector at the LHC, using pp collisions at a center of mass energy of $\sqrt{s} = 13$ TeV. Natural SUSY models suggest a light stop and higgsinos, and the stop mass below 1 TeV can be consistent with the mass of the observed Higgs boson in the case of the maximal mixing. Two searches are performed targeting large and small mass differences between the stop and LSP ($\Delta m(\tilde{t}_1, \tilde{\chi}_1^0)$).

The first search is performed for large $\Delta m(\tilde{t}_1, \tilde{\chi}_1^0)$ using data corresponding to an integrated luminosity of 36 fb^{-1} collected in 2015–2016, in which three decay modes are considered: $\tilde{t}_1 \to t\tilde{\chi}_1^0$, $t\tilde{\chi}_2^0$, and $b\tilde{\chi}_1^\pm$. The stop branching ratios depend on the MSSM parameters, hence the three scenarios: $\tilde{t}_1 \sim \tilde{t}_L$, $\tilde{t}_1 \sim \tilde{t}_R$, and large $\tan\beta$, are considered to cover wide phase space. The signature of $b\tilde{\chi}_1^\pm$ decay is characterized by a low p_{T} lepton produced from the $\tilde{\chi}_1^\pm$ decay, as well as large $E_{\mathrm{T}}^{\mathrm{miss}}$ from neutralinos. Since the traditional signal regions with a high p_{T} lepton is not sensitive to the $b\tilde{\chi}_1^\pm$ decay, a signal region is optimized for the $\tilde{t}_1 \to b\tilde{\chi}_1^\pm$ decay. The signal region is defined using the discriminating variables such as $p_{\mathrm{T}}^\ell / E_{\mathrm{T}}^{\mathrm{miss}}$, number of b-tagged jets, and am_{T2}. The SM background prediction is estimated by normalizing the main background processes ($t\bar{t}$, W+jets, and single top) in CRs. No significant excess over the SM prediction is observed, and the exclusion limits are derived. For $\Delta m(\tilde{\chi}_1^\pm, \tilde{\chi}_1^0) = 5$ GeV, the stop mass is excluded up to 800 GeV for the LSP mass of 150 GeV in all three scenarios. This is the first result for a realistic higgsino-like LSP model in which all decay modes are considered.

In the case of the small $\Delta m(\tilde{t}_1, \tilde{\chi}_1^0)$, the final state contains low p_{T} b-hadrons. Since the standard ATLAS b-tagging algorithm is not optimal for such low p_{T} hadrons, a new soft b-tagging algorithm has been developed. The algorithm utilizes the secondary vertex reconstruction. Due to a large number of tracks in an event, the track selection is essential in this new algorithm. Dedicated requirements for the low p_{T} b-hadrons are used, such as the loose requirements on the impact parameter or overlap removal between tracks and high

p_{T} jets. The fake rate is reduced by removing the tracks overlapping with high p_{T} jets. The efficiency of the soft b-tagging is about 10 times higher than that of the standard b-tagging at the same fake rate for b-hadron p_{T} between 5 and 15 GeV. The track-based reweighting method is developed and performed to correct the imperfect MC modeling.

Since no significant excess is found in large $\Delta m(\tilde{t}_1, \tilde{\chi}_1^0)$, the second search is performed targeting the small $\Delta m(\tilde{t}_1, \tilde{\chi}_1^0)$ with the data collected in 2015–2018, which corresponds to an integrated luminosity of 139 fb^{-1}. The stop four-body decay $\tilde{t}_1 \to bff'\tilde{\chi}_1^0$ is considered as a benchmark signal in the search. In addition to the small $p_{\mathrm{T}}^{\ell}/E_{\mathrm{T}}^{\mathrm{miss}}$ requirement, the soft b-tagging is used to strongly suppress the W+jets and $t\bar{t}$ backgrounds. The soft b-tagging expands the search sensitivity for the small $\Delta m(\tilde{\chi}_1^{\pm}, \tilde{\chi}_1^0)$ region, in particular $\Delta m(\tilde{\chi}_1^{\pm}, \tilde{\chi}_1^0)$ below 40 GeV. No excess is found in this search either, and the four-body decay is excluded up to the stop mass of 640 GeV at $m_{\tilde{\chi}_1^0} = 580$ GeV.

Unfortunately, no sign of natural SUSY has been found in the searches. However, the interpretation of the results also shows that there are still uncovered regions of the phase space to be searched at the LHC, such as mixed LSP scenarios.

Appendix A

Contributions of Signal Regions to Exclusion Limits

The exclusion limits from the results in the analysis targeting large $\Delta m(\tilde{t}_1, \tilde{\chi}_1^0)$ are derived using the `bCsoft_med` SR described in Chapter 7 and other SRs in Reference [1]. Figure A.1 and A.1 show the SRs used for the exclusion contours at each signal mass point. At each mass point, the SR that has the best expected CLs value is selected and used to draw the exclusion limits. Figure A.3 shows the same plot for the bino-higgsino mixed scenario discussed in Chapter 10.

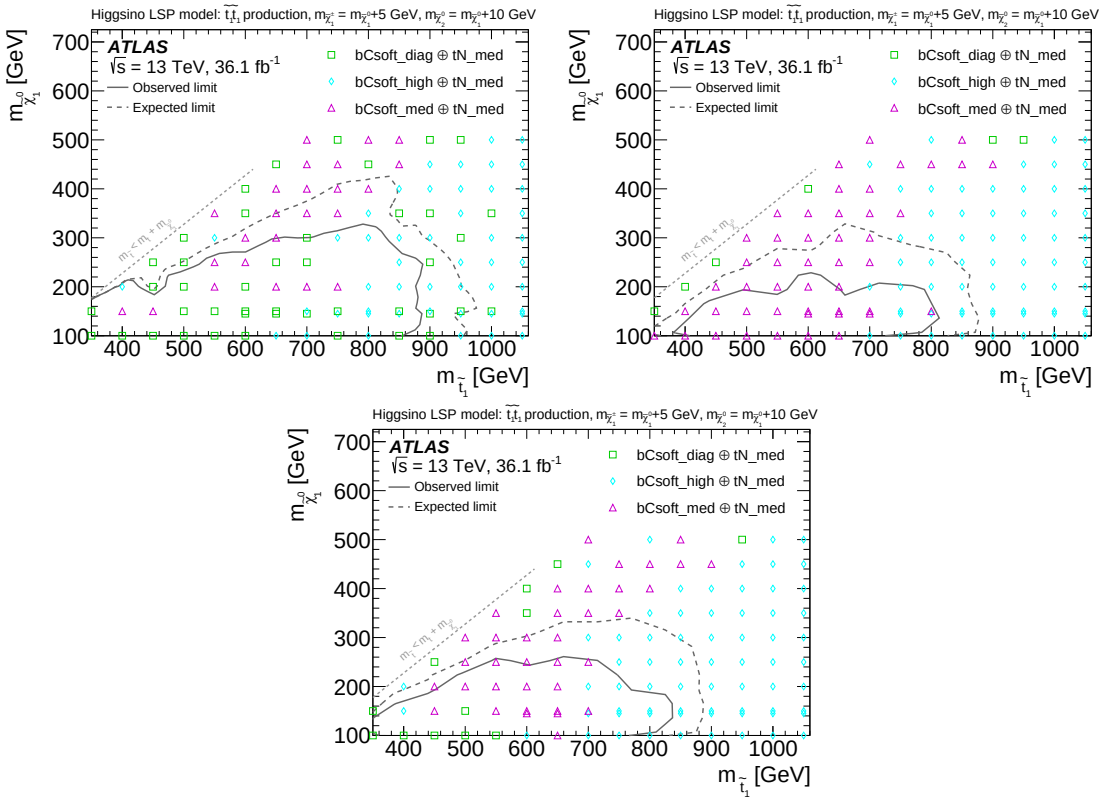

Figure A.1: The SR with the best CLs value for the higgsino-like LSP scenario in the plane of $m_{\tilde{t}_1}$ versus $m_{\tilde{\chi}_1^0}$: (top left) $\tilde{t}_1 \sim \tilde{t}_L$, (top right) $\tilde{t}_1 \sim \tilde{t}_R$, and (bottom) large $\tan\beta$ scenarios.

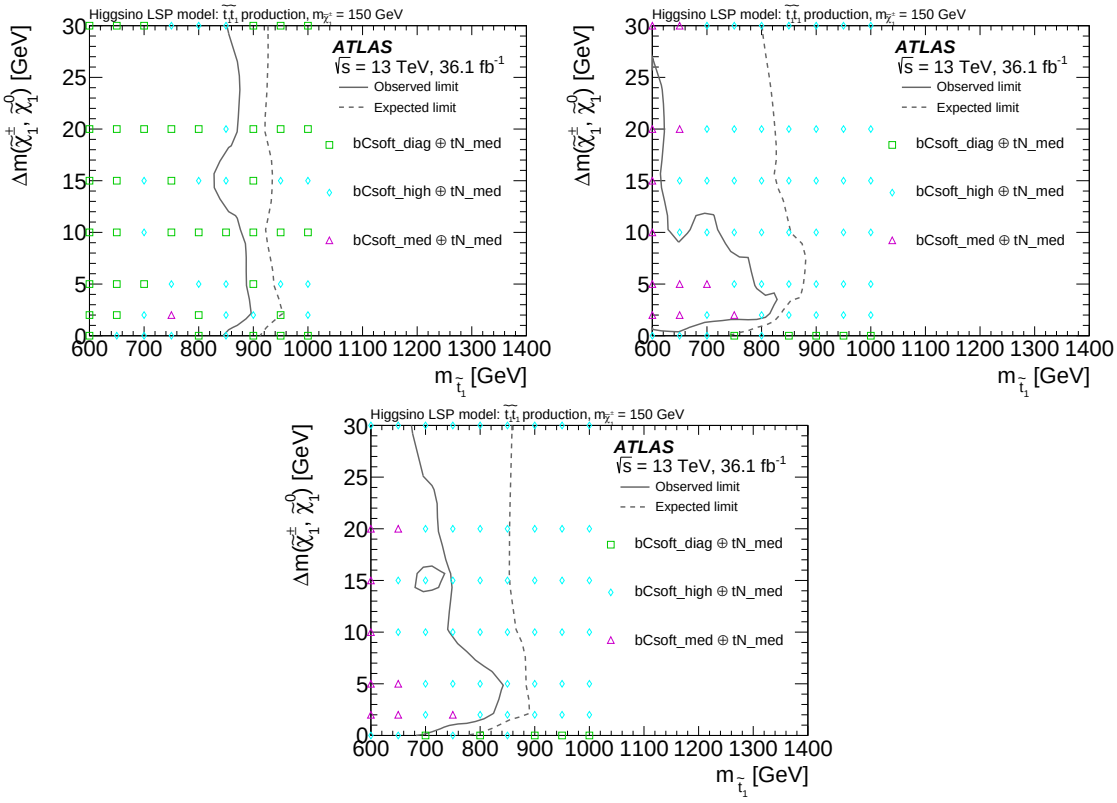

Figure A.2: The SR with the best CLs value for the higgsino-like LSP scenario in the plane of $m_{\tilde{t}_1}$ versus $\Delta m(\tilde{\chi}_1^\pm, \tilde{\chi}_1^0)$: (top left) $\tilde{t}_1 \sim \tilde{t}_L$, (top right) $\tilde{t}_1 \sim \tilde{t}_R$, and (bottom) large $\tan\beta$ scenarios.

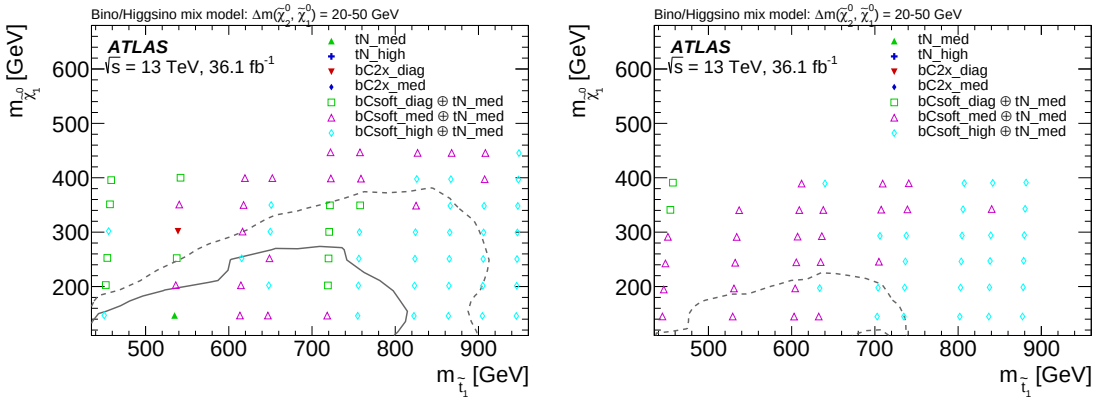

Figure A.3: The SR with the best CLs value for the bino-higgsino mixed scenario in the plane of $m_{\tilde{t}_1}$ versus $m_{\tilde{\chi}_1^0}$: (left) $\tilde{t}_1 \sim \tilde{t}_L$, (right) $\tilde{t}_1 \sim \tilde{t}_R$.

References

[1] ATLAS Collaboration, *Search for top-squark pair production in final states with one lepton, jets, and missing transverse momentum using* $36\,fb^{-1}$ *of* $\sqrt{s} = 13\,TeV$ *pp collision data with the ATLAS detector*, JHEP **06** (2018) 108, arXiv:1711.11520 [hep-ex].

[2] ATLAS Collaboration, *Soft b-hadron tagging for compressed SUSY scenarios*, ATLAS-CONF-2019-027, 2019, https://cds.cern.ch/record/2682131.

[3] ATLAS Collaboration, *Search for new phenomena with top quark pairs in final states with one lepton, jets, and missing transverse momentum in pp collisions at* $\sqrt{s} = 13$ *TeV with the ATLAS detector*, ATLAS-CONF-2020-003, 2020, https://cds.cern.ch/record/2711489.

[4] T. Yamazaki, *Aging studies on Micromegas detectors for the LHC-ATLAS upgrade*, https://www.icepp.s.u-tokyo.ac.jp/download/master/m2015_yamazaki.pdf, 2016.

[5] S. L. Glashow, *Partial-symmetries of weak interactions*, Nuclear Physics **22** (1961) 579 – 588.

[6] A. Salam, *Weak and electromagnetic interactions, Elementary Particle Theory: Relativistic Groups and Analyticity*, in *Proceedings of the Eighth Nobel Symposium, Almquist & Wiksell*, vol. 367. 1968.

[7] S. Weinberg, *A Model of Leptons*, Phys. Rev. Lett. **19** (1967) 1264–1266.

[8] G. 't Hooft and M. Veltman, *Regularization and renormalization of gauge fields*, Nuclear Physics B **44** (1972) 189 – 213.

[9] ATLAS Collaboration, *Observation of a new particle in the search for the Standard Model Higgs boson with the ATLAS detector at the LHC*, Phys. Lett. B **716** (2012) 1, arXiv:1207.7214 [hep-ex].

[10] CMS Collaboration, *Observation of a new boson at a mass of 125 GeV with the CMS experiment at the LHC*, Phys. Lett. B **716** (2012) 30, arXiv:1207.7235 [hep-ex].

[11] G. Hinshaw, D. Larson, E. Komatsu, D. N. Spergel, C. Bennett, J. Dunkley, M. Nolta, M. Halpern, R. Hill, N. Odegard, et al., *Nine-year Wilkinson Microwave Anisotropy Probe (WMAP) observations: cosmological parameter results*, The Astrophysical Journal Supplement Series **208** (2013) 19.

[12] Planck Collaboration, Y. Akrami et al., *Planck 2018 results. I. Overview and the cosmological legacy of Planck*, arXiv:1807.06205 [astro-ph.CO].

[13] V. Trimble, *Existence and Nature of Dark Matter in the Universe*, Annual Review of Astronomy and Astrophysics **25** (1987) 425–472.

[14] G. Bertoni et al., *Particle dark matter: evidence, candidates and constraints FERMILAB-Pub-04/047-A*, Physics Reports **405** (2005) 279 – 390.

[15] J. L. Feng, *Dark matter candidates from particle physics and methods of detection*, Annual Review of Astronomy and Astrophysics **48** (2010) 495–545.

[16] Y. Fukuda, T. Hayakawa, E. Ichihara, K. Inoue, K. Ishihara, H. Ishino, Y. Itow, T. Kajita, J. Kameda, S. Kasuga, et al., *Evidence for oscillation of atmospheric neutrinos*, Physical Review Letters **81** (1998) 1562.

[17] Q. R. Ahmad, R. Allen, T. Andersen, J. Anglin, G. Bühler, J. Barton, E. Beier, M. Bercovitch, J. Bigu, S. Biller, et al., *Measurement of the Rate of* $\nu_e + d \rightarrow p + p + e^-$ *Interactions Produced by* ^{8}B *Solar Neutrinos at the Sudbury Neutrino Observatory*, Physical Review Letters **87** (2001) 071301.

[18] Q. R. Ahmad, R. Allen, T. Andersen, J. Anglin, J. Barton, E. Beier, M. Bercovitch, J. Bigu, S. Biller, R. Black, et al., *Direct evidence for neutrino flavor transformation from neutral-current interactions in the Sudbury Neutrino Observatory*, Physical review letters **89** (2002) 011301.

[19] Y. Golfand and E. Likhtman, *Extension of the Algebra of Poincare Group Generators and Violation of P Invariance*, JETP Lett. **13** (1971) 323.

[20] D. Volkov and V. Akulov, *Is the neutrino a goldstone particle?*, Phys. Lett. B **46** (1973) 109.

[21] J. Wess and B. Zumino, *Supergauge transformations in four dimensions*, Nucl. Phys. B **70** (1974) 39.

[22] J. Wess and B. Zumino, *Supergauge invariant extension of quantum electrodynamics*, Nucl. Phys. B **78** (1974) 1.

[23] S. Ferrara and B. Zumino, *Supergauge invariant Yang-Mills theories*, Nucl. Phys. B **79** (1974) 413.

[24] A. Salam and J. Strathdee, *Super-symmetry and non-Abelian gauges*, Phys. Lett. B **51** (1974) 353.

[25] S. P. Martin, *A Supersymmetry Primer*, Adv. Ser. Direct. High Energy Phys. **18** (1998) 1, `arXiv:hep-ph/9709356`.

[26] N. Sakai, *Naturalness in supersymmetric GUTS*, Z. Phys. C **11** (1981) 153.

[27] S. Dimopoulos, S. Raby, and F. Wilczek, *Supersymmetry and the scale of unification*, Phys. Rev. D **24** (1981) 1681.

[28] L. E. Ibáñez and G. G. Ross, *Low-energy predictions in supersymmetric grand unified theories*, Phys. Lett. B **105** (1981) 439.

[29] S. Dimopoulos and H. Georgi, *Softly broken supersymmetry and SU(5)*, Nucl. Phys. B **193** (1981) 150.

[30] R. Barbieri and G. Giudice, *Upper bounds on supersymmetric particle masses*, Nucl. Phys. B **306** (1988) 63.

[31] B. de Carlos and J. Casas, *One-loop analysis of the electroweak breaking in supersymmetric models and the fine-tuning problem*, Phys. Lett. B **309** (1993) 320, `arXiv:hep-ph/9303291`.

[32] K. Inoue, A. Kakuto, H. Komatsu, and S. Takeshita, *Aspects of Grand Unified Models with Softly Broken Supersymmetry*, Prog. Theor. Phys. **68** (1982) 927.

[33] J. R. Ellis and S. Rudaz, *Search for supersymmetry in toponium decays*, Phys. Lett. B **128** (1983) 248.

[34] J. Alwall, M.-P. Le, M. Lisanti, and J. G. Wacker, *Searching for directly decaying gluinos at the Tevatron*, Phys. Lett. B **666** (2008) 34, `arXiv:0803.0019 [hep-ph]`.

[35] J. Alwall, P. Schuster, and N. Toro, *Simplified models for a first characterization of new physics at the LHC*, Phys. Rev. D **79** (2009) 075020, `arXiv:0810.3921 [hep-ph]`.

[36] D. Alves et al., *Simplified models for LHC new physics searches*, J. Phys. G **39** (2012) 105005, arXiv:1105.2838 [hep-ph].

[37] Particle Data Group Collaboration, P. D. Group, *Review of Particle Physics*, Phys. Rev. D **98** (2018) 030001.

[38] E. Corbelli and P. Salucci, *The extended rotation curve and the dark matter halo of M33*, Monthly Notices of the Royal Astronomical Society **311** (2000) 441–447.

[39] *NASA, Bullet Cluster 1E 0657-56*, https://apod.nasa.gov/apod/image/1701/bulletcluster_comp_2048.jpg.

[40] P. Fayet, *Supersymmetry and Weak, Electromagnetic and Strong Interactions*, Phys. Lett. B **64** (1976) 159.

[41] P. Fayet, *Spontaneously Broken Supersymmetric Theories of Weak, Electromagnetic and Strong Interactions*, Phys. Lett. B **69** (1977) 489.

[42] P. Fayet, *Supergauge Invariant Extension of the Higgs Mechanism and a Model for the Electron and Its Neutrino*, Nucl. Phys. B **90** (1975) 104.

[43] G. R. Farrar and P. Fayet, *Phenomenology of the production, decay, and detection of new hadronic states associated with supersymmetry*, Phys. Lett. B **76** (1978) 575.

[44] A. H. Chamseddine, R. L. Arnowitt, and P. Nath, *Locally Supersymmetric Grand Unification*, Phys. Rev. Lett. **49** (1982) 970.

[45] R. Barbieri, S. Ferrara, and C. A. Savoy, *Gauge Models with Spontaneously Broken Local Supersymmetry*, Phys. Lett. B **119** (1982) 343.

[46] G. L. Kane, C. F. Kolda, L. Roszkowski, and J. D. Wells, *Study of constrained minimal supersymmetry*, Phys. Rev. D **49** (1994) 6173, arXiv:hep-ph/9312272.

[47] M. Dine and W. Fischler, *A Phenomenological Model of Particle Physics Based on Supersymmetry*, Phys. Lett. B **110** (1982) 227.

[48] L. Alvarez-Gaume, M. Claudson, and M. B. Wise, *Low-Energy Supersymmetry*, Nucl. Phys. B **207** (1982) 96.

[49] C. R. Nappi and B. A. Ovrut, *Supersymmetric Extension of the SU(3) x SU(2) x U(1) Model*, Phys. Lett. B **113** (1982) 175.

[50] L. Randall and R. Sundrum, *Out of this world supersymmetry breaking*, Nucl. Phys. **B557** (1999) 79–118, arXiv:hep-th/9810155 [hep-th].

[51] G. F. Giudice, M. A. Luty, H. Murayama, and R. Rattazzi, *Gaugino mass without singlets*, JHEP **12** (1998) 027, arXiv:hep-ph/9810442 [hep-ph].

[52] M. Papucci, J. T. Ruderman, and A. Weiler, *Natural SUSY Endures*, JHEP **09** (2012) 035, arXiv:1110.6926 [hep-ph].

[53] R. Kitano and Y. Nomura, *Supersymmetry, naturalness, and signatures at the LHC*, Phys. Rev. **D73** (2006) 095004, arXiv:hep-ph/0602096 [hep-ph].

[54] A. Djouadi, J.-L. Kneur, and G. Moultaka, *SuSpect: A Fortran code for the supersymmetric and Higgs particle spectrum in the MSSM*, Comput. Phys. Commun. **176** (2007) 426–455, arXiv:hep-ph/0211331 [hep-ph].

[55] S. Heinemeyer, W. Hollik, and G. Weiglein, *FeynHiggs: A Program for the calculation of the masses of the neutral CP even Higgs bosons in the MSSM*, Comput. Phys. Commun. **124** (2000) 76–89, arXiv:hep-ph/9812320 [hep-ph].

[56] L. J. Hall, D. Pinner, and J. T. Ruderman, *A Natural SUSY Higgs Near 126 GeV*, JHEP **04** (2012) 131, arXiv:1112.2703 [hep-ph].

[57] F. Marcastel, *CERN's Accelerator Complex. La chaîne des accélérateurs du CERN*, https://cds.cern.ch/record/1621583, General Photo.

[58] ATLAS Collaboration, *The ATLAS Experiment at the CERN Large Hadron Collider*, JINST **3** (2008) S08003.

[59] The ATLAS TRT collaboration, *The ATLAS Transition Radiation Tracker (TRT) proportional drift tube: design and performance*, Journal of Instrumentation **3** (2008) P02013–P02013.

[60] ATLAS Collaboration, *ATLAS Muon Spectrometer: Technical Design Report*, Atlas-tdr-10, 1997, https://cds.cern.ch/record/331068.

[61] G. Avoni et al., *The new LUCID-2 detector for luminosity measurement and monitoring in ATLAS*, JINST **13** (2018) P07017.

[62] ATLAS Collaboration, *Performance of the ATLAS trigger system in 2015*, Eur. Phys. J. C **77** (2017) 317, arXiv:1611.09661 [hep-ex].

[63] ATLAS Collaboration, *Luminosity determination in pp collisions at* $\sqrt{s} = 13$ *TeV using the ATLAS detector at the LHC*, ATLAS-CONF-2019-021, 2019, https://cds.cern.ch/record/2677054.

[64] S. van der Meer, *Calibration of the effective beam height in the ISR*, Tech. Rep. CERN-ISR-PO-68-31. ISR-PO-68-31, CERN, Geneva, 1968. https://cds.cern.ch/record/296752.

[65] P. Grafström and W. Kozanecki, *Luminosity determination at proton colliders*, Prog. Part. Nucl. Phys. **81** (2015) 97–148.

[66] C. Barschel, *Precision luminosity measurement at LHCb with beam-gas imaging*, 2014. https://cds.cern.ch/record/1693671.

[67] A. Buckley et al., *General-purpose event generators for LHC physics*, Phys. Rept. **504** (2011) 145–233, arXiv:1101.2599 [hep-ph].

[68] NNPDF Collaboration, R. D. Ball et al., *Parton distributions from high-precision collider data*, Eur. Phys. J. **C77** (2017) 663, arXiv:1706.00428 [hep-ph].

[69] T. Gleisberg, S. Hoeche, F. Krauss, M. Schonherr, S. Schumann, F. Siegert, and J. Winter, *Event generation with SHERPA 1.1*, JHEP **02** (2009) 007, arXiv:0811.4622 [hep-ph].

[70] T. Sjöstrand, S. Mrenna, and P. Z. Skands, *PYTHIA 6.4 Physics and Manual*, JHEP **05** (2006) 026, arXiv:hep-ph/0603175.

[71] T. Sjöstrand, S. Mrenna, and P. Z. Skands, *A Brief Introduction to PYTHIA 8.1*, Comput. Phys. Commun. **178** (2008) 852, arXiv:0710.3820 [hep-ph].

[72] S. Catani, L. Cieri, G. Ferrera, D. de Florian, and M. Grazzini, *Vector boson production at hadron colliders: a fully exclusive QCD calculation at NNLO*, Phys. Rev. Lett. **103** (2009) 082001, arXiv:0903.2120 [hep-ph].

[73] S. Schumann and F. Krauss, *A Parton shower algorithm based on Catani-Seymour dipole factorisation*, JHEP **03** (2008) 038, arXiv:0709.1027 [hep-ph].

[74] T. Gleisberg and S. Höche, *Comix, a new matrix element generator*, JHEP **12** (2008) 039, arXiv:0808.3674 [hep-ph].

[75] F. Cascioli, P. Maierhofer, and S. Pozzorini, *Scattering Amplitudes with Open Loops*, Phys. Rev. Lett. **108** (2012) 111601, arXiv:1111.5206 [hep-ph].

[76] S. Höche, F. Krauss, M. Schönherr, and F. Siegert, *QCD matrix elements + parton showers: The NLO case*, JHEP **04** (2013) 027, arXiv:1207.5030 [hep-ph].

[77] P. Artoisenet, R. Frederix, O. Mattelaer, and R. Rietkerk, *Automatic spin-entangled decays of heavy resonances in Monte Carlo simulations*, JHEP **03** (2013) 015, arXiv:1212.3460 [hep-ph].

[78] P. Z. Skands, *Tuning Monte Carlo Generators: The Perugia Tunes*, Phys. Rev. D **82** (2010) 074018, arXiv:1005.3457 [hep-ph].

[79] ATLAS Collaboration, *ATLAS Pythia 8 tunes to 7 TeV data*, ATL-PHYS-PUB-2014-021, 2014, https://cds.cern.ch/record/1966419.

[80] GEANT4 Collaboration, S. Agostinelli et al., *GEANT4: A Simulation toolkit*, Nucl. Instrum. Meth. A **506** (2003) 250.

[81] ATLAS Collaboration, *The ATLAS Simulation Infrastructure*, Eur. Phys. J. C **70** (2010) 823, arXiv:1005.4568 [physics.ins-det].

[82] S. Alioli, P. Nason, C. Oleari, and E. Re, *A general framework for implementing NLO calculations in shower Monte Carlo programs: the POWHEG BOX*, JHEP **06** (2010) 043, arXiv:1002.2581 [hep-ph].

[83] H.-L. Lai, M. Guzzi, J. Huston, Z. Li, P. M. Nadolsky, J. Pumplin, and C. P. Yuan, *New parton distributions for collider physics*, Phys. Rev. D **82** (2010) 074024, arXiv:1007.2241 [hep-ph].

[84] M. Czakon, P. Fiedler, and A. Mitov, *Total Top-Quark Pair-Production Cross Section at Hadron Colliders Through $O(\alpha_S^4)$*, Phys. Rev. Lett. **110** (2013) 252004, arXiv:1303.6254 [hep-ph].

[85] M. Czakon and A. Mitov, *NNLO corrections to top pair production at hadron colliders: the quark-gluon reaction*, JHEP **01** (2013) 080, arXiv:1210.6832 [hep-ph].

[86] M. Czakon and A. Mitov, *NNLO corrections to top-pair production at hadron colliders: the all-fermionic scattering channels*, JHEP **12** (2012) 054, arXiv:1207.0236 [hep-ph].

[87] P. Bärnreuther, M. Czakon, and A. Mitov, *Percent Level Precision Physics at the Tevatron: First Genuine NNLO QCD Corrections to $q\bar{q} \to t\bar{t} + X$*, Phys. Rev. Lett. **109** (2012) 132001, arXiv:1204.5201 [hep-ph].

[88] M. Cacciari, M. Czakon, M. Mangano, A. Mitov, and P. Nason, *Top-pair production at hadron colliders with next-to-next-to-leading logarithmic soft-gluon resummation*, Phys. Lett. B **710** (2012) 612, arXiv:1111.5869 [hep-ph].

[89] M. Czakon and A. Mitov, *Top++: A Program for the Calculation of the Top-Pair Cross-Section at Hadron Colliders*, Comput. Phys. Commun. **185** (2014) 2930, arXiv:1112.5675 [hep-ph].

[90] N. Kidonakis, *Next-to-next-to-leading-order collinear and soft gluon corrections for t-channel single top quark production*, Phys. Rev. D **83** (2011) 091503, arXiv:1103.2792 [hep-ph].

[91] N. Kidonakis, *Two-loop soft anomalous dimensions for single top quark associated production with a W- or H-*, Phys. Rev. D **82** (2010) 054018, arXiv:1005.4451 [hep-ph].

[92] N. Kidonakis, *NNLL resummation for s-channel single top quark production*, Phys. Rev. D **81** (2010) 054028, arXiv:1001.5034 [hep-ph].

[93] NNPDF Collaboration, R. D. Ball et al., *Parton distributions for the LHC Run II*, JHEP **04** (2015) 040, arXiv:1410.8849 [hep-ph].

[94] R. D. Ball et al., *Parton distributions with LHC data*, Nucl. Phys. B **867** (2013) 244, arXiv:1207.1303 [hep-ph].

[95] C. Borschensky, M. Krämer, A. Kulesza, M. Mangano, S. Padhi, T. Plehn, and X. Portell, *Squark and gluino production cross sections in pp collisions at* $\sqrt{s} = 13, 14, 33$ *and* 100 *TeV*, Eur. Phys. J. C **74** (2014) 3174, arXiv:1407.5066 [hep-ph].

[96] M. Beneke, M. Czakon, P. Falgari, A. Mitov, and C. Schwinn, *Threshold expansion of the* $gg(q\bar{q}) \to Q\bar{Q} + X$ *cross section at* $\mathcal{O}(\alpha_s^4)$, Phys. Lett. B **690** (2010) 483, arXiv:0911.5166 [hep-ph].

[97] W. Beenakker, C. Borschensky, M. Krämer, A. Kulesza, and E. Laenen, *NNLL-fast: predictions for coloured supersymmetric particle production at the LHC with threshold and Coulomb resummation*, JHEP **12** (2016) 133, arXiv:1607.07741 [hep-ph].

[98] ATLAS Collaboration, *Performance of the ATLAS track reconstruction algorithms in dense environments in LHC Run 2*, Eur. Phys. J. C **77** (2017) 673, arXiv:1704.07983 [hep-ex].

[99] R. E. Kalman, *A new approach to linear filtering and prediction problems*, 1960.

[100] R. Frühwirth, *Application of Kalman filtering to track and vertex fitting*, Nuclear Instruments and Methods in Physics Research Section A: Accelerators, Spectrometers, Detectors and Associated Equipment **262** (1987) 444–450.

[101] ATLAS Collaboration, *Reconstruction of primary vertices at the ATLAS experiment in Run 1 proton–proton collisions at the LHC*, Eur. Phys. J. C **77** (2017) 332, arXiv:1611.10235 [hep-ex].

[102] ATLAS Collaboration, *Vertex Reconstruction Performance of the ATLAS Detector at* $\sqrt{s} = 13$ *TeV*, ATL-PHYS-PUB-2015-026, 2015, https://cds.cern.ch/record/2037717.

[103] W. Waltenberger, R. Frühwirth, and P. Vanlaer, *Adaptive vertex fitting*, Journal of Physics G: Nuclear and Particle Physics **34** (2007) N343–N356, https://doi.org/10.1088%2F0954-3899%2F34%2F12%2Fn01.

[104] ATLAS Collaboration, *Topological cell clustering in the ATLAS calorimeters and its performance in LHC Run 1*, Eur. Phys. J. C **77** (2017) 490, arXiv:1603.02934 [hep-ex].

[105] ATLAS Collaboration, *Jet energy measurement with the ATLAS detector in proton–proton collisions at* $\sqrt{s} = 7$ *TeV*, Eur. Phys. J. C **73** (2013) 2304, arXiv:1112.6426 [hep-ex].

[106] M. Cacciari, G. P. Salam, and G. Soyez, *The anti-k_t jet clustering algorithm*, JHEP **04** (2008) 063, arXiv:0802.1189 [hep-ph].

[107] M. Cacciari, G. P. Salam, and G. Soyez, *FastJet User Manual*, Eur. Phys. J. C **72** (2012) 1896, arXiv:1111.6097 [hep-ph].

[108] ATLAS Collaboration, *Jet energy scale measurements and their systematic uncertainties in proton–proton collisions at* $\sqrt{s} = 13$ *TeV with the ATLAS detector*, Phys. Rev. D **96** (2017) 072002, arXiv:1703.09665 [hep-ex].

[109] ATLAS Collaboration, *Performance of pile-up mitigation techniques for jets in pp collisions at* $\sqrt{s} = 8$ *TeV using the ATLAS detector*, Eur. Phys. J. C **76** (2016) 581, arXiv:1510.03823 [hep-ex].

[110] A. Collaboration, *Determination of jet calibration and energy resolution in proton-proton collisions at $\sqrt{s}$ = 8 TeV using the ATLAS detector*, arXiv:1910.04482 [hep-ex].

[111] ATLAS Collaboration, *Selection of jets produced in* 13 *TeV proton–proton collisions with the ATLAS detector*, ATLAS-CONF-2015-029, 2015, https://cds.cern.ch/record/2037702.

[112] ATLAS Collaboration, *ATLAS b-jet identification performance and efficiency measurement with $t\bar{t}$ events in pp collisions at $\sqrt{s} = 13$ TeV*, arXiv:1907.05120 [hep-ex].

[113] ATLAS Collaboration, *Optimisation and performance studies of the ATLAS b-tagging algorithms for the 2017-18 LHC run*, ATL-PHYS-PUB-2017-013, 2017, https://cds.cern.ch/record/2273281.

[114] M. Cacciari, G. P. Salam, and G. Soyez, *The Catchment Area of Jets*, JHEP **04** (2008) 005, arXiv:0802.1188 [hep-ph].

[115] ATLAS Collaboration, *Secondary vertex finding for jet flavour identification with the ATLAS detector*, ATL-PHYS-PUB-2017-011, 2017, https://cds.cern.ch/record/2270366.

[116] ATLAS Collaboration, *Optimisation of the ATLAS b-tagging performance for the 2016 LHC Run*, ATL-PHYS-PUB-2016-012, 2016, https://cds.cern.ch/record/2160731.

[117] ATLAS Collaboration Collaboration, G. Aad et al., *Expected Performance of the ATLAS Experiment - Detector, Trigger and Physics*, arXiv:0901.0512 [hep-ex].

[118] ATLAS Collaboration, *Measurements of b-jet tagging efficiency with the ATLAS detector using $t\bar{t}$ events at $\sqrt{s} = 13$ TeV*, JHEP **08** (2018) 089, arXiv:1805.01845 [hep-ex].

[119] ATLAS Collaboration, *Measurement of b-tagging efficiency of c-jets in $t\bar{t}$ events using a likelihood approach with the ATLAS detector*, ATLAS-CONF-2018-001, 2018, https://cds.cern.ch/record/2306649.

[120] J. Erdmann, S. Guindon, K. Kroeninger, B. Lemmer, O. Nackenhorst, A. Quadt, and P. Stolte, *A likelihood-based reconstruction algorithm for top-quark pairs and the KLFitter framework*, Nucl. Instrum. Meth. A **748** (2014) 18–25, arXiv:1312.5595 [hep-ex].

[121] ATLAS Collaboration, *Calibration of light-flavour b-jet mistagging rates using ATLAS proton–proton collision data at* $\sqrt{s} = 13$ *TeV*, ATLAS-CONF-2018-006, 2018, https://cds.cern.ch/record/2314418.

[122] ATLAS Collaboration, *Muon reconstruction performance of the ATLAS detector in proton–proton collision data at* $\sqrt{s} = 13$ *TeV*, Eur. Phys. J. C **76** (2016) 292, arXiv:1603.05598 [hep-ex].

[123] ATLAS Collaboration, *Electron reconstruction and identification in the ATLAS experiment using the 2015 and 2016 LHC proton–proton collision data at* $\sqrt{s} = 13$ *TeV*, Eur. Phys. J. C **79** (2019) 639, arXiv:1902.04655 [hep-ex].

[124] ATLAS Collaboration, *Electron and photon performance measurements with the ATLAS detector using the 2015-2017 LHC proton–proton collision data*, arXiv:1908.00005 [hep-ex].

[125] ATLAS Collaboration, *Improved electron reconstruction in ATLAS using the Gaussian Sum Filter-based model for bremsstrahlung*, ATLAS-CONF-2012-047, 2012, https://cds.cern.ch/record/1449796.

[126] ATLAS Collaboration, *Performance of missing transverse momentum reconstruction with the ATLAS detector using proton–proton collisions at* $\sqrt{s} = 13$ *TeV*, Eur. Phys. J. C **78** (2018) 903, arXiv:1802.08168 [hep-ex].

[127] *LHC SUSY Cross Section Working Group*, https://twiki.cern.ch/twiki/bin/view/LHCPhysics/SUSYCrossSections.

[128] W. Beenakker, M. Kramer, T. Plehn, M. Spira, and P. M. Zerwas, *Stop production at hadron colliders*, Nucl. Phys. **B515** (1998) 3–14, arXiv:hep-ph/9710451 [hep-ph].

[129] W. Beenakker, S. Brensing, M. Kramer, A. Kulesza, E. Laenen, and I. Niessen, *Supersymmetric top and bottom squark production at hadron colliders*, JHEP **08** (2010) 098, arXiv:1006.4771 [hep-ph].

[130] W. Beenakker, C. Borschensky, R. Heger, M. Krämer, A. Kulesza, and E. Laenen, *NNLL resummation for stop pair-production at the LHC*, JHEP **05** (2016) 153, arXiv:1601.02954 [hep-ph].

[131] ATLAS Collaboration, *Standard Model Summary Plots Summer 2019*, ATL-PHYS-PUB-2019-024, 2019, http://cds.cern.ch/record/2682186.

[132] ATLAS Collaboration, *Measurement of the $t\bar{t}$ production cross-section using $e\mu$ events with b-tagged jets in pp collisions at $\sqrt{s} = 13$ TeV with the ATLAS detector*, Phys. Lett. B **761** (2016) 136, arXiv:1606.02699 [hep-ex].

[133] ATLAS Collaboration, *Measurement of $W^{\pm}$ and Z-boson production cross sections in pp collisions at $\sqrt{s} = 13$ TeV with the ATLAS detector*, Phys. Lett. B **759** (2016) 601, arXiv:1603.09222 [hep-ex].

[134] ATLAS Collaboration, *Measurement of the cross-section for producing a W boson in association with a single top quark in pp collisions at $\sqrt{s} = 13$ TeV with ATLAS*, JHEP **01** (2018) 063, arXiv:1612.07231 [hep-ex].

[135] C. G. Lester and D. J. Summers, *Measuring masses of semiinvisibly decaying particles pair produced at hadron colliders*, Phys. Lett. **B463** (1999) 99–103, arXiv:hep-ph/9906349 [hep-ph].

[136] Y. Bai, H.-C. Cheng, J. Gallicchio, and J. Gu, *Stop the Top Background of the Stop Search*, JHEP **07** (2012) 110, arXiv:1203.4813 [hep-ph].

[137] A. J. Barr, B. Gripaios, and C. G. Lester, *Transverse masses and kinematic constraints: from the boundary to the crease*, JHEP **11** (2009) 096, arXiv:0908.3779 [hep-ph].

[138] P. Konar, K. Kong, K. T. Matchev, and M. Park, *Dark Matter Particle Spectroscopy at the LHC: Generalizing M(T2) to Asymmetric Event Topologies*, JHEP **04** (2010) 086, arXiv:0911.4126 [hep-ph].

[139] S. Frixione, E. Laenen, P. Motylinski, B. R. Webber, and C. D. White, *Single-top hadroproduction in association with a W boson*, JHEP **07** (2008) 029, arXiv:0805.3067 [hep-ph].

[140] G. Cowan, K. Cranmer, E. Gross, and O. Vitells, *Asymptotic formulae for likelihood-based tests of new physics*, Eur. Phys. J. **C71** (2011) 1554.

[141] A. L. Read, *Presentation of search results: The CL(s) technique*, J. Phys. **G28** (2002) 2693–2704.

[142] ATLAS Collaboration, *ATLAS Run 1 searches for direct pair production of third-generation squarks at the Large Hadron Collider*, Eur. Phys. J. C **75** (2015) 510, arXiv:1506.08616 [hep-ex].

[143] ATLAS Collaboration, *Search for a scalar partner of the top quark in the jets plus missing transverse momentum final state at $\sqrt{s} = 13$ TeV with the ATLAS detector*, JHEP **12** (2017) 085, arXiv:1709.04183 [hep-ex].

[144] ATLAS Collaboration, *Search for direct top squark pair production in final states with two leptons in $\sqrt{s} = 13$ TeV pp collisions with the ATLAS detector*, Eur. Phys. J. C **77** (2017) 898, arXiv:1708.03247 [hep-ex].

[145] ATLAS Collaboration, *Search for dark matter and other new phenomena in events with an energetic jet and large missing transverse momentum using the ATLAS detector*, JHEP **01** (2018) 126, arXiv:1711.03301 [hep-ex].

[146] ATLAS Collaboration, *Search for top squarks in final states with one isolated lepton, jets, and missing transverse momentum in $\sqrt{s} = 13$ TeV pp collisions with the ATLAS detector*, Phys. Rev. D **94** (2016) 052009, arXiv:1606.03903 [hep-ex].

[147] ATLAS Collaboration, *Search for top squark pair production in final states with one isolated lepton, jets, and missing transverse momentum in $\sqrt{s} = 8$ TeV pp collisions with the ATLAS detector*, JHEP **11** (2014) 118, arXiv:1407.0583 [hep-ex].

[148] ATLAS Collaboration, *Search for direct pair production of the top squark in all-hadronic final states in proton–proton collisions at $\sqrt{s} = 8$ TeV with the ATLAS detector*, JHEP **09** (2014) 015, arXiv:1406.1122 [hep-ex].

[149] ATLAS Collaboration, *Search for direct top-squark pair production in final states with two leptons in pp collisions at $\sqrt{s} = 8$ TeV with the ATLAS detector*, JHEP **06** (2014) 124, arXiv:1403.4853 [hep-ex].

[150] ATLAS Collaboration, *Search for a heavy top-quark partner in final states with two leptons with the ATLAS detector at the LHC*, JHEP **11** (2012) 094, arXiv:1209.4186 [hep-ex].

[151] ATLAS Collaboration, *Search for direct top squark pair production in final states with one isolated lepton, jets, and missing transverse momentum in $\sqrt{s} = 7$ TeV pp collisions using $4.7\,fb^{-1}$ of ATLAS data*, Phys. Rev. Lett. **109** (2012) 211803, arXiv:1208.2590 [hep-ex].

[152] ATLAS Collaboration, *Search for a supersymmetric partner to the top quark in final states with jets and missing transverse momentum at $\sqrt{s} = 7$ TeV with the ATLAS detector*, Phys. Rev. Lett. **109** (2012) 211802, arXiv:1208.1447 [hep-ex].

[153] CMS Collaboration, *Search for direct production of supersymmetric partners of the top quark in the all-jets final state in proton–proton collisions at* $\sqrt{s} = 13$ *TeV*, JHEP **10** (2017) 005, arXiv:1707.03316 [hep-ex].

[154] CMS Collaboration, *Search for top squark pair production in pp collisions at* $\sqrt{s} = 13$ *TeV using single lepton events*, JHEP **10** (2017) 019, arXiv:1706.04402 [hep-ex].

[155] CMS Collaboration, *Search for top squarks and dark matter particles in opposite-charge dilepton final states at* $\sqrt{s} = 13$ *TeV*, Phys. Rev. D **97** (2018) 032009, arXiv:1711.00752 [hep-ex].

[156] CMS Collaboration, *Search for top squarks decaying via four-body or chargino-mediated modes in single-lepton final states in proton–proton collisions at* $\sqrt{s} = 13$ *TeV*, JHEP **09** (2018) 065, arXiv:1805.05784 [hep-ex].

[157] CMS Collaboration, *Search for top-squark pair production in the single-lepton final state in pp collisions at* $\sqrt{s} = 8$ *TeV*, Eur. Phys. J. C **73** (2013) 2677, arXiv:1308.1586 [hep-ex].

[158] CMS Collaboration, *Search for direct pair production of supersymmetric top quarks decaying to all-hadronic final states in pp collisions at* $\sqrt{s} = 8$ *TeV*, Eur. Phys. J. C **76** (2016) 460, arXiv:1603.00765 [hep-ex].

[159] CMS Collaboration, *Search for direct pair production of scalar top quarks in the single- and dilepton channels in proton–proton collisions at* $\sqrt{s} = 8$ *TeV*, JHEP **07** (2016) 027, arXiv:1602.03169 [hep-ex].

[160] CMS Collaboration, *Searches for third-generation squark production in fully hadronic final states in proton–proton collisions at* $\sqrt{s} = 8$ *TeV*, JHEP **06** (2015) 116, arXiv:1503.08037 [hep-ex].

[161] CMS Collaboration, *Search for supersymmetry in events with soft leptons, low jet multiplicity, and missing transverse energy in proton–proton collisions at* $\sqrt{s} = 8$ *TeV*, Phys. Lett. B **759** (2016) 9, arXiv:1512.08002 [hep-ex].

[162] CMS Collaboration, *Search for supersymmetry in final states with missing transverse energy and 0, 1, 2, or* $\geq$ *3 b-quark jets in 7 TeV pp collisions using the variable* α_T, JHEP **01** (2013) 077, arXiv:1210.8115 [hep-ex].

[163] CMS Collaboration, *Inclusive search for supersymmetry using razor variables in pp collisions at* $\sqrt{s} = 7$ *TeV*, Phys. Rev. Lett. **111** (2013) 081802, arXiv:1212.6961 [hep-ex].

[164] *Summary plots from the ATLAS Supersymmetry physics group*, https://atlas.web.cern.ch/Atlas/GROUPS/PHYSICS/CombinedSummaryPlots/SUSY/index.html.

[165] ATLAS Collaboration, *Search for supersymmetry in final states with charm jets and missing transverse momentum in* 13 *TeV pp collisions with the ATLAS detector*, JHEP **09** (2018) 050, arXiv:1805.01649 [hep-ex].

[166] ATLAS Collaboration, *Probing the Quantum Interference between Singly and Doubly Resonant Top-Quark Production in pp Collisions at* $\sqrt{s} = 13$ *TeV with the ATLAS Detector*, Phys. Rev. Lett. **121** (2018) 152002, arXiv:1806.04667 [hep-ex].

[167] ATLAS Collaboration, *Athena*, 2020. https://gitlab.cern.ch/atlas/athena.

[168] V. Kostyukhin, *VKalVrt - package for vertex reconstruction in ATLAS.*, Tech. Rep. ATL-PHYS-2003-031, CERN, Geneva, Aug, 2003. https://cds.cern.ch/record/685551.

[169] ATLAS Collaboration, *Performance of vertex reconstruction algorithms for detection of new long-lived particle decays within the ATLAS inner detector*, ATL-PHYS-PUB-2019-013, 2019, https://cds.cern.ch/record/2669425.

[170] ATLAS Collaboration, *Search for direct top squark pair production in the 3-body decay mode with a final state containing one lepton, jets, and missing transverse momentum in* $\sqrt{s} = 13$ *TeV pp collision data with the ATLAS detector*, ATLAS-CONF-2019-017, 2019, https://cds.cern.ch/record/2676594.

[171] Planck Collaboration, P. A. R. Ade et al., *Planck 2013 results. XVII. Gravitational lensing by large-scale structure*, Astron. Astrophys. **571** (2014) A17, arXiv:1303.5077 [astro-ph.CO].

[172] ATLAS Collaboration, *Summary of the ATLAS experiment's sensitivity to supersymmetry after LHC Run 1 — interpreted in the phenomenological MSSM*, JHEP **10** (2015) 134, arXiv:1508.06608 [hep-ex].

[173] N. Arkani-Hamed, A. Delgado, and G. F. Giudice, *The Well-tempered neutralino*, Nucl. Phys. **B741** (2006) 108–130, arXiv:hep-ph/0601041 [hep-ph].

[174] *CMS Supersymmetry Physics Results*, https://twiki.cern.ch/twiki/bin/view/CMSPublic/PhysicsResultsSUS.

[175] ATLAS Collaboration, *Searches for electroweak production of supersymmetric particles with compressed mass spectra in* $\sqrt{s} = 13$ TeV *pp collisions with the ATLAS detector*, Phys. Rev. D **101** (2020) 052005, arXiv:1911.12606 [hep-ex].

[176] ATLAS Collaboration, *Search for long-lived charginos based on a disappearing-track signature in pp collisions at* $\sqrt{s} = 13$ *TeV with the ATLAS detector*, JHEP **06** (2018) 022, arXiv:1712.02118 [hep-ex].

[177] A. Heister, S. Schael, R. Barate, R. Bruneliere, I. De Bonis, D. Decamp, C. Goy, S. Jezequel, J.-P. Lees, F. Martin, et al., *Search for charginos nearly mass degenerate with the lightest neutralino in e+ e- collisions at centre-of-mass energies up to 209 GeV*, Physics Letters B **533** (2002) 223–236, arXiv:hep-ex/0203020.

[178] H. Fukuda, N. Nagata, H. Oide, H. Otono, and S. Shirai, *Cornering Higgsinos Using Soft Displaced Tracks*, Physical review letters **124** (2020) 101801, arXiv:1910.08065 [hep-ph].